

Dipartimento di / Department of

Fisica

Dottorato di Ricerca in / PhD program Fisica Ciclo / Cycle XXXIV

Curriculum in (se presente / if it is) Plasma Physics and Biophysics

TITOLO TESI / THESIS TITLE

Development of Nuclear Radiation Based Tomography Methods for Runaway Electrons and Fast Ions in Fusion Plasmas

Cognome / Surname Panontin Nome / Name Enrico

Matricola / Registration number 761719

Tutore / Tutor: Dott. Marco Tardocchi

Supervisor: Prof. Massimo Nocente

(se presente / if there is one)

Co-supervisor: Dott. Andrea Dal Molin

(se presente / if there is one)

Coordinatore / Coordinator: Prof. Marta Calvi

ANNO ACCADEMICO / ACADEMIC YEAR 2020/2021



UNIVERSITY OF MILANO-BICOCCA

DEPARTMENT OF PHYSICS "G. OCCHIALINI"

PHD PROGRAM IN PHYSICS AND ASTRONOMY – CYCLE XXXIII
PLASMA PHYSICS CURRICULUM

**DEVELOPMENT OF NUCLEAR RADIATION BASED
TOMOGRAPHY METHODS FOR RUNAWAY
ELECTRONS AND FAST IONS IN FUSION PLASMAS**

Candidate:
Enrico Panontin

Tutor:
Dr. Marco Tardocchi

Registration Number:
761719

Supervisor:
Prof. Massimo Nocente

Co-supervisor:
Dr. Andrea Dal Molin

Coordinator of the PhD Board of Professors for the Physics Department:
Prof. Marta Calvi

ACADEMIC YEAR 2020/2021

UNIVERSITY OF MILANO-BICOCCA

Summary

Department of Physics "G. Occhialini"

Doctor of Philosophy

DEVELOPMENT OF NUCLEAR RADIATION BASED TOMOGRAPHY METHODS FOR RUNAWAY ELECTRONS AND FAST IONS IN FUSION PLASMAS

by Enrico Panontin

Fast particles, both electrons and ions, play an important role for the success of the next generation of large tokamak devices, such as ITER, that will prove the feasibility of magnetically confined thermonuclear fusion as an energy source. Ions accelerated by external heating or born in fusion reactions can reach energies in the MeV range. Their primary role is to sustain the plasma temperature and the fusion reaction rate, thus significant efforts have been put into the development of efficient heating schemes and in the improvement of their confinement. On the other hand, during fast terminations of plasma pulses on tokamaks, electrons can accelerate to relativistic velocities, entering the runaway regime. Runaway electrons have enough energy to seriously damage the plasma facing components of large tokamaks, thus mitigation techniques are under study in view of ITER operations.

This thesis focuses on the implementation of deconvolution techniques for the reconstruction of the fast particles distributions from a measurement of their gamma/hard X-ray emission in the MeV energy range. The problem was approached from two different perspectives: the unfolding of the runaway electrons velocity-space distribution from spectroscopic measurements of their bremsstrahlung emission, and the tomographic reconstruction of the density distribution of both fast ions and runaway electrons from the integrated measurement of their MeV range emission performed with multiple detectors. These algorithms were implemented in an open source Python library.

Four deconvolution algorithms were implemented for the unfolding of runaway electrons energy distribution: singular value decomposition, maximum likelihood - expectation maximization, Tikhonov regularization and Poissonian regularization.

The transfer matrix necessary for this inversion was calculated using the GENESIS code for estimating the probability of bremsstrahlung emission and the MCNP code for computing the detector response function. The detector response function was calculated for all the hard X-rays diagnostics systems installed at the Joint European Torus and ASDEX Upgrade tokamaks. The performance of the four methods was then compared over both synthetic and experimental spectra, the latter being measured at ASDEX Upgrade. Maximum likelihood - expectation maximization was found to be the most accurate in the reconstruction of both the runaway electrons energy distribution and their average and maximum energies. The robustness of the four methods against experimental limitations, such as low-energy cut and low statistics, was also investigated.

In the path towards the generalization of these unfolding algorithms to the reconstruction of the runaway electrons 2D velocity-space distribution, the transfer matrices in energy and pitch were calculated for all the hard X-ray diagnostics installed at JET. The weight-function formalism was adopted, which allows studying the sensitivity of the detectors to different energy and pitch regions. The matrices showed a sensitivity peak in the pitch axis which is determined by the angle between the line of sight and the magnetic field.

Finally, the gamma camera upgrade installed at the Joint European Torus, with its 10 by 9 lines of sight that observe a poloidal section of the tokamak from two perpendicular projections, allows reconstructing the spatial distribution of fast particles. A tomographic algorithm that makes use of smoothing along the magnetic field lines was implemented. This tomography was first applied to recent three-ion radio frequency heating experiments in D-³He mixed plasmas, during which the gamma camera detected the 16.4 MeV γ -rays from ${}^3\text{He}(\text{D}, \gamma(16.4 \text{ MeV}){}^5\text{Li}$ reactions. The spatial distribution of the α -particles born in ${}^3\text{He}(\text{D}, p){}^4\text{He}$ reactions was reconstructed and the results were used to validate TRANSP simulations. This is particular relevant in view of the reconstruction of fusion alpha particles produced by the DT reaction in future burning plasmas experiments. The tomographic algorithm was also applied to the reconstruction of the runaway electrons spatial profiles during plasma disruptions.

Contents

Summary	iii
I Introduction	1
1 Introduction	3
1.1 Thermonuclear fusion	4
1.2 Plasma heating	7
1.3 Runaway electrons	10
1.4 Plasma disruptions	12
II Analysis Methods for HXR Detectors	15
2 Hard X-ray diagnostics system	17
2.1 ASDEX Upgrade	18
2.1.1 The detector in the Bragg bunker	18
2.1.2 REGARDS	19
2.2 Joint European Torus	21
2.2.1 The Gamma Camera Upgrade	21
2.2.2 The hard X-ray spectrometers	25
3 Deconvolution algorithms	27
3.1 Singular Value Decomposition	29
3.2 Tikhonov regularization	33
3.3 Poissonian regularization	34
3.4 Maximum Likelihood using Expectation Maximization	35
3.5 Confidence bands	40
3.6 Cumulative statistics	40
III Data Analysis	45
4 Reconstruction of the 1D energy distribution	47
4.1 Transfer matrix	48
4.2 Synthetic tests	52

4.3	Application at ASDEX Upgrade	59
5	Weight functions in 2D velocity-space	67
5.1	2D velocity-space weight functions	67
5.2	Application at JET	74
6	Tomography with the upgraded JET Gamma Camera	81
6.1	Tomographic reconstruction	82
6.2	Alpha-particles source in three-ions ICRF scheme heating	86
6.3	Runaway electrons spatial profile	95
	Conclusions	103
	Bibliography	109
IV	Papers	119

Part I

Introduction

Chapter 1

Introduction

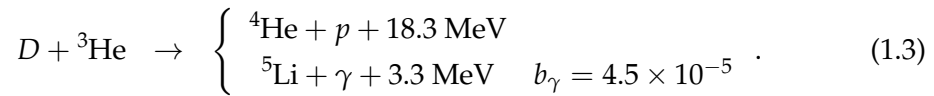
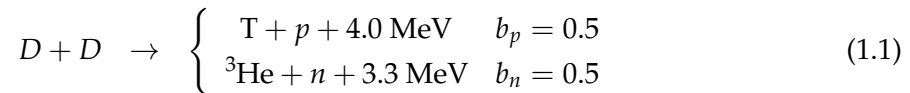
The environmental crisis that is prospecting in front of human kind, driven by the ever growing energetic consumption of modern society, is by all means the greatest issue we have to face in our near future. In order to stop, or at least slow down, the ongoing climate change, it is essential to reduce our emissions of greenhouse gas via a reorganization of the energetic chain production. The growth of electric devices, such as electric means of transport, could give a significant drive in that direction if combined with new, green energy sources. If we exclude nuclear fission, due to both its intrinsic safety risks and the production of long lasting radioactive wastes, at present no technology is ready to replace fossil fuels as the core source of energy of the electricity grid.

Many lines of research are currently active in this field, such as the development of battery-to-grid systems based on hydrogen for storing the energy produced by renewable sources. Among the others, nuclear fusion is one of the best candidates to fill this gap, thanks to its low carbon emissions and to abundant fuel supplies that could satisfy the global energy demand for thousands of years. Moreover, in contrast with nuclear fission power plants, the designs currently proposed for the realization of commercial fusion reactors are intrinsically safe. For instance, those devices that rely on magnetic confinement of the fuel operate at low pressures and in these working conditions a chain reaction cannot take place. In this design, external control over the fuel must be ensured at all time to keep the temperature high enough for the fuel to remain in the plasma state and produce energy. If the density increases by accident or if the control of the plasma is lost, the temperature of the fuel drops and the fusion reactions stop almost immediately. On the other hand, those devices that rely on inertial confinement generate low yield plasma discharges. Thus the maximum energy that can be released by a single pellet of fuel, in case the of a complete consumption of the pellet, is minimum and cannot damage the reactor components. Both the designs here cited are detailed in the remaining of the chapter, with particular attention to magnetic confinement fusion.

1.1 Thermonuclear fusion

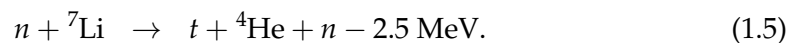
The aim of nuclear fusion research is to exploit, for the commercial production of energy, the same processes that take place in the core of the Sun, where light nuclei are combined together to form heavier elements. If the initial nuclei have atomic masses below $A = 56$, the total mass of the products will be lighter than the mass of the reactants and the reaction will be exothermic. For heavier elements, the inverse is true and energy can be released by splitting single atoms in smaller fragments, that is by nuclear fission [1].

When compared to the core of the Sun, the lower pressures that can be reached in a laboratory make the proton-proton cycle reactions non suitable for the design of a commercial fusion reactor. The desirable reactions should minimize the Coulomb repulsion between the reactants, that is low atomic number elements, and maximize the cross section of the fusion reaction, that is isotopes with high A [1]. The best candidates are those reactions involving deuterium (D) and tritium (T), which are heavy hydrogen isotopes with $A = 2$ and $A = 3$:



In equation (1.3) the less frequent gamma-ray branch [2] has been also reported because of its relevance for chapter 6, where it has been used for studying the generation of α -particles in D – ${}^3\text{He}$ mixed plasmas. Among the listed reactions, the deuterium tritium one is the most promising, since it has the highest cross section σ_{DT} at low centre-of-mass energies ($E < 200$ keV), reaching its maximum at $E = 65$ keV [3].

The abundance of deuterium on earth (it is $\approx 0.02\%$ of the hydrogen found in ocean water) makes it the perfect fuel for a long-lasting energetic source. Tritium, on the other hand, is a highly volatile element with a half-life of ≈ 12.3 years. It is produced on nuclear fission facilities as a radioactive product, but it can also be generated on site irradiating with fusion-born neutrons a breeding blanket made of Lithium. Lithium and neutrons generate tritium according to:



By moderating the fusion-born neutrons, the breeding blanket performs two tasks: transforming neutrons and Li into tritium that can be bred into the reactor and

converting the kinetic energy of the neutrons into thermal energy that can be further converted into thermoelectric power. Unfortunately, ${}^7\text{Li}$ is the most abundant isotope on earth, thus part of the net energy production of the DT reactions must be used either to sustain the $n + {}^7\text{Li}$ reactions or to enrich the blanket with ${}^6\text{Li}$.

The best strategy to extract energy from DT reactions is to heat a deuterium-tritium gas (50% each) so that a significant fraction of the particles population has a kinetic energy around 65 keV. The rate of the fusion reactions in a D-T plasma can be calculated as:

$$R = \int_V n_D n_T \int v_{rel} \sigma_{DT}(v_{rel}) f_D(\underline{x}, \underline{v}_D) f_T(\underline{x}, \underline{v}_T) d\underline{v}_D d\underline{v}_T d\underline{x} \quad (1.6)$$

where n_D and n_T are the deuterium and tritium densities, v_{rel} the relative velocity between a D and a T particles, and f_D and f_T are the deuterium and tritium phase-space distributions. The aim is to increase this reaction rate enough to produce more power than what is required for operating the device in use. For this to happen, the average temperature of the gas mixture must be of the order of 10 keV (approximately a order of magnitude more than the estimated temperature in the Sun core, which is about $T = 1.3$ keV), meaning that we are dealing with a hot ionized gas named plasma [4]. This is a direct consequence of the lower densities of laboratory plasmas when compared to the Sun core.

At present there are two leading lines of research for confining thermonuclear plasmas. The inertial confinement fusion (ICF) generates and confines a high-temperature and high-density plasma by means of high-energy lasers. The role of these lasers is to both compress and heat the pellet as uniformly as possible, in order to avoid the generation of Rayleigh–Taylor instabilities. To this extent, two scheme are currently under study: the *direct drive*, where lasers are pointed directly on the pellet, and the *indirect drive*, where lasers are used to heat small cylinders of heavy metal that in turn emit X-rays that heat the pellet. The second line of research for achieving commercial fusion is the development of magnetic confinement fusion (MCF) devices, that confine the plasma by means of magnetic fields. Here the plasma density is lower than ICF, thus higher temperatures and confinement times must be obtained. At present MCF is unanimously considered the most advanced line of research towards energy production, with the Joint European Torus (JET) that obtained in 1997 the record for the highest ratio $Q = \frac{\text{energy produced}}{\text{energy consumed}} \approx 0.67$ during a discharge, albeit in a transient phase. In 2021 JET also obtained the record for the highest total energy output during steady state operations ever achieved in a fusion reactor, with a energy production of $E = 59$ MJ in a 5 s pulse. In the next few years the MCF community aims at starting the operation on ITER, a new tokamak machine having ≈ 10 times the volume of JET. ITER should work as the "proof of principle"

for commercial fusion, proving that tokamaks are a mature technology able to sustain a $Q = 10$ for about 10 minutes. The great difference in the device size, with respect to its predecessors, poses a series of unknowns regarding ITER operations that drive the research conducted on present devices. There are some phenomena that do not represent a problem on present machines, which are now referred as middle-size tokamaks, but are expected to become a criticality on ITER. An example is the formation of relativistic particles during rapid and uncontrolled termination of a plasma pulse, which will be discussed in further details in section 1.3.

To describe the confinement of a MCF machine, let's consider a uniform magnetic field \underline{B} : it exerts a force on charged particles in motion, termed Lorentz force, perpendicular to their velocity and to the field itself. In this situation the particles are confined in the two directions perpendicular to \underline{B} , being free to move along the magnetic field lines. Some degree of confinement in the parallel direction can be achieved already in linear configurations by varying the module of \underline{B} along the field lines, such as in mirror machines. However a much more effective approach is to close the B-lines on themselves in a toroidal configuration. That is the main idea behind tokamak machines [5], which at present are the most successful design for a fusion reactor based on magnetic confinement. Assuming a purely toroidal magnetic field, the magnetic field would be curved and non uniform, in particular \underline{B} is more intense close to the axis of the torus. This leads to drifts in the particle motion directed away from the torus axis. In order to restore the confinement, a poloidal magnetic field is necessary: such poloidal field twists the magnetic field lines, which become helicoidal, and average to zero the particles drift. In tokamaks the poloidal B-field is mostly generated driving a toroidal plasma current, which is in turn inducted by an increasing external current driven in the central solenoid. Since the central solenoid cannot increase its current ad libitum, the tokamak is a pulsed machine. Moreover, if the coils generating the toroidal magnetic field are not actively cooled, they suffer from overheating and the operation time of the tokamak is further reduced.

The present thesis lies within the frame of MCF and has been partly conducted at JET and ASDEX Upgrade (AUG), two tokamak machines where I participated onsite to their experimental campaigns. During these missions, as part of the CNR-Bicocca Milan Neutron and Gamma-ray group, I mostly operated the hard X-ray diagnostics installed on those machines during plasma discharges. On AUG I also contributed to the installation and the definition of the shielding along the line of sight of REGARDS, a new hard X-ray diagnostics optimized for measuring the radiation emitted by runaway electrons in the MeV energy range. The work here presented covers the analysis of the data collected during the aforementioned experimental campaigns, in particular the tomography and unfolding of nuclear (mostly hard X-ray) spectra emitted by runaway electrons and fast ions. The experimental framework, on which the analysis technique introduced in the next chapters are build on, can be

divided in two main lines: the study of runaway electrons formation and mitigation in view of ITER operations (chapters 4, 5 and section 6.3) and the study of fast-ions dynamics in experiments where radio frequency heating has been employed to sustain the plasma (chapter 6).

1.2 Plasma heating

Plasma heating plays a key role both for starting a plasma discharge and, at least in the first generations of fusion reactors, for sustaining the desired reaction rate throughout the pulse. In this section, the auxiliary heating systems currently employed at JET and AUG are presented.

Ohmic heating

The first mechanism that heats the plasma at the beginning of a discharge, when the temperature is low, is ohmic heating. The toroidal plasma current, responsible for the generation of the poloidal magnetic field, dissipates part of its energy in the plasma according to Joule's first law:

$$P \propto IR^2 = \int_V \rho J^2 d\underline{x} \quad (1.7)$$

where J is the plasma current density and ρ the plasma resistivity. Since the resistivity decreases with the plasma temperature, according to $\rho \propto T^{-\frac{3}{2}}$ [4], while the power loss increases with the plasma temperature, this heating system is effective in the initial ramp up, approximately up to few keV. For further heating the plasma up to the 14 keV goal, other heating systems must be employed.

Neutral beam injection

Neutral beam injection (NBI), nomen omen, injects energetic particles into the plasma, which transfer their energy to the background plasma through collisions. The injected particles must be neutral so to elude the magnetic confinement and penetrate as close to the plasma core as possible: their penetration length depends on the efficiency with which the plasma is able to ionize them. Once ionized, the beam forms a population of suprathermal particles with energies up to hundreds of keV that can be accelerated further by ion cyclotron resonance heating in some scenarios. The NBI direction can be normal or tangential, in the latter case the injected particles also contribute to drive part of the toroidal plasma current, reducing the requirements on the central solenoid and thus increasing the duration of a pulse.

On JET these neutrals are generated from positive ions accelerated in strong electric fields up to 160 keV and then neutralized [6]. This system can produce routinely up to 30 MW of power injected into the plasma. On ITER, in order to reach the plasma

core, each particle must enter the plasma with an energy of ≈ 1 MeV, otherwise it would be ionized right in the plasma edge [7]. At those energies, neutralization of positive ions becomes poorly efficient and a new generation of NBI based on the acceleration of negative ions is currently under development [8–10].

Ion cyclotron resonance heating

A particle moving in a magnetic field follows a helicoidal trajectory along the field lines with a rotation frequency $\omega_c = \frac{|q|B}{m}$, named cyclotron frequency. It can efficiently absorb the energy carried by an electromagnetic wave having frequency ω if the following resonance condition holds:

$$\omega = N\omega_c - \underline{k} \cdot \underline{v}_{\parallel} \quad (1.8)$$

with $N \in \mathbb{N}$, \underline{k} being the wave-number of the electromagnetic oscillation, $\underline{v}_{\parallel}$ being the component of the particle velocity parallel to the magnetic field and $\underline{k} \cdot \underline{v}_{\parallel}$ representing the Doppler shift. In order to couple with the particles gyration, the wave must further have an elliptic polarization and rotate according to the particle rotation: the left-handed component (E_+) couples with the ions, while the right-handed one (E_-) with the electrons. Since the magnetic field B radial profile is not uniform in a tokamak, the choice of the wave frequency set both the species which will absorb its energy and the position of the resonant layer.

The heating by means of an electromagnetic wave with left-handed polarization (i.e. polarized in the ions direction of rotation) and having a multiple of the ion cyclotron frequency is termed *ion cyclotron resonance heating* (ICRH). If the plasma is made of a single ion species, the response of the resonant particles blocks the propagation of the left-handed component of the fundamental harmonic (i.e. of those waves having $N = 1$) and $E_+ \approx 0$ in the ion cyclotron layer [11]. For higher harmonics ($N \geq 2$) the fraction $\frac{E_+}{E_-}$ of the left hand component that propagates to the resonant layer is significantly higher than when $N = 1$, since [12]:

$$\left| \frac{E_+}{E_-} \right|^2 \approx \left(\frac{N-1}{N+1} \right)^2 \quad (1.9)$$

and plasma heating is still possible. In this case the energy is transferred most to fast ions, thus harmonic heating should be used in combination with other heating systems, such as NBI, that creates a supra-thermal population [12, 13].

The propagation of the fundamental harmonic is still possible in a plasma made of two ion species having different $\frac{Z}{m}$ ratio [11], where Z is the particle atomic number and m is its mass. In this situation the fraction of left-handed component $\frac{E_+}{E_-}$ is enhanced in proximity of the ion-ion hybrid layer. Depending on the concentration of the second species, there can be two heating scheme. For high concentrations (e.g.

$n(^3\text{He}) > 10\%$ in D plasmas) the external wave is converted into short wavelength Bernstein waves at the ion-ion hybrid resonance layer, which in turn transfer their energy to the plasma electrons [14]. This is called *mode conversion scheme*. If the concentration of the second species is reduced to few percents of the main species, than *minority heating* takes place. In this situation the minority cyclotron resonance layer is close to the ion-ion hybrid layer and most of the wave energy is damped on the minority species [11, 15]. On JET, D plasmas with hydrogen impurities are often heated using the deuterium second harmonic because its frequency corresponds to the fundamental harmonic of the hydrogen, resulting in a more efficient plasma heating.

A novel minority heating scheme, called *three ion radio frequency heating scenario*, makes use of three ion species [12, 15]. The third species is injected with concentration of few per mille or higher in a mixed plasma with two main species. The latter two determine the wave propagation and if the charge-to-mass ratio of the minority species is $\frac{Z_2}{A_2} < \frac{Z_i}{A_i} < \frac{Z_1}{A_1}$ (with the subscripts 1 and 2 indicating the two main species), then its cyclotron resonance layer lies in a region where the wave is almost completely E_+ polarized. Thanks to the favourable conditions near the minority resonance, this scheme is more efficient than traditional minority heating and it can work even if the third species is present at impurity concentrations. An alternative scheme, where the third species can have same $\frac{Z}{A}$ ratio as one of the two main species, takes advantage of the Doppler shift in equation (1.8) [16, 17]. The injected power then is absorbed by fast particles, typically injected by NBI in a two-stage heating scheme, in proximity of the ion-ion hybrid layer. This is the case of the experiments analysed in section 6.2, where D_{NBI} are accelerated in a $D^3\text{He}$ mixed plasma from tens of keV up to energies in the MeV range [17]. Apart from an efficient particles acceleration, these experiments also reported the generation of co-passing fast deuterons and the intrinsic generation of a non-monotonic q-profile [17], suggesting future use of this scheme for driving the plasma current and modifying the q-profile.

Ignition

In DT reactions, the fusion-born neutrons with 14 MeV of energy escape the magnetic confinement and are captured by the breeding blanket, producing tritium and heat that will be converted into electricity. On the other hand, analogously to NBI, the 3.5 MeV α -particles generated in this reactions remain confined in the plasma core and transfer their energy to the plasma itself through collisions [18]. The alphas transfer their energy mostly to electrons, which in turn will heat the ions. This process takes place in few seconds (≈ 2 s), meaning that the energy confinement time of a tokamak must be comparable with this interval of time in order to allow the alphas effectively heating the plasma.

α -particles heating is the mechanism through which fusion sustains itself. The power released into the plasma by the DT fusion reactions via the α -particles can be calculated as:

$$P_\alpha = \frac{Q_{DT}}{5} R_{DT} \quad (1.10)$$

where the energy released in the DT reaction Q_{DT} can be read from (1.2), the factor 5 at denominator comes from the conservation of the centre-of-mass energy of the system and the reaction rate R_{DT} can be calculated according to 1.6. If the plasma could reach a state in which $P_\alpha > P_{loss}$ than there would be no need for external heating: this is the so called ignition. In the near future, one of the main ITER goals is to multiply the energy needed for operating the machine by a factor $Q = 10$, in this scenario the power released into the plasma by fusion-born α -particles should be $P_\alpha = 100$ MW. For this reason lots of efforts have been made to study of α -particles dynamics on present machines, such as JET, and to prove the actual feasibility of alpha heating.

1.3 Runaway electrons

The motion of an electron in a plasma is subject to a friction force that is induced by the sum of all the Coulomb collisions with the background particles in the plasma. This dissipative force is always directed opposite to the particle velocity, while its magnitude depends on the speed of the particle.

For low-energy particles, the friction force depends linearly on the electron speed v , which means that, if the electron is subject to an external acceleration, it will accelerate up to a velocity for which the friction force equals the external force (for a visual description of the velocity dependence of the friction force, see figure 1 of [19]). This is the so called *resistive regime*, in which the dragging force is able to control the maximum velocity of the plasma particles. The resistive regime extends up to approximately the electron thermal speed, for which the friction force has a maximum. For non relativistic particles moving faster than the thermal speed the friction force decays as v^{-2} [19, 20], meaning that there exists a critical magnitude above which an external force will be able to accelerate an electron up to relativistic energies without any control from the plasma viscosity. This is the *runaway regime*. When the electron becomes relativistic (i.e. $v \approx m_0 c^2$) the friction experienced by the particle starts increasing again as its velocity approaches c , thanks to relativistic effects and to radiative losses due to bramsstrahlung and synchrotron emissions [19, 21].

From classic electrodynamics, the friction force for electrons having speed $v_{th} < v < m_0 c^2$ can be expressed as [20]:

$$F = \frac{1}{4\pi\epsilon_0} \frac{e^4 n_e \ln \Lambda}{m_e v^2} \quad (1.11)$$

where ϵ_0 is the vacuum permittivity, e the electron charge, n_e the background electron density, $\ln \Lambda$ the Coulomb logarithm and m_e the electron mass. Consider an external electric field applied to the plasma, such as the electric field associated with the loop voltage $E = \frac{V_{loop}}{2\pi R}$. Since the friction force has a minimum for $v_e = m_e c^2$, there exists a *critical field* E_C below which the external electric field is always balanced by the friction force, regardless of the electron speed [20, 21]:

$$E_C = \frac{1}{4\pi\epsilon_0} \frac{e^3 n_e \ln \Lambda}{m_e c^2} \approx 0.08 n_{20} \quad (1.12)$$

where n_{20} is the electron density in units of 10^{20} m^{-3} . Since the resistivity is maximum for $v = v_{th}$, there also exists a *Dreicer field* above which the external electric field is able to accelerate all electrons in the plasma population to the runaway regime [20, 22, 23]:

$$E_D = \frac{1}{4\pi\epsilon_0} \frac{e^3 n_e \ln \Lambda}{m_e v_{th}^2}. \quad (1.13)$$

For an electric field E such that $E_C < E < E_D$, there will be a certain electron velocity v_C for which the external force is equal to the plasma friction force. The plasma population, then, can be divided into two parts: those particles having $v < v_C$ remain in the resistive regime, while those particles moving faster than the critical velocity ($v > v_C$) are accelerated to relativistic energies and are termed *runaway electrons*.

During tokamak operations, strong electric fields may arise in the initial and final phases of a discharge. In particular during plasma disruptions, which are discussed in more details in section 1.4, strong inductive fields can accelerate the high energy tail of the electron population into the runaway regime. Coulomb collisions can help this process as a slow electron might gain enough momentum to enter the runaway regime as a result of a collision with another thermal electron. This generation process is known as the *primary production* of runaway electrons and it is the most relevant mechanism in middle size tokamaks [19, 24]. Once a seed of runaway electrons has been created, an avalanche mechanism might establish in which thermal electrons enter the runaway regime after a collision with a relativistic electron. This is the *secondary generation* [24, 25] and it becomes more relevant as the size of the tokamak increases. For ITER it is expected that the secondary production can exponentially increase the runaway electron population during disruptions. This poses a serious threat to ITER operations, since simulations predict that runaway electrons might reach tens of MeV of energy and some MA of current, having enough power to damage the ITER first wall. For this reason lots of efforts have been put into the study of runaway electrons generation and suppression on present machines.

One possible way for studying the runaway electrons dynamics is by measuring the radiation they emit. The present work, in particular, is centered on the study of the bremsstrahlung emission during Coulomb collisions between runaway electrons

and ions in the background plasma. In this process a photon is emitted with an energy equal to the difference between the initial and final energy of the electron (due to the difference in mass and energy the ion is considered to be fixed throughout the collision). Since runaway electrons can reach energies in excess of 10 MeV on AUG and JET, the emitted bremsstrahlung spectrum will be in the hard X-ray region and its measurement rest on the detectors illustrated in chapter 2. An example of a bremsstrahlung spectrum measured during a AUG pulse is shown in figure 4.8(a). The final energy of the particle after the collision depends on the impact parameter b , which is the distance between the unperturbed trajectory of the particle and the ion position. This allows a statistical treatment of the bremsstrahlung interaction, which results in the calculation of the probability, for a runaway electron of fixed energy, of emitting a photon with a certain energy as a result of the collisions experienced in a ion plasma [26, 27]. Analysis techniques for reconstructing the runaway electrons distribution from HXR spectroscopic measurements using the semi-empirical cross-section introduced in ref. [26, 27] are the topic of chapters 4 and 5, which are based on the deconvolution methods presented in chapter 3.

1.4 Plasma disruptions

Under certain conditions, plasma discharges may encounter an abrupt and rapid termination, called disruption, during which the plasma energy as well as the energy stored in the external magnetic field are dissipated on the plasma facing components of the tokamak [28]. These events represent a major threat to large machines, such as ITER, structural integrity on two basis. On one hand the fast dissipation of the plasma energy is expected to induce a non negligible erosion on ITER divertor that will reduce its usable lifetime. On the other hand, the strong inductive electric fields induced by these events can accelerate a significant fraction of plasma electrons to relativistic energies. This so called *runaway electron* population has enough energy to locally damage ITER first wall.

Disruptions are usually started by the growth of magnetohydrodynamic instabilities that dissipate a large fraction of the plasma thermal energy [24, 28]. This first phase, that is expected to last $\approx 100 \mu\text{s}$ in current middle size tokamaks and 1 ms on ITER, is called *thermal quench*. The subsequent drop in temperature increases the plasma resistivity, which in turn make the plasma current decrease. This is the second phase of the disruption, named *current quench*, that can last ≈ 5 ms on middle size tokamaks and ≈ 35 ms on ITER. As a consequence of the current quench, strong toroidal electric fields are induced. If these electric fields are strong enough, the force they exerted on the plasma electrons exceeds the plasma friction force and a fraction of the electron population is accelerated to relativistic energies. On ITER it is expected

that these runaway electrons may reach tens of MeV of energy and drive up to 10 MA of current (approximately 70% of the pre-disruption plasma current).

Disruptions events on present machines are not common, thus, for studying the runaway electron generation, dedicated scenarios have been developed to trigger a disruption [29]. At AUG and JET, this is achieved by means of the injection of massive quantities of a noble gas, typically Ar. This increases the plasma density (and its resistivity) abruptly, forcing a fast reduction of the plasma current and the insurgence of plasma instabilities that trigger the thermal and current quench.

As already said, due to the danger related to the occurrence of runaway electrons, there is much interest in the study of effective means for mitigating their effects on future machines. Various mitigation techniques have been proposed to prevent that a runaway electron beam born during a disruption provokes critical damages to ITER components [24, 29, 30]. A first approach on middle size tokamaks is to inject high quantities of noble gases into the plasma, in the so called *massive gas injection* (MGI) [29, 31, 32]. This has two main effects: first it increases the plasma density, inducing a higher plasma resistivity that dissipates the runaway electrons beam via Coulomb collisions, and second it increases the critical electric field E_C reducing the fraction of electron population that could lead to the primary production. If high-Z noble gases are used, such as Ar, this technique also increases the runaway electron radiation losses due to bremsstrahlung emission. A drawback is that noble gases are hard to clean from the vessel after the termination of the disruption and might remain at trace levels in subsequent pulses. On larger size tokamaks, such as ITER, the MGI could hardly penetrate into the plasma core and a sudden increase in the plasma density can be achieved using the *shattered pellet injection* (SPI) [30] instead. SPI shoots a cryogenic pellet of noble gases whose fragments can penetrate deeper into the plasma than MGI.

A second method for runaway electrons mitigation is to deteriorate the beam confinement by means of (resonant) magnetic perturbations (RMP) [24], which break the closed flux surfaces for the time they are applied to the plasma. The early rupture of the runaway electron confinement reduces the acceleration exerted by the inductive fields on the particles, so that they may be less energetic when they will impact on the machine vessel. Also, a shorter confinement time helps at reducing the contribution of secondary production, limiting the avalanche multiplication of runaway electrons in large machines. Finally, the third mitigation technique follows the opposite approach: the confinement of the runaway electron beam is maintained as long as possible and its energy is reduced via loop voltage control [24].

Lots of efforts have been put in place to assess the efficacy of the aforementioned

mitigation techniques in view of ITER operations. In this context, the reconstruction of runaway electron phase-space distribution could give fundamental information about the beam dynamics and how the mitigation techniques modify the runaway electron population. In chapter 4, the reconstruction of the 1D energy distribution of runaway electrons from the bremsstrahlung HXR spectrum measured during plasma disruption is discussed. In chapter 5, the transfer matrices necessary for a 2D reconstruction of the velocity-space distribution of runaway electrons are calculated for the first time for JET HXR diagnostics. In section 6.3 a novel reconstruction of the poloidal distribution of runaway electrons from the entire HXR profile measured by the JET gamma-rays camera is presented. Finally, a technical note: in both chapters 4 and 5, the quality of several images (especially the transfer matrices and weight matrices plots) has been compressed to respect the maximum file size set by the PhD school of my institution. A high definition version of those plots is also available and can be asked to the author of this thesis.

Part II

Analysis Methods for HXR Detectors

Chapter 2

Hard X-ray diagnostics system

Hard X-ray spectrometers are precious diagnostics for the study of fast particles in thermonuclear plasmas. Detectors based on inorganic LaBr_3 scintillator crystals, doped with Ce, have been recently installed at JET and at AUG. Thanks to their high resolution (from 3% to 5% at the 662 keV energy of the ^{137}Cs characteristic peak) and their high counting rate capabilities (in excess of 1 MCps), they are able to perform spectroscopic measurements of both the characteristic gamma-ray lines emitted by fast ions in nuclear fusions reactions and the bremsstrahlung radiation emitted by runaway electrons. In the case of fast-ions the analysis of the spectral lines measured by a single LOS gives information about the plasma composition, telling which species and impurities are present in the plasma as well as the energy reached by such particles (some reactions can reach significant reaction rates only if one of the reactants has energy higher than a cut-off) [17, 33]. Also, if the intrinsic line broadening (e.g. due to doppler broadening) is comparable or higher than the diagnostics energy resolution, the velocity distribution of the reactants can be reconstructed, by means of both forward models [17, 33] or unfolding techniques [34–37].

In the case of runaway electrons, the complex dynamics of relativistic particles in plasmas as well as the fact that bremsstrahlung emission generates a continuum spectrum complicate the implementation of forward models. For these particles, their distribution functions can be reconstructed solving the inverse problem with one of the methods introduced in chapter 3. As will be discussed in chapters 4 and 5, a key element for this analysis is the detector response function (DRF), which is one of the two factors that compose the transfer matrix used to perform the unfolding of the spectrum. The DRF of all the $\text{LaBr}_3(\text{Ce})$ spectrometers described in this chapter has been calculated using the MCNP code [38], enabling the unfolding of the REs velocity space distribution function from their bremsstrahlung emission on both AUG and JET. Each DRF takes into account both the transport of a hard X-ray from the tokamak to the detector and the interaction between the photon and the scintillator. As an example, the DRF of the spectrometer installed in the Bragg bunker at ASDEX Upgrade is shown in figure 4.1(a). The DRF of the other detectors described in this chapter are similar to figure 4.1(a); they differ from this example mainly in the

crystal size and in the collimation of the line of sight. For instance REGARDS has a cleaner LOS than the detector behind the Bragg spectrometer and should not suffer from significant back scattering. The crystal dimension, on the other hand, affects both the detector response to mono-energetic photon beams and the detector efficiency: the lower the volume, the lower the detector efficiency. For examples the JET spectrometers, having bigger size than the detector in the Bragg bunker, can stop the photo-electrons more easily and thus the photo-peak is visible at higher energies.

Finally, if an array of detectors is installed along multiple lines of sight, a spatial reconstruction of the fast-particles density can be conducted using dedicated tomographic techniques. This is the case of the gamma camera upgrade installed at JET, which will be introduced in section 2.2.1. The tomography of the profiles measured by this camera will be discussed in chapter 6 for both fast-ions and runaway electron. In section 2.2.2, the other spectrometers that complete the JET hard X-ray diagnostics system are presented; while section 2.1 is entirely dedicated to the two hard X-ray radial spectrometers installed at AUG.

2.1 ASDEX Upgrade

ASDEX Upgrade is equipped with two radial hard X-ray spectrometers installed at different toroidal positions [39, 40]. They have been developed prevalently for measuring the bremsstrahlung emission in the hard X-ray energy region of the runaway electrons, which on AUG can reach up to few tens of MeV of energy (see section 4.3). From their measurements, the RE energy distribution can be inferred using the unfolding techniques introduced in section 3 and studied in section 4.

2.1.1 The detector in the Bragg bunker

The first HXR detector installed at AUG took advantage of the experience developed in the upgrade of the JET gamma camera, whose characteristics are discussed in section 2.2.1. It mounts a crystal identical to the ones installed at the JET gamma camera upgrade (GCU): a LaBr_3 inorganic crystal doped Ce, having cylindrical shape with $25 \text{ mm} \times 17 \text{ mm}$ (diameter \times depth) dimensions, fast decay time of 16 ns and high light yield of 63 photons/keV. A traditional photomultiplier tube (PMT) produced by Hamamatsu (model RS6231) has been chosen as conversion and multiplication stage. PMTs have a very linear response in energy, but are also highly sensitive to external magnetic fields due to the relatively long distance that the electrons have to travel in vacuum during the multiplication stage before being collected by the PMT anode. The PMT is shielded against the tokamak magnetic by means of soft-iron, that ensures less than 1% drift of the PMT gain during plasma discharges [39]. The digital acquisition system (DAQ) is based on the same architecture exploited on JET, the Advanced Telecommunication Computing Architecture (ATCA) [41], and

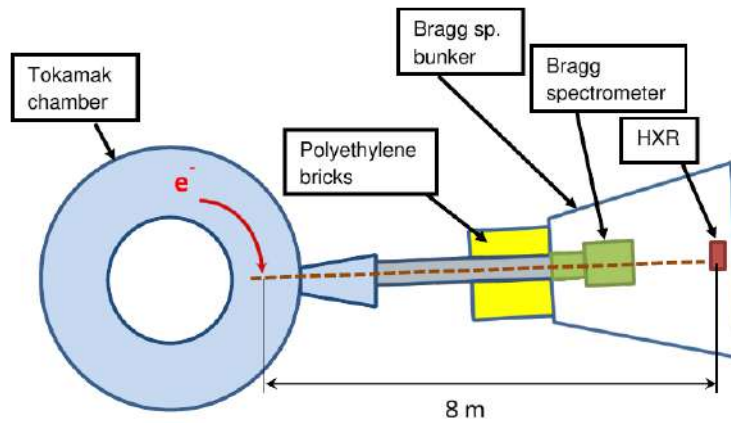


FIGURE 2.1: Sketch of the LOS and collimation of the detector placed in the Bragg bunker at AUG. Reproduced from [39] with the permission of AIP Publishing and the author.

can acquire 14 bit samples at 400 MHz. In this implementation the DAQ only works in *segmented mode* and saves only those events that generate an electric signal whose maximum amplitude exceeds a threshold set by the user. For each event a time series of 128 samples, termed waveform, is saved.

The detector exhibits an energy resolution of 4% at the ^{137}Cs characteristic peak ($E_\gamma = 662 \text{ keV}$), a dynamic range up to 30 MeV and counting rate capabilities in excess of 1 MCps. During plasma disruptions with production of runaway electrons, the detector has been able to sustain counting rates up to 10 MCps which could be analysed by mean of dedicated off-line pile-up restoration algorithms [39]. The radial line of sight (LOS) is sketched in figure 2.1: the diagnostics is placed inside the Bragg bunker, behind the Bragg spectrometer. It benefits from the collimation of the Bragg spectrometer that consists of a 1m thick layer of polyethylene followed by a 20 cm thick concrete wall. Further shielding against the backscattering of the photons inside the Bragg bunker is ensured by 10 cm of lead. This geometry has been implemented in the detector response function (DRF) shown in figure 4.1 and used in section 4 to unfold the RE energy distribution from the HXR spectrum measured by this detector during plasma disruptions. An example of such a spectrum is shown in figure 4.8(a) for the AUG pulse #34084.

2.1.2 REGARDS

The runaway electron gamma-ray detection system (REGARDS) is a portable HXR detector developed specifically for measuring the bremsstrahlung emission of runaway electrons on multiple tokamaks participating to the middle size tokamas (MST) program. It has already performed measurements both at AUG and at COMPASS tokamaks and in the future it is supposed to operate also at TCV [40]. The detector

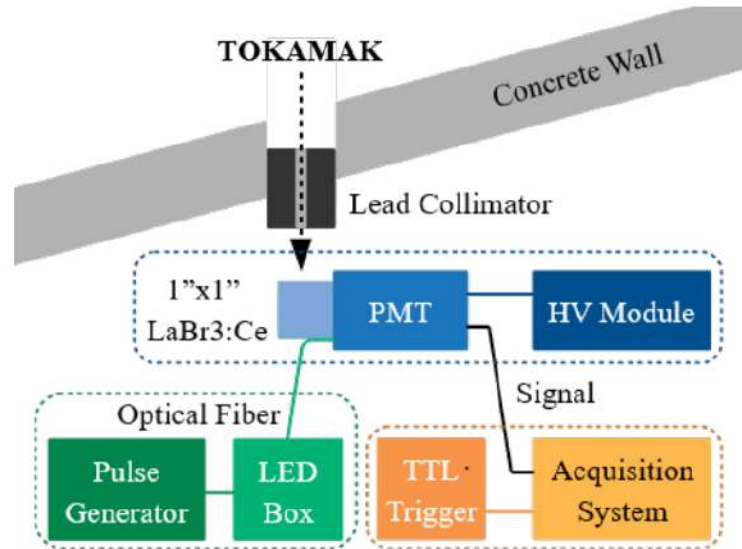


FIGURE 2.2: Sketch of the collimation of the REGARDS detector LOS at AUG. All components of REGARDS are here shown schematically. Reproduced from [40] with the permission of the author.

is based on a $\text{LaBr}_3 : \text{Ce}$ cylindric scintillator with dimensions $25 \text{ mm} \times 25 \text{ mm}$ (diameter \times depth) coupled to a traditional photomultiplier tube, model R9420 from Hamamatsu. The PMT is shielded from the influence of the external magnetic field by a inner tube composed by μ -metal that surrounds the PMT alone and by a outer cylinder made of soft-iron that surrounds both PMT and the scintillator [40]. The DAQ, produced by National Instruments, works in *continuous mode*, i.e. it receive an external trigger and then start acquiring samples at a rate of 400 MHz for 10 s. After the discharge, data are tranfered from the Ram memory to the hard disk of the PD. The time trace of the entire plasma pulse is then analysed off-line using the DeGaSum code [42].

REGARDS reaches an energy resolution of 3% at the ^{137}Cs characteristic peak ($E_\gamma = 662 \text{ keV}$), counting rate capability in excess of 1 MCps and a dynamic range up to 40 MeV [40]. Differently from the detector in the Bragg bunker, this detector should be positioned distant from the machine, in a position with a limited flux incident on the scintillator. At AUG it is positioned outside of the torus hall on a collimated radial line of sight shared the a neutron liquid scintillator. A sketch of this set-up is reported in figure 2.2. When REGARDS in on line, the LOS is further shielded using either a block 3.0 mm thick of lead or a cylindrical collimator 10 cm long, with a central hole of 1 cm of diameter. The collimator has been designed using MCNP code [38] to reduce by roughly an order of magnitude the flux of photons that reaches the detector with respect to the lead attenuator. At the same time the spectrum that reaches the detector is less perturbed by the collimator than by the attenuator.

The diagnostics is also equipped with a pulser that sends to the PMT photocathode a LED pulse at 10 MHz [40]. The shape of the pulse has been designed so that it resembles the signal induced in the detector by a 12.5 MeV photon that interacts through photo-absorption with the scintillator. This system is used to monitor during the acquisition the shift in the PMT gain due to both the magnetic field of the tokamak and the high counting rates experienced during runaway electrons experiments. The LED waveform is different from the one produced by gamma-rays, so it can be discerned during the off-line analysis of the data set. The time evolution of the energy of the LED pulses through the discharge gives an estimate of the time evolution of the PMT gain. The analysis of the pulses measured at AUG shows that, at fluxes in excess of 1 MCps, REGARDS has experienced a gain shift below 3% [40].

2.2 Joint European Torus

JET is equipped with a set of hard X-ray spectrometers deployed on multiple lines of sight. They can be divided in three groups: the gamma camera upgrade (GCU), which is discussed in details in section 2.2.1, a set of gamma-ray spectrometers having vertical line of sight (V-GRS) and a spectrometer having a tangential line of sight (T-GRS). The latter two are discussed in the present section and differ from the GCU principally for a bigger volume of the scintillator crystals used, which in turn ensures them an enhanced energy resolution and detection efficiency.

2.2.1 The Gamma Camera Upgrade

JET is equipped with a neutron/gamma camera that share the same LOS system and observe a poloidal section of the tokamak. They are composed by 19 detectors each divided in two projections: a horizontal array with 10 LOS and a vertical array with 9 LOS. Each detector observes the plasma through a collimation system that can assume two openings: 21 mm and 11 mm, with the exception of the vertical channels observing the high-field side (channels 11 to 14) that have a smaller aperture. The detectors of the gamma camera are normally positioned out of sight in order to ensure the cleanest LOS possible to the neutron-camera. They can be moved between the collimator and the neutron camera detectors with a remote mechanical control. When the gamma camera is on the line of sight, the flux of particles impinging on the neutron camera is globally reduced by about 20%. The gamma camera is also equipped with water attenuators that can reduce by 2 order of magnitudes the flux of 2.5 MeV neutrons and by a factor 15 the flux of the 14 MeV neutrons. These attenuators, however, have not been used during the experiments discussed in section 6.2.

The detectors of the gamma camera have been recently upgraded in prevision of the current DT campaign [43]. The goal of the upgrade was to install a custom made

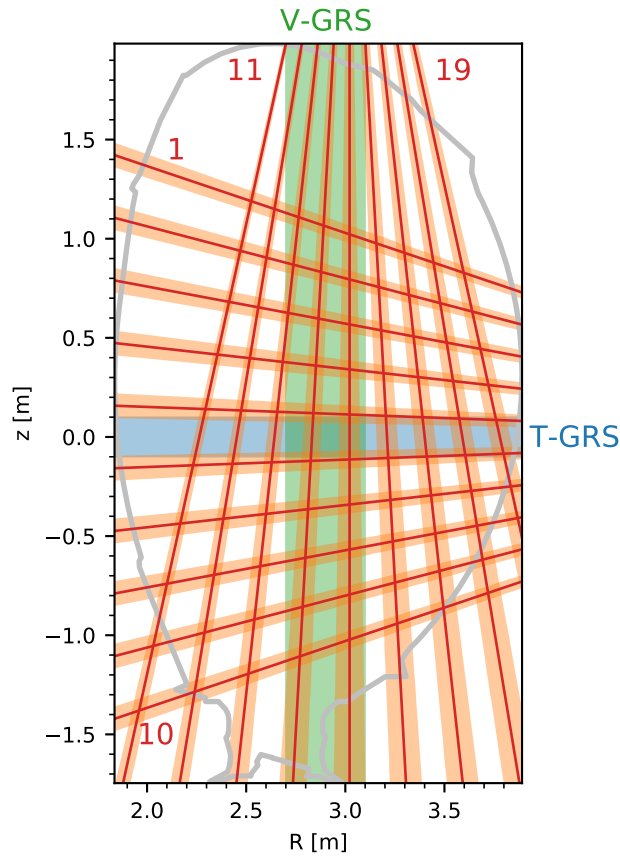


FIGURE 2.3: Projection on the poloidal plane of the lines of sight of the vertical gamma-ray detectors (green band labelled V-GRS), the tangential gamma-ray detector (blue band labelled T-GRS) and the 19 channels of the gamma camera upgrade (red bands). The numbering of the gamma camera channels is also reported.

solution able to sustain the high neutron fluxes (up to few 10^{17} n/s [44]) expected during DT operations, while improving the diagnostics counting rate capability (up to 1 MCps) and energy resolution (few % in the [1, 5] MeV range) [44, 45]. Cylindrical crystals made of LaBr_3 doped with Ce, with dimensions $25.4 \text{ mm} \times 16.9 \text{ mm}$ have been used. These scintillators ensure an energy resolution of 3% or lower at 4.44 MeV. Since the new system had to fit into the support of the old camera, compact silicon photomultiplier (SiPM) with dimensions $12 \text{ mm} \times 12 \text{ mm} \times 2 \text{ mm}$ (width, height, thickness) have been selected for the conversion and multiplication stage of the detector [46]. Apart from their dimensions another advantage of SiPMs is their insensitivity to external magnetic field. They can perform measurements without magnetic shielding even in the presence of magnetic fields of 100 Gauss or higher, making them excellent solutions for detectors installed closed to the tokamak vessel [40]. On the other hand, SiPMs have a strong temperature dependent gain, which is corrected real time with a dedicated read-out board [46], and they are non-linear

in energy, requiring an exponential calibration (see figure 2.3). Finally, their gain shifts when the detector is subject to high fluxes and as a result the same signal is measured at an energy lower than usual when high count rates are registered. Even if it is not installed on the JET gamma camera, it is worth mentioning that on more recent detectors developed by the Milano neutron and gamma group, an optic fiber has been installed to convey a LED pulse with constant low rate (≈ 10 MHz) on the SiPM. The gain shift related to high-fluxes can thus be corrected looking at the shift in the energy of the LED signal. The low rates employed and the different shapes of gamma and LED signals, make this solution non perturbative on the detector measurement [40].

Each SiPM is connected to a CR differentiator circuit that shapes the time length of the electronic signal generated by the SiPM to a full width half maximum (FWHM) of about 41 ns [46]. The detectors then feed into a digital acquisition system (DAQ) able to process samples of 16 bits at a rate of 200 MSamples/s and to store up to 680 MB of data during a single plasma pulse [41]. The DAQ architecture, named Advanced Telecommunications Computing Architecture (ATCA), allows three operation modes. Let's first consider standard plasma shots in which the expected fraction of pile-up events is low and the duration of the discharge does not saturate the DAQ memory. In these pulses the DAQ works in segmented mode, saving only those events that generate an electric signal whose maximum amplitude exceeds a threshold set by the user. For each event, a waveform composed by 128 samples is stored in the DAQ temporary memory. This mode allows to perform measurements with a counting rate capability in excess of 1 MCps [46, 47] and it has been used in every experiment analysed in the next chapters. If high fluxes are expected on the detectors for a short interval of time (up to about 1 s), the GCU can be operated in *continuous mode*. A trigger is sent to the DAQ, which starts acquiring samples continuously and no events are lost due to the detector dead time. The measured waveform of the whole experiment is then analysed offline: it is first separated into the waveforms of single events and then converted in the pulse height spectrum. This mode might come in handy in experiments such as runaway disruption as it simplify the pile-up restoration of the recorded waveforms and it minimizes loss of data due to the detector dead time. On the other hand it requires to know exactly at what time the burst of events will be generated to trigger the start of the acquisition and it is associated with the risk of losing data in the final part of the disruption due to memory saturation. Finally, if a low flux is expected on the detector, but the length of the experiment is long enough to saturate the memory where the waveforms are temporary saved, the *processed mode* should be employed. The DAQ is equipped with an FPGA able to perform a real-time analysis of the measured waveforms and store only the pulse height and the time stamp of each event [48]. This last mode reduces the memory necessary for saving the entire plasma discharge, but does not

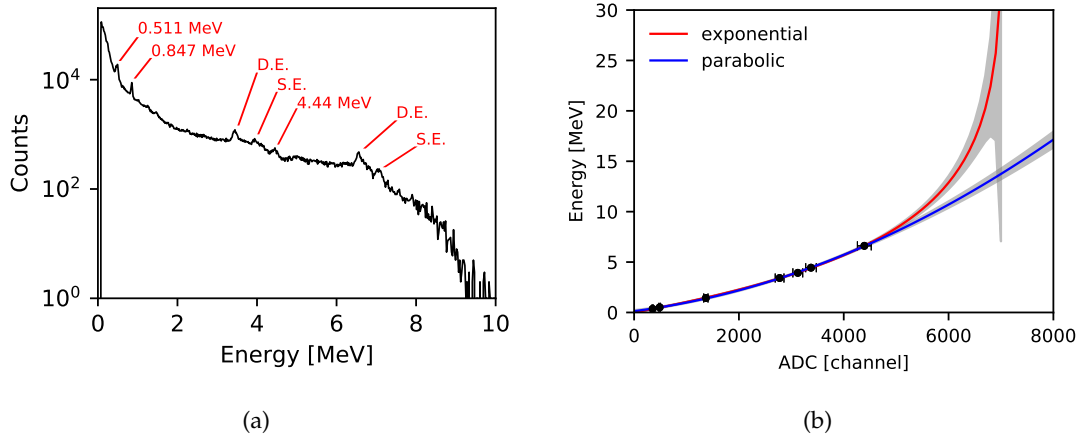


FIGURE 2.4: (a) Calibration spectrum emitted by the Am-Be source and measured by channel 4 of the gamma camera upgrade. The characteristic peaks are also reported, from high to low energy: single and double escape (S.E. and D.E.) peaks due to the 7.63 MeV prompt gamma-rays emitted by the ^{56}Fe neutron capture; photo-peak, single and double escape of the α -Be 4.44 MeV peak; the 0.511 MeV and 0.847 MeV peaks corresponding to respectively the ^{27}Al and ^{55}Mn neutron activation. (b) Fit of the peaks shown in figure (a) performed with both the exponential and quadratic calibration functions for channel 4 of the GCU. The gray band shows the 95% confidence band for each fit. When non visible, the error on the peaks position is smaller than the marker size. Reproduced from [49] with the permission of AIP Publishing and the author.

allow to correct the measured spectrum for pile-up events.

The GCU collimator system incorporates ^{137}Cs , ^{133}Ba , and ^{22}Na radioactive sources which can be brought on the detectors LOS by mean of a remote mechanical control system. Also the ^{138}La present in the detector crystal emits two characteristic lines at 798 keV and 1436 keV with a branching ratio of 34% and 66% respectively, with a total count rate of 20 Cps for every square inch of detector (low enough not to perturb the measurements during plasma discharges) [40]. These sources can be used in between pulses to calibrate each channel of the camera up to 1.5 MeV. In this energy range, the SiPMs have an approximately linear response. Due to the non-linearity of the SiPMs at higher energies, this procedure results in an imprecise calibration already at 4 – 5 MeV, which is of interest for measuring the 4.44 MeV gamma-ray emitted in $^9\text{Be}(\alpha, n)^{12}\text{C}^*$ reactions. A more precise calibration is performed more rarely using an $^{241}\text{Am} - \text{Be}$ source, which emits both neutrons and gamma-rays up to an energy of 7.6 MeV [49]. The response of GCU channel 4 to this source is shown in figure 2.4(a). From low to high energy: the spectrum shows the 0.511 MeV and 0.847 MeV peaks corresponding to respectively the ^{27}Al and ^{55}Mn neutron activation. The photo-peak, single and double escapes (S.E. and D.E.) peaks of the 4.44 MeV gamma-rays emitted in the $\alpha - ^9\text{Be}$ reactions has been detected. Single and double escapes peaks of the 7.63 MeV gamma-rays emitted after neutron capture in

^{56}Fe are also visible.

In principle SiPMs have an exponential energy calibration formula:

$$E(ch) = -\frac{A}{B} \log\left(1 - \frac{ch}{A}\right) + \frac{C}{B} \quad (2.1)$$

with E energy in MeV of the measured signal, ch ADC channel associated to the energy of the signal, A , B and C parameters of the fit. This formula can be used to calibrate the detectors up to approximately 10 MeV. In fact, as shown in figure 2.4(b), this calibration diverges at about 7000 ADC energy channels. In the experiments discussed in section 6.2, 16.4 MeV gamma-rays are emitted in $^3\text{He}(D, \gamma(16.4 \text{ MeV}))^5\text{Li}$ reactions and the events measured by GCU channel 4 reach energies as high as 10000 ADC channels. When a spectrum that extends much higher than 10 MeV is expected, a second-degree polynomial can be used as calibration function with the $^{241}\text{Am} - \text{Be}$ source. The calibration at energies above 10 MeV, then, can be extrapolated from the quadratic fit. This quadratic calibration is shown in figure 2.4(b) and will be fully discussed in section 6.2.

2.2.2 The hard X-ray spectrometers

The T-GRS has a line of sight that intersect two times the plasma center with an angle of 50° with respect to the toroidal axis. Considering a standard JET magnetic equilibrium, this tangential LOS is positioned 30 cm below the magnetic axis [17]. T-GRS has been recently upgraded from a Bismuth Germanate (BGO) detector to a $7.62 \text{ cm} \times 15.2 \text{ cm}$ (width \times depth) cylindrical LaBr_3 scintillator, coupled to a R10233 PMT from Hamamatsu [17]. The upgrade resulted in an improved energy resolution (3.5% at the 662 keV ^{137}Cs characteristic peak, 3 times lower than the previous detector) and a factor of ten times improvement in the counting rate capability (which now can reach few MCps), at similar total detection efficiency (93% for the new LaBr_3 crystal) [17]. A new attenuator system based on a block of 66 cm of LiH has also been installed. A second block of 30 cm can be inserted on the detector LOS to ensure a total attenuation factor of 275 for 14 MeV neutrons and 900 for 2.5 MeV ones, ensuring the capability of performing spectroscopic measurements also during DT operations, when rates 10^{18} neutrons per second are expected [17, 43]. During the upgrade, a LED control similar to the one described in section 2.1 for the RE-GARDS detector has been installed [17, 40]. This LED signal is used to monitor the drifts in the PMT gain due to the influence of the high counts rates sustained by the diagnostics. As in the case of the vertical LaBr_3 discussed below, the digital acquisition system is based on the ATCA architecture, that ensures an acquisition rate of 400 MSamples/s, with a sample size of 14 bit [41]. However, during the high power DT campaign, it was necessary to install a portable DAQ capable of sustaining the operation in continuous mode for the entire duration of the JET discharge.

The V-GRS system, on the other hand, is composed by two different lines of sight, with three spectrometers: two LaBr₃ (KM6S1 and KM6S2), both of size 7.62 cm × 15.2 cm (width × height), and one high purity germanium HpGe (KM6G). KM6G and KM6S1 share the same LOS and can be used alternately, depending on the experimental conditions. The HpGe is slower and has a lower detection efficiency above 10 MeV when compared to the LaBr₃ detectors. For instance the total efficiency of the HpGe is approximately 70% or lower in that energy range [17]. On the other hand, the HpGe has a very high resolution: 0.26% at the ¹³⁷Cs characteristic peak at 662 keV. The LaBr₃ spectrometers, on the other hand, have a resolution between 3.2 and 3.5% at 662 keV [17, 50]. This makes the HpGe suitable for highly resolved measurements up to 5 MeV in pulses with modest rates and a stable plasma dynamics. This is the case of the three-ions scheme experiments introduced in section 1.2 and analysed with a tomographic inversion in section 6.2. In such experiments, however, the HpGe was not able to detect the 16.5 MeV gamma-rays emitted in D-³He fusion reactions [17]. Thus, during plasma discharges where high energies (above 5 MeV) and high-rates are expected, LaBr₃ is usually chosen. This is in particular the case of disruptions with formation of an RE beam, where the RE bremsstrahlung emission reaches rates in excess of 1 MCps and high energies [40].

Chapter 3

Deconvolution algorithms

In both runaway electrons (RE) and fast ions experiments, the plasma emits radiation in the hard X-ray (HXR) energy region of the spectrum: either through bremsstrahlung collisions between a RE and an ion or through fusion reactions between ions in the case of fast ions. The experimental HXR spectrum, measured with the diagnostics described in chapter 2, contains information about the phase-space distribution function of the emitting species. There exists two approaches to unlock such information. In the so called *forward model* the distribution function is simulated from first principle, then it is validated using synthetic diagnostics to generate expected signals which are finally compared with experimental data. On the contrary, the *backward model* reconstruct the particles distribution function from the experimental data by mean of dedicated algorithms that can invert the equation that links the plasma emission to the particles distribution. Since this equation is usually a convolution, the inversion is also termed *deconvolution*. The main advantage of the backward model is that first principle simulations are slower to perform, while the inversion of experimental data can be performed routinely. Deconvolutions, then, can be used as a first analysis tool to orient the theoretical analysis. Moreover, in the case of REs, first principle simulations are not able to reconstruct the experimental data with sufficient accuracy at present. The inverse approach can help improving simulations as it decouples the description of the physical system from the one of the diagnostics, allowing to directly compare the output of simulations with distribution functions reconstructed from experimental data.

On those machines where an array of detectors arranged in a grid is present, the deconvolution of the total number of counts measured by each channels can reconstruct the spatial distribution of fast particles and the inversion is called *tomography*. For instance this is the case of the Gamma Camera Upgrade (GCU) at JET, whose tomographic inversion will be covered in chapter 6. On the other hand, as discussed in more details in chapter 4, the cross sections of the listed processes depends on the velocity of the emitting particles, thus the signal measured by a single spectrometer can also be inverted in the velocity space. In this case the inversion takes the name of *unfolding*.

For the sake of clarity, the rest of the present chapter will make use of the unfolding of RE 1D energy distribution as an example to introduce the inverse problem and four algorithms for solving it. Consider the discretized experimental data \underline{S} : this vector contains the energetic HXR spectrum emitted by REs in bremsstrahlung collisions as measured by a single spectrometer (multiple spectrometers can also be inverted simultaneously following the prescriptions contained in [34]). The emitting particle distribution \underline{F} , which in this case is the 1D energy distribution, is related to \underline{S} through the linear equation:

$$\underline{S} = \underline{W} \cdot \underline{F} + \underline{n}_e \quad (3.1)$$

where \underline{W} is the *transfer matrix* that contains the probability for a particle in a certain position and with a certain velocity to generate a signal measured in a specific diagnostic with a specific energy, while \underline{n}_e is the experimental noise introduced by the specific set-up used for measuring \underline{S} . In the case of the unfolding of runaway electrons energy distribution, \underline{W} contains the emission probability of a HXR photon via bremsstrahlung collisions, its propagation to the detector and its interaction with the detector. The latter is called Detector Response Function (DRF) (see figs. 4.1 to 4.3).

We can assume that \underline{n}_e is a random variable with zero mean, thus retrieving the emitting particle distribution from (3.1) becomes equivalent to the problem of inverting \underline{W} . Even when \underline{W} cannot be inverted, e.g. when it is a rectangular matrix, one can still try a direct approach using the matrix $\underline{W}^T \underline{W}$, which is symmetric and positive semidefinite and thus admits an inverse. The solution then reads:

$$\underline{F} = (\underline{W}^T \underline{W})^{-1} \underline{W}^T \underline{S} \quad (3.2)$$

and the problem becomes equivalent to solve the following equation:

$$\underline{W}^T \cdot \underline{S} = (\underline{W}^T \cdot \underline{W}) \cdot \underline{F}.$$

As will become more clear in section 3.1, the computational complexity of this problem is extremely high. Instead of attempting a direct calculation of $(\underline{W}^T \underline{W})^{-1}$, it is more reliable to use a regularization algorithm to invert equation (3.1) either explicitly or implicitly.

Regardless to the inversion method adopted, the experimental noise will degrade the reconstruction giving birth to nonphysical artifacts. The origin of \underline{n}_e can be many-fold, such as the electronic noise generated by the digital acquisition chain of the diagnostic, the statistical uncertainty of the physical processes used to perform a measurement (e.g. the electron avalanche of a photonmultiplier tube) or even the computational noise related to the specific architecture of the electronic devices used

for data analysis (e.g. due to the finite precision of computers' variables and calculations). Since the modelling of such processes is extremely challenging, they are usually not included in \underline{W} . On the other hand, the fact that all these sources of noise have zero mean suggests that we can reduce their effect on the final reconstruction adopting a suitable *smoothing operator*. The details are discussed in the next sections, however each smoothing procedure is roughly similar to performing a sliding window average over the neighborhood of each point.

Four inversion methods with dedicated smoothing operators are presented in the remaining of the chapter. They have been implemented in a Python library dedicated to the analysis of the hard X-ray spectra measured at JET and ASDEX Upgrade. The performance of such algorithms when reconstructing the runaway electrons 1D energy distribution is also compared in chapter 4.

3.1 Singular Value Decomposition

Singular Value Decomposition (SVD) is a linear algebra technique that generalizes the Eigenvalue Decomposition (EVD) to the case of rectangular matrices [51]. Among its many applications, it was also proposed as a regularization method for problem (3.1) [52–54]. The theoretical justification behind this decomposition method is straightforward [52] and it is based on the EVD of $\underline{W}^T \underline{W}$, which ensures the uniqueness of the decomposition.

Given an arbitrary rectangular matrix \underline{W} with dimensions $m \times n$, the matrix $\underline{W}^T \underline{W}$ is a symmetric, $n \times n$, positive semidefinite matrix. Thus the *Spectral Theorem* holds and $\underline{W}^T \underline{W}$ can be decomposed as:

$$\underline{W}^T \underline{W} = \underline{V} \underline{D} \underline{V}^T$$

where \underline{V} and \underline{D} are squared $n \times n$ matrices containing respectively the eigenvectors $\{\underline{v}_1, \dots, \underline{v}_n\}$ and eigenvalues $\{\lambda_1, \dots, \lambda_n\}$ of $\underline{W}^T \underline{W}$. $\{\underline{v}_1, \dots, \underline{v}_n\}$ compose an orthonormal basis of \mathbb{R}^n , while $\underline{u}_i = \frac{\underline{W} \underline{v}_i}{\sqrt{\lambda_i}}$ represent a orthogonal basis in \mathbb{R}^m , in fact:

$$\underline{u}_i \cdot \underline{u}_j = \frac{1}{\sqrt{\lambda_i} \sqrt{\lambda_j}} (\underline{W} \underline{v}_i)^T \cdot (\underline{W} \underline{v}_j) = \frac{1}{\sqrt{\lambda_i} \sqrt{\lambda_j}} \underline{v}_i^T (\underline{W}^T \underline{W} \underline{v}_j) = \frac{1}{\sqrt{\lambda_i} \sqrt{\lambda_j}} \underline{v}_i^T \lambda_j \underline{v}_j = \delta_{ij}.$$

The action of \underline{W} on the eigenspace \underline{V} can be written in vector form as: $\underline{W} \underline{V} = \underline{U} \underline{\Sigma}$, where $\underline{\Sigma}$ is a $m \times n$ diagonal matrix that contains on its diagonal the so called *singular values* of \underline{W} : $\sigma_i = \sqrt{\lambda_i}$. Finally, the singular value decomposition states that $m \times n$ matrix \underline{W} can be decomposed as:

$$\underline{W} = \underline{U} \underline{\Sigma} \underline{V}^T, \quad (3.3)$$

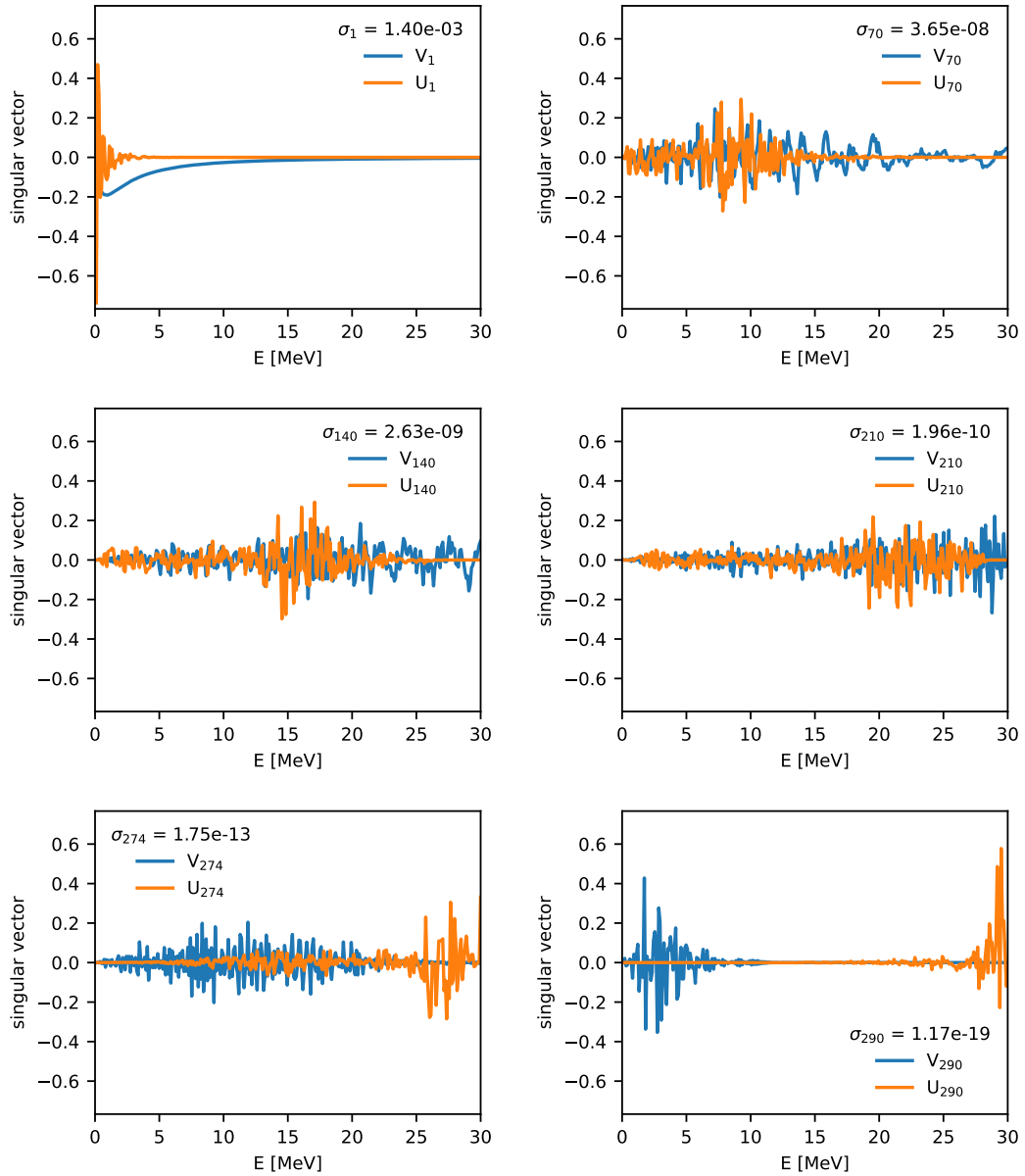


FIGURE 3.1: Left (u_i) and right (v_i) singular vectors for different values of i . For each pair of vectors, the corresponding singular value σ_i is reported in the graph legend. $i = 274$ corresponds to the last singular value considered for the inversion shown in figure 4.8(b).

the decomposition is based on two abstract basis of \mathbb{R}^m and \mathbb{R}^n named *left* (\underline{U}) and *right* (\underline{V}) *singular vectors*. Some examples of vectors composing such basis are shown in figure 3.1. Equation (3.3) gives a global constraint over the dimensions of the matrix generated by the product $\underline{U}\underline{\Sigma}\underline{V}^T$, however the dimension of each matrices cannot be univocally determined.

Coming back to the inversion problem, SVD decomposes any matrix in terms of two orthogonal matrices \underline{U} and \underline{V} and a diagonal one $\underline{\Sigma}$, which can be easily inverted to

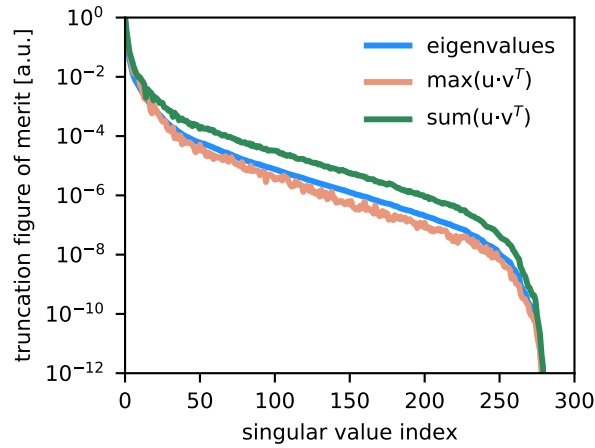


FIGURE 3.2: Comparison of three figure of merits for the truncation of SVD generalized inverse: the singular values σ_i , the sum of all entries of the outer product $\underline{u}\underline{v}^T$ and its maximum. All figures are normalized to their maximum value.

find the so called *generalized inverse*:

$$\underline{W}^+ = \underline{V}\underline{\Sigma}^{-1}\underline{U}^T \quad (3.4)$$

where Σ^{-1} is a diagonal $n \times m$ matrix with entries $\sigma_i^{-1} = \frac{1}{\sigma_i}$. Equation (3.1) can be inverted using this generalized inverse (3.4): $\underline{F} \approx \underline{W}^+ \underline{S}$. This explicit approach will be used in chapter 4 to retrieve the runaway electrons 1D energy distribution \underline{F} . It is worth noting that, if the singular values are all greater or equal to 0, the singular vectors can have negative entries (see figure 3.1). This implies that the reconstruction \underline{F} might also have unphysical negative entries and the current SVD implementation cannot guarantee the positivity of the SVD reconstruction.

This deconvolution method suffers from two types of noise which degrade the reconstruction and require some kind of regularization: experimental and computational noise. The latter is generated by the fact that computers save real numbers as rational numbers of finite precision, thus any calculation is affected by the so called *rounding error*. The computational noise contained in \underline{W} propagates to \underline{U} , \underline{V} and $\underline{\Sigma}$ and for each entry the signal to noise ratio will decrease with the absolute value of the entry itself. A possible strategy to limit the propagation of such noise to the reconstructed \underline{F} is to cut small singular values and their corresponding singular vectors, i.e. to truncate the reconstruction of \underline{W} in equation (3.3). The decomposition of \underline{W} then reads:

$$\underline{W} = \underline{U}\underline{\Sigma}\underline{V}^T = \sum_{i=0}^m \sigma_i \underline{u}_i \underline{v}_i^T = \sum_{i=0}^k \sigma_i \underline{u}_i \underline{v}_i^T. \quad (3.5)$$

with $k < m$ (also assume that $m \leq n$, which is desirable condition when dealing with the inversion problem) and $\underline{u}_i \underline{v}_i^T$ is the *outer product* of \underline{u} and \underline{v} . It has been proved

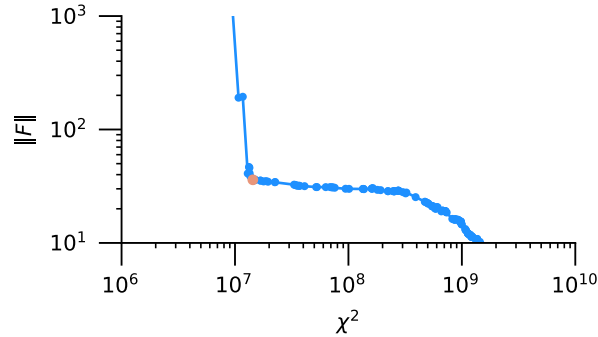


FIGURE 3.3: SVD L-Curve calculated for AUG shot #34084. The orange point represents the cutoff applied to the reconstruction. The final reconstruction is reported in figure 4.8(b).

that, under certain hypothesis on \underline{W} , this cut is equivalent to apply the Tikhonov smoothing operator [55, 56] (see section 3.2 for a full description of Tikhonov regularization) and it can be used also to limit the effect of experimental noise on the reconstruction \underline{F} .

One might wonder if the singular values σ_i truly depict the relevance of each term $\sigma_i \underline{u}_i \underline{v}_i^T$ and if the smoothing operator might be improved by applying the cut-off to other quantities. For example it would seem more appropriate to consider all the addend or simply the outer product $\underline{u}_i \underline{v}_i^T$ instead of σ_i , but actually figure 3.2 shows that all these figures of merit of the relevance of $\sigma_i \underline{u}_i \underline{v}_i^T$ behave similarly and can be equivalently used to chose the best truncation for the smoothing operator.

Another important application of SVD is the estimate of the condition number of a matrix [57]:

$$\kappa(\underline{W}) = \|\underline{W}\| \|\underline{W}^{-1}\| = \frac{\sigma_1}{\sigma_k}$$

where σ_1 is the highest singular value of \underline{W} and σ_k is the lowest one different from zero. A high condition number ($\kappa \gg 1$) tells that the problem (3.1) is ill-posed, i.e. small variations in \underline{S} generates substantial variations in \underline{F} . Conversely the ill-posed condition states that there exist different plausible solutions \underline{F}_S to the problem (3.1) and that the best solution among them must be chosen using a suitable smoothing operator. In order to determine the condition number of a matrix we must estimate its smaller singular value. This operation is not trivial as in fact rounding errors affect also singular values equal to zero, changing their value to arbitrary small numbers. Fortunately the rank, or equivalently the smaller singular value, can be

assessed by studying the L-Curve of the SVD [53].

If we consider the matrix that describes the Bremsstrahlung emission of REs (see figure 4.3 for a visual representation of \underline{W} and figure 3.3 for its L-Curve), it has dimension 300×300 , rank estimated as ≈ 274 and condition number of the order of $\kappa(\underline{W}) \approx 10^{11}$, which means we are dealing with an ill-posed problem. This analysis also suggests us that the inversion of $\underline{W}^T \underline{W}$ in (3.2) would return extremely poor results, as in fact $\kappa(\underline{W}^T \underline{W}) = \kappa(\underline{W})^2$. We can also expect that implicit inversion methods will probably give better results than SVD when applied to the reconstruction of the REs 1D energy distribution.

3.2 Tikhonov regularization

Tikhonov regularization [58, 59] is the most famous inversion method of the Regularized Least Squares family. Due to its intuitiveness and flexibility, its properties have been widely studied and it has rapidly become the golden standard for method comparison: see e.g. [53, 55, 56], where the use of SVD as a regularization method has been justified by proving its equivalence to Tikhonov, or [60], where the performance of various methods have been compared. Its applications in fusion plasmas range from the tomography of the radiation profiles acquired with detector cameras [60–62], to the 2D reconstruction of the velocity-space distribution of fast ions [34, 35, 63–70].

Tikhonov regularization minimizes the distance between the reconstruction and the experimental data \underline{S} , calculated as the Euclidean l^2 norm, to find the best solution $\hat{\underline{F}}$ to the linear system (3.1):

$$\hat{\underline{F}} = \arg \min [\|\underline{W} \cdot \underline{F} - \underline{S}\|_2^2 + \alpha \|\underline{L} \cdot \underline{F}\|_2^2] \quad (3.6)$$

where \underline{L} is the regularization matrix, $\alpha \geq 0$ is the regularization parameter and $\|\cdot\|_2$ is the Euclidean 2-norm.

\underline{L} implements the smoothing of the solution $\hat{\underline{F}}$ and its shape is chosen according to the problem that must be inverted. The most general regularization matrices implement the n -th order derivative of \underline{F} and they define the n^{th} -order Tikhonov Regularization. The 0^{th} -order matrix is the identity \underline{I} and simply penalizes high modules in the final reconstruction $\hat{\underline{F}}$. On the other hand, the 1^{th} -order matrix penalizes the first derivative of $\hat{\underline{F}}$, calculated on the closest bin of the vector, and actually force the minimizer to look for smoother solutions. When applied to the reconstructions presented in chapter 4, the 1^{st} order better reconstruct synthetic spectra, especially in the high-energy tail, thus 0^{th} order will not be considered in the present work. More exotic matrices can also be implemented, e.g. in chapter 6 \underline{L} will calculate the first derivative of a 2D image along the magnetic flux surfaces.

The smoothing parameter α defines the relative importance of the smoothing operator $\|\underline{L} \cdot \underline{F}\|_2^2$ over the minimization of the squared residuals $\|\underline{W} \cdot \underline{F} - \underline{S}\|_2^2$, which implement the physics of the inverse problem (3.1). In other words, α defines the intensity of the smoothing in the reconstruction. If α is set to a high value, i.e. if the minimizer over-smooths the reconstruction, the solution will badly reconstruct the experimental data and the χ^2 of the reconstruction will not be satisfactory. On the other extent, if α is too close to 0, i.e. if the minimizer over-fits the data, the minimizer will try fitting the experimental noise included in \underline{S} and this will generate un-physical structures in $\hat{\underline{F}}$, which in turn will increase its euclidean norm. The level of smoothing, i.e. the value of α , can be set using empirical methods (e.g. [55, 71]) that make a trade-off between oversmoothing and overfitting. In the present work, the L-Curve method [53, 71] has been used, which makes α range from 0 to ∞ and plots $\|\hat{\underline{F}}\|_2(\alpha)$ versus $\|\underline{W} \cdot \underline{F} - \underline{S}\|_2^2(\alpha)$ on a log-log scale: this plot has a characteristic L shape and α is set to a adequate value around the point of maximum curvature of the curve.

Additional physical conditions on $\hat{\underline{F}}$, such as monotonicity or non-negativity, can be added to the minimization process of equation (3.6). For instance probability density functions are positive definite, thus in our applications we can look for $\hat{\underline{F}} \geq 0$. This constraint can be easily included in minimization process if (3.6) is reshaped as a least-square problem:

$$\hat{\underline{F}} = \arg \min_{nls} \left\| \begin{bmatrix} \underline{W} \\ \underline{L} \end{bmatrix} \cdot \underline{F} - \begin{bmatrix} \underline{S} \\ \underline{0} \end{bmatrix} \right\|_2^2 \quad (3.7)$$

where the block-matrix notation has been used to define a new transfer matrix $\underline{\tilde{W}} = \begin{bmatrix} \underline{W} \\ \underline{L} \end{bmatrix}$ that incorporates also the smoothing operator. In this shape, the problem can be solved using the Non-Negative Least Square (nnls) algorithm [72] that assures the non-negativity of the solution.

3.3 Poissonian regularization

Tikhonov regularization started a family of regularization methods that only differ in the first term of (3.6): in fact each inversion problem has an appropriate statistics that better resembles the physics of the process described by \underline{W} in (3.1). Tikhonov regularization, in particular, uses the Pearson χ^2 as a statistics, with the further assumption that all errors on the single bins of \underline{S} are equal to 1. This holds only when the statistics of each S_i is gaussian, with $\sigma = 1$ and if the number of counts in each bin is high enough (as a rule of thumb $S_i > 5 \forall i$).

The bremsstrahlung emission analysed in chapter 4, on the other hand, has a Poissonian statistics in each bin and measurements always exhibit a high-energy tail with few counts (< 5), which contains most of the information about the high energy part of the runaway electrons (RE) 1D energy distribution function. When applied to this problem, Tikhonov regularization underestimates the importance of high energy counts and often fails at reconstructing the maximum energy of the RE beam (see chapter 4 for further details).

A natural modification to Tikhonov regularization is the negative Poisson log likelihood derived in [73, 74] especially for counting problem such as the one mentioned above. The square of the residuals is replaced by:

$$l(\underline{W} \cdot \underline{F} | \underline{S}) = \sum_{i=1}^m ([\underline{W} \cdot \underline{F}]_i + \beta) - \sum_{i=1}^m (S_i \log([\underline{W} \cdot \underline{F}]_i + \beta)) \quad (3.8)$$

where $0 < \beta \ll 1$ is a small positive parameter that prevents the log likelihood from diverging when $[\underline{W} \cdot \underline{F}]_i = 0$, and at the same time it must be small enough for not perturbing the data. The regularization method then reads:

$$\hat{\underline{F}} = \arg \min [l(\underline{W} \cdot \underline{F} | \underline{S}) + \alpha \|\underline{L} \cdot \underline{F}\|_2^2] \quad (3.9)$$

and once again \underline{L} has been set to be of the 1st-order.

3.4 Maximum Likelihood using Expectation Maximization

Maximum Likelihood using Expectation Maximization (ML-EM) is an iterative method proposed, independently, by Richardson [75] and Lucy [76]. It was first derived as a rectification method applied to degraded images or astrophysical measurements affected by observational errors. Thanks to its versatility, it is now extremely popular for performing spatial tomography reconstructions from emission signals, especially for the human Positron Emission Tomography (PET) [77–79].

The method is derived from the Bayesian statistics: consider $F(x) dx$ to be the probability density function of the quantity that we would like to measure, e.g. the 1D energy distribution of runaway electrons in a plasma, so that $x = E_{RE}$. $S(y) dy$ is the probability density functions describing the unbinned measured data, e.g. the measured energy of the Bremsstrahlung photons emitted by the runaway electrons, in this case $y = E_{measured}$. $W(y, x)$ is the conditional probability introduced in (3.1) and here expressed as a continuous function. Then equation (3.1) can be written as an integral equation of the first kind:

$$S(y) = \int_{-\infty}^{\infty} W(y, x) F(x) dx \quad (3.10)$$

with kernel $W(y, x)$. Bayes theorem states that the probability of measuring a signal in $(y, y + dy)$ given a source in $(x, x + dx)$ can be equivalently written as:

$$P = [S(y) y] [W^{-1}(x, y) dx] = [F(x) dx] [W(y, x) dy] \quad (3.11)$$

where $W^{-1}(x, y)$ is the inverse of $W(y, x)$. Bayes integrated over y gives the inverse equation of (3.10):

$$F(x) = \frac{\int_{-\infty}^{\infty} W^{-1}(x, y) S(y) dy}{\int_{-\infty}^{\infty} W(y, x) dy} \quad (3.12)$$

and, by substituting (3.10) into Bayes theorem, $W^{-1}(x, y)$ can be written in terms of $W(y, x)$ and $F(x)$:

$$W^{-1}(x, y) = \frac{F(x) W(y, x)}{\int_{-\infty}^{\infty} W(y, x) dy \int_{-\infty}^{\infty} F(x) W(y, x) dx'} \quad (3.13)$$

in discrete form:

$$W_{ij}^{-1} = \frac{F_i W_{ji}}{\sum_{h=1}^n W_{hi} \sum_{k=1}^n F_k W_{jk}}. \quad (3.14)$$

The idea behind ML-EM is to use an estimate of F to compute W^{-1} using (3.13), and then substitute W^{-1} into (3.12) to iteratively update the estimate of F . Falling back to the discrete problem and substituting (3.13) into (3.12), the method is illustrated by a single formula:

$$F_i^{p+1} = \frac{F_i^p}{\sum_{h=1}^n W_{hi}} \sum_{j=1}^m \left[W_{ji} \frac{S_j}{\sum_{k=1}^n W_{jk} F_k^p} \right] \quad (3.15)$$

where p is the iteration number. At each step the estimate \underline{F} is increased or decreased on average if $\frac{S_j}{\sum_{k=1}^n W_{jk} F_k^p}$ lower or greater than 1 and the method converges when: $\frac{S_j}{\sum_{k=1}^n W_{jk} F_k^p} \xrightarrow{n \rightarrow \infty} 1$. In this perspective, $\frac{W_{hi}}{\sum_{h=1}^n W_{hi}}$ works very similarly to the weight functions of chapter 5 and it can be seen as an estimate of the probability that a count in S_j (and so the discrepancy between S_j and its reconstruction) is generated by F_i .

The first guess \underline{F}^0 can be set at will and three different initializations, which are plotted in figure 3.4, will be used in the next chapters:

$$\underline{F}^0 = \underline{\mathbb{1}} \quad \text{Uniform first guess} \quad (3.16)$$

$$\underline{F}^0 = \frac{\underline{S}}{\|\underline{W}^T \cdot \underline{S}\|} \quad \text{First guess proposed in [42]} \quad (3.17)$$

$$\underline{F}_i^0 = \sum_{j=1}^m \left(\frac{W_{ji}}{\sum_k W_{jk}} \right) \cdot S_j \quad (3.18)$$

the last one in particular has been derived from the constant initialization using

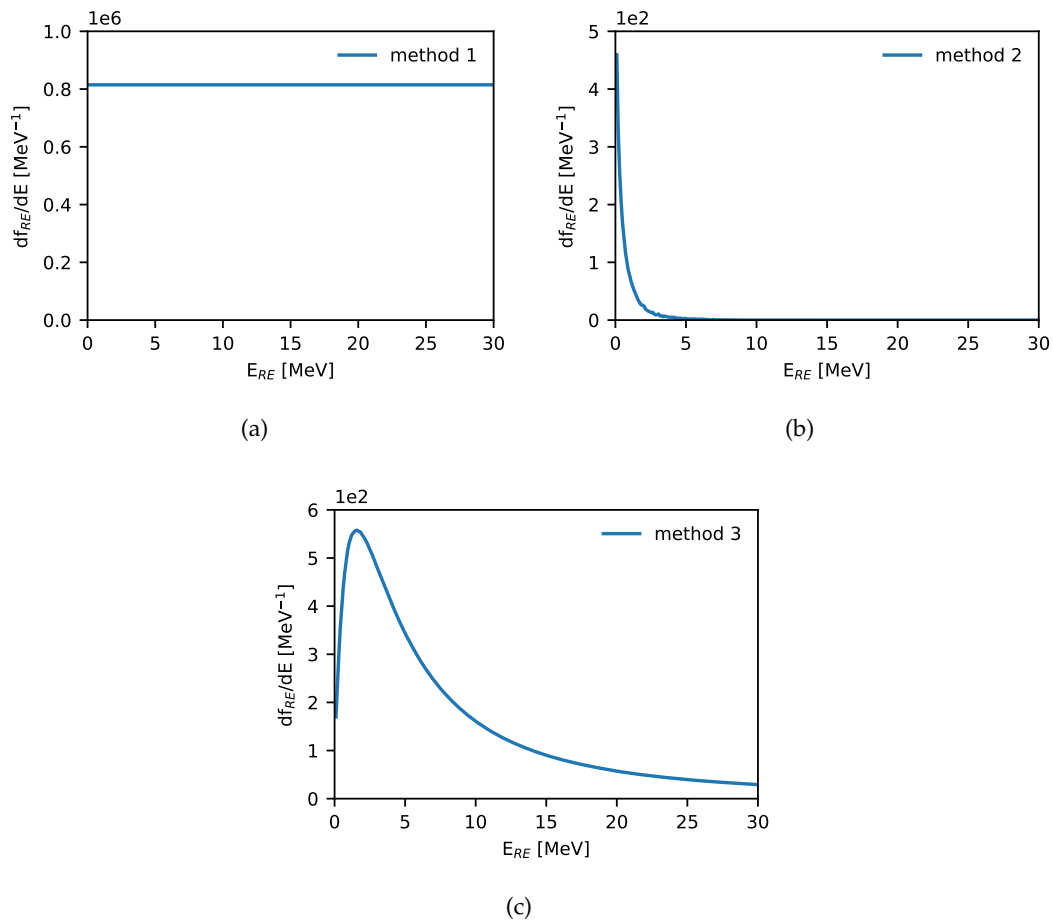


FIGURE 3.4: Plot of the initialization options for the first iteration of the ML-EM reconstruction of AUG discharge #34084 inverted in figure 4.8(b). Figure (a) is the uniform first guess introduced in equation (3.16); figure (b) is the first guess introduced in equation (3.17); figure (c) is the first guess introduced in equation (3.18).

Bayesian inference. In all the applications faced so far, all initializations converge to the same reconstruction: this suggests (but does not guarantee) that for our problem ML-EM converges regardless to the first guess and that the first guess only determines the number of iterations required for convergence. In the case of the 1D reconstruction of the REs' energy distribution, after roughly one iteration both (3.16) and (3.17) retrieve the shape of (3.18): this is negligible when the number of iterations is of the order of 10^2 or greater, such as in chapter 4, but it might represent a useful speedup in the case of the spatial tomography (chapter 6), where the number of iterations is usually less than 20.

The smoothing operator of ML-EM is three-fold. First of all, a full convergence (i.e. all ratios $\frac{S_j}{\sum_{k=1}^n W_{jk} F_k^p} = 1$) is not desirable as it would lead to an *over-fitting* of the experimental noise [76]. An early stop helps preventing the formation of artefacts in the reconstructed distribution. Different methods for deciding the maximum number of iterations have been proposed in literature [42, 76, 80, 81]. Usually they minimize

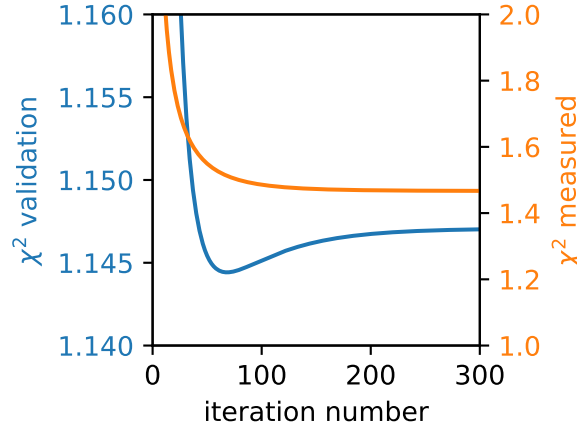


FIGURE 3.5: $\chi^2(\underline{W} \cdot \underline{E}, \underline{S})$ calculated over a validation sub-sample \underline{S}_c drawn from the experimental spectrum \underline{S} shown in figure 4.8(a) and over the experimental spectrum itself $\underline{S}_r = \underline{S} - \underline{S}_{validation}$.

a statistics such as the Pearson $\chi^2(\underline{S}, \underline{W} \cdot \underline{E})$ or the L^p norm. Another approach is to stop the reconstruction when a single iteration does not update the solution significantly, e.g. by setting a threshold under which the reconstruction is stopped on the correlation between two iterations, defined in equation (5) of [80], or on the difference of the residuals between iterations $\|\underline{S} - \underline{W} \cdot \underline{E}^{p-1}\| - \|\underline{S} - \underline{W} \cdot \underline{E}^p\| < \epsilon$ [42]. However Lucy [76] pointed out that these statistics often have a monotonic decreasing behaviour, in which case they fail at detecting at which iteration the method starts over-fitting the solution. When the statistics of \underline{S} is high enough, the experimental data has been divided in two different data-set: one with higher statistics, \underline{S}_r , which is used for reconstructing \underline{E} , and one with lower statistics, \underline{S}_c , which is used to evaluate the goodness of the reconstruction as $\chi^2(\underline{S}_c, \underline{W} \cdot \underline{E})$. Since the two data-set are statistically independent, so will be their experimental noise and the overfitting will cause the χ^2 to start increasing after a certain number of iterations as in figure 3.5.

Since the noise on different bins in the measured spectra is not correlated and it has zero mean, the average over closest points can help reducing its propagation through the reconstruction. Every $n_{smoothing}$ iteration, then, a sliding window average is performed on the reconstruction. The user can set the intensity of this smoothing by selecting an appropriate $n_{smoothing}$, i.e. the frequency at which the reconstruction is smoothed, and the width of the window, i.e. the number of bins over which the average is calculated. Usually this is equivalent to apply to the reconstruction a moving filter $\underline{\underline{L}}$ which recalls Tikhonov $\underline{\underline{L}}$ operator or the filter used in convolutional neural networks, e.g. for 1D reconstructions where the mean is calculated over the closest pixels the filter would be $\underline{\underline{L}} = [1, 1, 1]$. For most applications this is enough to smooth the reconstruction, however the procedure described so far is intrinsically limited and it has proven to be unsatisfactory in certain synthetic tests

(see section 4.2). If a stronger smoothing is required, the convergence of the algorithm can be slowed down by mean of a parameter $\lambda \in (0, 1] \subseteq \mathbb{R}$ [82], which works as follows. At each iteration \underline{F}^{p+1} is calculated as a weighted average of \underline{F}^p and \underline{F}^{p+1} itself:

$$F_i^{p+1} = \lambda \frac{F_i^p}{\sum_{h=1}^n W_{hi}} \sum_{j=1}^m \left[W_{ji} \frac{S_j}{\sum_{k=1}^n W_{jk} F_k^p} \right] + (1 - \lambda) F_i^p \quad (3.19)$$

in this way n_{iter} required to reconstruct a certain solution will be increased by roughly $\frac{1}{1-\lambda}$ with respect to (3.15). Similarly the intensity of the smoothing operator will increase by the same fraction. λ and $n_{smoothing}$ combined together can be seen as a rational version of the real parameter α used to select the intensity of the smoothing operator in Tikhonov reconstruction (see section 3.2).

Equations (3.15) and (3.19) preserves the normalization of $\underline{W} \cdot \underline{F}$, as in fact, inverting the order of the sums and using simple algebra, it can be proven that:

$$\sum_{i=1}^m \left(\sum_{j=1}^n W_{ij} F_j^p \right) = \sum_{i=1}^m S_i \quad \forall p.$$

If $\sum_{h=1}^n W_{hi} = 1$ ML-EM also preserves the normalization of $\|\underline{F}\| = \|\underline{S}\|$, but it is not the case of the application considered in this work. On the other hand, the smoothing average does not preserves the normalization of the reconstruction, which must be recovered after every application of the smoothing operator. Since every \underline{W} calculated in this work has $W_{ij} \geq 0$, the positivity of the first guess is naturally preserved by the algorithm.

It is worth citing one last property of ML-EM: the reconstruction \underline{F} is the one that maximizes the likelihood of $\underline{\tilde{S}} = \underline{W} \cdot \underline{F}$ defined as $\mathcal{L} = \sum_{i=1}^m \tilde{S}_i \ln(S_i)$: nomen omen.

In summary, the method works as follows:

1. the reconstruction is initialized according to (3.16), (3.17) or (3.18)
2. the smoothing intensity is set choosing appropriate:
 - $n_{iter} \in [1, \infty) \subseteq \mathbb{N}$
 - $n_{smoothing} \in [1, \infty) \subseteq \mathbb{N}$
 - smoothing filter \underline{L}
 - $\lambda \in (0, 1] \subseteq \mathbb{R}$
3. the reconstruction is updated according to (3.19) for n_{iter} iterations
4. every $n_{smoothing}$ iterations the moving filter is applied to the reconstruction, which is then renormalized so that $\sum_{i=1}^m \left(\sum_{j=1}^n W_{ij} F_j \right) = \sum_{i=1}^m S_i$.

3.5 Confidence bands

The interval of confidence of the reconstruction of \underline{F} can be estimated propagating the errors on both the measurements and, optionally, the simulated quantities (i.e. $\delta\underline{S} \approx \sqrt{\underline{S}}$ and $\delta\underline{W}$) using standard (analytic) error propagation techniques. Among the methods considered in the present work, this approach however can be used only with SVD and ML-EM, i.e. inversion algorithms that make use of an explicit formula for reconstructing $\underline{F} = \underline{F}(\underline{S}, \underline{W})$.

A more general approach has been implemented, which make use of a Monte Carlo error analysis technique [83] that propagates random perturbations in \underline{S} through the deconvolution process. Given the experimental data \underline{S} , the number of counts in each bin of the spectrum is used to estimate the mean of the underlying Poissonian distribution. N random variations of \underline{S} , denoted by $\tilde{\underline{S}}_r$, are generated and deconvolved. If N is high enough, say $N \geq 100$, the single bins of the reconstructions $\tilde{\underline{F}}_r$ follow a Gaussian distribution around the true reconstruction \underline{F} and their standard deviation can be used to estimate its error band $\delta\underline{F}$.

This Monte Carlo error analysis can also be applied to all the statistics $s(\underline{F})$ that can be extracted from \underline{F} (see chapter 4). In this case each bin F_i is supposed to follow a Gaussian distribution with $\sigma_{F_i} = \delta F_i$: the desired statistics $s_r = s(\tilde{\underline{F}}_r)$ is calculated from N distributions $\tilde{\underline{F}}_r$ randomly generated around the true distribution \underline{F} and the error is again calculated as a standard deviation $\delta s(\underline{F}) = \sigma(s_r)$.

As discussed in chapter 4, this method works nicely with SVD and ML-EM, which show a linear relation between \underline{F} and \underline{S} : the mean of the perturbed reconstructions $\tilde{\underline{F}}_i$ lies on the true inversion \underline{F} and the confidence band is smooth. The same holds for the evaluation of the error on the statistics estimation. The two regularization approaches of sections 3.2 and 3.3 on the other hand show wider confidence bands which suggests that the minimizer might bump into a local minimum when reconstructing a perturbation.

3.6 Cumulative statistics

In the case of REs the reconstructed energy distribution can be used to estimate different plasma parameters such as the plasma current I_p driven by REs during disruptions, i.e. the RE beam average energy $\langle E \rangle$, and the maximum energy of the beam E_{max} . These quantities has been calculated according to:

$$\langle E_{RE} \rangle = \sum_i F_i E_{RE,i} \quad (3.20)$$

$$E_X^{max} = \hat{E}, \text{ such that: } \int_0^{\hat{E}} F(E) dE = X. \quad (3.21)$$

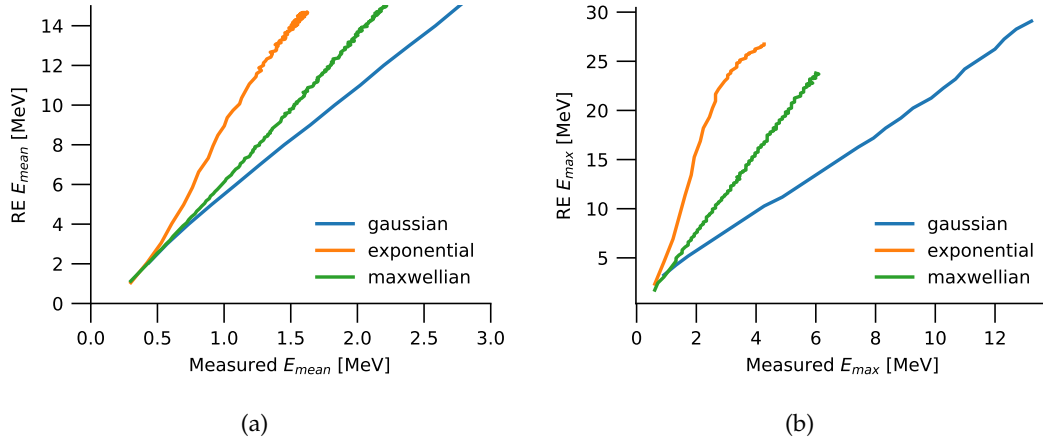


FIGURE 3.6: Comparison of the mean $\langle E \rangle$ and maximum E^{90} energy of the HXR measured spectrum and the RE beam for different synthetic RE distributions. Three synthetic RE distribution have been used: the gaussian distribution (4.7), the exponential distribution (4.8) and the maxwellian distribution (4.9). In each case the HXR spectrum has been calculated using the forward model \underline{W} shown in figure 4.3(a).

In (3.21), X is the percentile at which the maximum energy is calculated and is usually set to $X = 90, 99$ or 99.9% . As said, the plasma current during plasma disruptions is driven solely by REs and can be computed from the mean energy as:

$$I_p = Ae^- n_{RE} \mu_{RE} \quad (3.22)$$

where A is the beam cross section, e^- is the electron unitary charge, n_{RE} the RE volume density and μ_{RE} the REs mean velocity which can be calculated as:

$$\mu_{RE} = \int_0^\infty v f(v) dv = \int_0^\infty v(E) f(v(E)) \frac{dv}{dE} dE = \int_0^\infty v(E) f(E) dE. \quad (3.23)$$

Here the same approximation used in section 4.1 has been used, i.e. all RE are considered having pitch $p_{RE} = 1$, thus $v_{RE} \parallel \mu_{RE} \parallel \hat{n}(A)$. Moreover, since $E_{RE} = (\gamma(v_{RE}) - 1)mc^2$ is the kinetic energy of the RE, (3.23) becomes:

$$\mu_{RE} = \int_0^\infty \frac{c}{E + mc^2} \sqrt{E^2 + 2mc^2E} f(E) dE \quad (3.24)$$

The calculations conducted so far are based on the fact that v_{RE} is a deterministic function of $E = E_{RE}$. On the other hand $E_{HXR}(E_{RE})$ depends on probabilistic processes and an analysis such as the one above is not possible in this case. However there is a relationship between the RE beam cumulative statistics and the HXR measured spectrum ones, which is worth noting. Let's consider the HXR mean measured

energy:

$$\begin{aligned}\langle E_{measured} \rangle &= \int_0^{\infty} E_{measured} S(E_{measured}) dE_{measured} \\ &= \int_0^{\infty} E_{measured} \int_0^{\infty} W(E_{measured}, E_{RE}) F(E_{RE}) dE_{RE} dE_{measured} \quad (3.25)\end{aligned}$$

$\langle E_{measured} \rangle$ is proportional to $\langle E_{RE} \rangle$ if and only if:

$$\begin{aligned}0 &= \langle E_{measured} \rangle - C \langle E_{RE} \rangle \\ 0 &= \int_0^{\infty} \int_0^{\infty} E_{measured} W(E_{measured}, E_{RE}) dE_{measured} F(E_{RE}) dE_{RE} - C \int_0^{\infty} E_{RE} F(E_{RE}) dE_{RE} \\ 0 &= \int_0^{\infty} \left(\int_0^{\infty} E_{measured} W(E_{measured}, E_{RE}) dE_{measured} - CE_{RE} \right) F(E_{RE}) dE_{RE} \quad (3.26)\end{aligned}$$

with C as constant of proportionality. If $\exists! C$ such that:

$$\int_0^{\infty} E_{measured} W(E_{measured}, E_{RE}) dE_{measured} = CE_{RE} \quad \forall E_{RE},$$

than (3.26) would hold $\forall \underline{F}$. Unfortunately this is not the case, as in fact figure 3.6 proves that different \underline{F} have different constant of proportionality C . However the following statement still holds:

$$\forall \underline{F}, \exists! C = C(\underline{F}) \text{ such that:} \quad \text{the equality (3.26) is true.}$$

From a practical point of view this statement implies that $\langle E_{RE} \rangle$ can be calculated directly from $\langle E_{measured} \rangle$ knowing the constant of proportionality $C(\underline{F})$ in two situations: if two experiments generate the same energy distribution \underline{F} and if the energy distribution \underline{F} is preserved in two distinct time intervals of the same experiment. Inversely, having $\langle E_{RE} \rangle = \frac{1}{C} \langle E_{measured} \rangle$ with the same constant C in two different experiments is a necessary (but not sufficient) condition that \underline{F} is the same in both experiments. With some more algebra, it can be shown that the same statement holds for $\langle E_{measured} \rangle$ and μ_{RE} , thus if $I_p(t)$ can be reconstructed from $\langle E_{measured} \rangle(t)$ using the same constant C over all the disruption, this is a good indication that $\underline{F}(t)$ has a constant shape throughout the experiment.

Figure 3.6 shows the relation between RE and HXR mean and maximum E_{max}^{90} energy. Three synthetic RE distribution have been used: the gaussian distribution (4.7), the exponential distribution (4.8) and the maxwellian distribution (4.9). For each family of distribution functions, the initial parameters were changed so that E_{max} and $\langle E \rangle$ could span all the dynamic range of the detector $[0, 30]$ MeV. The HXR spectrum was synthetically generated using the forward model calculated for the detector installed in the Bragg Bunker at AUG, whose transfer matrix \underline{W} is shown in figure 4.3. The same graph can be reproduced also for E_{max}^{99} and $E_{max}^{99.9}$ and in all

the four estimates here considered a proportionality between the HXR and the RE statistics have been detected. In the case of the maximum energy of the exponential distribution, the graph loses its linearity only when the RE maximum energy is approaching the the end of the detector dynamic range, which in figure 3.6 is 30 MeV.

The analysis conducted in [40] shows that for many discharges of JET and AUG, the constant of proportionality between both RE and HXR statistics is the same. This might indicate that that kind of experiments, where the plasma disruption is generated with a MGI, always generates the same RE beam with similar energy distribution \underline{E} . A more specific analysis should be performed in order to exclude that this is instead the result of an over-smoothing of the experimental data. For JET discharges, where the GCU data are available and complete, this can be done by reconstructing I_p directly from $\langle E_{measured} \rangle$.

Part III

Data Analysis

Chapter 4

Reconstruction of the 1D energy distribution

Spectroscopic measurements of the bremsstrahlung emission from REs have been made possible by the installation of new detectors such as the ones introduced in chapter 2, which were developed specifically for fast (counting rates up to 1 MCps), high resolution (energy resolution $< 5\%$ at the ^{137}Cs gamma-ray peak, $E_\gamma = 661$ keV) measurements in high magnetic fields ($B \approx 1$ T). As outlined in chapter 1, the bremsstrahlung spectrum is an indirect measurement of the 1D energy distribution of the runaway electron beam, which can be unfolded from the experimental data by means of the inversion approach presented in chapter 3.

This analysis of the HXR spectra has been applied to RE experiments conducted at JET and ASDEX Upgrade [39, 40, 42, 81] allowing the reconstruction of important beam parameters, such as the average and maximum energy as well as the plasma current driven by the RE. However the deconvolution process is a delicate operation, due to its ill-posed condition, and each algorithm performs differently depending on the physical problem analyzed, i.e. the shape of \underline{W} . This poses some problems when interpreting the results of the analysis from a physics point of view. An example of this issue comes from the analysis of AUG shot #34084 [39, 81], which was part of a series of experiments where a first MGI of Ar at 1.00 s has been used to induce a plasma disruption and to generate a RE beam, while a second massive quantity of Ar was successively injected at 1.13 s to mitigate the REs. The ML-EM analysis of the HXR spectrum in the time intervals 1.00-1.13 s and 1.13-1.45 s has pointed out that the RE beam maximum energy, defined as $E^{99.9}$, decreases from roughly 24 MeV to 17 MeV after the second MGI. In order to prove that the mitigation technique has effectively modified the RE energy distribution, suppressing the high energy component of the beam, one should first rule out that the structure above 20 MeV is an artefact generated by the reconstruction technique.

Standard validation procedures for deconvolution methods make use of real phantoms designed to test different aspects of the method in use. Examples of these

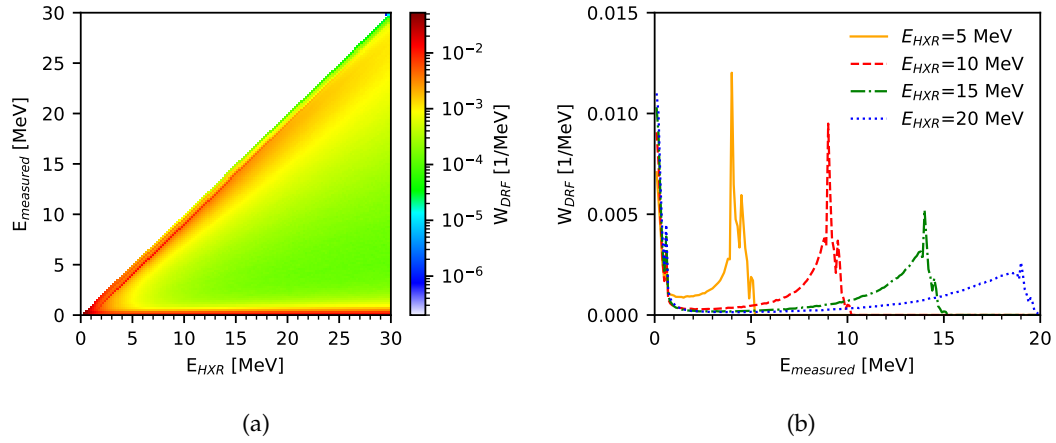


FIGURE 4.1: (a) The detector response function \underline{W}_{DRF} for the LaBr₃ scintillator installed in the Bragg Bunker at AUG, calculated with the MCNP code. (b) The detection probability of four gamma-ray energies ($E_{HXR} = 5, 10, 15$ and 20 MeV), i.e. four columns of \underline{W}_{DRF} . (b) is reproduced from [85] with permission of the publisher.

procedures are the NEMA protocols for positron emission tomographs (PET), which aim at assessing the spatial resolution, the sensitivity and other characteristics of PET scanners. In such protocols, the radiation emitted by each phantom is first measured by the PET scanner and then the spatial distribution of the original phantom is reconstructed performing a tomographic inversion. The comparison between the original phantom and its reconstruction allow to evaluate three aspects of the analysis: the performance of the detectors used to measure the phantom emission, the performance of the deconvolution method and the validity of the transfer matrix used for the inversion. The use of real phantoms is not an option with relativistic runaway electrons, since it would require a facility able to generate relativistic electrons with known energy distribution. However one can still test the inversion algorithm using synthetic phantoms that emulate RE beams with different energy distributions, such as gaussian or exponential [84, 85]. This is the approach adopted in section 4.2, where the four inversion methods introduced in chapter 3 are compared. In section 4.3, on the other hand, experimental data acquired at AUG are analyzed. Different number of counts and low energy cut in the measured spectra are considered in order to assess the stability of the reconstruction retrieved by those four methods. The reliability of the reconstruction of the RE beam average energy $\langle E_{RE} \rangle = \sum_i F_i E_{RE,i}$ and maximum energy (see section 3.6 for its definition) is finally discussed.

4.1 Transfer matrix

Let's consider the discretized inverse problem (3.1). In the reconstruction of the 1D RE energy distribution, the transfer matrix \underline{W} is a function of the REs energy E_{RE}

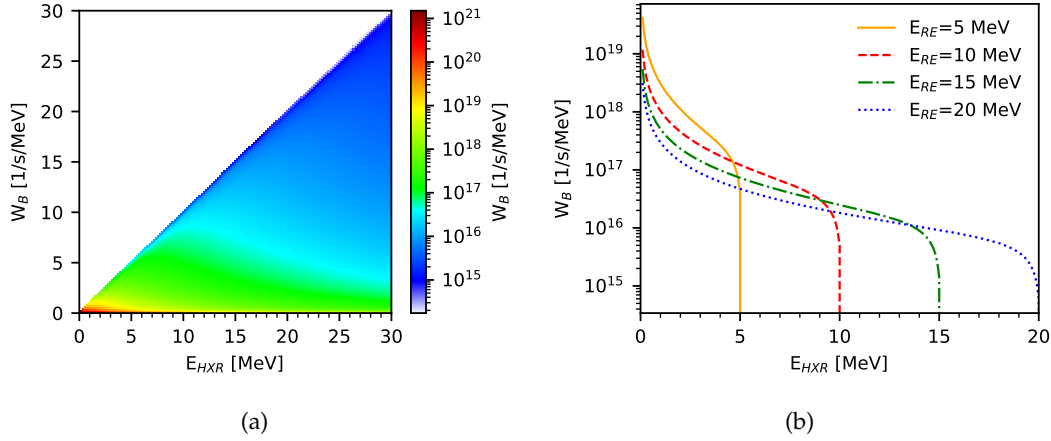


FIGURE 4.2: (a) Bremsstrahlung emission probability rate \underline{W}_B for a RE beam in an Argon plasma, calculated using the GENESIS code. (b) Four bremsstrahlung emission spectra for monoenergetic RE beams having $E_{RE} = 5, 10, 15$ and 20 MeV, i.e. four columns of \underline{W}_B .

and the energy measured by the detector, $E_{measured}$ [85]:

$$\underline{S}(E_{measured}) = \underline{W}(E_{measured}, E_{RE}) \cdot \underline{F}(E_{RE}). \quad (4.1)$$

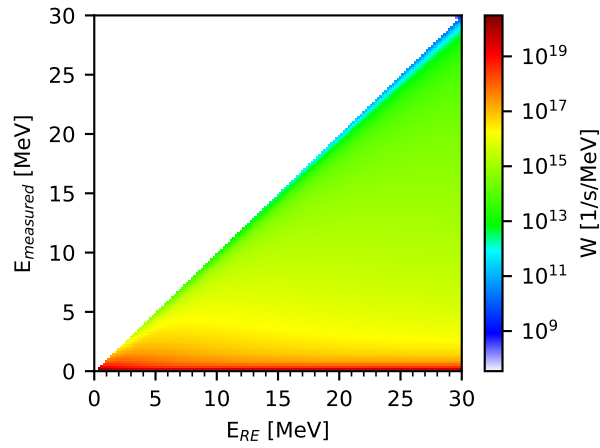
In order to compute \underline{W} from (4.1), consider the case of a mono energetic RE population: E_{RE} is fixed and the particle distribution can be written as $\underline{F} = N_{RE} \delta(E - E_{RE})$. Substituting in equation (5.1):

$$W(E_{RE} = E) = \frac{1}{N_{RE}} \underline{S},$$

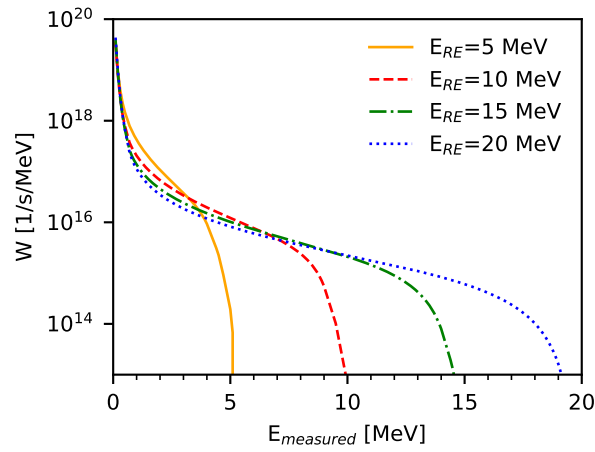
i.e. the transfer matrix contains the expected spectra measured from a mono-energetic population, normalized to the number of particles. In particular \underline{W} describes three independent processes, which can be considered separately: the emission of a HXR photon in a bremsstrahlung collision between a RE and a thermal ion in the background plasma, its propagation to the detector and its interaction with the scintillator crystal. In this work, the latter two processes are described in the detector response function (DRF). The matrix then can be factorized in two parts:

$$\underline{W} = \underline{W}_{DRF} \cdot \underline{W}_B \quad (4.2)$$

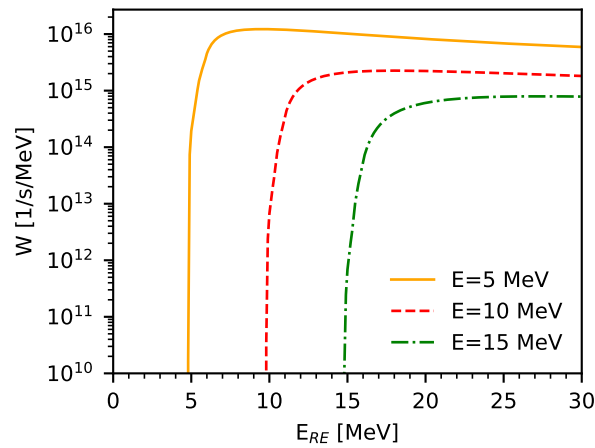
with \underline{W}_{DRF} describing the detector response function and \underline{W}_B describing the bremsstrahlung emission. The first factor has been calculated using the MCNP code [38] for the HXR detectors installed at AUG and at JET. All these detectors use LaBr₃ crystals as active medium and what changes from a simulation to another is the dimensions of the detector and its line of sight. In figure 4.1, the DRF of the detector installed in the Bragg bunker at AUG is shown as an example. The columns of this



(a)



(b)



(c)

FIGURE 4.3: (a) Transfer probability matrix $\underline{W} = \underline{W}_{DRF} \cdot \underline{W}_B$ for the LaBr₃ scintillator installed in the Bragg Bunker at AUG (for \underline{W}_{DRF} and \underline{W}_B see figs. 4.1 and 4.2). (b) Four expected spectra generated by a monoenergetic RE beam for different energies ($E_{RE} = 5, 10, 15$ and 20 MeV), i.e. four the columns of \underline{W} . (c) Weight functions for three signals of energy $E = E_{measured} = 5, 10, 15$ and 20 MeV, i.e. three rows of \underline{W} . (b) and (c) are reproduced from [85] with permission of the publisher.

matrix, i.e. $\underline{W}_{DRF}(E_{HXR} = const)$, represent the expected measured spectrum induced by an ideally monoenergetic γ -ray beam. For low energies (below ≈ 3 MeV) this spectrum exhibits a prominent photo-peak. As the energy increases, pair production becomes more important: the photo-peak reduces its intensity, while the single and double escape peaks increase theirs. For energies higher that ≈ 20 MeV the only relevant interaction is the Compton scattering and the Compton shoulder exhibits the Klein-Nishina shift towards the incident photon energy. The overall detection efficiency decreases as the energy increases.

The bremsstrahlung emission probability matrix can be computed as the density reaction rate of bremsstrahlung photons divided by the RE density [86], in functional form:

$$W_B(E_{HXR}, E_{RE}, p_{RE}) = |\underline{v}_{RE}| \Delta t \int_{LOS} n_i d\Omega \frac{d\sigma}{dW d\Omega}(E_{HXR}, E_{RE}, \theta) d\phi d\underline{x} \quad (4.3)$$

here $|\underline{v}_{RE}| = c \sqrt{1 - \left(\frac{mc^2}{E_{RE} + mc^2}\right)^2}$ is the module of the velocity of the RE, $n_i(\underline{x})$ is the ions density in the background plasma, $d\Omega(\underline{x})$ is the solid angle subtended by the detector, Δt is the time interval of the measurement and θ is the angle of emission. $\frac{d\sigma}{dE_{HXR} d\Omega}$ is the double differential cross section for bremsstrahlung collisions and has been calculated with the GENESIS code [47, 87], which implements the semi-empirical formula derived by Salvat in [26, 27]:

$$\frac{d^2\sigma}{dE_{HXR} d\Omega} = \frac{d\sigma}{dW}(Z, E_{RE}, k) p(Z, E_{RE}, k | \cos \theta) \quad (4.4)$$

where $k = \frac{E_{HXR}}{E_{RE}}$. The cross section is divided in two factors, here termed *angular factor* and *energy factor*. The angular term describes the anisotropy of bremsstrahlung emission, which is calculated using equation (25) of [27] (except for the normalization, which here is set to unity):

$$p(Z, E, k | \cos \theta) = \frac{3}{8} \left[1 + \left(\frac{\cos \theta - \beta}{1 - \beta \cos \theta} \right)^2 \right] \frac{1}{\gamma^2 (1 - \beta \cos \theta)^2}. \quad (4.5)$$

The energy factor describes the energy loss probability using the Bethe-Heitler differential cross section, with the exponential screening factor from Wentzel (for further details refer to [26], equation (49)). In principle the angle of emission θ depends on the position, pitch and gyro-phase of the RE, namely $\theta = \theta(p_{RE}, \phi, \underline{x})$ [86], however in this chapter all REs are considered to be on the magnetic axis and with $p_{RE} = 1$ [85], thus the integral in (4.3) drops and θ can be set to $\frac{\pi}{2}$:

$$W_B(E_{HXR}, E_{RE}, p_{RE}) \approx \frac{|\underline{v}_{RE}| \Delta t}{2\pi} n_i d\Omega \frac{d\sigma}{dE_{HXR} d\Omega}(E_{HXR}, E_{RE}, \frac{\pi}{2}). \quad (4.6)$$

In figure 4.2, \underline{W}_B of the detector installed in the Bragg bunker at AUG is shown as an example.

It is worth noting that the final shape of \underline{W} , which is presented in figure 4.3(a), is mostly determined by \underline{W}_B . However, as discussed in more details in section 4.3, a correct evaluation of W_{DRF} is still important, especially for the reconstruction of the REs' distribution at low energies. In figure 4.3(a) the columns of \underline{W} are also presented: they are called *weight functions* [36, 37, 88] and represent the probability that a given signal measured in the detector has been generated by a RE of a certain energy.

4.2 Synthetic tests

In this section, the performance of the four unfolding techniques introduced in chapter 3 are tested over synthetic HXR spectra generated from known REs' energy distribution. The main goal is to verify the capability of each method to resolve specific features in the REs' distribution. The estimates of the RE average and maximum energies (see section section 3.6 for their definition) are also compared with their true value. The accuracy of these estimates and the validity of the Monte Carlo procedure used for assessing the interval of confidence of the estimates (see section section 3.5 for its definition) are finally discussed.

Four different distributions have been tested:

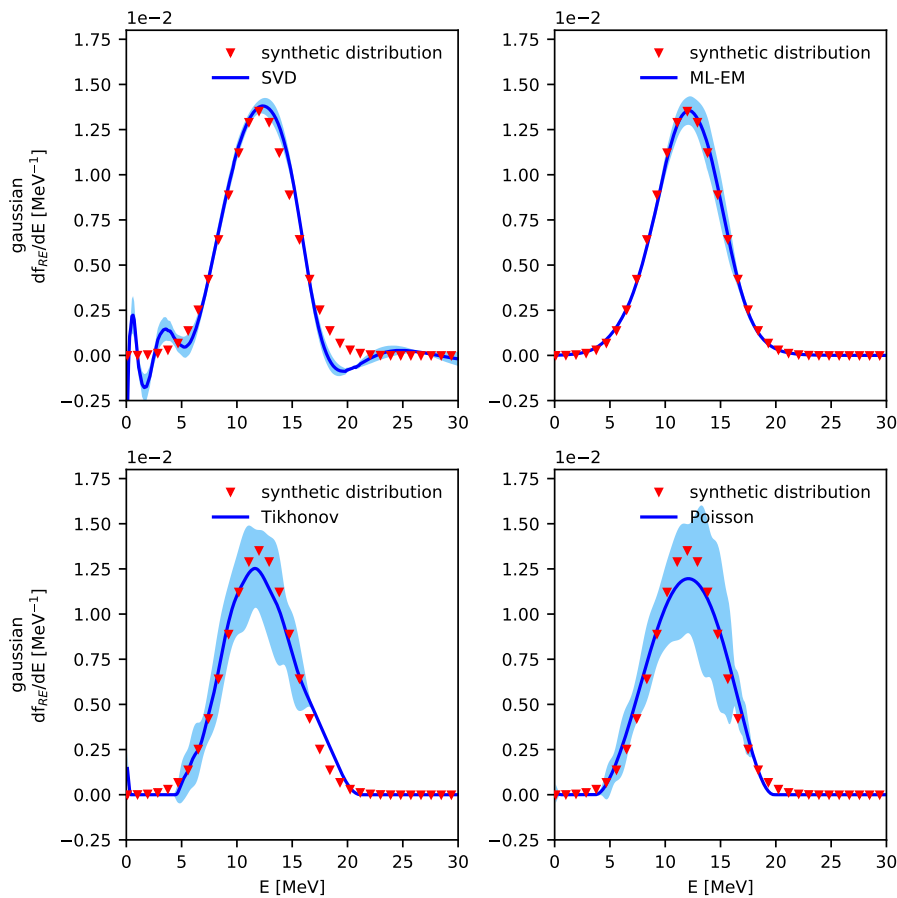
$$\text{Gaussian} \quad F_{synth} = \frac{A}{2\pi\sigma} e^{-\frac{(E_{RE}-\mu)^2}{2\sigma^2}} \quad (4.7)$$

$$\text{Exponential} \quad F_{synth} = A e^{-\frac{E_{RE}}{\tau}} \quad (4.8)$$

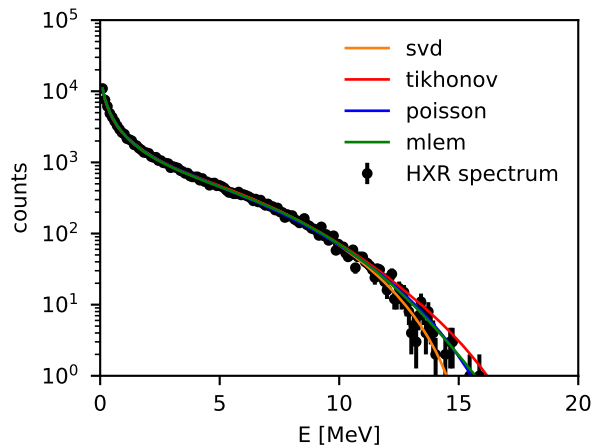
$$\text{Maxwellian} \quad F_{synth} = \frac{A}{\sqrt{\tau}} E_{RE}^2 e^{-\frac{E_{RE}^2}{\tau}} \quad (4.9)$$

$$\text{Maxwellian + Gaussian} \quad F_{synth} = \frac{A_1}{\sqrt{\tau}} e^{-\frac{E_{RE}^2}{\tau}} + \frac{A_2}{2\pi\sigma} e^{-\frac{(E_{RE}-\mu)^2}{2\sigma^2}} \quad (4.10)$$

Gaussian and exponential distributions represent the expected shape of respectively primary and secondary generation RE beams. (4.9) has been chosen to reproduce the shape of the first prominent peak that often appears in the analysis of experimental data (see the following works [39, 40, 42] and section 4.3). This distribution is here termed Maxwellian distribution. The comparison between the exponential distribution and this Maxwellian distribution aims at testing the reliability of the prominent peak between 2 – 4 MeV retrieved in figure 4.8. While the comparison between the purely Maxwellian distribution and the superposition of a Maxwellian and a Gaussian distribution aims at determining whether the high energy peaks ($E > 5$ MeV) could be real features or reconstruction artefacts.



(a)



(b)

FIGURE 4.4: (a) Reconstruction of a synthetic Gaussian ($\mu = 12$ MeV, $\sigma = 3$ MeV) RE distribution with the four methods of chapter 3. The red markers represent the original distribution used to generate the synthetic spectra, the blue solid line is its reconstruction and the light-blue area is the confidence band. (b) Black markers are the synthetic HXR spectrum; lines are the convolution of the REs' energy distribution of figure (a), with the transfer matrix \underline{W} of figure 4.3(a). (a) is reproduced from [85] with permission of the publisher.

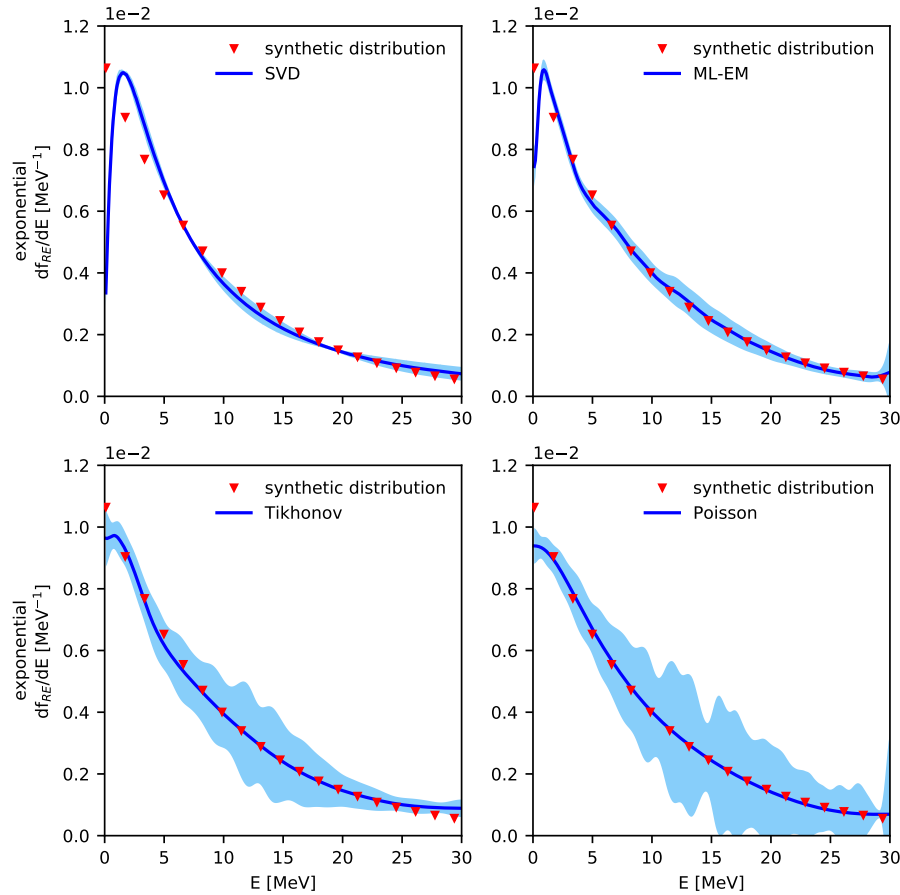


FIGURE 4.5: Reconstruction of a synthetic exponential ($\tau = 10$ MeV) RE distribution with the four methods illustrated in chapter 3. The red markers represent the original distribution used to generate the synthetic spectra, the blue solid line is its reconstruction and the light-blue area is the confidence band computed with the Monte-Carlo method of section 3.5 (when non visible the error bands are smaller than the line size). Reproduced from [85] with permission of the publisher.

For each distribution, a scan of the distribution parameters have been conducted. However, in this section one example for each family of distributions is shown: a ($\mu = 12$ MeV, $\sigma = 3$ MeV) Gaussian distribution (figure 4.4), an exponential ($\tau = 10$ MeV) (figure 4.5), a Maxwellian ($\tau = 40$ MeV) (figure 4.6) and the sum of a maxwellian and a gaussian ($\tau = 40$ MeV, $\mu = 12$ MeV, $\sigma = 1$ MeV) (figure 4.7). The latter has also been chosen also as an indication of the resolution capability of the algorithms in that energy region: if the distance of the Maxwellian and the Gaussian peaks, normalized by the sum of their standard deviations, is reduced, then none of the methods here tested would be able to resolve the second peak, which would appear as a small bump in the Maxwellian tail.

Among the four deconvolution methods, ML-EM is the one that gives the best results in term of both the ability to retrieve the shape of the initial distribution and

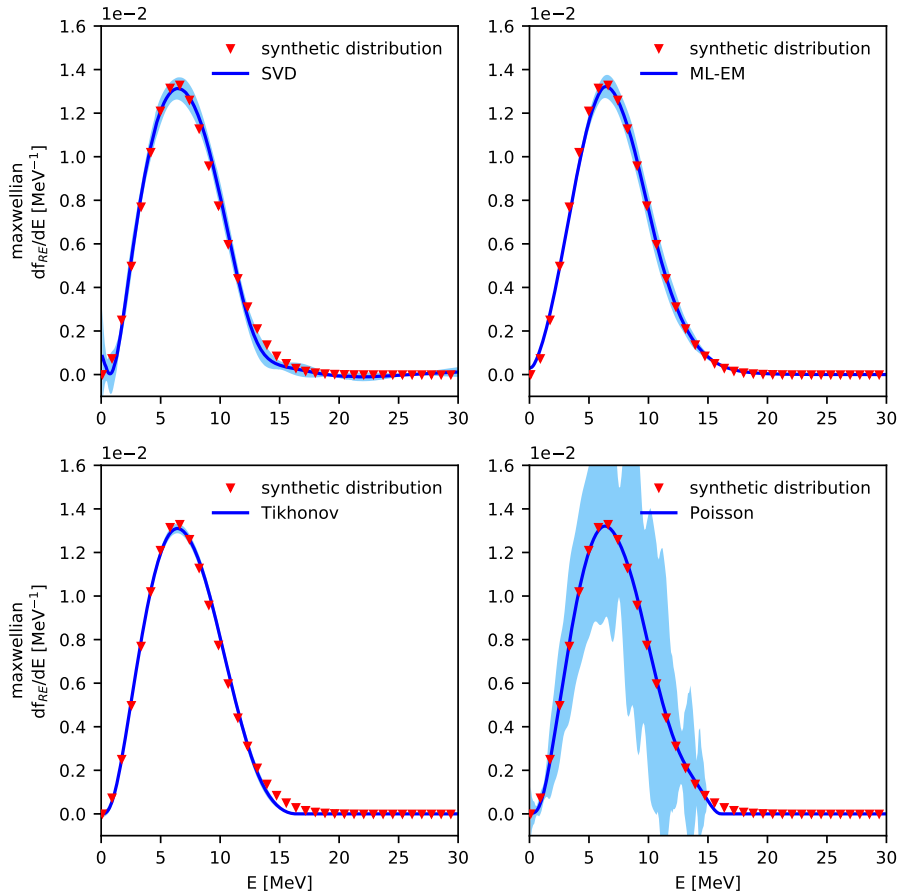


FIGURE 4.6: Reconstruction of a synthetic Maxwellian ($\tau = 40$ MeV) RE distribution with the four methods illustrated in chapter 3. The red markers represent the original distribution used to generate the synthetic spectra, the blue solid line is its reconstruction and the light-blue area is the confidence band computed with the Monte-Carlo method of section 3.5 (when non visible the error bands are smaller than the line size). Reproduced from [85] with permission of the publisher.

the confidence bar accuracy. Tikhonov and Poissonian regularization perform acceptable reconstructions as well, even though Tikhonov regularization is prone to miss-reconstruct the high-energy part of the distribution and in particular it underestimates the high-energy tail of Maxwellians distributions. Moreover, as already discussed in section 3.5, their confidence bands are wider than the other two methods. In particular, in the reconstruction performed with Poisson regularization in figure 4.7, the second peak at 12 MeV is smaller than the error band. This suggests that Poisson regularization is strongly sensitive to the noise in \underline{S} and that it needs more counts in the measured spectrum to converge to the correct distribution than the other methods (see also section 4.3). Finally SVD's reconstructions are often affected by evident artefacts: the gaussian distribution oscillates around zero on the tails, reaching also negative values; the exponential distribution shows an abrupt decrease towards 0 for $E_{RE} \rightarrow 0$, which is more pronounced than the other methods;

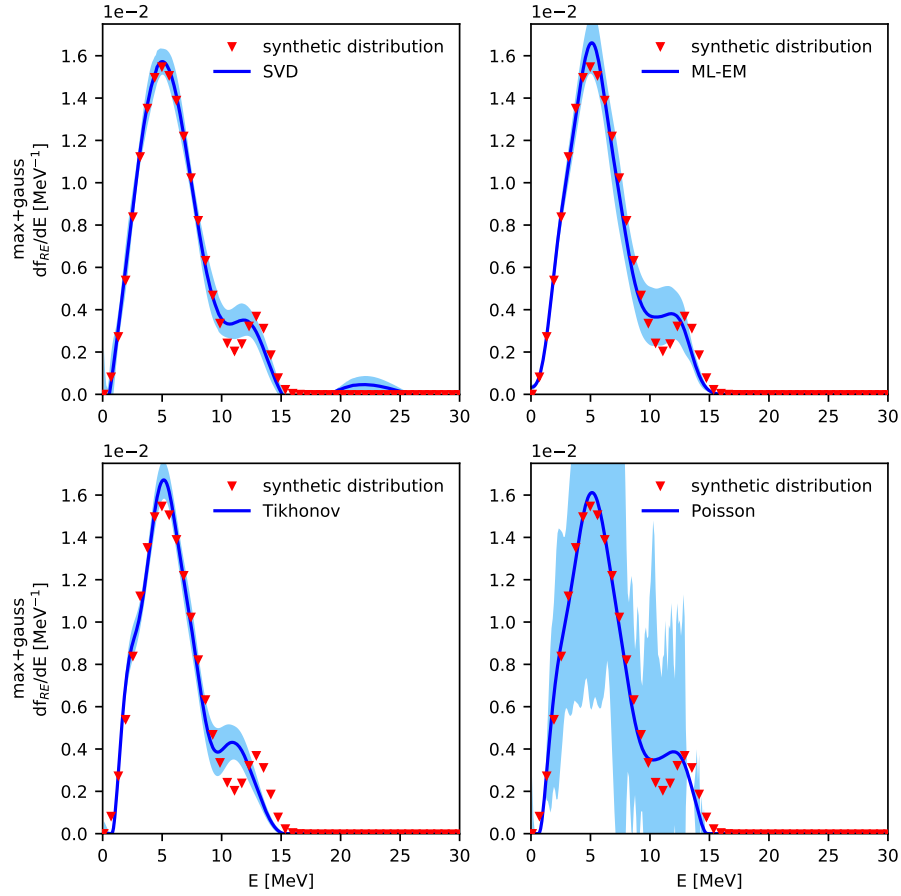


FIGURE 4.7: Reconstruction of the superposition of two synthetic RE distribution, a Maxwellian ($\tau = 25$ MeV) and a Gaussian ($\mu = 13$ MeV, $\sigma = 1$ MeV), using the four methods illustrated in chapter 3. The red markers represent the original distribution used to generate the synthetic spectra, the blue solid line is its reconstruction and the light-blue area is the confidence band computed with the Monte-Carlo method of section 3.5 (when non visible the error bands are smaller than the line size). Reproduced from [85] with permission of the publisher.

and figure 4.7 shows some structures for $E_{RE} > 20$ MeV which are not present in the original signal. The limits of SVD are most probably related to its discrete smoothing operator, whose maximum intensity is limited by the number of singular values of \underline{W} : the inversion obtained with this method is always under-smoothed; ML-EM and the regularization methods on the other hand do not have upper bounds on the intensity of the smoothing operator.

It is worth noting that regardless to the performance discussed above, all four solutions are compatible with the synthetic spectra \underline{S} . This is shown for the gaussian distribution in figure 4.4(b), all the distributions here tested give similar results. An overestimation or underestimation of the high-energy part of the REs energy distribution is reflected in the reconstruction of the experimental HXR spectrum, e.g. see Tikhonov reconstruction in figure 4.4(b). The fact that a reconstruction affected by

TABLE 4.1: For each of the synthetic distribution shown in figs. 4.4 to 4.7, here are compared the true value of the mean energy and maximum energy (defined as the 90, 99 and 99.9 percentiles of the reconstructed distribution) and its estimate, calculated on the reconstructions calculated with SVD and ML-EM. For each entry two errors are given: σ_T/σ_M . σ_T is the true error, i.e. the difference between the true value and its estimate, while σ_M is the error computed with the Monte Carlo method explained in section 3.5 and applied on the reconstructions shown in figs. 4.4 to 4.7. Reproduced from [85] with permission of the publisher.

gaussian [MeV]	SVD [MeV]	ML-EM [MeV]
$\langle E \rangle = 12.000$	$11.80 \pm 0.2/0.10$	$12.007 \pm 0.007/0.12$
$E^{90} = 15.762$	$15.15 \pm 0.6/0.10$	$15.774 \pm 0.012/0.10$
$E^{99} = 18.915$	$16.58 \pm 2/2$	$18.919 \pm 0.004/1.7$
$E^{99.9} = 21.25$	$25.83 \pm 5/0.3$	$21.66 \pm 0.4/5$
exponential [MeV]	SVD [MeV]	ML-EM [MeV]
$\langle E \rangle = 8.48$	$8.55 \pm 0.07/0.06$	$8.54 \pm 0.07/0.09$
$E^{90} = 19.32$	$20.03 \pm 0.7/0.3$	$19.22 \pm 0.10/0.4$
$E^{99} = 28.27$	$28.68 \pm 0.4/0.5$	$28.47 \pm 0.2/0.9$
$E^{99.9} = 29.80$	$29.90 \pm 0.1/0.4$	$29.90 \pm 0.10/0.5$
maxwellian [MeV]	SVD [MeV]	ML-EM [MeV]
$\langle E \rangle = 7.14$	$7.04 \pm 0.10/0.07$	$7.18 \pm 0.05/0.06$
$E^{90} = 11.08$	$10.78 \pm 0.3/0.10$	$11.19 \pm 0.10/0.15$
$E^{99} = 15.05$	$14.13 \pm 0.9/7$	$15.46 \pm 0.4/1.1$
$E^{99.9} = 18.00$	$22.78 \pm 5/2$	$19.22 \pm 1.2/7$
maxwellian + gaussian [MeV]	SVD [MeV]	ML-EM [MeV]
$\langle E \rangle = 6.25$	$6.06 \pm 0.2/0.11$	$6.18 \pm 0.08/0.12$
$E^{90} = 10.98$	$10.47 \pm 0.5/0.4$	$10.88 \pm 0.10/0.4$
$E^{99} = 14.13$	$13.32 \pm 0.8/5$	$13.63 \pm 0.5/4$
$E^{99.9} = 15.35$	$13.73 \pm 1.6/6$	$14.74 \pm 0.6/4$

artifacts can still justify the experimental data is a consequence of the ill-posedness condition of the problem, which allows multiple admissible solution. This represents a serious limitation to a forward fit analysis that aims at fitting the HXR experimental spectrum starting from first principle simulations of the REs energy distribution. Due to the ill-posedness of the problem, a successful fit does not guarantee that the simulated RE distribution is the correct one and that the simulation correctly describes the physics of REs.

The estimates of the mean and maximum energy of the RE distribution are reported in tables 4.1 and 4.2. Two errors are also reported for each entry: the true error (i.e. the difference from the statistics calculated on the original synthetic distribution and the reconstructed one) and the Monte-Carlo error calculated as described in section 3.5. These tables quantitatively confirms what it has already been qualitatively

TABLE 4.2: For each of the synthetic distribution shown in figs. 4.4 to 4.7, here are compared the true value of the mean energy and maximum energy (defined as the 90, 99 and 99.9 percentiles of the reconstructed distribution) and its estimate, calculated on the reconstructions calculated with Tikhonov and Tikhonov with Poissonian statistics. For each entry two errors are given: σ_T/σ_M . σ_T is the true error, i.e. the difference between the true value and its estimate, while σ_M is the error computed with the Monte Carlo method explained in section 3.5 and applied on the reconstructions shown in figs. 4.4 to 4.7.

Reproduced from [85] with permission of the publisher.

gaussian [MeV]	Tikhonov [MeV]	Poisson [MeV]
$\langle E \rangle = 12.00$	$12.18 \pm 0.2/0.3$	$11.95 \pm 0.05/0.4$
$E^{90} = 15.76$	$16.47 \pm 0.7/0.5$	$15.97 \pm 0.2/0.5$
$E^{99} = 18.91$	$19.22 \pm 0.3/1.5$	$18.10 \pm 0.8/1.3$
$E^{99.9} = 21.25$	$20.24 \pm 1.0/1.3$	$19.02 \pm 2/1.2$
exponential [MeV]	Tikhonov [MeV]	Poisson [MeV]
$\langle E \rangle = 8.48$	$8.79 \pm 0.3/0.19$	$8.53 \pm 0.05/0.4$
$E^{90} = 19.32$	$20.34 \pm 1.1/1.1$	$19.22 \pm 0.10/1.6$
$E^{99} = 28.27$	$28.88 \pm 0.6/1.4$	$28.58 \pm 0.3/2$
$E^{99.9} = 29.80$	$29.90 \pm 0.10/0.9$	$29.90 \pm 0.10/1.8$
maxwellian [MeV]	Tikhonov [MeV]	Poisson [MeV]
$\langle E \rangle = 7.14$	$7.05 \pm 0.08/0.02$	$7.10 \pm 0.03/0.5$
$E^{90} = 11.08$	$10.88 \pm 0.2/0.1$	$10.98 \pm 0.10/1.0$
$E^{99} = 15.05$	$13.63 \pm 1.4/0.2$	$14.13 \pm 0.9/2.0$
$E^{99.9} = 18.00$	$15.05 \pm 3/1.0$	$15.25 \pm 3/1.9$
maxwellian + gaussian [MeV]	Tikhonov [MeV]	Poisson [MeV]
$\langle E \rangle = 6.25$	$6.11 \pm 0.14/0.08$	$6.18 \pm 0.07/0.6$
$E^{90} = 10.98$	$10.58 \pm 0.4/0.2$	$10.88 \pm 0.10/2$
$E^{99} = 14.13$	$13.32 \pm 0.8/0.9$	$13.52 \pm 0.6/1.7$
$E^{99.9} = 15.35$	$14.34 \pm 1.0/0.9$	$14.24 \pm 1.1/1.6$

noticed observing the reconstruction plots: i.e. ML-EM returns the best reconstruction of the original distributions. In the case of ML-EM, also, the true difference between the original and reconstructed statistics is always less than $\approx 5\%$ and always lies within one Monte-Carlo sigma. At the opposite end, SVD is still able to reconstruct most of the statistics, which prove to be robust against artifacts in the reconstruction. In some occasions, SVD misses the original statistics by more than 10% and given the poor performance shown in this section it will not be considered for the analysis of experimental data included in section 4.3. Overall Tikhonov and Poisson regularization give fair reconstructions of the original statistics, with Poisson that gets closer to ML-EM in terms of accuracy. The large Monte Carlo error bands are however reflected in the σ_M s larger than ML-EM, especially for the mean

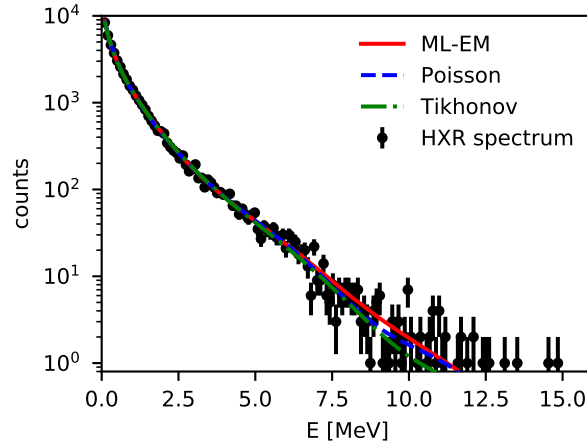
energy (the maximum energy, being a non linear estimate, tends to mask this problem). For all the methods, the 99.9% estimate of the maximum energy is particularly difficult to reconstruct, while the 99% is more reliable.

4.3 Application at ASDEX Upgrade

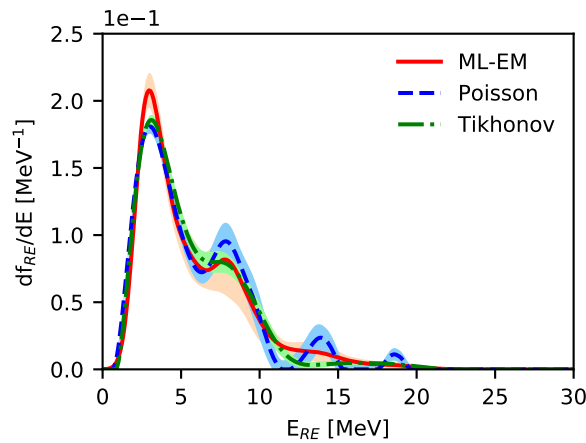
In this section, the performance of the four unfolding techniques introduced in chapter 3 are tested over the HXR spectrum measured by the detector installed in the Bragg bunker at AUG (see section 2.1.1) during shot #34084. The main goal is to assess the robustness of the methods against the experimental limitations that affect the measured spectra, such as the cut at low energy and the finite number of counts in the measurement. Also the reliability of the RE energy distribution is here discussed by comparing the results of the four different reconstructions. Since the \underline{W} matrix for the detector considered in this section differs from other detectors (e.g. the ones introduced in chapter 2) only in the part that describes the transport of the hard X-rays from the tokamak to the scintillator, the results obtained in this section can be extended to all the measurements of the bremsstrahlung HXR emission of REs performed with HXR diagnostics based on LaBr₃ scintillators.

Figure 4.8(b) shows three reconstructions of the RE energy distribution in the time interval 1.00-1.13 s before the mitigation of the RE beam : with ML-EM, Tikhonov and Poisson regularization (SVD has not been included due to the poor results obtained with the synthetic tests of section 4.2). They are in agreement below 10 MeV, while they differ significantly in the reconstruction of the high energy tail of the distribution. ML-EM returns a smooth tail with two small peaks at ≈ 14 and ≈ 19 MeV, while Tikhonov sees almost no REs above ≈ 13 MeV and Poisson regularization resolves two distinct and isolated peaks that seem nonphysical. The HXR spectrum of #34084 is shown in figure 4.8(a), the three lines represent the reconstruction of the experimental data calculated convolving the reconstructions of figure 4.8(b) with the transfer matrix \underline{W} of figure 4.2. This is a ill-posed problem and as expected, all three reconstructions fit the experimental spectrum. However ML-EM follows the high energy tail of the data better than the other two methods, suggesting that its reconstruction may be the most reliable of the three. In particular Tikhonov regularization underestimates such tail, which confirms what has been shown in section 4.2: the regularization of χ^2 statistics does not take into account the Poissonian statistics of the counting measurement of the RE's bremsstrahlung emission. Thus this method is prone to underestimate the high energy tail of the RE energy distribution.

Experimental data suffer from electronic noise at low energy, which is due to the digital acquisition chain. To esclude such noise from the experimental data, a low energy cut at $E_{cut} \in [0, 1]$ MeV is routinely applied at run time. Figure 4.3(b) shows that for every E_{RE} , most of the bremsstrahlung photons are measured in the energy



(a)



(b)

FIGURE 4.8: Analysis of AUG shot #34084 in the time interval 1.00 - 1.13 s. (a) Black markers are the experimental HXR spectrum measured with the detector in the Bragg Bunker (when non visible the errors are smaller than the marker size). The three lines are the convolution of the reconstruction of the RE's energy distribution shown in figure (b), with the transfer matrix \underline{W} of figure 4.3(a). (b) RE's energy distribution reconstructed with ML-EM (red solid line), Poisson regularization (blue dashed line) and Tikhonov regularization (green point-dashed line). The colored areas represent the interval of confidence of the reconstruction computed according to section 3.5 (when non visible the error bands are smaller than the line size). Reproduced from [85] with permission of the publisher.

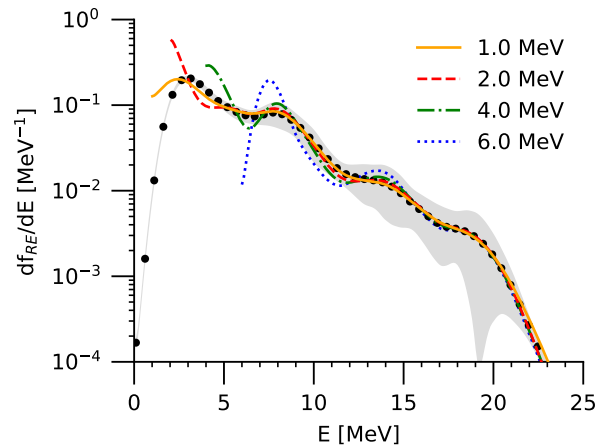


FIGURE 4.9: Low energy cut test: comparison of the RE's energy distribution reconstructed using ML-EM and applying increasing low energy cuts to the experimental spectrum of AUG shot #34084 shown in figure 4.8(a). The energy cuts were applied at 1 (yellow solid line), 2 (red dashed line), 4 (green dot-dashed line) and 6 (blue dotted line) MeV. Black markers show the original ML-EM reconstruction of figure 4.8(b), while the gray area is the confidence band of the original ML-EM reconstruction (when non visible the error bands are smaller than the line size). Reproduced from [85] with permission of the publisher.

range $[0, 3]$ MeV. The low energy cut, then, may cause a loss of information which might degrade the reconstruction of the RE's energy distribution at all energies. The effect that this cut has on the reconstruction can be studied by applying multiple energy cuts, from 1 to 6 MeV, during the post-processing of the experimental spectrum of shot #34084. Figure 4.9 shows the comparison between the reconstruction performed with full statistics and the reconstructions performed the data sets obtained after the application of the low energy cuts. Each reconstruction is affected by some artifacts in an energy interval $\approx 2 - 3$ MeV wide right above the cut: $[E_{cut}, E_{cut} + \Delta]$, with width $\Delta \approx 2 - 3$ MeV. In that region the reconstruction cannot be trusted, which suggests that the fact that the RE distribution goes to 0 for $E_{RE} \rightarrow 0$ in figure 4.8(b) is an artefact generated by the low energy cut applied to the experimental data. The reconstruction at energies close to $E_{RE} = 0$ might also be underestimated due to an underestimation of the shielding around the detector in the simulations for \underline{W} computation. In fact equation (3.1) tells that \underline{F} and \underline{W} are inversely proportional and, as pointed out in [82], the materials on the detector LOS mostly attenuate low energies photons, changing the measured spectrum mostly in the low energy region. If the shielding on the detector LOS is too simplified, the expected spectrum generated by a low energy RE, i.e. $\underline{W}(E_{RE})$, will be overestimated and the reconstructed $\underline{F}(E_{RE})$ will be underestimated. Thus, the modelling of the detector LOS is crucial for reconstructing $\underline{F}(E_{RE})$ at low energies.

On the other hand, in figure 4.9, the reconstructions are in good agreement with

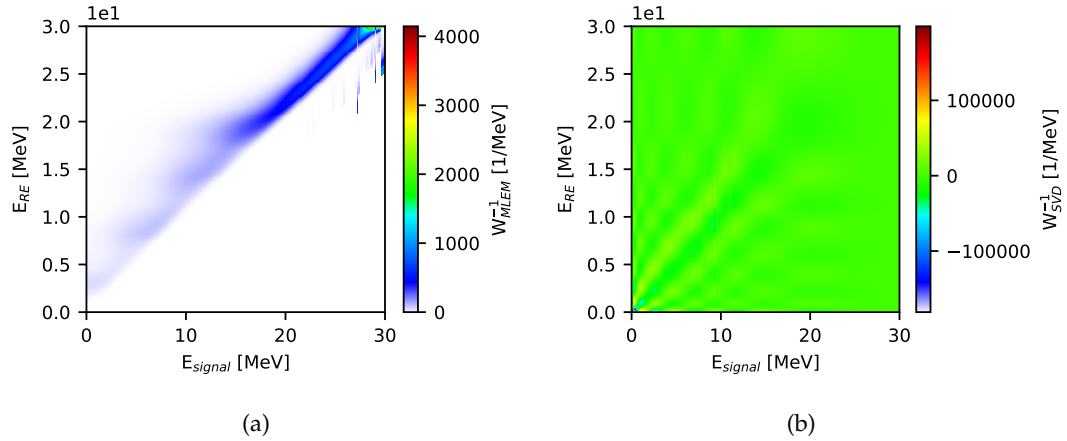


FIGURE 4.10: Inverse of the transfer probability matrix \underline{W} shown in figure 4.3(a). Figure (a) has been calculated using MLEM, i.e. equation (3.14). Figure (b) has been calculated using SVD.

one another above $E_{cut} + \Delta$. The only difference is that the peaks are slightly accentuated in the reconstructions with higher E_{cut} . In figure 4.9 all reconstructions have been performed using ML-EM, however the same results can be reproduced using Tikhonov regularization. The behaviour of the low energy cut here reported can be explained by studying the inverse of the transfer matrix \underline{W} . In figure 4.10, the inverse \underline{W}^{-1} has been calculated on AUG shot #34084 using both MLEM and SVD algorithms. More precisely, $\underline{W}_{MLEM}^{-1}$ in figure 4.10(a) has been calculated applying equation (3.14) on the last iteration of the reconstruction, which is shown in figure 4.8(b). The SVD inverse has both positive and negative values, which justify the negative artefacts present in most of SVD reconstructions, e.g. in figs. 4.4 to 4.7. The MLEM is positive definite and, apart from some computational noise, is a banded matrix on the counter diagonal. Thus there is a sort of bijective correspondence between energy regions in the detector and RE spaces: the low energy part of the measured spectrum contains information that are used mainly in the reconstruction of the low energy part of the RE's energy distribution (the same holds for the high energy region). This justify the fact that the low energy cut modify the reconstruction only in an energy interval $\approx 2 - 3$ MeV wide right above the cut.

Another experimental limitation is that HXR measurements in RE experiments often collect few counts: [40] shows that roughly 40% of the RE experiments considered generated less than 1k counts on the HXR diagnostics installed at AUG (see section 2.1). On the other hand, even when the statistics of the experimental data is higher, the time traces of the plasma currents and the reconstruction of the magnetic equilibrium evolve extremely fast suggesting the necessity to perform an analysis on small time intervals to fully describe the time evolution of the RE's energy distribution function over the disruption. Then it becomes crucial to assess which is

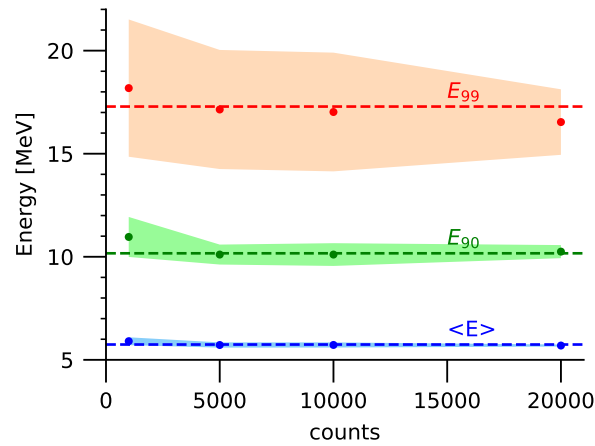


FIGURE 4.11: Minimum number of counts in measured HXR spectrum test: the RE's energy distribution for AUG shot #34084 has been reconstructed with ML-EM from random sub-samples, with 1, 5, 10, 20 kcounts, of the experimental spectrum in figure 4.8(a). For each number of counts, 10 extractions have been made: the markers represent the average value of the RE's mean ($\langle E \rangle$) and maximum energy (E_{90} and E_{99}) in each set of extractions, while the colored areas show their standard deviation. For reference, dashed lines show the estimate of these statistics obtained from the ML-EM reconstruction in figure 4.8(b). Reproduced from [85] with permission of the publisher.

the minimum number of events in the measured spectrum necessary for a successful inversion of the RE's 1D energy distribution with the methods implemented. To this extent, the complete statistics of AUG shot #34084 was considered: an event list has been generated from the measured spectrum. The REs energy distribution was considered to be constant during the interval of time considered for the measurement, thus the same hypothesis holds for the measured HXR spectrum. From this event list, random sub-samples with 1, 5, 10 and 20 kcounts were uniformly drawn to generate smaller, statistically independent measurements of the HXR spectrum of AUG shot #34084. For each number of counts 10 samples have been drawn, which were then analyzed with ML-EM, Tikhonov and Poisson regularizations. Figure 4.12 shows three reconstructions for each number of counts. All reconstructions are performed with ML-EM and, in each graph, the reconstruction retrieved with the complete statistics of AUG shot #34084 is also shown for reference. From figure 4.12, the stability of the reconstruction can be studied and the minimum number of counts necessary for performing an inversion can be determined.

ML-EM is able to retrieve the general shape of the energy distribution even at 5k counts, giving the most reproducible reconstructions and proving to be the more robust method against low statistics, i.e. high noise, in the experimental data. ML-EM performance suggests it can reconstruct the RE's energy distribution with a time resolution of roughly 5 – 10 ms, assuming a signal of 1 MCps incident on the detector.

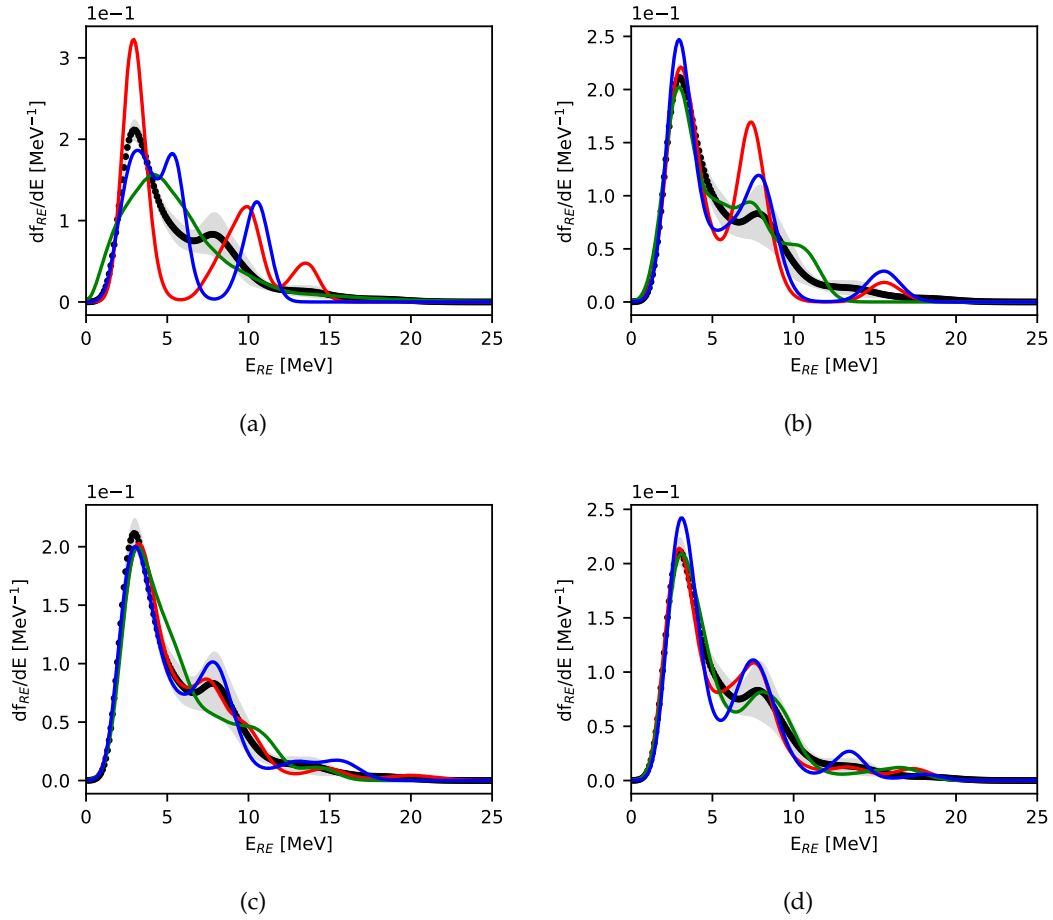


FIGURE 4.12: Stability of the reconstruction of independent random draws of AUG shot #34084 with (a) 1k, (b) 5k, (c) 10k, (d) 20k counts. For each number of counts, three reconstructions are shown with solid blue, red and green lines. Each reconstruction was performed on a different independent random draw, using ML-EM. For comparison, black markers show the original ML-EM reconstruction of figure 4.8(b), while the gray area is the confidence band of the original ML-EM reconstruction (when non visible the error bands are smaller than the line size).

Poisson regularization is far less reliable than ML-EM, showing substantial differences, especially in the high-energy part of the RE's energy distribution, between reconstructions performed over different draws of 20k counts each. This suggests that Poisson minimization is strongly influenced by the high level of noise in the high-energy tail of the measured spectrum. On these basis, also the two peaks structure between 10 and 20 MeV shown in 4.8(b) are probably artefacts. Better results are given by the χ^2 statistics of Tikhonov regularization, which, as already pointed out, penalizes the high-energy counts in the measured spectrum. Similar to ML-EM, Tikhonov retrieves the main features of the RE's energy distribution already with 5 – 10 kcounts.

As shown in section 4.2, also in this case the estimates of RE beam statistics have

proved to be robust against the presence of artefacts in the reconstruction. For each set of random draws, figure 4.11 shows the average and the dispersion of the mean and maximum energy. $\langle E_{RE} \rangle$ has a relative small dispersion around the value reconstructed using the full statistics, meaning that it can be reliably reconstructed also when the inversion is performed on as little as 1k counts. Assuming again a signal incident on the detector of 1 MCps, the average energy can in principle be reconstructed with a time resolution as high as 1 ms. E_{90} has a relatively larger dispersion, but can still be reconstructed quite accurately with as little as 5k counts. Higher percentage estimators, like E_{99} , have a even wider dispersion, which make them not suitable for use with discharges where low number of counts have been detected. On the other hand, all four estimators retrieve on average the value reconstructed using the full statistics, regardless of the number of counts in the draw used for the inversion. Assuming a signal of 1 MCps incident on the detector, the maximum energy of the RE beam can in principle be reconstructed with a time resolution of roughly 5 ms, depending on the estimate.

Chapter 5

Weight functions in 2D velocity-space

Chapter 4 is dedicated to the reconstruction of the REs' 1D energy distribution. The model implemented in the transfer matrix \underline{W} is based on the assumption that the RE beam is mono-pitch, with $p_{RE} = -1$ (i.e. the REs moves counterclockwise with a velocity antiparallel to the magnetic field). Since the cross section for bremsstrahlung emission is also a function of the angle of emission with respect to the particle velocity, in section 5.1 the inverse model \underline{W} is generalized to the 2D velocity-space expressed in energy and pitch (E_{RE}, p_{RE}) . A paper on the calculations of the 2D weight functions here presented was submitted for publishing and a copy of the submitted manuscript is included in part IV.

The matrices \underline{W} are here presented in the weight function formalism [36, 37], that focuses on $\underline{W}(E_{signal} = const)$, i.e. on the probability that the detected signal has been emitted by an RE with a certain energy and pitch. This is a visual representation of the sensitivity of the detector in the 2D velocity-space and will be used in section 5.2 to determine the region of higher sensitivity of the HXR diagnostics installed at JET as well as their capability of accessing all regions of the (E_{RE}, p_{RE}) plane. Apart from being used for solving the inverse problem and reconstruct the REs' 2D velocity-space distribution, weight functions can be employed as synthetic diagnostics in the forward model to generate the expected HXR spectra to be compared with the experimental data. In this context, the weight function formalism can also tell the fraction of the measured spectrum generated by different intervals of the (E_{RE}, p_{RE}) velocity space.

5.1 2D velocity-space weight functions

The bremsstrahlung cross section, introduced in equations (4.4) and (4.5) of section 4.1, depends on the energy E_γ of the emitted photon, the energy E_{RE} of the

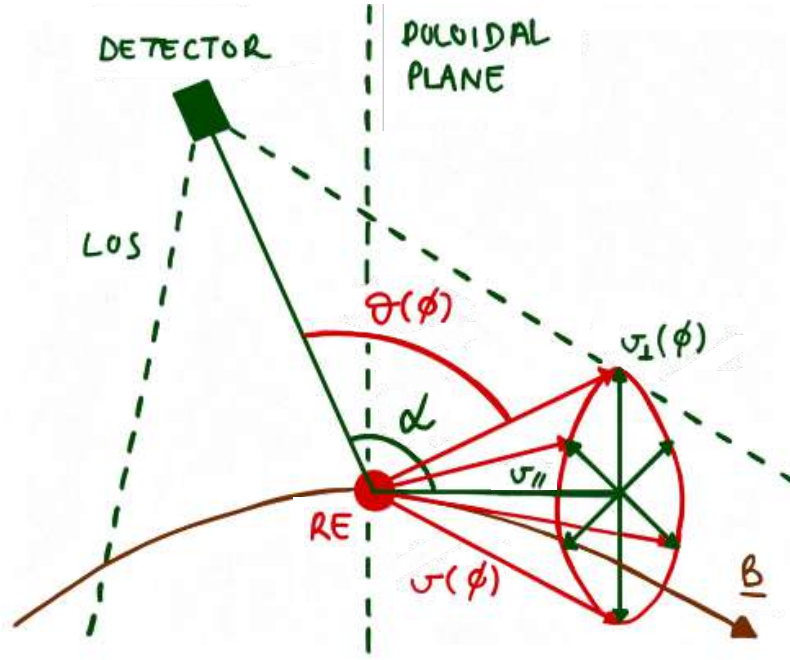


FIGURE 5.1: Visual representation of the geometry implemented for computing the 2D velocity-space weight functions for REs' bremsstrahlung emission $\underline{W}_B(E_{HXR}, E_{RE}, p_{RE})$. The results of such calculations are presented in figs. 5.4 to 5.6.

emitting RE and the angle of emission θ . In particular θ is the angle between the particle velocity and the versor defining the direction of the detector LOS ($L\hat{O}S$). It is determined by the versor $L\hat{O}S$, the magnetic field \underline{B} , the RE pitch $p_{RE} = \frac{v_{RE\parallel}}{v_{RE}}$ and its gyro-phase ϕ_{RE} . The inverse problem (4.1) thus can be promoted to a 2 dimensional convolution that links the measured energy of the bremsstrahlung HXR with both the RE energy and pitch angle:

$$S(E_{measured}) = \int_0^\infty \int_{-1}^1 W(E_{measured}, E_{RE}, p_{RE}) F(E_{RE}, p_{RE}) dp_{RE} dE_{RE} \quad (5.1)$$

as usual $E_{measured}$ represents the measured energy of a bremsstrahlung photon, \underline{S} represents the measured HXR spectrum, \underline{F} the REs energy distribution function and $W(E_{RE}, p_{RE}, E_{HXR})$ the transfer matrix. In this case \underline{F} can be expressed in matrix form as it spans the 2D velocity space defined by E_{RE} and p_{RE} .

Following section 4.1, $W(E_{RE} = E, p_{RE} = p)$ is the expected spectrum emitted by a mono energetic and mono pitch beam. It contains the combined probability that three independent processes take place: the bremsstrahlung emission of a HXR photon from the interaction between a relativistic RE and a thermal ion (whose probability is described by \underline{W}_B), its propagation to the detector and its detection by the scintillator crystal or any active medium of the detector in use (the last two processes

are usually condensed into the Detector Response Function (DRF) \underline{W}_{DRF} :

$$W(E_{measured}, E_{RE}, p_{RE}) = \int_0^\infty W_{DRF}(E_{measured}, E_\gamma) \cdot W_B(E_{HXR}, E_{RE}, p_{RE}) dE_{HXR}. \quad (5.2)$$

Similarly to chapter 4, \underline{W}_{DRF} has been computed using the MCNP code [38], while $W_B(E_{HXR}, E_{RE}, p_{RE})$ has been computed according to:

$$W_B(E_{HXR}, E_{RE}, p_{RE}) = \frac{|v_{RE}| \Delta t}{2\pi} n_i d\Omega \int_0^{2\pi} \frac{d\sigma}{dE_{HXR} d\Omega}(E_{HXR}, E_{RE}, \theta(p_{RE}, \phi)) d\phi. \quad (5.3)$$

In this chapter \underline{W}_B has been calculated considering only the signals emitted by REs positioned at the center of the LOS under consideration. For this reason, in equation (5.3), the LOS collapses to a single point and θ loses its spatial and magnetic dependency. Also, the magnetic field is assumed to be purely toroidal and uniform over the poloidal plane, so to make the relation between \underline{B} and the LOS direction evident.

Similarly to chapter 4, $\frac{d\sigma}{dE_{HXR} d\Omega}$, that appears in (5.3), has been computed using the semi-empirical cross sections derived by Salvat in refs. [26, 27], which can be expressed as the product (4.4) of two factors, here termed *energy factor* $\frac{d\sigma}{dW}(Z, E_{RE}, k)$ and *angular factor* $p(Z, E_{RE}, k | \cos \theta)$ (here k is defined as $k = \frac{E_{HXR}}{E_{RE}}$). The former is defined in equation (49) in ref. [26], while the latter is defined in (4.5). Given a certain position, the signal generated by REs with a given energy and pitch is the sum of the signals generated by REs having all the possible gyro-angles. Thus in (5.3) the double differential cross section is integrated over all the gyro-phases of the RE motion. Figure 5.1 shows the geometry used for the calculations here described. A visual representation of the two factors of (4.4) is presented in figure 5.3 for channel 5 of the GCU and a Ar background plasma. It can be compared with the corresponding \underline{W} presented in figure 5.4. It is worth noting that most of the characteristics displayed in figs. 5.4 to 5.6 are already contained in the angular factor (4.5), which does not depend on the energy of the emitted photon. The low energy cuts in figs. 5.4 to 5.6, instead, are due to the fact that bremsstrahlung photons are emitted with an energy lower than the energy of the RE particle: $E_{HXR} < E_{RE}$. These low energy cuts are introduced by the energy factor shown in figure 5.3(b). The factorization of the bremsstrahlung cross section into the two factors here described comes in handy when computing \underline{W}_B as it allows to reduce the computation of a 3D tensor to the computation of two 2D matrices.

The probability function of the emission angle θ generated by the uniform scan of the gyro-angle phase ϕ is plotted in figure 5.2. A LOS observing the plasma with an angle $\alpha = 60$ deg is considered and multiple values of the particle pitch angle are shown. Let's define $\theta_p = \arccos p_{RE}$ the pitch-angle of the particle. The width of the distribution is equal to two times the angle α between the LOS direction \hat{l} and the magnetic field \underline{B} , if $\alpha < \theta_p < \pi - \alpha$, otherwise the width of the distribution is simply

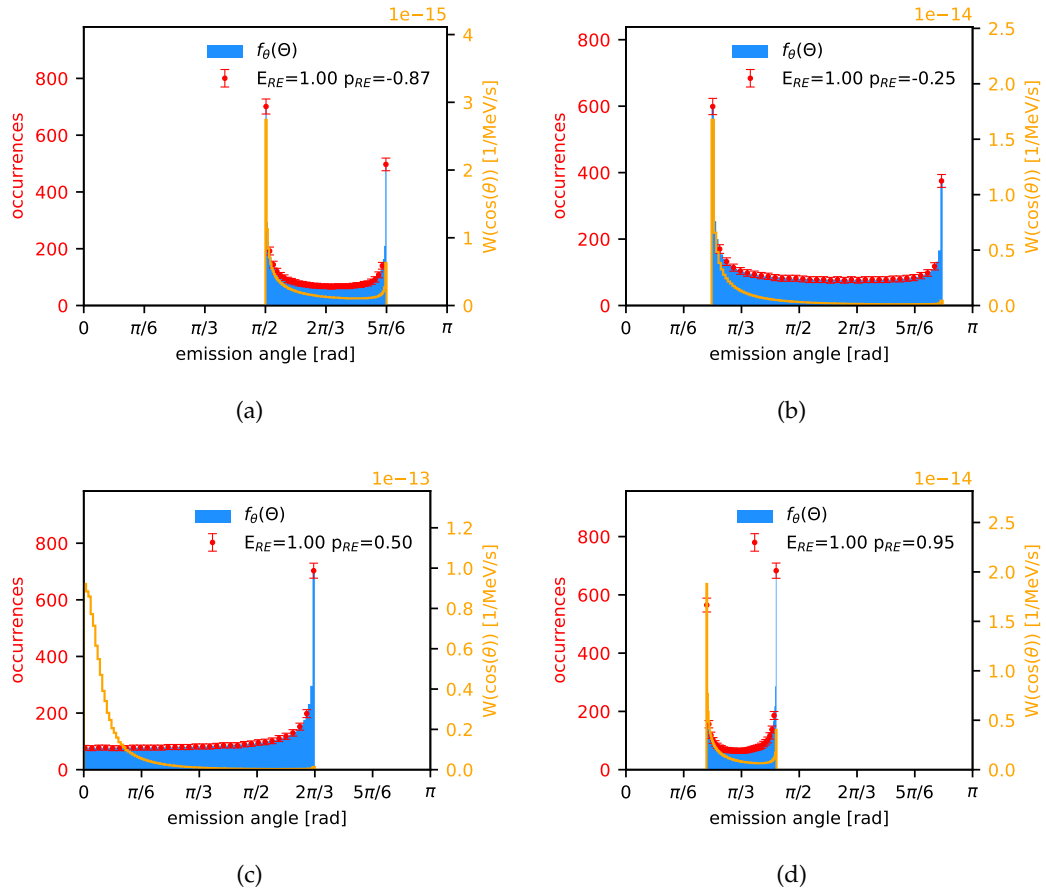


FIGURE 5.2: Scan of the angle of emission θ towards a hypothetical LOS that observes the plasma with a inclination of $\alpha = \frac{\pi}{3}$ rad with respect to the toroidal versor of the poloidal plane defined by the GCU LOS (see figure 5.5 for the respective 2D weight function). $E_{RE} = 1$ MeV for all plots, while $p_{RE} = -0.87$ (a), -0.25 (b), 0.5 (c) and 0.95 (d). The blue histogram is θ pdf as defined in (5.13); the red markers are the emission angles resulted from the uniform scan of the RE gyro-phase space prescribed in (5.3) for the calculation of \underline{W}_B ; the orange histogram is the contribution to \underline{W}_B of the corresponding angle

$$\text{of emission, i.e. } \frac{d\sigma}{dE_{HXR} d\Omega}(E_{HXR}, E_{RE}, \theta) d\theta.$$

$\Delta = 2\theta_p$ and converges to $\alpha, \pi - \alpha$ for $p_{RE} = 1, -1$ respectively. The distribution is convex and the magnitude of this convexity depends again on α . If $\alpha = 0$, then the LOS is tangent to \underline{B} and the REs emit with a fixed angle, regardless of their gyro-phases. On the other hand, a radial LOS is perpendicular to \underline{B} and this ensures that the distribution of θ is symmetric around $\frac{\pi}{2}$ regardless of p_{RE} . The characteristics of $f(\theta)$ shown in figure 5.2 can be interpreted by deriving an analytical expression for this distribution function.

Let's start from calculating the distribution of $\cos(\theta)$. Consider a purely toroidal magnetic and define the \hat{y} axis such that $\hat{B} \parallel -\hat{y}$. The other two dimensions can be defined as follows: \hat{x} is the versor parallel to the component of the LOS direction perpendicular to the magnetic field, while $\hat{z} = \hat{x} \times \hat{y}$. The LOS, then, lies in the

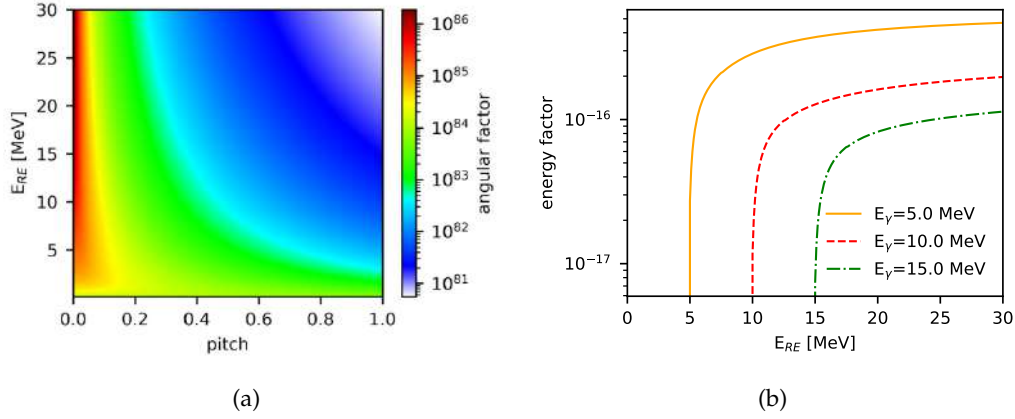


FIGURE 5.3: The (a) angular and (b) energy factors of (4.4) calculated for channel 5 of the GCU considering a Ar plasma in background and a HXR emission of $E_{HXR} = 1$ MeV. (a) shows the angular emission probability defined in (4.5) calculated for the emission angle defined by the RE velocity and the detector LOS, note that this probability is symmetric around $p_{RE} = 0$ in the case of a radial LOS such as the ones of KN3G channels (see also figure 5.4). (b) shows the energy probability factor $\frac{d\sigma}{dW}(Z, E_{RE}, k)$.

$x - y$ plane. If we term α the angle between the LOS and the magnetic field, then the versor defining the LOS is: $L\hat{O}S = \cos(\alpha)\hat{B} + \sin(\alpha)\hat{x}$. The velocity of the particle can be expressed as:

$$\underline{v} = v \cos(\theta_p)\hat{B} + v \sin(\theta_p)\hat{B}_\perp,$$

where $\theta_p = \arccos(p)$ is the pitch angle and \hat{B}_\perp is the versor that defines the direction of the perpendicular velocity of the particle. \hat{B}_\perp can be expressed as a function of the gyro-phase: $\hat{B}_\perp = \cos(\phi)\hat{x} - \sin(\phi)\hat{y}$. The cosine of the emission angle θ , then, can be expressed as:

$$\begin{aligned} \cos(\theta) &= L\hat{O}S \cdot \hat{v} \\ &= (\cos(\alpha)\hat{B} + \sin(\alpha)\hat{x}) \cdot (\cos(\theta_p)\hat{B} + \sin(\theta_p)\hat{B}_\perp) \\ &= \cos(\alpha)\cos(\theta_p) + \sin(\alpha)\sin(\theta_p)\cos(\phi). \end{aligned} \quad (5.4)$$

Assume that the gyro-phase of the particle is uniformly distributed, the distribution of the cosine of the emission angle can be derived applying two changes of variable for probability density functions. Consider two generic random variables A and B with pdf $f_A(a)$ and $f_B(b)$. If there exists a function g such that $a = g(b)$, then the change of variables reads:

$$\begin{aligned} f_A(a) &= f_B(b) \left| \frac{db}{da} \right| \\ &= f_B(g^{-1}(a)) \left| \frac{d}{da} g^{-1}(a) \right|. \end{aligned} \quad (5.5)$$

To retrieve the pdf of $\cos(\theta)$, let's first calculate the pdf for $\cos(\phi)$, which for brevity will be referred as to $p_\phi = \cos(\phi)$. The inverse function in this case is:

$$\phi = \begin{cases} \arccos(p_\phi) & \text{if } 0 \leq \phi < \pi \\ 2\pi - \arccos(p_\phi) & \text{if } \pi \leq \phi < 2\pi \end{cases}$$

so the distribution function for p_ϕ is:

$$f_{p_\phi}(p_\phi) = \frac{1}{2\pi} \left(\left| \frac{d}{dp_\phi} \arccos(p_\phi) \right| + \left| \frac{d}{dp_\phi} (2\pi - \arccos(p_\phi)) \right| \right) \quad (5.6)$$

$$= \frac{1}{\pi} \frac{1}{\sqrt{1-p_\phi^2}}. \quad (5.7)$$

Then, we must change variables from p_ϕ to $\cos(\theta)$, obtaining the distribution function of $\cos(\theta)$:

$$f(\cos(\theta)) = \frac{1}{\pi} \frac{1}{\sin(\alpha) \sin(\theta_p)} \frac{1}{\sqrt{1-\cos^2(\phi)}}. \quad (5.8)$$

Equation (5.8) is valid for: $\alpha \neq 0$, $\theta_p \neq \{0, \pi\}$ and $\phi \neq \{0, \pi\}$. It is minimum for $\phi = \frac{\pi}{2}$, which corresponds to a particle having \underline{v}_\perp perpendicular to \hat{x} , which is the projection of the LOS versor on the $x-y$ plane. Since $\phi \in [0, 2\pi)$, (5.4) implies that the domain of (5.8) is:

$$\cos(\theta) \in [\cos(\alpha + \theta_p), \cos(\alpha - \theta_p)]. \quad (5.9)$$

If $\theta_p = 0$ or π , i.e. $p_{RE} = \pm 1$, this domain collapses to a single point and the emission angle θ can assume a fixed value regardless of the gyro-angle ϕ . In particular $\theta = \alpha$ if $p_{RE} = 1$ and $\theta = \pi - \alpha$ if $p_{RE} = -1$. Since $\theta \in [0, \pi]$, the cosine is symmetric around 0 and it is a monotonic decreasing function, then the width Δ of the distribution of θ can be retrieved from equation 5.9:

$$\Delta = \begin{cases} 2\alpha & \text{if } \alpha < \theta_p \\ 2\theta_p & \text{if } \alpha > \theta_p \end{cases}. \quad (5.10)$$

This confirms what has been observed in figure 5.2. Finally, let's consider those situations for which (5.8) does not hold. If $\alpha = 0$, then $L\hat{O}S \parallel \hat{B}$. From (5.4), the emission angle is fixed: $\theta = \theta_p$, regardless of the gyro-phase ϕ .

If the poloidal magnetic field is also considered, \hat{B} is no longer parallel to the toroidal axis and (5.8) does not hold. A more general formula for the distribution of the emission angle θ , f_θ can be analytically derived by considering the emission angle

as a function of the gyro-phase of the particle:

$$\begin{aligned}\theta &= g(\phi) \\ &= \arccos \left\{ \frac{\underline{v}_{RE} \cdot (\underline{D} - \underline{P})}{v_{RE} \|\underline{D} - \underline{P}\|} \right\} \approx \arccos \left\{ \frac{\underline{v}_{RE} \cdot (-\hat{l})}{v_{RE}} \right\}\end{aligned}\quad (5.11)$$

$$= \arccos \left\{ \left[p_{RE} \hat{B} + \sqrt{1 - p_{RE}^2} (\cos(\phi) \hat{g}_x + \sin(\phi) \hat{g}_y) \right] \cdot \hat{D}P \right\}.\quad (5.12)$$

Here $\hat{g}_x = \begin{pmatrix} -B_y - B_z \\ B_x \\ B_x \end{pmatrix}$ and $\hat{g}_y = \hat{g}_x \wedge \hat{B}$ are the two vectors perpendicular to

\hat{B} that define the gyro-plane where \underline{v}_\perp lives, \underline{D} is the position of the center of the detector and \underline{P} is the particle position. In equation (5.3), the scan in ϕ has been conducted using a uniform probability in $[0, 2\pi)$, thus the probability distribution of the emission angle θ can be explicitly retrieved as a change of variable:

$$f_\theta(\theta) = f_\phi(g^{-1}(\theta)) \left| \frac{d}{d\theta} g^{-1}(\theta) \right| \quad (5.13)$$

$$= \frac{1}{2\pi} \left| \frac{d}{d\theta} g^{-1}(\theta) \right|.\quad (5.14)$$

(5.12) can be inverted by noticing that it is an equation of the type $A \cos(\phi) + B \sin(\phi) + C = 0$:

$$\frac{\cos(\theta) - p_{RE} \hat{B} \cdot \hat{D}P}{\sqrt{1 - p_{RE}^2}} = \hat{g}_x \cdot \hat{D}P \cos(\phi) + \hat{g}_y \cdot \hat{D}P \sin(\phi),$$

which can be solved by substituting the sine and cosine of ϕ with the tangent half-angle formulas. The inverse function then reads:

$$\phi = 2 \arctan \left[\frac{\sqrt{1 - p_{RE}^2} \hat{g}_y \cdot \hat{D}P \pm \sqrt{(1 - p_{RE}^2) [(\hat{g}_x \cdot \hat{D}P)^2 + (\hat{g}_y \cdot \hat{D}P)^2] - (\cos(\theta) - p_{RE} \hat{B} \cdot \hat{D}P)}}{\sqrt{1 - p_{RE}^2} \hat{g}_x \cdot \hat{D}P - p_{RE} \hat{B} \cdot \hat{D}P + \cos(\theta)} \right].\quad (5.15)$$

The domain of this function is $\phi \in [0, 2\pi) - \{0, \pi\}$, which comes from the fact that $\tan(\frac{\phi}{2})$ and $\cot(\frac{\phi}{2})$ diverge respectively for $\phi = \pi, 0$. (5.15) can finally be substituted in (5.13) to obtain the probability density function of θ . The comparison between f_θ calculated according to (5.13) and the sampling of the emission angle resulting from a uniform scan of the RE gyro-phase space, ensures the reliability of the gyro-phase scan performed in \underline{W}_B calculations. At the same time, (5.13) can be used to sensibly reduce the dimension of the gyro-phase scan by orders of magnitudes, thus saving computational time while preserving the accuracy of \underline{W}_B .

Figure 5.2 also shows $\underline{W}_B(\cos(\theta))$ as a function of the emission angle θ . This profile represents the relative importance of each emission angle θ to the calculation of \underline{W}_B and shows that \underline{W}_B is dominated by the emission corresponding to the minimum θ ,

regardless of p_{RE} . If the same matrices were to be calculated using only the gyro-phases corresponding to the minimum angle of emission, the resulting W_B would still retrieve all the qualitative characteristics displayed in figures 5.4, 5.6 and 5.5, its absolute value however would have been orders of magnitude below the one obtained from a full scan of the particles gyro-phases. This is not surprising given the high anisotropy of the bremsstrahlung emission at relativistic energies such as the ones reached by REs during plasma disruptions.

Finally it is worth noting that, in this simplified model, $\underline{W}_B(E_{RE} = E, p_{RE} = p)$ is the sum of the emission probability related to REs that are following different trajectories: each trajectory intersects in \underline{x} , with the corresponding RE having $E_{RE} = E$, $p_{RE} = p$, but different values of ϕ . In other words, the value of ϕ defines the trajectory followed by the RE. This is the opposite reasoning of orbit-based weight functions, where \underline{W}_B is the sum of all the signals emitted by REs following the same orbit, in different positions inside the detector LOS (see refs.[88–91] for orbit-based weight functions applied to fast-ions).

5.2 Application at JET

JET is equipped with a set of hard X-ray spectrometers which can be divided into three groups: the gamma camera upgrade (GCU), which is discussed in details in section 2.2.1, a set of gamma-ray spectrometers having vertical line of sight (V-GRS) and a spectrometer having a tangential line of sight (T-GRS), the latter two being introduced in section 2.2.2.

The weight functions in 2D velocity-space for the HXR diagnostics installed at JET, in the case of a purely toroidal magnetic field and point source of photons, have been calculated using (5.3) and are here presented in figs. 5.4 to 5.6. All LOS considered in the present section have dynamic range [0,30] MeV and, for each of them, three $E_{measured}$ energies are presented: 1, 10 and 20 MeV. Here the particle pitch is defined as $p_{RE} = \frac{v_{parallel}}{v}$ and, even if REs are expected to have mostly pitch close to 1, in the following calculations the pitch scans the interval $[-1, 1]$.

In figure 5.4, the weight functions for channel 5 of the GCU is presented. The LOS of both the GCU and KM6S are radial and perpendicular to the toroidal magnetic field considered in this section, regardless of their orientation in the poloidal plane. Thus figure 5.4 is also representative of all other channels of the GCU, as well as the two radial spectrometers KM6S. For the present analysis, the only differences are due to the scintillators dimensions and the detectors distance from the machine. Radial LOS are most sensitive to particles having $p_{RE} = 0$, regardless of their energy. In fact, consider a particle having $p_{RE} = 0$ on the detector LOS, its velocity is completely perpendicular to the toroidal magnetic field and lies on the poloidal

plane. Depending on the gyro-phase of the particles motion on the LOS, the angle between the particle velocity and the LOS varies between $[0, \pi]$. Thus there exists at least a particle having a gyro-phase such that the detector observes the bremsstrahlung photons emitted by the particles with null emission angle, $\theta = 0$. If the particle has $p_{RE} \neq 0$, the angle between the particle velocity and the detector LOS varies between $[\frac{\pi}{2} - \arccos(p_{RE}), \frac{\pi}{2} + \arccos(p_{RE})]$, thus the minimum angle of emission towards the detector is $\theta_{min} = \frac{\pi}{2} - \arccos(p_{RE}) > 0$. Since the bremsstrahlung emission is anisotropic, the detection probability has its maximum for $\theta_{min} = 0$, i.e. for $p_{RE} = 0$. The perpendicularity between the radial LOS and the magnetic field is responsible for the symmetry around $p_{RE} = 0$ of the weight function in figure 5.4, i.e. $p_{RE} > 0$ and $p_{RE} < 0$ particles have the same probability of detection.

The weight function of the tangential LOS of KM6T strongly depends on the position and width of the RE beam core. In the calculations here presented, the width of the beam has been considered negligible and a toroidal symmetry has been supposed. The poloidal position of the RE beam defines the angle α between KM6T LOS and the magnetic field. This is shown in figure 5.7, where the toroidal sketch of KM6T LOS and different RE beam positions are presented. Since the RE beam often drifts to the high-field side on JET (see for example figures 6.17 and 6.18) and the RE dynamics evolves rapidly throughout a disruption, the angle α can vary significantly in the span of a ms. This means that the analysis of KM6T data requires the calculation of multiple weight functions, one for every reconstruction of the magnetic equilibrium during the plasma disruption. In this section two examples of KM6T weight functions are presented.

Let's first consider an RE beam positioned roughly at the centre of the poloidal plane, in this scenario the angle α between KM6T LOS and the magnetic field is approximately of 50 degrees. The resulting weight function is shown in figure 5.5. The detector sensitivity is maximum for those particles having pitch of $p_{RE} = \cos(50) = 0.64$, regardless of their energy. For such REs, the velocity is parallel to the detector LOS and the detector observes their frontward emission. Overall the weight function loses the symmetry around $p_{RE} = 0$ that has been found in the radial LOS: the detector is significantly more sensitive to those particles having positive pitch when they cross the LOS, with respect to those particles having negative pitch. In figure 5.6 the probability of detection for radiation emitted by REs moving towards and away from the detector has been separated: in fact the detector is 3 order of magnitudes more sensitive to particles with $p_{RE} > 0$ and using two color scales reveal that the shape of the weight function differ in the two regions of the pitch-space. For $p_{RE} < 0$ the (relative) sensitivity peak is localized at RE energies E_{RE} close to $E_{measured}$, especially if weight functions for low $E_{measured}$ are considered. This is due to the anisotropy of the bremsstrahlung emission, as in fact $p \in [-1, 0]$ corresponds

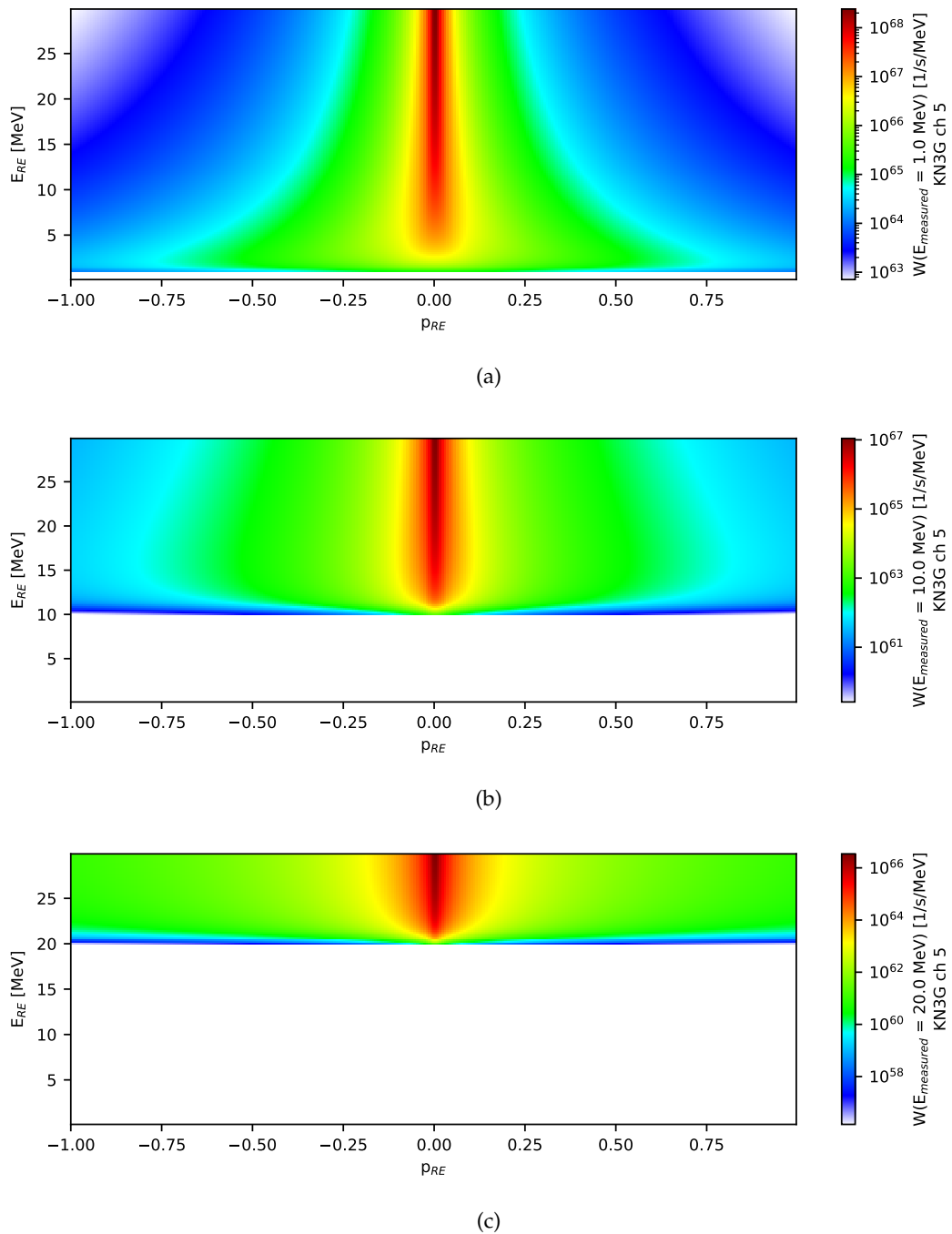


FIGURE 5.4: 2D velocity-space weight functions for the channel 5 spectrometer of the JET GCU (KN3G), with radial LOS. Three signal's energies have been considered: (a) $E_{measured} = 1$ MeV, (b) $E_{measured} = 10$ MeV, (c) $E_{measured} = 20$ MeV. Similar results have been obtained for the other channels of the GCU and for the two radial spectrometers KM6S1 and KM6S2.

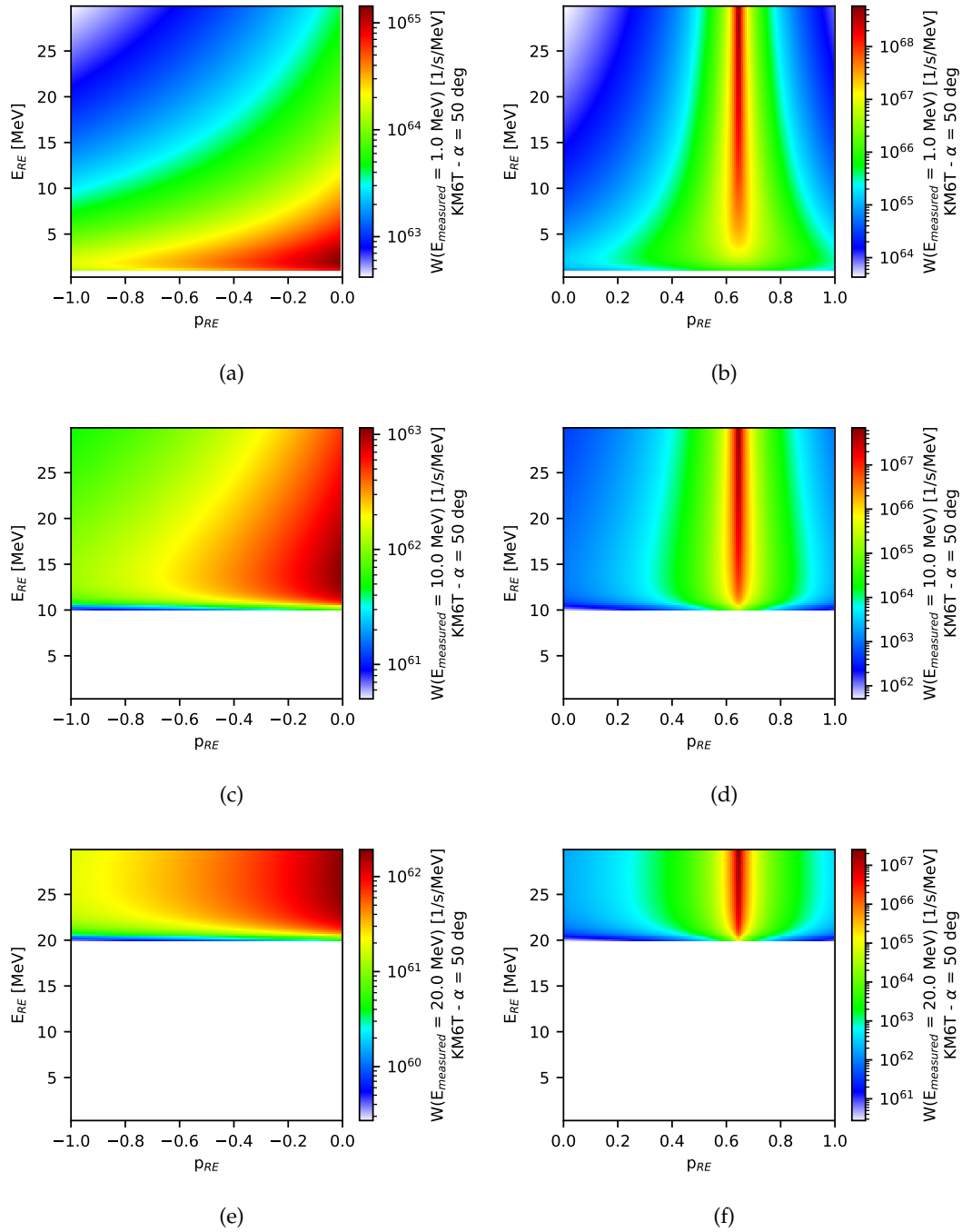


FIGURE 5.5: 2D velocity-space weight functions for the JET tangential spectrometer KM6T, assuming that the RE beam is on the center of the poloidal plane and the angle with the magnetic field is $\alpha = 50$ deg. Three signal's energies have been considered: (a)(b) $E_{\text{measured}} = 1$ MeV, (c)(d) $E_{\text{measured}} = 10$ MeV, (e)(f) $E_{\text{measured}} = 20$ MeV. For including as many details as possible, each weight function has been plotted with two colormaps: one for particles having negative pitch ((a), (c), and (e)) and one for particles having positive pitch ((b), (d), and (f)).

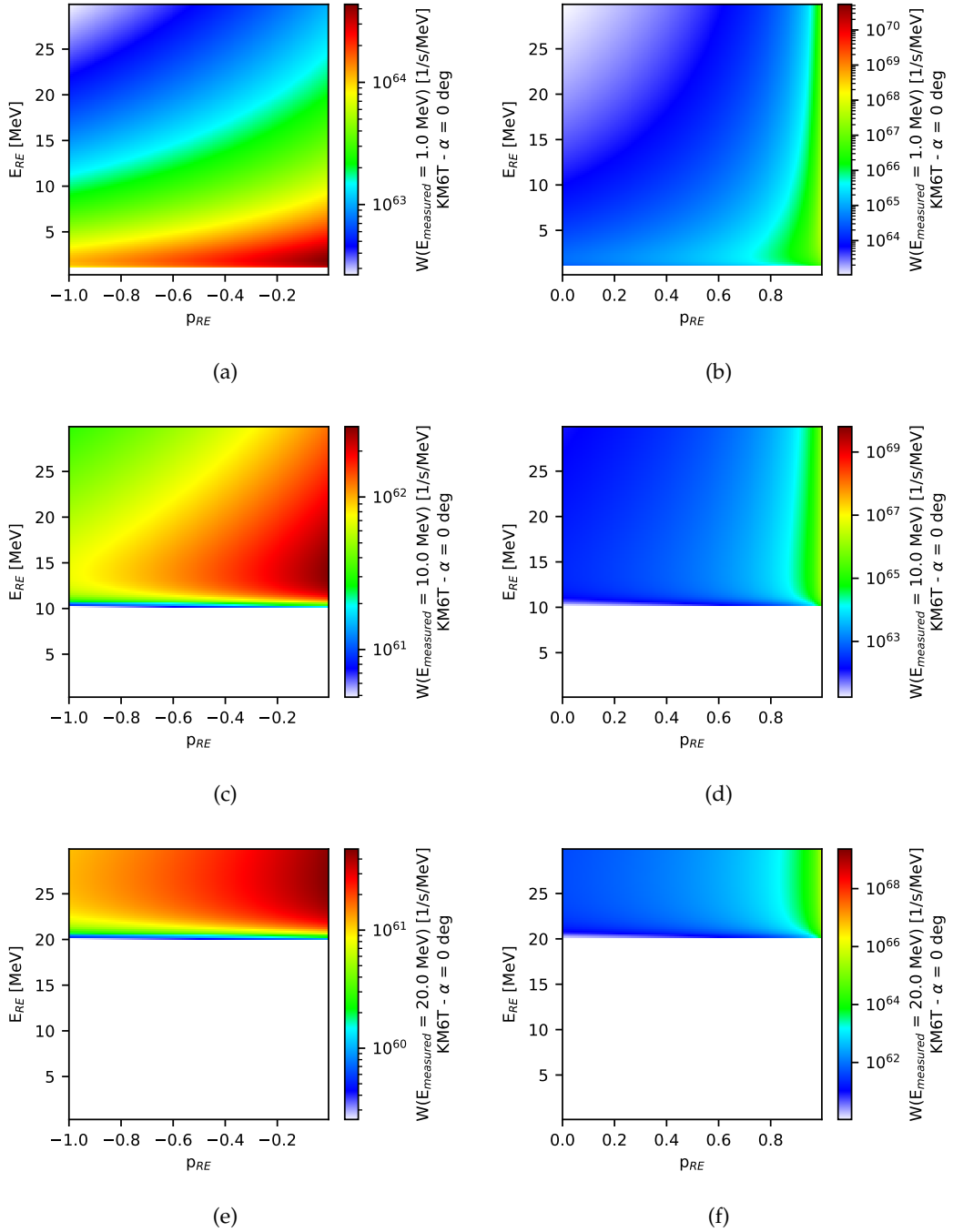


FIGURE 5.6: 2D velocity-space weight functions for the JET tangential spectrometer KM6T, assuming that the RE beam has drifted towards the high-field side and the angle with the magnetic field is $\alpha = 0$. Three signal's energies have been considered: (a)(b) $E_{measured} = 1$ MeV, (c)(d) $E_{measured} = 10$ MeV, (e)(f) $E_{measured} = 20$ MeV. For including as many details as possible, each weight function has been plotted with two colormaps: one for particles having negative pitch ((a), (c), and (e)) and one for particles having positive pitch ((b), (d), and (f)).

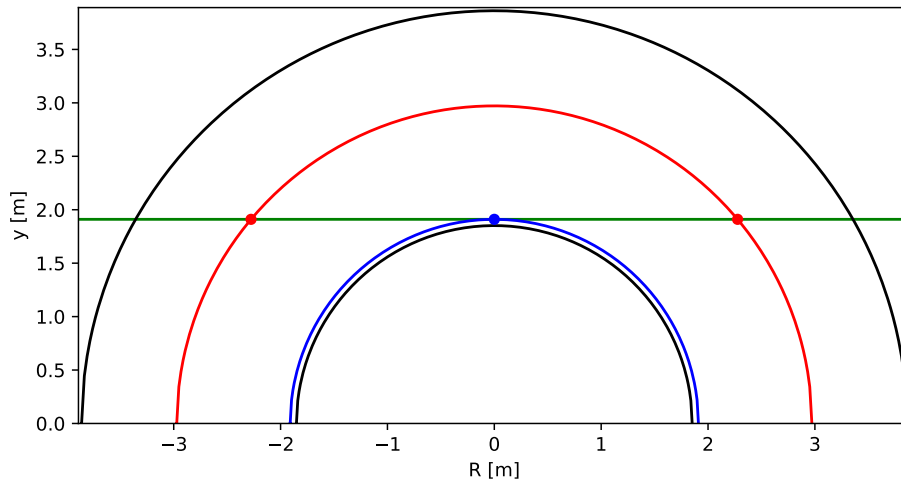


FIGURE 5.7: KM6T tangential line of sight. Black lines are the JET wall on the equatorial plane, the red circumference passes through the center of the poloidal plane, the blue circumference is the position the RE beam should assume in order to make the angle between KM6T LOS and the magnetic field equal to 0.

to an emission angle $\theta \in [40, 130]$ deg. The more energetic is the RE, the more anisotropic is the bremsstrahlung emission increases with the REs energy: thus it is relatively more probable that a low energy RE emits backward than a high energy RE.

If the RE beam drifts towards the high-field side, the angle α decreases. In figure 5.6, the infimum case of $\alpha = 0$ is considered as a limit example of how the weight function of KM6T is modified by this drift. The maximum of the weight function is moved to $p_{RE} = 1$. It is worth noting that in this special case the LOS is parallel to the magnetic field: the LOS lies on the axis of symmetry of the gyro-motion. Thus the emission angle is defined by E_{RE} and p_{RE} only and the scan over the gyro-phases is no longer necessary. In this case the difference in sensitivity between particles having $p > 0$ and $p < 0$ is accentuated: the detector is 4 orders of magnitude more sensitive to the former ones. In fact for $\alpha = 0$, the semi-axis $p \in [-1, 0]$ corresponds to an emission angle $\theta \in [\frac{\pi}{2}, \pi]$. The observations made for KN3G and KM6T can be extended to LOS having a generic orientation with respect to the toroidal vector. Defining α the angle between the LOS and the magnetic field at the position of the core of the RE beam, the detector is most sensitive to those particles having $p_{RE} = \cos(\alpha)$, for which there exists at least one gyro-phase that corresponds to a head-on emission towards the detector. Moreover the weight function is always an even function around $p_{RE} = \cos(\alpha)$. The width of the sensitivity peak is also proportional to α .

The weight functions here calculated take into account a point RE beam in a purely toroidal magnetic field. The poloidal magnetic field is expected to generate small

corrections in the weight functions: the position of the peak in sensitivity should be slightly shifted on the pitch-axis according to the change in the angle between $L\hat{O}S$ and \hat{B} . If the width of the RE beam is also taken into account, on the other hand, the weight function should be calculated performing a scan over the intersection between the LOS and the RE beam spatial distribution. The weight function, then, can be considered as the sum of many different matrices \underline{W} calculated as in section 5.2, one for each position considered in the scan. This sum should be also weighted for the RE density in each position of the scan. In each position the angle between $L\hat{O}S$ and \hat{B} differs, resulting in a broader sensitivity peak. This effect is expected to be more pronounced for the tangential LOS of KM6T, for which the angle between $L\hat{O}S$ and \hat{B} can vary from 0 rad to 60 deg. At the moment no solid estimate of the spatial distribution of the RE density is available for such calculations, however in section 6.3 some steps towards the reconstruction of the RE poloidal distribution are presented.

Chapter 6

Tomography with the upgraded JET Gamma Camera

The operation of the JET gamma-ray camera upgrade (GCU) started during JET campaign C38 with two main goals: the detection of the gamma-ray radiation emitted by fast ions, especially during ion cyclotron resonance heating (ICRH) experiments, and the observation of the bremsstrahlung radiation emitted by runaway electrons during plasma disruptions.

In particular one experiment of the C38 campaign aimed at studying the application of the three ion scheme for ion cyclotron resonance heating (ICRH), introduced in section 1.2, to D^3 -He mixed plasmas [17]. In these discharges, the NBI was used as a source of fast deuterium D_{NBI} that was further accelerated to energies in the MeV range by the ICRH power. These experiments were also intended as a mock up of the alpha generation in DT plasmas and they aimed at studying the dynamics of the α -particles born in ${}^3\text{He}(D, p)\alpha$ reactions before the 2021 DT campaign [43].

Thanks to its improved resolution (5% at 662 keV), dynamic range ([0, 30] MeV) and counting rate capability (up to 1 MCps) [45, 46, 92], the GCU has been able to detect γ -rays at the energy of 16.4 MeV born from the ${}^3\text{He}(D, \gamma){}^5\text{Li}$ reaction during the (D)-(D_{NBI})-(${}^3\text{He}$) three ions scheme experiments. This reaction is a minor branch of the ${}^3\text{He}(D, p)\alpha$ reaction (see section 1.1) and thus the tomographic reconstruction of its emissivity spatial distribution is equivalent to the α -particles source spatial distribution. At the same time, the alphas are generated by D_{NBI} and their distribution also has information on the RF energy deposition profile.

In this chapter, a new implementation of the tomographic algorithm introduced in ref. [49, 60, 80] for the reconstruction of the plasma emissivity spatial distribution in the poloidal plane [93–95] is presented. The method is then applied to three ion scheme experiments for the reconstruction of the α -particles spatial distribution. A runaway electron mitigation experiment is also considered and a preliminary attempt to reconstruct the runaway electrons spatial distribution is presented.

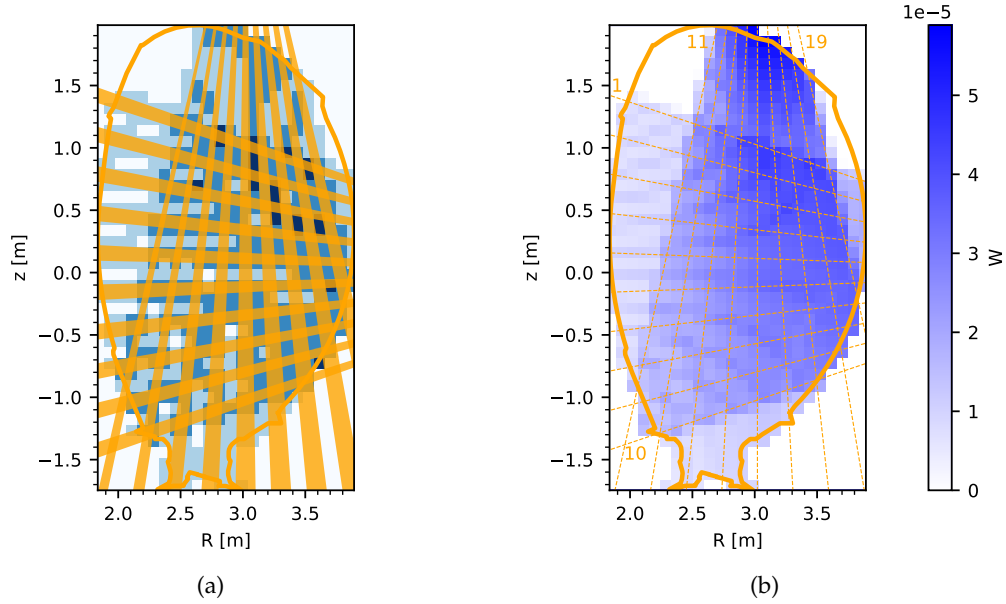


FIGURE 6.1: (a) The orange bands represent the fan geometry of the LOS of each channel of the GCU, while in blue are shown the pixels that intersect at least with one LOS. (b) Probability that a photon emitted in a certain position will be measured in any channel of the GCU, i.e. the sum of all rows of the transfer matrix: $\sum_i W_{ij}$. The LOS centre of each GCU channel is shown in orange dotted lines and the numbering of the GCU channels is also reported in orange.

6.1 Tomographic reconstruction

The tomographic inversion problem is based on the same formalism adopted in chapters 3 and 4, where four deconvolution methods have been presented in the context of the REs 1D energy distribution reconstruction during plasma disruptions. The poloidal section spanned by the GCU is divided into pixels and the plasma emissivity can be discretized over such pixels to form the image \underline{F} . The inverse problem, then, is:

$$\underline{S} = \underline{W} \cdot \underline{F} \quad (6.1)$$

with \underline{S} being a 19 entries vector containing the total number of counts measured by each channel of the GCU. If necessary, \underline{S} might be restricted to an arbitrary energy window to select a specific radiation emitted by the plasma: that is the case of section 6.2, where a $E_{signal} > 10$ MeV cut is applied to the spectra measured during the three-ions ICRH scheme experiments in D – ^3He mixed plasmas to select the 16.4 MeV signal emitted by $^3\text{He}(D, \gamma(16.4 \text{ MeV}))\alpha$ fusion reactions. Each entry of \underline{S} contains a measurement of the plasma emissivity integrated over the respective detector LOS.

All that is left to do is to calculate the matrix entries W_{ij} , which are the probability

that the radiation emitted in the j -th pixel will be detected by the i -th channel of the GCU, under the hypothesis that the emission is isotropic. This probability depends on the geometry of the pixel-LOS system, which is shown in figure 6.1(a), and not on the energy of the emitting particles. As a first, naive model that takes into consideration only the intersection between the LOS fan and the pixel, W_{ij} can be expressed as a Boolean variable:

$$W_{ij} = \begin{cases} 0 & \text{if } \text{LOS} \cap \text{pixel} = \emptyset \\ 1 & \text{if } \text{LOS} \cap \text{pixel} \neq \emptyset \end{cases} . \quad (6.2)$$

A global representation of this model is included in figure 6.1(a): each pixel has associated the probability that an emitted photon will be measured by any channel of the GCU, i.e. $\sum_i W_{ij}$. Since each pixel intersects three GCU LOS at most and there are white regions that contain pixels that do not lie on any LOS, the matrix \underline{W} can be said to be sparse. The pixel grid can be adjusted to maximize the number of pixels observed by the GCU, however figure 6.1(a) still shows some pixels that do not lie on any LOS especially in the high-field side. In order to better cover the poloidal plane in its entirety, thus, one should interpolate the experimental data with virtual lines of sight. The model (6.2) has been applied to the neutron camera and the previous gamma camera system [60, 80, 93, 96] obtaining good results, especially in the reconstruction of the spatial distribution of the neutrons source. On the other hand, when applied to the $D - {}^3\text{He}$ experiments discussed in section 6.2, the same model has generated artefacts in the reconstruction of the α -particle source, probably due to the lack of statistics in the measurements of the 16.4 MeV gamma emission.

In order to analyze this emission, the LOS and pixel geometry must be included in \underline{W} . The probability W_{ij} is then proportional to the fraction of the pixel area observed by the LOS multiplied to the solid angle subtended by the detector as seen from the pixel centre:

$$W(\text{LOS}, \text{pixel}) = \frac{A(\text{LOS} \cap \text{pixel})}{A(\text{pixel})} \frac{d\Omega(\text{LOS}, \text{pixel})}{4\pi},$$

$d\Omega(\text{LOS}, \text{pixel})$ is the solid angle of a cone with its apex at the center of the pixel and its base at the detector. It can be calculated as $4\pi \sin^2\left(\frac{\beta}{2}\right)$, with β the angle at the apex of the cone, which is equal to $\arctan\left(\frac{d}{2|DP|}\right)$ with apex of the solid angle. So the matrix can be calculated as:

$$W(\text{LOS}, \text{pixel}) = \frac{A(\text{LOS} \cap \text{pixel})}{A(\text{pixel})} \sin^2 \left[\frac{1}{2} \arctan \left(\frac{d}{2|DP|} \right) \right] \quad (6.3)$$

where A is the area of the object between parenthesis, $d\Omega$ the solid angle, d the scintillator diameter and $|DP|$ the distance between the pixel and the detector. This model is shown in figure 6.1(b), where the poloidal plane has been divided into

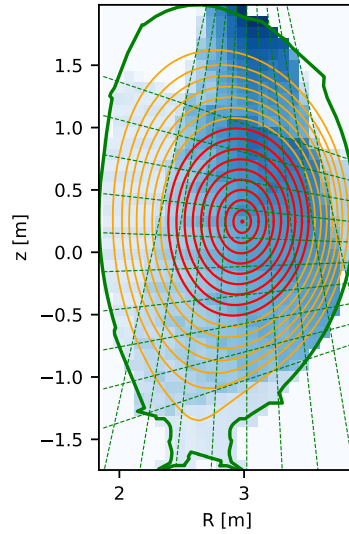


FIGURE 6.2: Reconstruction of the standard JET magnetic equilibrium in divertor configuration inside the LCFS. The flux lines have been downloaded from Flush for JET discharge #95679 at the instant $t = 10$ s.

9×9 mm pixels arranged in a 25×42 image (1050 pixels in total). The comparison with figure 6.1(a) also shows that (6.2) overestimates W_{ij} for the vertical channels that observe the high-field side ($j = 11, 12, 13$ and 14). The smaller opening of the collimator of such channels, in fact, reduces their solid angle of observation. This has limited effects on fast ions experiments, where most of the gamma emission is localized close to the magnetic axis. Runaway electrons, on the other hand, often drift to the high-field side during plasma disruptions and for such reason their bremsstrahlung emission needs to be analyzed using (6.3).

Even after interpolating the GCU profiles with virtual LOS and excluding all pixels outside JET inner wall, \underline{W} is a 36×783 matrix and it defines a highly undetermined inverse problem (6.1). In addition to this, the GCU is arranged into two arrays of detectors and it observes the plasma from two perpendicular projections, which is the minimum number of projections necessary to reconstruct convex spatial distributions. In order to reconstruct concave or non-simply connected profiles, such as hollow profiles, magnetic information must be included in the reconstruction [80, 97, 98]. Since particles transport is higher in the directions parallel to the magnetic flux surfaces than in the perpendicular direction, plasma emissivity can be considered to be uniform along magnetic flux surfaces. This can be included in the reconstruction by modifying the smoothing operator of the method in use (see chapter 3 for the description of four deconvolution methods) so that it penalizes the gradients along the flux surfaces.

Previous works on the JET neutron and gamma camera [60, 80], that share the same

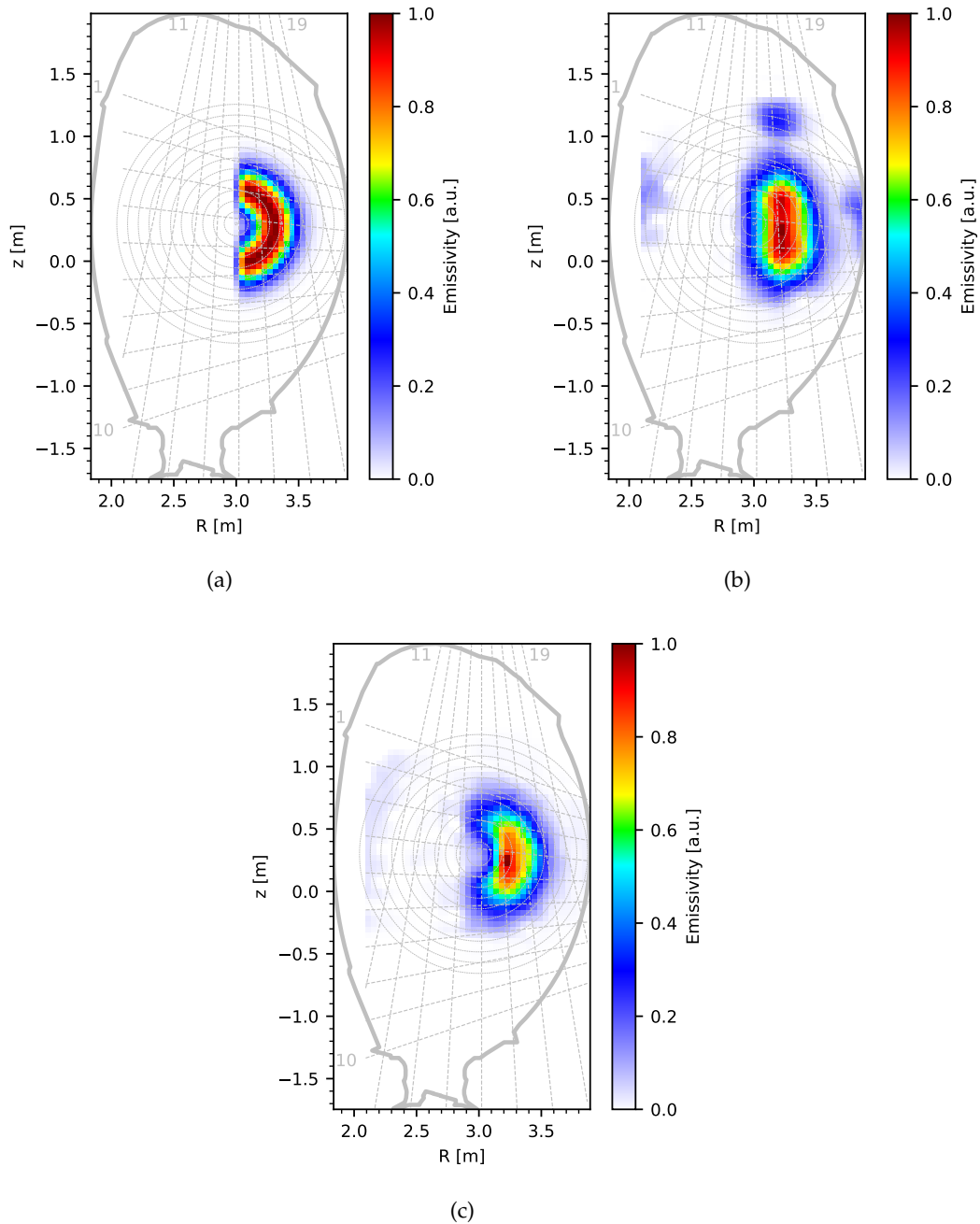


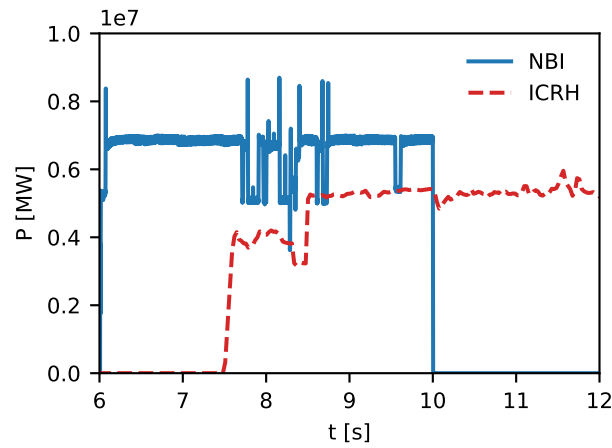
FIGURE 6.3: Example of synthetic test: (a) synthetic plasma emissivity used to generate the synthetic data over which the reconstruction has been calculated; (b) reconstruction performed using ML-EM and smoothing over the closest pixels; (c) reconstruction performed using ML-EM and smoothing along the magnetic field lines.

LOS system, have shown that the best method for the tomographic inversion of the cameras profile is ML-EM (see section 3.4). Therefore ML-EM has been used to perform the tomographic inversion presented in the remaining of the chapter. Incidentally, this is in line with the findings of chapter 4, where ML-EM has proved to be the best choice also in the unfolding of γ -ray spectra for the reconstruction of the 1D energy distribution of REs. In order to adapt the method to the tomographic problem at hand, its smoothing operator has been modified as follows: the moving average is calculated over the closest pixels that lie within $\frac{1}{10}$ -th of that surface. In some experiments, such as the fast-ions experiments considered in section 6.2, most of the emission takes place close to the magnetic axis. If this is the case, only those surfaces that are contained inside the LOS grid (red surfaces in figure 6.2) can be considered for the reconstruction. This operation reduces the size of the reconstructed image and so the degree of freedom of the inverse problem. This reduction works only if the tomography returns an emissivity close to zero on the last magnetic surface considered.

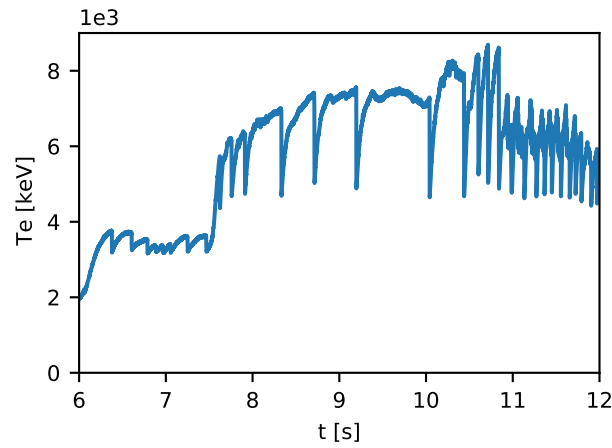
The effect of the magnetic smoothing can be appreciated in figure 6.3, where a hollow profile has been reconstructed with both traditional and magnetic smoothing. In the former case (figure 6.3(b)) the reconstruction returns an erroneously convex profile. On the other hand, in the latter case (figure 6.3(c)) the original distribution has been correctly retrieved, even though the edges of the profile at $R \approx 2.7$ m are over-smoothed: this is a side effect of implementing the equi-emissivity of the magnetic flux surfaces in the smoothing algorithm as a moving window average. It is worth noting that in both reconstructions there are artefacts in the outer flux surfaces, especially in those regions outside of the LOS grid of the GCU. In the case of traditional smoothing, the artefacts are more prominent and are a symptom of an erroneous reconstruction: the algorithm is unable to retrieve the correct spatial distribution and compensates for it by adding artificial structures where the discrepancy between the reconstruction and the experimental data is higher. In the case of magnetic smoothing the artefacts in the high-field side shows that, even when the correct distribution has been reconstructed, the algorithm tends to over-fit the experimental profiles by generating some structures where there is no vertical LOS that binds the reconstruction. This further stress the necessity to consider only those magnetic flux lines that lie within the LOS grid.

6.2 Alpha-particles source in three-ions ICRF scheme heating

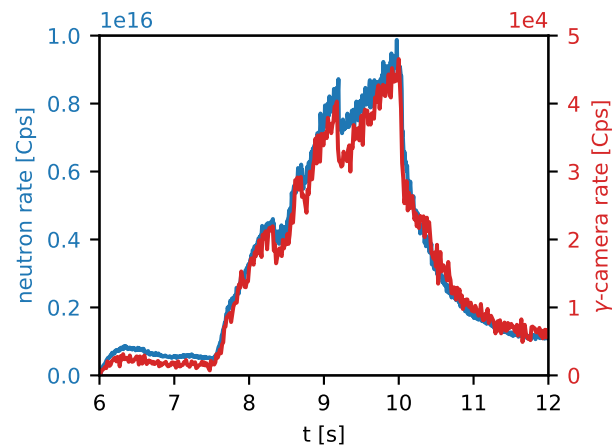
As an example of the capabilities of the GCU, JET discharge #95689 in the time window $t=47.5-52.5$ s is here analysed. The discharge belongs to a series of experiments on the ‘three-ion’ radio frequency heating [12, 15, 17], where radio-frequency



(a)



(b)



(c)

FIGURE 6.4: Overview of JET discharge #95689 in the time interval $t = 6 - 12$ s. (a) Time trace of the NBI (solid blue line) and ICRH (dashed red line) power heating injected in the plasma. (b) Electron temperature temporal evolution measured by channel 25 of the ECE. (c) Neutron yield measured by the fission chambers (blue) compared with the counting rate measured by channel 4 of the GCU.

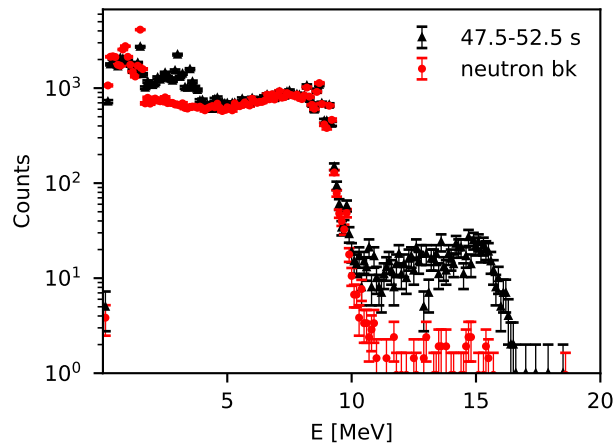
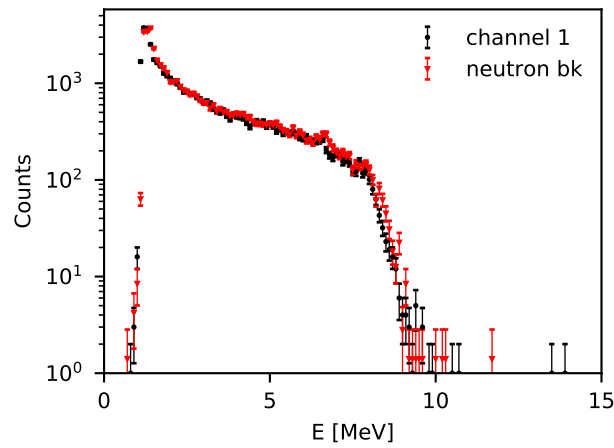


FIGURE 6.5: Black triangles show the gamma-ray spectrum measured by KM6T spectrometer, having tangential LOS, in the time interval $t=47.5-52.5$ s for JET shot #95689. Red circles show the neutron induced background experimentally estimated for KM6T.

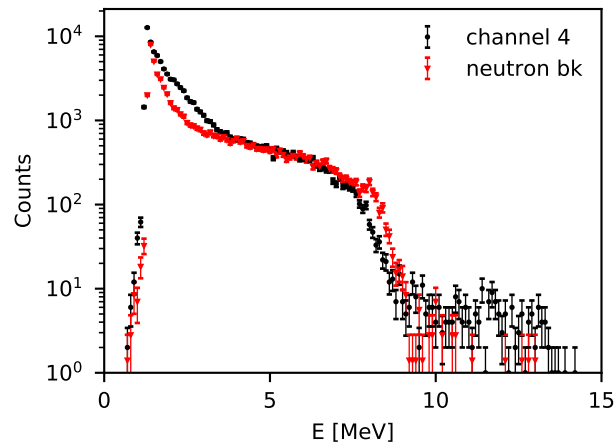
(RF) waves are used to accelerate a beam of deuterium ions up to energies in the MeV range in a plasma made of deuterium and ^3He , with relative concentrations of 50% and 25% respectively. The aim of the experiments was to tailor the $\text{D}+^3\text{He}$ reaction rate by accelerating deuterium at different energies, which is in turn obtained by changes of the ratio between the NBI and ICRH powers [17]. The main reaction channel of $\text{D}+^3\text{He}$ is the production of alpha particles and protons, i.e. $\text{D}+^3\text{He} \rightarrow \alpha + p$. However, there is also a weaker ($\approx 10^5$ relative probability [2]) electromagnetic channel of this reaction, $\text{D}+^3\text{He} \rightarrow \gamma + ^5\text{Li}$, which leads to the generation of 16.4 MeV gamma-rays and is of interest for the quantification of the fusion power from the $\text{D}+^3\text{He}$.

Figure 6.6 reports the gamma-ray spectra measured by three channels of the GCU during discharge #95689 for $t=47.5-50.0$ s: channel 1 (fig. 6.6(a)), which observes a peripheral region in the upper part of the poloidal plane with a horizontal LOS, and channels 4 (fig. 6.6(b)) and 15 (fig. 6.6(c)), which observe a region close to the magnetic axis and have respectively a horizontal and a vertical LOS. All three spectra are compared with the neutron-induced background, which has been experimentally estimated by summing up the spectra measured during the initial NBI phase of the three-ions heating scheme experiments in $\text{D}-^3\text{He}$ plasmas. The results are in agreement with the findings reported in refs. [99, 100], where the detector response function of $\text{LaBr}_3:\text{Ce}$ scintillators, induced by 2.5 and 14 MeV neutrons, has been measured at the Frascati Neutron Generator.

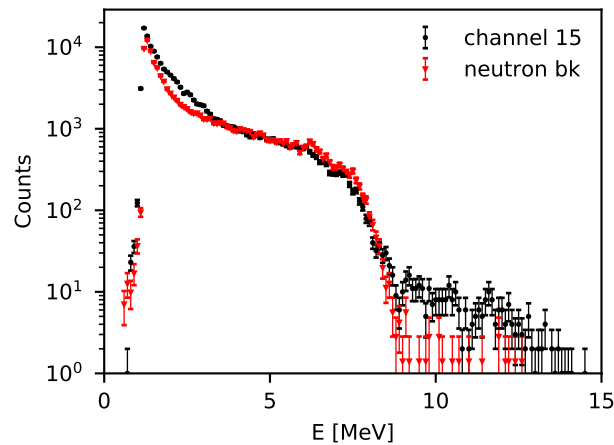
In all three spectra, most of the recorded events are contained in the region below 10 MeV: in that interval the spectrum is dominated by the neutron-induced background. This justifies why the count rate measured by the hard-X ray spectrometers has a time evolution very similar to the neutron yield measured by the JET fission



(a)



(b)



(c)

FIGURE 6.6: Black triangles show the gamma-ray spectrum measured by (a) channel 1, (b) channel 4 and (c) channel 15 of the gamma camera upgrade (the former two having horizontal LOS, the latter a vertical one) in the time interval $t=47.5-52.5$ s for JET shot #95689. Red circles show the neutron induced background experimentally estimated for each channel. (a) and (c) are reproduced from [49] with the permission of AIP Publishing.

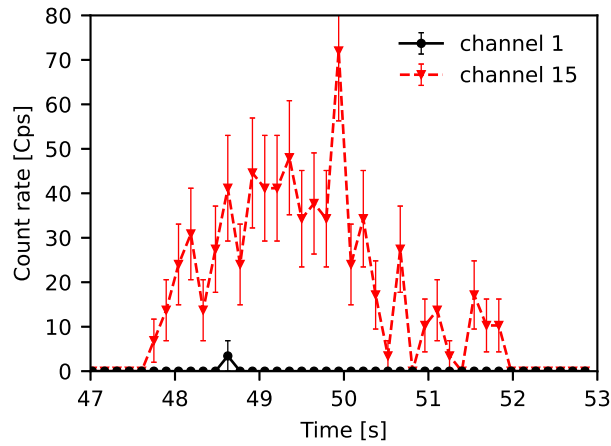


FIGURE 6.7: Time trace of the counting rate, for signals having energies greater than 10 MeV, measured by channel 1 (solid black line with circular markers) and channel 15 (dashed red line with triangular markers) of the GCU for JET shot #95689. Reproduced from [49] with the permission of AIP Publishing and the the author.

chambers (see figure 6.4(c)). For $E_{signal} < 10$ MeV, the only difference between the three channels is that, in the channels that observe the plasma core, there are counts in excess of the neutron-induced background in the energy region between 2 and 5 MeV. However the unfavourable signal to background ratio of this measurement (i.e. the ratio between incident gamma and incident neutrons) does not allow the detector to resolve the spectral structure of this radiation. On the other hand, above 10 MeV, the peripheral channels, such as channel 1, measure almost no events, while the central channels see a structure that extends up to approximately 14.5 MeV. This is also visible in figure 6.7, where the counting rate for events with $E_{signal} > 10$ MeV is shown for channel 15 and channel 1: the former has an average rate of about 30 Hz, while the latter is almost zero.

The nature of the radiation that exceeds the neutron background in the channels observing the region close to the magnetic axis can be asserted by looking at the spectrum measured by the tangential LaBr₃ spectrometer KM6T (figure 6.5). KM6T is equipped with a PMT, which is more stable than SiPM, and a LiH attenuator that substantially reduces the neutron-induced background incident on the detector [101]. In the region between 2 and 5 MeV, KM6T measures the 4.4 MeV γ -rays born in ${}^9\text{Be}(\alpha, n\gamma){}^12\text{C}$ reactions, while above 10 MeV it detects the 16.4 MeV γ -rays born in ${}^3\text{He}(\text{D}, \gamma){}^5\text{Li}$ fusion reactions.

The discrepancy between the 16.4 MeV signal and the 14.5 MeV energy measured by the GCU cannot be justified solely by the energy calibration reported in figure 2.4, whose confidence band at 14.5 MeV is only $\approx 5\%$. There are other factors at play. Let's first consider the physics of the ${}^3\text{He}(\text{D}, \gamma){}^5\text{Li}$ reactions. The γ -rays emitted are not perfectly mono-energetic, but are affected by the ≈ 1.5 MeV mass broadening

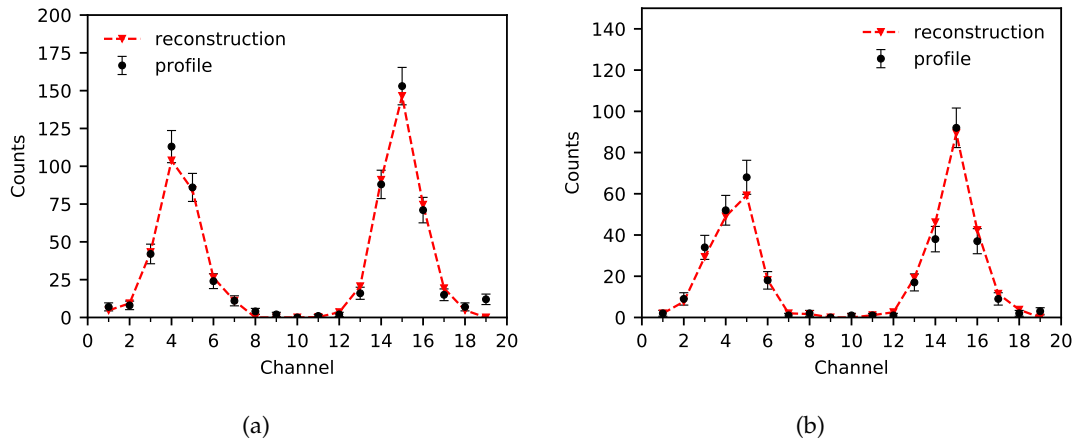


FIGURE 6.8: Circular black markers show the gamma-ray profile, i.e. channel by channel integration of the counts having energy greater than 10 MeV, measured by the GCU during JET shot #95689 in the time intervals: (a) $t=47.5 - 50.0$ and (b) $t=50.0 - 51.5$ s. Red dashed lines with triangular markers report the estimate of the experimental profile calculated as the convolution between the tomographies reported in figure 6.9 and the transfer matrix \underline{W} shown in figure 6.3. The p-value of the Pearson χ^2 statistics for these reconstructions is (a) $p=0.82$ and (b) $p=0.93$. (b) is reproduced from [49] with the permission of AIP Publishing and the the author.

due the unstable ${}^5\text{Li}$ [102]. They also interact with the detector mainly via Compton scattering and pair production [47], thus they do not deposit all their energy in the scintillator. MCNP simulations of the KN3G crystals showed that the Compton shoulder for a mono-energetic 16.4 MeV γ -ray beam is shifted towards the incident beam energy due to the Klein-Nishina effect and it is peaked at around 15 MeV, then decays rapidly. On the other hand, from the diagnostics point of view, the SiPMs non linearity in energy might be under-estimated by the quadratic formula used in section 2.2.1 for the calibration of the GCU. Also, figure 6.6(b) shows that the neutron-induced background estimated in the NBI phase of the discharge, stands above the spectrum measured during the NBI+ICRH phase. This is a symptom of a drift in the energy gain of some channels of the GCU induced by the higher count rate measured during the NBI+ICRH phase of the discharge. The energies measured in these channels are thus some percents lower due to a temporary saturation of the SiPM pixels.

Due to the lack of a LED signal to be used as a guide, the restoration of such gain drifts becomes a complex exercise: for this reason instead of subtracting the neutron background from the measurements, the counts induced in the GCU by the 16.4 MeV signal have been assessed applying an energy cut at ≈ 10 MeV, above which the neutron-induced background generated almost no events as shown in figure 6.5. This is a good approximation for central channels, for which the γ -ray signal dominates the few counts induced by neutrons in that region. On the other hand, in

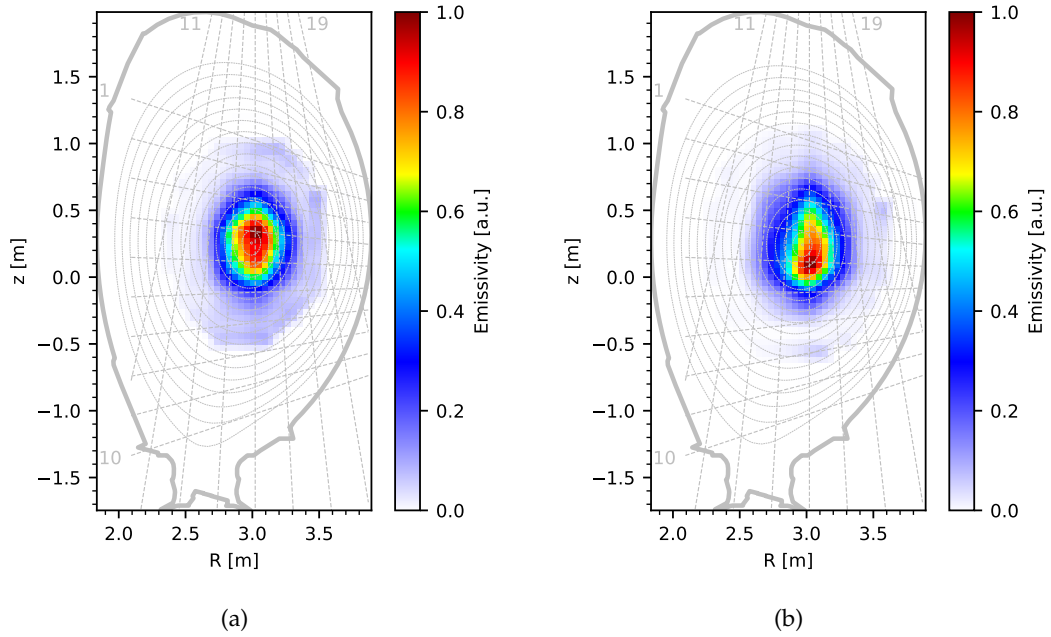


FIGURE 6.9: Tomographic inversion of the experimental gamma-ray profiles measured by the GCU in JET shot #95689 during time intervals (a) $t=47.5 - 50.0$ s and (b) $t=50.0 - 51.5$ s, and reported in figure 6.8. i.e. 2D reconstruction of the poloidal distribution of the gamma-ray emissivity for the reaction $D + {}^3\text{He} \rightarrow \gamma(16.4 \text{ MeV}) + {}^5\text{Li}$. The magnetic equilibrium, the GCU channels grid and their numbering are also reported in gray.

peripheral channels, where almost no counts are expected, this procedure might considerably overestimate the number of counts ascribable to the 16.4 MeV γ -rays. Thus it might become a source of artefacts in the outer region of the tomographic reconstruction of the α -particles poloidal distribution that is discussed in the rest of this section.

Figure 6.8 shows the total number of counts above 10 MeV measured by each channel of the GCU during JET experiment #95689, i.e. the integration of the experimental spectrum after the 10 MeV cut has been applied. This is proportional to the total number of counts induced by the 16.4 MeV gamma-rays and since all channels mount similar LaBr_3 scintillators, i.e. have the same response function to that signal, the constant of proportionality is approximately the same. In figure 6.8, the discharge has been divided in two time intervals: $t=47.5 - 50.0$ s for figure 6.8(a) and $t=50.0 - 52.5$ s for figure 6.8(b). In the first interval, both NBI and ICRH heating were on, while in the second one, termed *after-glow*, NBI heating was turned off. Some general features of the emission can be already inferred from these profiles. First of all the total number of counts measured by the GCU is reduces by $\approx 40\%$, which is expected as, in the absence of NBI heating, the generation of energetic deuterons that sustain the (D)-(D_{NBI})-(${}^3\text{He}$) ICRH scheme is interrupted. Also the emissivity peak vertically moves from channel 4 to channel 5, i.e. downwards, while still remaining

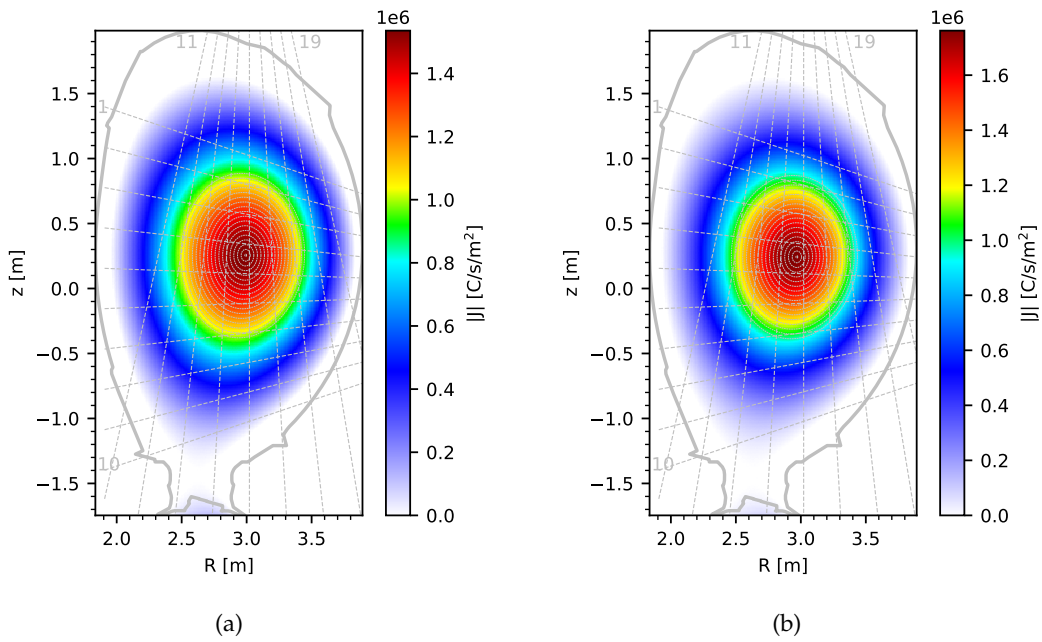


FIGURE 6.10: 2D spatial profile in the poloidal plane of the plasma current density J downloaded from FLUSH for JET pulse #95689 at (a) $t=49.0$ s and (b) $t=51.0$ s. The magnetic equilibrium, the GCU channels grid and their numbering are also reported in gray.

well localized horizontally.

A more detailed analysis of these data involves their tomographic inversion with the transfer matrix and the smoothing over magnetic flux surfaces illustrated in section 6.1. The poloidal distribution of the emissivity for the 16.4 MeV gamma-ray is reported in figure 6.9 for the two time intervals $t=47.5 - 50.0$ s (fig. 6.9(a)) and $t=50.0 - 52.5$ s (fig. 6.9(b)). Figure 6.8 also shows in red the convolution between the tomographic images with the transfer matrix \underline{W} . The agreement between the experimental data and their reconstruction $\underline{W} \cdot \underline{F}$ is significant, with a p-value of the Pearson χ^2 statistics of 0.82 and 0.93 for the two time intervals, meaning that the algorithm has converged to an admissible solution.

The physical meaning of this tomography is two-fold. Since ${}^3\text{He}(\text{D}, \gamma){}^5\text{Li}$ is a minor branch of the more frequent ${}^3\text{He}(\text{D}, p)\alpha$ fusion reaction, figure 6.9 is also proportional to the spatial distribution of the source of α -particles, with a constant of proportionality given by the ratio between the cross sections of the two channels: $\approx 10^5$. At the same time, according to radio frequency simulations [17], this emissivity spatial profile, i.e. the spatial profile of the fusion reactions rate, gives a hint on where the ICRH power has been deposited in the plasma. As expected from theory, the heating power is absorbed, and equivalently the alpha particles are produced, mainly in a narrow, elliptic area centered around the magnetic axis. In the time interval 50.0 – 52.5 s, figure 6.9(b) shows that the deposition site is slightly off-axis, on

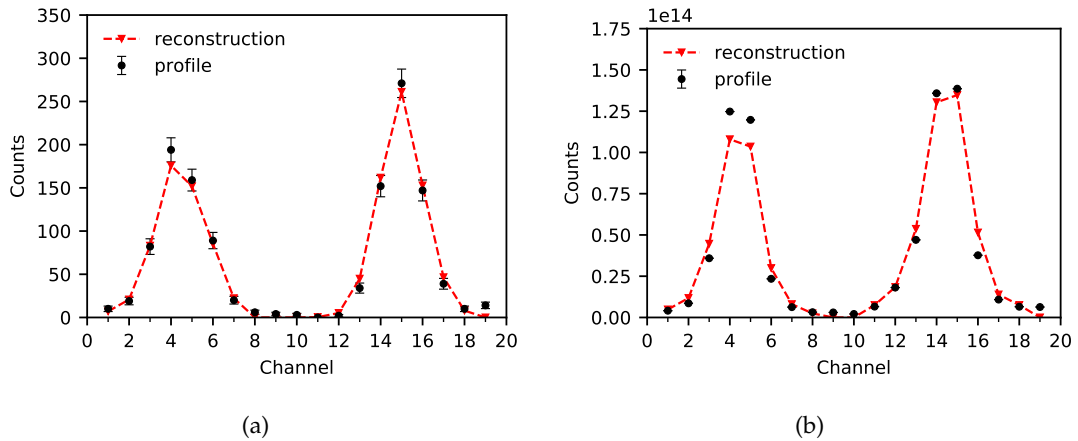


FIGURE 6.11: Experimental (a) gamma-ray and (b) neutron profiles measured by the gamma and neutron cameras during JET shot #95679 in the time interval $t=49.0 - 52.0$ s. Their reconstruction is shown in figure 6.12.

the low-field side. The two tomographies also show that this region slightly drifts downwards during the after-glow and the deposition site shrinks by approximately 20%, with the width of the reconstructed peak, estimated as the FWHM of the peak, that goes from ≈ 42 cm to ≈ 34 cm in the two time intervals. The same dynamics can be observed also in the plasma column, as shown by the spatial distribution of the plasma density current $|J|$, which has been downloaded from Flush and is reported in figure 6.10.

The same analysis has been conducted for JET discharge #95679, which has similar injected heating power as #95679, with $P_{NBI} = 7$ MW and $P_{ICRH} = 5.5$ MW. In this shot, both heating systems were turned off at $t=12.5$ s and the time interval $t=9.0-12.0$ s has been considered for the analysis. Figure 6.11 shows the profiles of the γ -ray and neutron emissivity measured by the JET cameras. The neutrons profile is wider than the gamma profile, especially in the vertical camera. This is reflected also in the tomography of the gamma and neutron profiles shown in figure 6.12. Both the gamma and neutron emissivity are centered close to the magnetic axis and have a symmetric profile, with the α -particles source reconstruction slightly more elongated than the neutron one. As already said, figure 6.12(a) is a reconstruction of the spatial distribution of the $D-^3\text{He}$ reactions, which is proportional to the product of the densities of the two species. Neutrons, instead, are here generated in $D - D_{NBI}$ and $D - T_{burnup}$ reactions, thus the differences between the two reconstructions reflects the different spatial distributions of ^3He and mostly D_{NBI} .

A reconstruction of the neutron source for shot #95679 has previously been performed in ref. [17], using the implementation of the tomographic algorithm presented in refs. [60, 80]. Figure 6.12(b) then can be compared with figure 1 in ref. [17] as a bench-mark of the implementation used in the present work [103]. On the

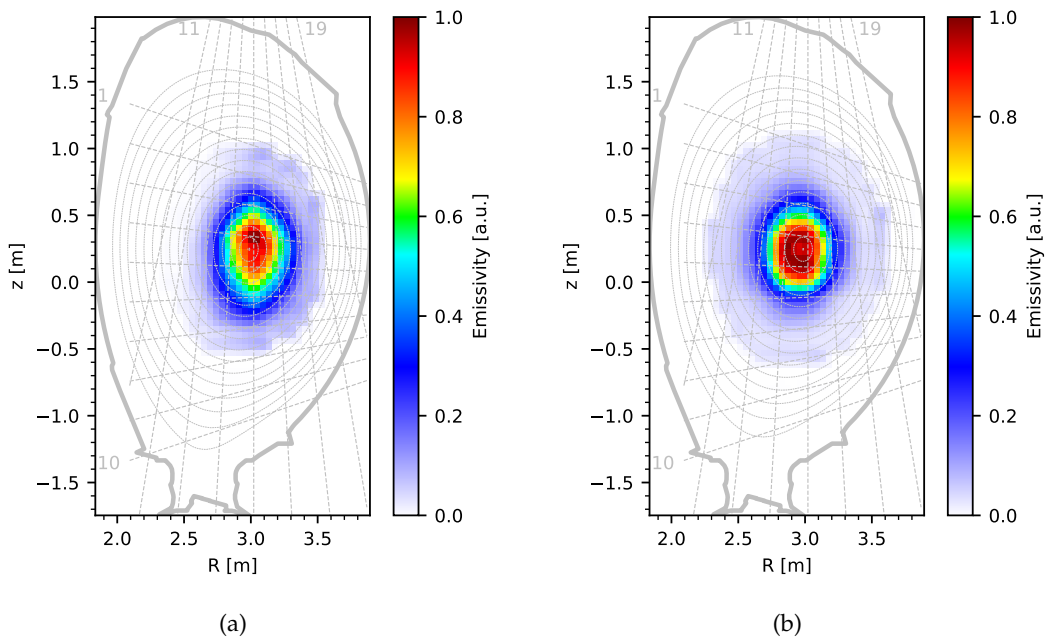


FIGURE 6.12: Tomographic inversion of the experimental (a) gamma-ray and (b) neutron profiles measured by the gamma and neutron cameras during JET shot #95679 in the time interval $t=49.0 - 52.0$ s. In particular (a) is the 2D reconstruction of the poloidal distribution of the gamma-ray emissivity for the reaction $D + {}^3\text{He} \rightarrow \gamma(16.4 \text{ MeV}) + {}^5\text{Li}$. The magnetic equilibrium, the GCU channels grid and their numbering are also reported in gray.

other hand, figure 6.12(a) has been compared with the α -particles source distribution simulated with TRANSP for JET shot #95679 and averaged over the time interval $t = 49.0 - 52.0$ s. TRANSP provides n_α as a function of the normalized effective radius $\rho_{eff} = \sqrt{\Psi_N}$ (Ψ_N is the toroidal magnetic flux normalized so that $\Psi_N = 0$ on magnetic axis and $\Psi_N = 1$ on the LCFS). Thus the spatial profile of figure 6.12(a) has been averaged over the magnetic flux surfaces and then normalized to the integral of the TRANSP simulation (i.e. the total number of α -particles according to TRANSP). The result is shown in figure 6.13. The high relative uncertainties on the profile inferred from the tomography are due to the lack of statistics in the spectra measured by the GCU. The two profiles are in agreement with one another up to the experimental uncertainties, even though the profile derived by the tomography is less peaked than the TRANSP one towards $\rho_{eff} = 0$. The reasons for this difference are still under investigation.

6.3 Runaway electrons spatial profile

The HXR spectra, measured by the GCU during plasma disruptions where REs are formed, contain information about the spatial distribution of the emissivity of the bremsstrahlung interactions between the REs and the ions in the background

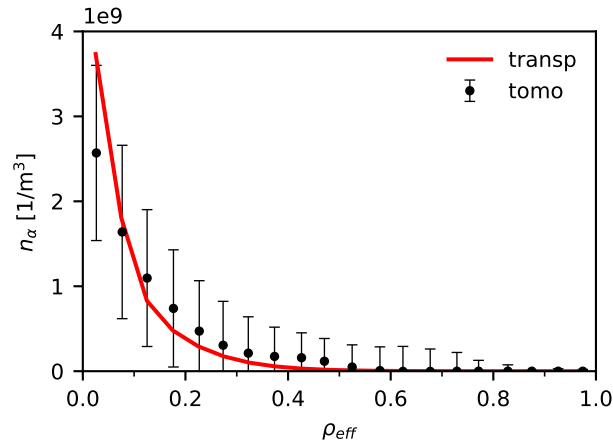


FIGURE 6.13: Comparison between (solid red line) the TRANSP simulation of the α -particles density profile, expressed as a function of the normalized effective radius and time averaged over the interval $t = 49.0 - 52.0$ s, and (black circles) the average over the magnetic flux surfaces of the tomographic reconstruction in the time interval $t = 49.0 - 52.0$ s of the α -particles source density profile shown in figure 6.12(a). The errors associated with black circles are calculated using the standard error propagation formula, from the errors of the tomography calculated with the Monte Carlo algorithm discussed in section 3.5.

plasma. The intensity of the tomographic reconstruction of these data is proportional to the product of the RE and ions densities: $n_{RE}n_I$, giving information about the REs spatial distribution. This is of interest for the study of the beam dynamics, as it allow to study the confinement of such particles and whether the RE beam can assume a hollow profile. Also the evolution of the REs spatial distribution gives information about the effect of the mitigation techniques introduced in section 1.3, e.g. it can help visualizing the depth of penetration of MGI and SPI, as well as estimating when mitigation techniques have an effect on the runaway electron beam after its generation.

Such reconstruction is extremely challenging because of the fast dynamics of the RE beam (see figures 6.17 and 6.18), which often drifts outside the GCU LOS grid on the high-field side. To allow for a complete reconstruction of the RE profile, information on the magnetic equilibrium is added under the assumption that RE orbits closely follow the magnetic field lines. Moreover, the fast evolution of the RE beam requires the use of magnetic equilibrium with high temporal resolution (approximately 1 ms). When the tomographic method discussed in section 6.1 is used and the LCFS is not entirely contained in the LOS grid, i.e. a part of the RE beam lies outside the vertical camera field of view, a discontinuity is observed in the reconstruction at the edge of the vertical camera field of view. The algorithm tends to overfit the experimental data by locating a relevant part of the emissivity outside of the LOS grid, where the lack of a second perpendicular LOS observing the same portion of plasma reduces

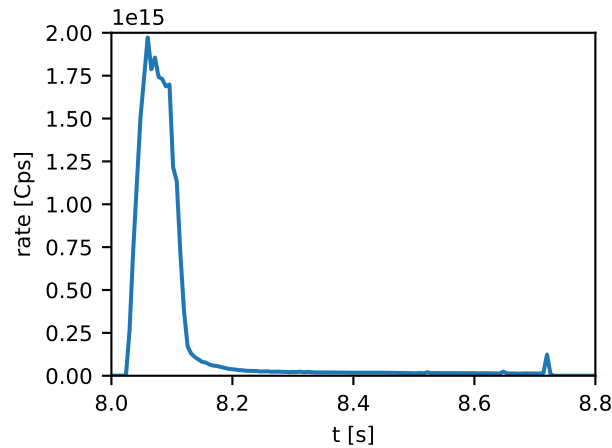


FIGURE 6.14: Count rate measured by the fission chambers during the plasma disruption in JET pulse #95774.

the constraints on the reconstruction. To avoid this kind of artefacts, the parameters of the smoothing operator are set to be $n_{smoothing} = 2$ and $\lambda < 1$ (see section 3.4) and the reconstructions here presented consider only the HXR profile measured by the horizontal camera. The effect that the lack of the vertical camera has on the reconstruction can be seen in figure 6.16, where the RE beam spatial distribution in JET pulse #95774 is reconstructed at $t = 8.21$ s. At that instant most of the RE beam is inside of the LOS grid and a reconstruction with both the vertical and the horizontal cameras is still possible. The two reconstructions locate the RE beam in the same poloidal region. Moreover, both profiles are hollow and asymmetric. However, the lack of the vertical camera does not allow to reconstruct profiles that are horizontally asymmetric. This can be seen in figure 6.16(b), where the spatial distribution of the RE beam is rotated of approximately 45 deg so that the distribution becomes vertically asymmetric.

In this section, JET pulse #95774 has been considered. In this experiment the disruption has been initiated at $t = 8$ s with a standard MGI of Ar at a pressure of 1.4 bar. Subsequently a deuterium SPI has been triggered at $t = 8.05$ s, with the aim of mitigating the RE beam. The change in the plasma effective atomic number Z_{eff} reduces the bremsstrahlung emissivity since the bremsstrahlung cross section is proportional to Z_{eff}^2 . This is clearly visible in the count rate measured by the JET fission chambers, figure 6.14: at $t = 8.092$ s there is a sudden drop in the measured rate due to the change of composition of the ion population in the post-disruption plasma.

Shot #95774 is ideal for attempting a preliminary reconstruction of the RE spatial distribution for several reasons. The absence of spikes in the count rate measured by the fission chambers, with the exception of the pulse termination at $t = 8.72$ s, suggests that the RE beam was well confined and there were no localized impacts with the inner wall. We can then consider all the counts measured by the GCU

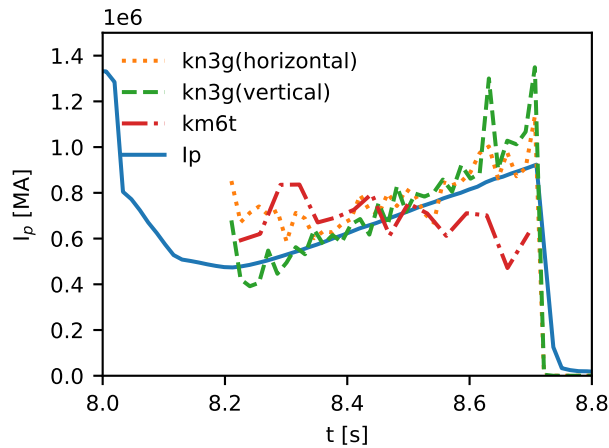


FIGURE 6.15: Measured plasma current I_p (blue solid line) compared with the current drive by the REs I_{RE} estimated from the data collected by the tangential spectrometer KM6T (red dash-dotted line), the sum of the channels in the vertical gamma camera (green dashed line) and the sum of the channels in the horizontal gamma camera (yellow dotted line).

as coming from the interaction between the RE beam and the background plasma. Moreover, all GCU channels worked correctly in this experiment and the incident flux of hard X-rays was low enough to avoid an early saturation of the memory in which the GCU data are stored during the pulse.

The completeness of the GCU measurement can be further assessed by comparing the plasma current measured during the disruption, which is mostly driven by REs, and its reconstruction based on the spectra measured by the GCU channels (see section 3.6 for further details). This is shown in figure 6.15. A single spectrometer often fails at reconstructing the plasma current when the RE beam drifts outside its LOS (a more extensive discussion of the matter can be found in ref. [40]). In figure 6.15, the reconstruction based on the inversion of the spectrum measured by the tangential detector KM6T has been reported (red dash-dotted line): even if the plasma current ramps up after the deuterium SPI, KM6T predicts a flat evolution. On the other hand, figure 6.15 also shows the reconstruction based on the average HXR energy measured by the vertical and horizontal gamma cameras (green dashed and orange dotted lines respectively). Both cameras correctly follow the ramp up of the plasma current after the deuterium SPI thanks to their wider fields of view, that allow them to observe the RE beam during the whole plasma disruption. As already discussed in section 3.6, when the plasma current can be reconstructed directly from the average energy of the measured HXR spectrum, then it is possible that the RE energy distribution preserves its shape throughout the disruption (it is a necessary condition, but not sufficient). This is consistent with the findings of ref. [40], where the RE energy distribution has been reconstructed in multiple experiments at JET and AUG and small differences in the retrieved distribution were reported.

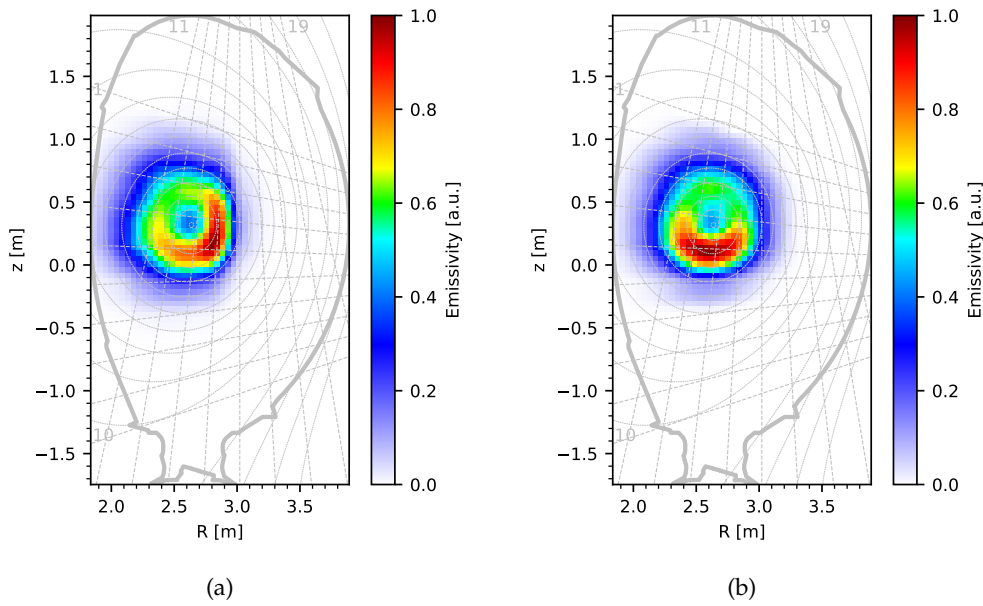


FIGURE 6.16: Tomographic reconstruction of the bremsstrahlung emissivity in JET pulse #95774 at $t = 8.21$ s. (a) has been reconstructed using the profiles measured by both the horizontal and the vertical cameras. (b) has been reconstructed using the profile measured by the horizontal camera only.

Finally figures 6.17 and 6.18 show the tomographic reconstruction of the bremsstrahlung emissivity in JET pulse #95774 from the HXR profile measured by the horizontal gamma camera only. Eight time instants are considered and for each reconstruction the GCU data have been integrated over a time interval of 1 ms. The evolution of the RE beam is also compared with the pictures recorded by the IR cameras installed at JET. The reconstructions converge in all the time intervals considered as shown in the comparison between the profiles measured by channels 1 to 10 in each time interval with their reconstruction calculated as the convolution of the tomography with the transfer matrix \underline{W} of figure 6.1(b). The high accuracy with which the experimental profiles are reconstructed shows that one of main challenges in this kind of tomography is to prevent over-fitting, which is probably the source of the artefacts reconstructed in the high-field side when both the vertical and the horizontal cameras are taken into account. Even though they were not used in the tomographic inversions here shown, in most of the time intervals considered the profile measured by channels 11 to 19 is well reconstructed within the experimental uncertainties. The tomographies show a drift of the RE beam towards the divertor which is consistent with the IR pictures. Some of the reconstructions here reported, especially the one in figs. 6.17(b), 6.17(f) and 6.18(d), suggest that the RE beam has assumed a hollow profile during those time intervals. In order to confirm this hypothesis one should be able to separate from the bremsstrahlung emissivity profile the contribution of the REs density distribution from the one of the background ions. This is a non-trivial

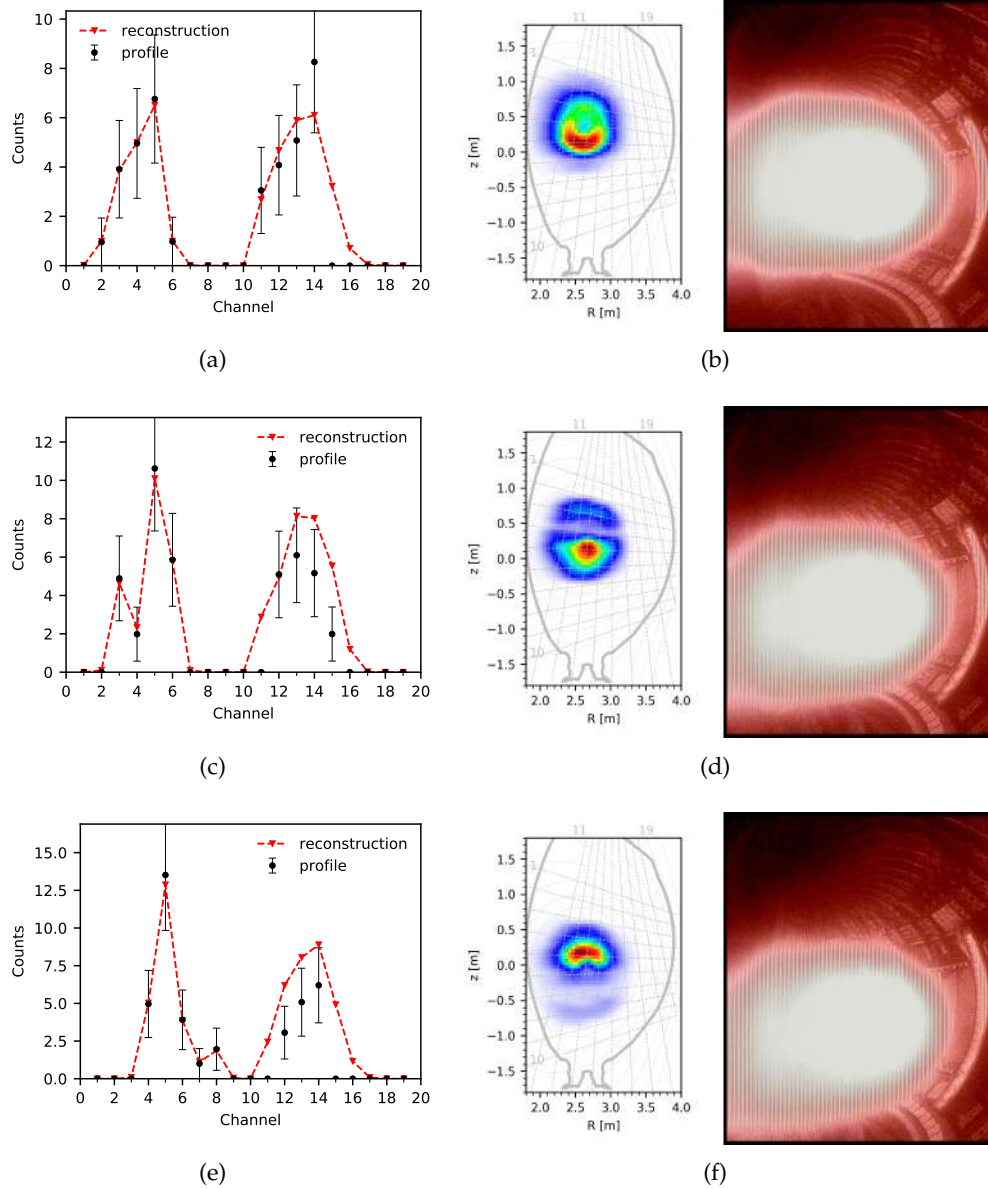


FIGURE 6.17: Tomographic reconstruction of the bremsstrahlung emissivity in JET pulse #95774 compared with the images acquired by the IR camera. The reconstructions refer to the time instants: 8.21 s (b), 8.30 s (d) and 8.38 s (f). Next to each reconstruction, the experimental data acquired by the GCU and their reconstruction calculated as the convolution of the tomography with the transfer matrix \underline{W} (see figure 6.1(b)) is shown.

activity for which different possible solutions are currently under study.

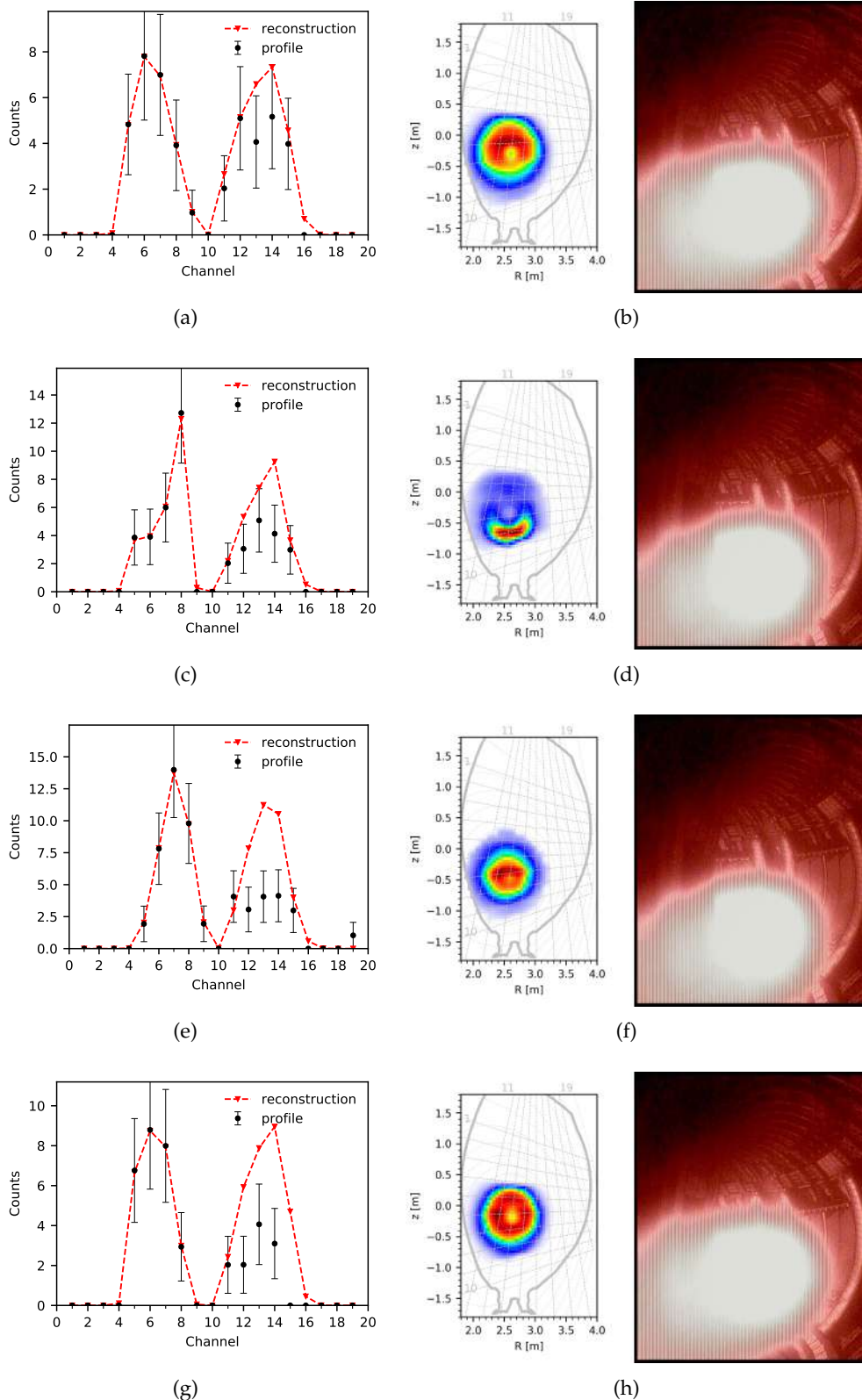


FIGURE 6.18: Tomographic reconstruction of the bremsstrahlung emissivity in JET pulse #95774 compared with the images acquired by the IR camera. The reconstructions refer to the time instants: 8.45 s (h), 8.53 s (b), 8.61 s (d), 8.70 s (f). Next to each reconstruction, the experimental data acquired by the GCU and their reconstruction calculated as the convolution of the tomography with the transfer matrix \underline{W} (see figure 6.1(b)) is shown.

Conclusions

The understanding of the dynamics of energetic particles in thermonuclear plasmas is essential both to approach the self-sustainment of the fusion process and to safeguard the structural integrity of the ITER machine, and large tokamaks in general. Fast ions as well as fast electrons are accelerated mostly due to three processes: external plasma heating, intrinsic heating via fusion reactions and plasma disruptions. External plasma heating can accelerate both ions and electrons up to energies in the MeV range. Ions in the MeV range, called fusion products, can also be generated by fusion reactions, as in the case of the 3.5 MeV alpha particles born in deuterium-tritium reactions. The confinement of the fast particles generated by these two processes is crucial to ensure the heating of the background plasma via Coulomb collisions. The development of efficient heating schemes and the improvement of the MeV range particle confinement is relevant to magnetic fusion confinement machines as they can help achieving the energy gain regime, where the energy generated by the plasma will be higher than the energy required to sustain it. Finally, plasma disruptions are fast terminations of a plasma discharge, during which strong inductive electric fields arise. Under the action of such fields, the plasma electrons are accelerated up to relativistic velocities and enter the runaway regime, in which the effect of collisions with the bulk plasma can be neglected and the particles lose energy mostly due to the emission of bremsstrahlung and synchrotron radiation. Due to the high currents driven by runaway electrons, the thermal load produced by a localized impact on large tokamaks inner wall, such as ITER, could damage the plasma facing components. Thus avoidance and mitigation techniques are currently under study to prevent plasma disruptions or at least reduce the generation of runaway electrons.

A key element in the studies of fast particle dynamics is the reconstruction of their phase-space distribution. The time evolution of this distribution allows studying the effects of plasma heating, external as well as intrinsic. On the other hand, in the case of a plasma disruption, the runaway electron distribution can be used to study the effect of mitigation techniques. When the fast particle distribution is inferred from experimental data, it can be further used to validate first-principles models. The recent development of a new generation of hard X-rays spectrometers, with high energy resolution and counting rate capabilities in excess of the MCps, allows conducting spectroscopic measurements of both the gamma-rays emitted by fast ions in

fusion reactions and the bremsstrahlung emission of runaway electrons. The measured hard X-ray spectrum contains information about the spatial and velocity distribution of fast particles. More precisely such a spectrum is the convolution of the fast particle distribution with a so called transfer matrix that describes the generation and the measurement of the hard X-ray photons.

In this thesis, an open source Python library with C submodules has been implemented to analyze the hard X-ray measurements conducted at the Joint European Torus and ASDEX Upgrade. The library contains dedicated deconvolution algorithms for the reconstruction of the spatial or velocity distribution function of fast particles in both fast ions and runaway electrons experiments. The velocity distribution of a particle population can be deconvoluted from the spectroscopic measurement of the radiation they emit. This operation is termed unfolding and requires a single line of sight, eventhough multiple lines of sight can be combined together to improve the accuracy of the reconstruction. In the present work, in particular, the unfolding was applied to the reconstruction of runaway electrons energy distribution from their bremsstrahlung emission. The reconstruction of the spatial distribution of a particle population, on the other hand, is termed tomography and requires multiple detectors organized in two or more arrays that observe the plasma from different projections. In particular, this thesis dealt with the tomographic reconstructions of the spatial distribution of both runaway electrons and fast ions at the Joint European Torus.

Four unfolding methods have been implemented for the reconstruction of the 1D energy distribution of the runaway electron beam from the measured bremsstrahlung spectrum: singular value decomposition, maximum likelihood - expectation maximization, Tikhonov regularization and Poissonian regularization. The transfer matrix necessary for this inversion was calculated in two steps: a first term describing the bremsstrahlung emission by the interaction of the runaway electrons beam with the plasma and a second term describing the photon transport to and interaction with the diagnostics. The bremsstrahlung emission was calculated using the GENESIS code, which implements a semi-empirical cross-section for the bremsstrahlung collisions. Detector response function matrices were calculated for all the hard X-ray spectrometers installed at the Joint European Torus and at ASDEX Upgrade using the MCNP code.

Since the performance of a deconvolution algorithm is strongly influenced by the transfer matrix that describes the physical process under analysis, the aforementioned four deconvolution methods were compared on the analysis of both synthetic spectra generated by known runaway electrons distributions and experimental data collected at ASDEX Upgrade. The maximum likelihood - expectation maximization algorithm has been proved to be the most reliable in the reconstruction of synthetic

spectra, especially in the reconstruction of the high-energy tail of the runaway electrons distribution. Except few cases, in which the singular value decomposition was employed, all methods had proven to be able to retrieve the mean and maximum energy of the synthetic distribution with a 5% accuracy. These statistics were correctly retrieved even in the presence of artifacts in the reconstruction, thus proving them to be a robust parameter for the analysis. Singular value decomposition generated severe artifacts in all the attempted reconstruction and was considered not suitable for this kind of analysis. Maximum likelihood - expectation maximization, Tikhonov regularization and Poissonian regularization were further tested on experimental data measured during AUG shot #34084. The three reconstructions were in agreement up to 10 MeV and slightly differ on the reconstruction of the high-energy tail, with the maximum likelihood - expectation maximization that better adheres to the experimental spectrum. From this reconstruction, the inverse of the transfer matrix has also been calculated using maximum likelihood - expectation maximization. This inverse matrix is a banded matrix on the counter diagonal, thus the reconstruction of the runaway electrons distribution at a certain energy E is based on the hard X-ray spectrum contained in a small energy interval $[E - \Delta E, E]$, where Δ is the width of the matrix band. The robustness of the four methods against experimental limitations, in particular low-energy cut and low statistics, was also tested. Multiple reconstructions, with increasing low-energy cutoffs, were performed. The shape of the inverse matrix ensures that the cutoff affects the reconstruction in an energy interval close to the cut itself. The minimum statistics necessary for performing the unfolding has been estimated with a bootstrap analysis: multiple reconstructions of sub-samples that were randomly drawn from the experimental spectrum were compared with the reconstruction achieved using the complete statistics. Poisson regularization generated artifacts in the high-energy tail of the reconstruction at every number of counts tested. Maximum likelihood showed to be the most reliable for the analysis of spectra with low statistics, being able to reconstruct the runaway electrons distribution already with 5 k counts. This gives an indication of the time resolution that can be reached with this analysis: supposing a count rate of 1 MCps, the runaway spectrum can be reconstructed every ≈ 10 ms, while its cumulative statistics every ≈ 1 ms.

The cross section of the bremsstrahlung emission depends on both the runaway electron energy and the angle of emission, thus the 1D analysis of the runaway electrons energy distribution can be generalized to 2 dimensions: energy and pitch. Even though an explicit reconstruction of the 2D distribution of runaway electrons has not been yet achieved, in this work the 2D transfer matrices necessary to perform the reconstruction of the runaway electrons velocity-space distribution were also calculated for all hard X-rays diagnostics installed at JET. These matrices were presented

using the weight function formalism, which allows studying the sensitivity of the diagnostics in the energy and pitch space. The calculations were performed assuming a point-shaped runaway electron population and a perfectly collimated line of sight. Effects of the toroidal magnetic field were included. The signals generated in each diagnostics by a population of particles having same energy and pitch, but different gyro-phase, have been analyzed. This showed that the weight functions are dominated by the emission of those particle whose angle of emission is minimum. This observation justifies the fact that these weight functions show a sensitivity peak in correspondence to the pitch equal to the cosine of the angle between the diagnostics line of sight and the magnetic field. The results shown also suggest that the angle between the line of sight and the magnetic field determines the particle orbit to which the diagnostics are more sensitive to. This paves the way to a 3D orbit-based analysis of the bremsstrahlung spectra measured by these diagnostics. In the assumption of a runaway electron beam toroidally symmetric, such an analysis would allow to fully reconstruct the phase-space distribution of the runaway electrons.

Finally, the reconstruction of the spatial distribution of the fast particles can be performed at the Joint European Torus thanks to the gamma-ray camera: a system of 19 detectors arranged in two perpendicular arrays that observe a poloidal section of the torus. A dedicated tomographic method was implemented to reconstruct the spatial distribution of both fast ions and runaway electrons. Due to the scarcity of lines of sight and projections, this algorithm makes use of smoothing along the magnetic field lines. The assumption behind this smoothing operator is that the emissivity is roughly constant along the magnetic field lines thanks to the fact that the particles transport is higher in the parallel direction than in the perpendicular one. This tomographic library was first applied to the gamma-ray measurements conducted during recent three-ion radio frequency heating experiments in D – ^3He mixed plasmas. The fusion reaction between D and ^3He has two branches: $^3\text{He}(D, p)^4\text{He}$ and $^3\text{He}(D, \gamma(16.4 \text{ MeV})^5\text{Li}$, the latter being 10^{-5} times less frequent than the former. Since the product of the first branch are charged particles, which are confined by the magnetic field, the gamma-rays emitted by the second branch can be used to study this reaction. During these experiments the upgraded gamma-ray camera was able to measure the 16.4 MeV gamma-ray emission due to $D + ^3\text{He} \rightarrow \gamma + ^5\text{Li}$ fusion reactions. The analysis of these measurements shows that the quadratic energy calibration of the gamma camera based on the Am-Be spectrum underestimates the 16.4 MeV energy by approximately 10%, suggesting the necessity to improve the calibration of this diagnostics above 10 MeV. The tomography of the gamma-ray profile measured by the gamma camera, i.e. the total number of counts generated by the 16.4 MeV photons in each channel, allowed the reconstruction of the spatial distribution of the source of α -particles born in $D + ^3\text{He}$ fusion reactions, which cannot be provided by any other diagnostics. These were the first tomographic reconstruction

performed with gamma-camera after the upgrade of its detector with new LaBr_3 scintillator crystals. In particular, JET pulse #95689 was analysed, showing that the alphas are born in a narrow region of 40 cm of diameters around the magnetic axis. The reconstruction of the alphas profile in the after glow phase shows a modification of the deposition site, which might be due to the different ratios between NBI and ICRH power. The results of the analysis of JET pulse #95679 were used to calculate the α -particles distribution as a function of the normalized effective radius and validate the TRANSP simulation for this discharge. In addition, the neutron profile was reconstructed for this pulse and used for a benchmark of the present implementation. Finally, the tomographic algorithm has been adapted for the analysis of the runaway electrons distribution. In this case, the reconstruction took into account the profile measured by the horizontal camera only. JET pulse #95774 was analyzed, the resulting profiles suggest that the runaway electron beam has assumed a hollow profile in different time intervals.

The work conducted in this thesis opens new possibilities in the analysis of fast particles in thermonuclear plasmas. The comparison between the unfolding methods has given precious information about the best algorithm to use and the selection of the optimal parameters for the reconstruction. These information can be used in future analysis of the bremsstrahlung emission of runaway electrons. A 2D reconstruction of the velocity-space distribution of runaway electrons can also be attempted based on the transfer matrices presented in this work. The computational framework developed can be further expanded to the calculation of orbit-based weight-matrices, which are necessary for a 3D reconstruction of the runaway electrons distribution functions: 2D in the velocity-space plus the toroidal radius. Thanks to the tomographic algorithm implemented, a systematic analysis of the α -particles source in the three-ions scheme experiments could be conducted both to further validate the TRANSP simulations and to study the shape of the energy deposition site in different discharges. The possibility to perform tomography of the runaway electrons density distribution, on the other hand, allows studying the runaway electrons confinement during plasma disruptions. In particular, the present algorithm could be combined with the unfolding techniques studied in this thesis to perform a 3D reconstruction of the runaway electron phase-space distribution. In this case, the dimensions considered for the reconstruction are different from the orbit-based tomography, as in fact, they are 2 spatial dimensions scanning the poloidal plane and 1 dimension describing the particles speed. From such a 3D map, the spatial distribution of the runaway electrons average velocity can be retrieved, which in turn is of interest for both the validation and the initialization of first-principle simulations. The spatial tomography of runaway electrons presented in this work reconstructs the bremsstrahlung emissivity, which is proportional to the product of the runaway electrons and plasma ions densities. The aforementioned 3D reconstruction might be used to

separate the contribution of the two species in the spatial tomography. From the spatial distribution of the average velocity, in fact, the runaway electron density distribution can be reconstructed with a fluid model. The ions density distribution can be estimated as the ratio between the bremsstrahlung and the runaway electron spatial distributions. Finally, it is worth noting that assuming the phase-space distribution of runaway electrons has a toroidal symmetry, then 3 dimensions fully describe the particles distribution and the two 3D reconstructions here described provide two alternative descriptions of the same distribution function.

Bibliography

- [1] K. S. Krane. *Introductory nuclear physics*. Wiley, 1991. ISBN: 978-0-471-80553-3. DOI: [10.1088/0741-3335/48/8/r01](https://doi.org/10.1088/0741-3335/48/8/r01).
- [2] F. E. Cecil et al. "Reaction $2\text{H}(3\text{He},\gamma)^5\text{Li}$ at center-of-mass energies between 25 and 60 keV". In: *Phys. Rev. C* 32 (1985), pp. 690–693. DOI: [10.1103/physrevc.32.690](https://doi.org/10.1103/physrevc.32.690).
- [3] H. S. Bosch and G.M. Hale. "Improved formulas for fusion cross-sections and thermal reactivities". In: *Nuclear Fusion* 32.4 (1992), p. 611. DOI: [10.1088/0029-5515/32/4/I07](https://doi.org/10.1088/0029-5515/32/4/I07).
- [4] P. M. Bellan. *Fundamentals of plasma physics*. Cambridge University Press, 2006.
- [5] J. Wesson. *Tokamaks*. Oxford University Press, 2011. ISBN: 9780199592234.
- [6] J. Jacquinet, Martin Keilhacker, and Paul-Henri Rebut. "Mission and highlights of the JET Joint Undertaking: 1978-1999". In: *Fusion Science and Technology* 53.4 (2008), pp. 866–890. DOI: [10.13182/FST08-A1742](https://doi.org/10.13182/FST08-A1742).
- [7] I. Mario. "Correlation between plasma and beam properties at the ELISE test facility". PhD thesis. Universität Augsburg, 2020. URL: <https://opus.bibliothek.uni-augsburg.de/opus4/frontdoor/index/index/docId/86048>.
- [8] V. Toigo et al. "The ITER Neutral Beam Test Facility towards SPIDER operation". In: *Nuclear Fusion* 57.8 (2017), p. 086027. DOI: [10.1088/1741-4326/aa7490](https://doi.org/10.1088/1741-4326/aa7490).
- [9] V. Toigo et al. "The PRIMA Test Facility: SPIDER and MITICA test-beds for ITER neutral beam injectors". In: *New Journal of Physics* 19.8 (2017), p. 085004. DOI: [10.1088/1367-2630/aa78e8](https://doi.org/10.1088/1367-2630/aa78e8).
- [10] I. Mario et al. "Reconstruction of the large multi-aperture beam via IR calorimetry technique and beam emission spectroscopy at the ELISE test facility". In: *Nuclear Fusion* 6 (2020). DOI: [10.1088/1741-4326/ab8573](https://doi.org/10.1088/1741-4326/ab8573).
- [11] J Adam. "Review of Tokamak plasma heating by wave damping in the ion cyclotron range of frequency". In: *Plasma Physics and Controlled Fusion* 29.4 (1987), pp. 443–472. DOI: [10.1088/0741-3335/29/4/001](https://doi.org/10.1088/0741-3335/29/4/001).
- [12] Ye.O. Kazakov et al. "On resonant ICRF absorption in three-ion component plasmas: a new promising tool for fast ion generation". In: *Nuclear Fusion* 55.3 (2015), p. 032001. DOI: [10.1088/0029-5515/55/3/032001](https://doi.org/10.1088/0029-5515/55/3/032001).

- [13] C. Hellesen et al. "Fast-ion distributions from third harmonic ICRF heating studied with neutron emission spectroscopy". In: *Nuclear Fusion* 53.11 (2013), p. 113009. DOI: [10.1088/0029-5515/53/11/113009](https://doi.org/10.1088/0029-5515/53/11/113009).
- [14] N. Bonanomi. "Experimental investigation and gyro-kinetic modelling of turbulent transport in thermonuclear plasmas". PhD Dissertation. Department of Physics: Università degli Studi di Milano-Bicocca, 2018. URL: <https://boa.unimib.it/handle/10281/198976>.
- [15] Ye. O. Kazakov et al. "Efficient generation of energetic ions in multi-ion plasmas by radio-frequency heating". In: *Nature Phys* 13 (2017), 973–978. DOI: [10.1038/nphys4167](https://doi.org/10.1038/nphys4167).
- [16] Ye.O. Kazakov et al. "Plasma heating and generation of energetic D ions with the 3-ion ICRF + NBI scenario in mixed H-D plasmas at JET-ILW". In: *Nuclear Fusion* 60.11 (2020), p. 112013. DOI: [10.1088/1741-4326/ab9256](https://doi.org/10.1088/1741-4326/ab9256).
- [17] M. Nocente et al. "Generation and observation of fast deuterium ions and fusion-born alpha particles in JET D –³He plasmas with the 3-ion radio-frequency heating scenario". In: *Nuclear Fusion* 60.12 (2020), p. 124006. DOI: [10.1088/1741-4326/abb95d](https://doi.org/10.1088/1741-4326/abb95d).
- [18] J. P. Freidberg. *Plasma physics and fusion energy*. Cambridge University Press, 2007. ISBN: 9780511755705.
- [19] Boris N. Breizman et al. "Physics of runaway electrons in tokamaks". In: *Nuclear Fusion* 59.8 (2019), p. 083001. DOI: [10.1088/1741-4326/ab1822](https://doi.org/10.1088/1741-4326/ab1822).
- [20] R. S. Granetz et al. "An ITPA joint experiment to study runaway electron generation and suppression". In: *Physics of Plasmas* 21.7 (2014), p. 072506. DOI: [10.1063/1.4886802](https://doi.org/10.1063/1.4886802).
- [21] R. J. Hastie J. W. Connor. "Relativistic limitations on runaway electrons". In: *Nuclear Fusion* 15.3 (1975), p. 415. DOI: [10.1088/0029-5515/15/3/007](https://doi.org/10.1088/0029-5515/15/3/007).
- [22] H. Dreicer. "Electron and Ion Runaway in a Fully Ionized Gas. I". In: *Physical Review* 115.2 (1959), pp. 238–249. DOI: [10.1103/physrev.115.238](https://doi.org/10.1103/physrev.115.238).
- [23] H. Dreicer. "Electron and Ion Runaway in a Fully Ionized Gas. II". In: *Physical Review* 117.2 (1960), pp. 329–342. DOI: [10.1103/physrev.117.329](https://doi.org/10.1103/physrev.117.329).
- [24] M. Gobbin et al. "Runaway electron mitigation by 3D fields in the ASDEX-Upgrade experiment". In: *Plasma Physics and Controlled Fusion* 60.1 (2018), p. 014036. DOI: [10.1088/1361-6587/aa90c4](https://doi.org/10.1088/1361-6587/aa90c4).
- [25] M.N Rosenbluth and S.V Putvinski. "Theory for avalanche of runaway electrons in tokamaks". In: *Nuclear Fusion* 37.10 (1997), pp. 1355–1362. DOI: [10.1088/0029-5515/37/10/i03](https://doi.org/10.1088/0029-5515/37/10/i03).
- [26] F. Salvat et al. "Semiempirical cross sections for the simulation of the energy loss of electrons and positrons in matter". In: *Nuclear Instruments and Methods in Physics Research, Section B* 63.3 (1992), pp. 255–269. DOI: [10.1016/0168-583X\(92\)95108-4](https://doi.org/10.1016/0168-583X(92)95108-4).

- [27] F. Salvat et al. "Monte Carlo simulation of bremsstrahlung emission by electrons". In: *Radiation Physics and Chemistry* 75.10 (2006). DOI: [10.1016/j.radphyschem.2005.05.008](https://doi.org/10.1016/j.radphyschem.2005.05.008).
- [28] T.C Hender et al. "Chapter 3: MHD stability, operational limits and disruptions". In: *Nuclear Fusion* 47.6 (2007), S128–S202. DOI: [10.1088/0029-5515/47/6/s03](https://doi.org/10.1088/0029-5515/47/6/s03).
- [29] G. Pautasso et al. "Disruption mitigation by injection of small quantities of noble gas in ASDEX Upgrade". In: *Plasma Physics and Controlled Fusion* (2017), p. 014046. DOI: [10.1088/0741-3335/59/1/014046](https://doi.org/10.1088/0741-3335/59/1/014046).
- [30] L.R. Baylor et al. "Disruption Mitigation System Developments and Design for ITER". In: *Fusion Science and Technology* 68.2 (2015), pp. 211–215. DOI: [10.13182/fst14-926](https://doi.org/10.13182/fst14-926).
- [31] M. Bakhtiari et al. "Fast plasma shutdown scenarios in the JT-60U tokamak using intense mixed gas puffing". In: *Nuclear Fusion* 42.10 (2002), pp. 1197–1204. DOI: [10.1088/0029-5515/42/10/304](https://doi.org/10.1088/0029-5515/42/10/304).
- [32] G Pautasso et al. "Plasma shut-down with fast impurity puff on ASDEX Upgrade". In: *Nuclear Fusion* 47.8 (2007), pp. 900–913. DOI: [10.1088/0029-5515/47/8/023](https://doi.org/10.1088/0029-5515/47/8/023).
- [33] M. Nocente et al. "MeV range particle physics studies in tokamak plasmas using gamma-ray spectroscopy". In: *Plasma Physics and Controlled Fusion* 62.1 (2019), p. 014015. DOI: [10.1088/1361-6587/ab4f32](https://doi.org/10.1088/1361-6587/ab4f32).
- [34] M. Salewski et al. "Combination of fast-ion diagnostics in velocity-space tomographies". In: *Nuclear Fusion* 53 (2013), p. 063019. DOI: [10.1088/0029-5515/55/9/093029](https://doi.org/10.1088/0029-5515/55/9/093029).
- [35] M. Salewski et al. "Measurement of a 2D fast-ion velocity distribution function by tomographic inversion of fast-ion D-alpha spectra". In: *Nuclear Fusion* 54.2 (2014), p. 023005. DOI: [10.1088/0029-5515/54/2/023005](https://doi.org/10.1088/0029-5515/54/2/023005).
- [36] M Salewski et al. "Velocity-space observation regions of high-resolution two-step reaction gamma-ray spectroscopy". In: *Nuclear Fusion* 55 (2015), p. 093029. DOI: [10.1088/0029-5515/55/9/093029](https://doi.org/10.1088/0029-5515/55/9/093029).
- [37] M Salewski et al. "Fast-ion energy resolution by one-step reaction gamma-ray spectrometry". In: *Nucl. Fusion* 56 (2016), p. 046009. DOI: [10.1088/0029-5515/56/4/046009](https://doi.org/10.1088/0029-5515/56/4/046009).
- [38] T. Goorley et al. "Initial MCNP6 Release Overview". In: *Nuclear Technology* 180 (2012), pp. 298–315. DOI: [10.13182/NT11-135](https://doi.org/10.13182/NT11-135).
- [39] M. Nocente et al. "High resolution gamma-ray spectrometer with MHz capabilities for runaway electron studies at ASDEX Upgrade". In: *Review of Scientific Instruments* 89 (2017), p. 10I124. DOI: [10.1063/1.5036658](https://doi.org/10.1063/1.5036658).

- [40] A. Dal Molin. "Reconstruction of the velocity space of runaway electrons by spectral measurements of the hard X-ray emission in tokamaks". PhD Dissertation. Department of Physics: Università degli Studi di Milano-Bicocca, 2021. URL: <https://boa.unimib.it/handle/10281/304289>.
- [41] R. C. Pereira et al. "Pulse Analysis for Gamma-Ray Diagnostics ATCA Sub-Systems of JET Tokamak". In: *IEEE Transactions on Nuclear Science* 58.4 (2011), pp. 1531–1537. DOI: [10.1109/TNS.2011.2159391](https://doi.org/10.1109/TNS.2011.2159391).
- [42] A.E. Shevelev et al. "Reconstruction of distribution functions of fast ions and runaway electrons in fusion plasmas using gamma-ray spectrometry with applications to ITER". In: *Nuclear Fusion* 53 (2013), p. 123004. DOI: [10.1088/0029-5515/53/12/123004](https://doi.org/10.1088/0029-5515/53/12/123004).
- [43] E. Joffrin et al. "Overview of the JET preparation for deuterium–tritium operation with the ITER like-wall". In: *Nuclear Fusion* 59.11 (2019), p. 112021. DOI: [10.1088/1741-4326/ab2276](https://doi.org/10.1088/1741-4326/ab2276).
- [44] D. Rigamonti et al. "Characterization of a compact LaBr₃(Ce) detector with Silicon photomultipliers at high 14 MeV neutron fluxes". In: *Journal of Instrumentation* 12.10 (2017), pp. C10007–C10007. DOI: [10.1088/1748-0221/12/10/c10007](https://doi.org/10.1088/1748-0221/12/10/c10007).
- [45] D. Rigamonti et al. "Performance of the prototype LaBr₃ spectrometer developed for the JET gamma-ray camera upgrade". In: *Review of Scientific Instruments* 87 (2016), 11E717. DOI: [10.1063/1.4961060](https://doi.org/10.1063/1.4961060).
- [46] D. Rigamonti et al. "The upgraded JET gamma-ray cameras based on high resolution/high count rate compact spectrometers". In: *Review of Scientific Instruments* 89 (2018), p. 10I116. DOI: [10.1063/1.5038839](https://doi.org/10.1063/1.5038839).
- [47] M. Nocente et al. "Conceptual design of the radial gamma ray spectrometers system for α -particle and runaway electron measurements at ITER". In: *Nuclear Fusion* 57.7 (2017), p. 076016. DOI: [10.1088/1741-4326/aa6f7d](https://doi.org/10.1088/1741-4326/aa6f7d).
- [48] A. Fernandes et al. "New FPGA based hardware implementation for JET gamma-ray camera upgrade". In: *Fusion Engineering and Design* 128 (2018), pp. 188–192. ISSN: 0920-3796. DOI: [10.1016/j.fusengdes.2018.02.038](https://doi.org/10.1016/j.fusengdes.2018.02.038).
- [49] E. Panontin, D. Rigamonti et al. "First spatially resolved measurements of the D–³He α -particle source with the upgraded JET gamma-ray camera". In: *Review of Scientific Instruments* (2021), p. 053529. DOI: [10.1063/5.0043776](https://doi.org/10.1063/5.0043776).
- [50] M. Nocente et al. "High Resolution Gamma Ray Spectroscopy at MHz Counting Rates With LaBr₃Scintillators for Fusion Plasma Applications". In: *IEEE Transactions on Nuclear Science* 60.2 (2013), pp. 1408–1415. DOI: [10.1109/TNS.2013.2252189](https://doi.org/10.1109/TNS.2013.2252189).
- [51] G. Strang. *Linear Algebra and Its Applications*. 2nd ed. Academic Press, 1980.
- [52] D. Kalman. "A Singularly Valuable Decomposition: The SVD of a Matrix". In: *The College Mathematics Journal* 27 (1996), pp. 2–23. DOI: [10.1080/07468342.1996.11973744](https://doi.org/10.1080/07468342.1996.11973744).

- [53] P. C. Hansen. "The truncated SVD as a method for regularization". In: *BIT Numerical Mathematics* 27 (1987), pp. 534–553. DOI: [10.1007/BF01937276](https://doi.org/10.1007/BF01937276).
- [54] L. E. Zakharov et al. "The theory of variances in equilibrium reconstruction". In: *Physics of Plasmas* 15 (2008), p. 092503. DOI: [10.1063/1.2977480](https://doi.org/10.1063/1.2977480).
- [55] P. C. Hansen. "Regularization, GSVD and truncated GSVD". In: *BIT Numerical Mathematics* 29 (1989), pp. 491–504. DOI: [10.1007/BF02219234](https://doi.org/10.1007/BF02219234).
- [56] P. C. Hansen. "Truncated singular value decomposition solutions to discrete ill-posed problems with ill-determined numerical rank". In: *SIAM Journal on Scientific and Statistical Computing* 11 (1990), pp. 503–518. DOI: [10.1137/0911028](https://doi.org/10.1137/0911028).
- [57] G. H. Golub and C. F. Van Loan. *Matrix Computations*. Johns Hopkins University Press, 1983.
- [58] A. N. Tikhonov. "Solution of incorrectly formulated problems and the regularization method". In: *Doklady Akademii Nauk SSSR* 4 (1963), pp. 1035–1038.
- [59] A. N. Tikhonov et al. *Numerical Methods for the Solution of Ill-Posed Problems*. Springer Netherlands, 1995. DOI: [10.1007/978-94-015-8480-7](https://doi.org/10.1007/978-94-015-8480-7).
- [60] T. Craciunescu et al. "A comparison of four reconstruction methods for JET neutron and gamma tomography". In: *Nucl. Instrum. Methods Phys. Res.* 605 (2009), pp. 374–383. ISSN: 0168-9002. DOI: [10.1016/j.nima.2009.03.224](https://doi.org/10.1016/j.nima.2009.03.224).
- [61] J. Bielecki et al. "Phillips-Tikhonov regularization with a priori information for neutron emission tomographic reconstruction on Joint European Torus". In: *Review of Scientific Instruments* 86.9 (2015), p. 093505. DOI: [10.1063/1.4931680](https://doi.org/10.1063/1.4931680).
- [62] D. Vezinet et al. "Non-monotonic growth rates of sawtooth precursors evidenced with a new method on ASDEX Upgrade". In: *Nuclear Fusion* 56.8 (2016), p. 086001. DOI: [10.1088/0029-5515/56/8/086001](https://doi.org/10.1088/0029-5515/56/8/086001).
- [63] M Salewski et al. "High-definition velocity-space tomography of fast-ion dynamics". In: *Nuclear Fusion* 56.10 (2016), p. 106024. DOI: [10.1088/0029-5515/56/10/106024](https://doi.org/10.1088/0029-5515/56/10/106024).
- [64] M Weiland et al. "Enhancement of the FIDA diagnostic at ASDEX Upgrade for velocity space tomography". In: *Plasma Physics Controlled Fusion* 58.2 (2016), p. 025012. DOI: [10.1088/0741-3335/58/2/025012](https://doi.org/10.1088/0741-3335/58/2/025012).
- [65] A. S. Jacobsen et al. "Inversion methods for fast-ion velocity-space tomography in fusion plasmas". In: *Plasma Physics and Controlled Fusion* 58.4 (2016), p. 045016. DOI: [10.1088/0741-3335/58/4/045016](https://doi.org/10.1088/0741-3335/58/4/045016).
- [66] M Salewski et al. "MeV-range velocity-space tomography from gamma-ray and neutron emission spectrometry measurements at JET". In: *Nuclear Fusion* 57.5 (2017), p. 056001. DOI: [10.1088/1741-4326/aa60e9](https://doi.org/10.1088/1741-4326/aa60e9).
- [67] M Weiland et al. "Phase-space resolved measurement of 2nd harmonic ion cyclotron heating using FIDA tomography at the ASDEX Upgrade tokamak". In: *Nuclear Fusion* 57.11 (2017), p. 116058. DOI: [10.1088/1741-4326/aa7e0a](https://doi.org/10.1088/1741-4326/aa7e0a).

- [68] M. Salewski et al. "Alpha-particle velocity-space diagnostic in ITER". In: *Nuclear Fusion* 58.9 (2018), p. 096019. DOI: [10.1088/1741-4326/aace05](https://doi.org/10.1088/1741-4326/aace05).
- [69] B. Madsen et al. "Fast-ion velocity-space tomography using slowing-down regularization in EAST plasmas with co- and counter-current neutral beam injection". In: *Plasma Physics and Controlled Fusion* 62 (2020), p. 115019. DOI: [10.1088/1361-6587/abb79b](https://doi.org/10.1088/1361-6587/abb79b).
- [70] B. Madsen et al. "Tomography of the positive-pitch fast-ion velocity distribution in DIII-D plasmas with Alfvén eigenmodes and neoclassical tearing modes". In: *Nuclear Fusion* 60.6 (2020), p. 066024. DOI: [10.1088/1741-4326/ab82b5](https://doi.org/10.1088/1741-4326/ab82b5).
- [71] P. C. Hansen. "The L-Curve and its Use in the Numerical Treatment of Inverse Problems". In: *in Computational Inverse Problems in Electrocardiology*, ed. P. Johnston, *Advances in Computational Bioengineering*. WIT Press, 2000, pp. 119–142.
- [72] C. Lawson and R. J. Hanson. *Solving Least Squares Problems*. SIAM, 1987. DOI: [10.1137/1.9781611971217](https://doi.org/10.1137/1.9781611971217).
- [73] Johnathan M. Bardsley and Curtis R. Vogel. "A Nonnegatively Constrained Convex Programming Method for Image Reconstruction". In: *SIAM Journal on Scientific Computing* 25.4 (2004), pp. 1326–1343. DOI: [10.1137/s1064827502410451](https://doi.org/10.1137/s1064827502410451).
- [74] J. M. Bardsley and N. Laobeul. "Tikhonov regularized Poisson likelihood estimation: theoretical justification and a computational method". In: *Inverse Problems in Science and Engineering*. 2nd ser. 16 (2008), 199–215. DOI: [10.1080/17415970701404235](https://doi.org/10.1080/17415970701404235).
- [75] W. H. Richardson et al. "Bayesian-Based Iterative Method of Image Restoration". In: *Journal of the Optical Society of America* 62 (1972), pp. 55–59. DOI: [10.1364/josa.62.000055](https://doi.org/10.1364/josa.62.000055).
- [76] L. B. Lucy. "An iterative techniques for the rectification of observed distribution". In: *The Astronomical Journal* 79.6 (1974), pp. 745–754. DOI: [10.1086/111605](https://doi.org/10.1086/111605).
- [77] L. A. Shepp and Y. Vardi. "Maximum likelihood reconstruction for emission tomography". In: *IEEE Transactions on Medical Imaging* 1 (1982), p. 113. DOI: [10.1109/TMI.1982.4307558](https://doi.org/10.1109/TMI.1982.4307558).
- [78] K. Lange and R. Carson. "EM reconstruction algorithms for emission and transmission tomography". In: *Journal of Computer Assisted Tomography* 8.2 (1984), p. 306. DOI: [10.1109/42.276147](https://doi.org/10.1109/42.276147).
- [79] A. Del Guerra. "Positron Emission Tomography: Its 65 years". In: *Rivista del nuovo cimento* 39.4 (2016), pp. 155–223. DOI: [10.1393/ncr/i2016-10122-6](https://doi.org/10.1393/ncr/i2016-10122-6).
- [80] T. Craciunescu et al. "The maximum likelihood reconstruction method for JET neutron tomography". In: *Nucl. Instrum. Methods Phys. Res.* 595.3 (2008), pp. 623–630. ISSN: 0168-9002. DOI: [10.1016/j.nima.2008.07.145](https://doi.org/10.1016/j.nima.2008.07.145).

- [81] E. Panontin. "Analysis Methods for Gamma Ray Measurements from Runaway Electron Experiments at ASDEX Upgrade". MA thesis. Università degli Studi di Milano-Bicocca, 2017.
- [82] A.E. Shevelev et S.V. Lebedev. *Reconstruction of the Runaway Electron Distribution Function in the ASDEX Upgrade Tokamak*. Ioffe Institute, 2017, internal report.
- [83] D. G. Shirk and N. M. Hoffman. "Monte-Carlo error analysis in x-ray spectral deconvolution". In: *Review of Scientific Instruments* 56 (1985), p. 809. DOI: [10.1063/1.1138180](https://doi.org/10.1063/1.1138180).
- [84] E. Panontin et al. "Development of Nuclear Radiation Based Tomography Methods for Runaway Electrons in Fusion Plasmas: First Results and Prospects". In: *Proceedings of the 46th EPS Conference on Plasma Physics*. Vol. 43C. European Physical Society, 2019, P4.1002. URL: <http://ocs.ciemat.es/EPS2019ABS/pdf/P4.1002.pdf>.
- [85] E. Panontin et al. "Comparison of Unfolding Methods for the Inference of Runaway Electron Energy Distribution from γ -ray Spectroscopic Measurements". In: *Journal of Instrumentation* 16 (2021), p. C12005. DOI: [10.1088/1748-0221/16/12/C12005](https://doi.org/10.1088/1748-0221/16/12/C12005).
- [86] E. Panontin et al. "Runaway electrons' velocity-space observation regions of bremsstrahlung hard X-ray spectroscopy". In: *arxiv physics.plasm-ph* (2022). v1. DOI: [10.48550/arXiv.2204.14140](https://doi.org/10.48550/arXiv.2204.14140). URL: <https://arxiv.org/abs/2204.14140v1>.
- [87] M. Nocente. "Neutron and gamma-ray emission spectroscopy as fast ion diagnostics in fusion plasmas". PhD thesis. Università degli Studi di Milano-Bicocca, 2012. URL: <http://hdl.handle.net/10281/28397>.
- [88] H. Järleblad et al. "Orbit Weight Functions for Neutron Emission and One-step Reaction Gamma-ray Spectroscopy". In: *17th IAEA Technical Meeting on Energetic Particles and Theory of Plasma Instabilities in Magnetic Confinement Fusion* (2021).
- [89] L. Stagner and W. W. Heidbrink. "Action-angle formulation of generalized, orbit-based, fast-ion diagnostic weight functions". In: *Physics of Plasmas* 24 (2017), p. 092505. DOI: [10.1063/1.4990391](https://doi.org/10.1063/1.4990391).
- [90] H. Järleblad et al. "Fast-ion orbit sensitivity of neutron emission spectroscopy diagnostics". In: *Review of Scientific Instruments* 92.4 (2021), p. 043526. DOI: [10.1063/5.0040696](https://doi.org/10.1063/5.0040696).
- [91] L. Stagner et al. "Orbit Tomography of energetic particle distribution functions". In: *Nuclear Fusion* (2021), accepted. DOI: [10.1088/1741-4326/ac3ed2/meta1](https://doi.org/10.1088/1741-4326/ac3ed2/meta1).

- [92] M. Nocente et al. "Gamma-ray spectroscopy at MHz counting rates with a compact LaBr₃ detector and silicon photomultipliers for fusion plasma applications". In: *Review of Scientific Instruments* 87 (2016), 11E714. DOI: [10.1063/1.4961073](https://doi.org/10.1063/1.4961073).
- [93] V.G. Kiptily et al. "Gamma-ray imaging of D and 4He ions accelerated by ion-cyclotron-resonance heating in JET plasmas". In: *Nucl. Fusion* (2005), p. L21. DOI: [10.1088/0029-5515/45/5/101](https://doi.org/10.1088/0029-5515/45/5/101).
- [94] J. Bielecki et al. "Phillips-Tikhonov regularization with a priori information for neutron emission tomographic reconstruction on Joint European Torus". In: *Review of Scientific Instruments* 86 (2015), p. 093505. DOI: [10.1063/1.4931680](https://doi.org/10.1063/1.4931680).
- [95] E. Panontin et al. " γ -ray emission from radio frequency heating experiments with the three-ion schemes at the Joint European Torus". In: *Proceedings of the 47th EPS Conference on Plasma Physics*. Vol. 43C. European Physical Society, 2021, P1.1011. URL: <http://ocs.ciemat.es/EPS2021PAP/pdf/P1.1011.pdf>.
- [96] V. G. Kiptily, F E Cecil, and S S Medley. "Gamma ray diagnostics of high temperature magnetically confined fusion plasmas". In: *Plasma Physics and Controlled Fusion* 48.8 (2006), R59–R82. DOI: [10.1088/0741-3335/48/8/r01](https://doi.org/10.1088/0741-3335/48/8/r01).
- [97] L.C. Ingesson et al. "Soft X ray tomography during ELMs and impurity injection in JET". In: *Nuclear Fusion* 38.11 (1998), pp. 1675–1694. DOI: [10.1088/0029-5515/38/11/307](https://doi.org/10.1088/0029-5515/38/11/307). URL: <https://doi.org/10.1088/0029-5515/38/11/307>.
- [98] V.G. Kiptily et al. " γ -ray diagnostics of energetic ions in JET". In: *Nuclear Fusion* 42.8 (2002), pp. 999–1007. DOI: [10.1088/0029-5515/42/8/308](https://doi.org/10.1088/0029-5515/42/8/308). URL: <https://doi.org/10.1088/0029-5515/42/8/308>.
- [99] C. Cazzaniga et al. "Response of LaBr₃(Ce) scintillators to 2.5 MeV fusion neutrons". In: *Review of Scientific Instruments* 84 (2013), p. 123505. DOI: [10.1063/1.4847056](https://doi.org/10.1063/1.4847056).
- [100] C. Cazzaniga et al. "Response of LaBr₃(Ce) scintillators to 14MeV fusion neutrons". In: *Nuclear Instruments and Methods in Physics Research Section A: Accelerators, Spectrometers, Detectors and Associated Equipment* 778 (2015), pp. 20–25. ISSN: 0168-9002. DOI: [10.1016/j.nima.2015.01.002](https://doi.org/10.1016/j.nima.2015.01.002).
- [101] M. Nocente et al. "A new tangential gamma-ray spectrometer for fast ion measurements in deuterium and deuterium-tritium plasmas of the Joint European Torus". In: *Review of Scientific Instruments* 92.4 (2021), p. 043537. DOI: [10.1063/5.0043806](https://doi.org/10.1063/5.0043806).
- [102] M. Nocente et al. "Gamma-ray emission spectrum from thermonuclear fusion reactions without intrinsic broadening". In: *Nuclear Fusion* 55.12 (2015), p. 123009. DOI: [10.1088/0029-5515/55/12/123009](https://doi.org/10.1088/0029-5515/55/12/123009).

- [103] E. Panontin and A. Dal Molin. <https://gitlab.com/unimib-fusion/inversion-python>. Write to e.panontin@campus.unimib.it to get access to the repository.

Part IV

Papers

Development of Nuclear Radiation Based Tomography Methods for Runaway Electrons in Fusion Plasmas: First Results and Prospects

E. Panontin¹, A. Dal Molin¹, M. Nocente^{1,2}, M. Tardocchi², F. Causa², J. Eriksson³, L. Giacomelli², G. Gorini^{1,2}, D. Rigamonti², M. Salewski⁴, and the ASDEX Upgrade Team⁵.

¹Department of Physics, Università degli Studi di Milano-Bicocca, Milan, Italy

²Istituto di Fisica del Plasma, CNR, Milan, Italy

³Department of Physics and Astronomy, Uppsala University, Sweden

⁴Department of Physics, Technical University of Denmark, Kgs. Lyngby, Denmark

⁵ See the author list of “H. Meyer et.al. 2019 Nucl. Fusion accepted

(<https://doi.org/10.1088/1741-4326/ab18b8>)”

Electronic mail: e.panontin@campus.unimib.it

INTRODUCTION

The study of Runaway Electron (RE) physics and their response to mitigation strategies is crucial to safeguard ITER structural integrity. During their motion REs collide with background ions before hitting the inner vessel of the machine and thus they emit Bremsstrahlung photons in the gamma range of the spectrum. It is possible to detect such radiation using a LaBr₃(Ce) spectrometer with counting rate capability in the MHz range and high energy resolution [1][5]. The measured spectra contain information about the RE energy distribution, which can be reconstructed using specific inversion (or deconvolution) algorithms. The deconvolution operation is computationally faster than first principles simulations and its use in RE studies might be many fold: it can be used to improve synthetic diagnostic calculations or as a preliminary method for RE spectra analysis.

THE INVERSION PROBLEM

The RE energy distribution F is related to the measured gamma-ray spectrum S through a matrix W , which describes the probability for an electron of energy E to produce a signal of energy E^{II} in the diagnostics system, as follows:

$$S = W * F \quad .$$

The operation of reconstructing F , known W and S , is called inversion and it has been solved here using three different methods for comparison. ML-EM [2], an iterative algorithm which,

starting from a first guess of the type $F^0 = \frac{S}{\|W^T S\|}$, makes the estimate evolve according to

$$F_i^{n+1} = \frac{F_i^n}{\sum_j W_{ji}} \sum_j W_{ji} \frac{S_j}{\sum_k W_{jk} F_k^n} \quad \text{and applies a first close bins average every } n_{\text{smooth}}$$

iterations to smooth the solution. Tikhonov [7], which evaluates the non negative least squares minimum of $\min_{nls} \|WF - S + \alpha F\|$, where the minimization is performed over a χ^2 statistics which includes a smoothing operator. Singular Value Decomposition (SVD) [3], which employs a generalization of the matrix spectral decomposition for rectangular matrices $W = U \Sigma V^T$ to calculate a truncated pseudo inverse $W^{-1} = V \Sigma^{-1} U^T$, where Σ is a diagonal matrix. Varying degrees of smoothing is possible by varying the number of singular values taken into account to evaluate Σ .

THE TRANSFER MATRIX W

The transfer matrix (figure 1) has been estimated for the two LaBr₃(Ce) gamma-ray spectrometers installed at ASDEX Upgrade (AUG) and described in [1] and [5]. It can be factorized into $W(E_d, E_{RE}) = W_d(E_d, E_\gamma) * W_b(E_\gamma, E_{RE})$, where W_b describes the Bremsstrahlung generation of gamma rays inside the tokamak, W_d describes both the transport of photons to the detector and the Detector Response Function (DRF) and E_{RE}, E_γ, E_d are respectively the energy scale of REs, emitted gamma-ray and the detector. In this work W_b includes only the emission on the line of sight due to REs scattering on plasma ions and impurities, in particular Argon40 which is typically used for Massive Gas Injection (MGI). In the hypothesis of a radially collimated diagnostic and relativistic REs, it can be approximated at 0th order as:

$$W_b(E_\gamma, E_{RE}) \propto \frac{d\sigma_B}{dE_\gamma d\Omega}(E_\gamma, E_{RE}, \frac{\pi}{2}) \approx \frac{d\sigma_B}{dE_\gamma}(E_\gamma, E_{RE}, Z) \frac{1}{2\pi} p(E_{RE}, \frac{\pi}{2})$$

where Z is the atomic number of the ion under consideration, $\frac{\pi}{2}$ is the angle of emission and the Bremsstrahlung cross section σ_B has been factorized according to [4].

The contribution of Bremsstrahlung photons that experience Compton scattering on plasma ions before being detected has been neglected, since it gives a second order correction. Also

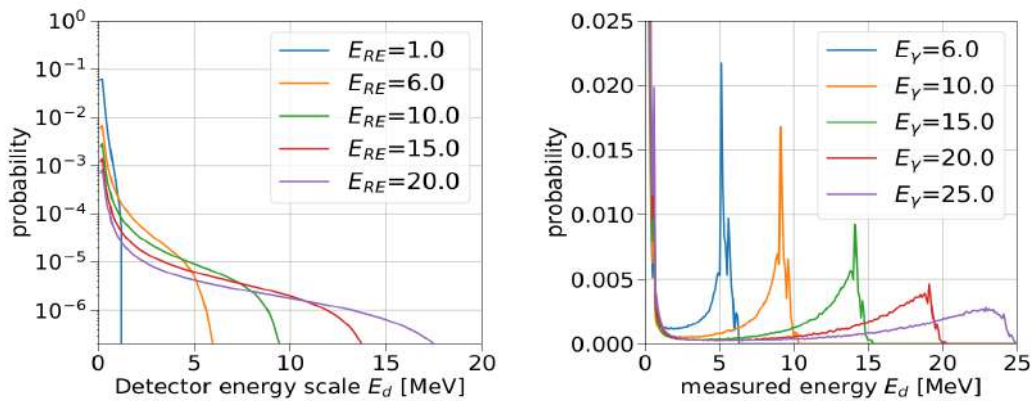


Figure 1: Left: $W(E_d, E_{RE})$ at different RE energies E_{RE} (given in MeV). Right: LaBr₃(Ce) detector response function at different gamma-ray energies E_γ (given in MeV) for [5]

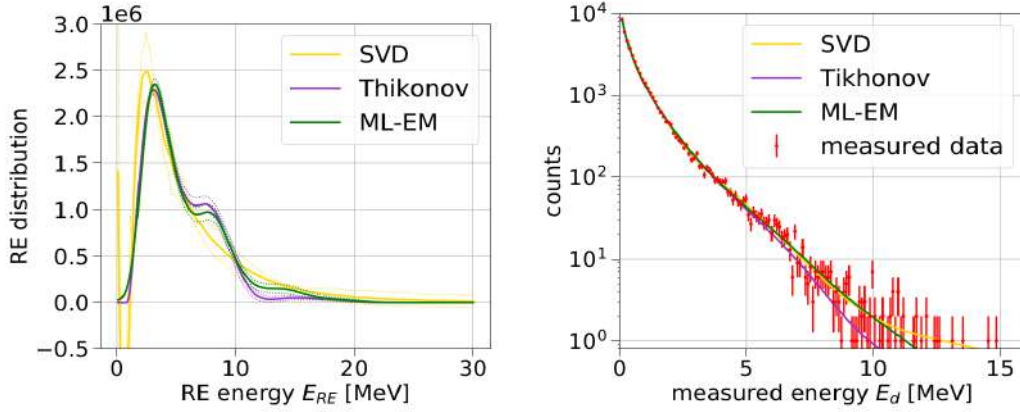


Figure 2: AUG shot #34084 Left: RE energy distribution reconstruction performed with three algorithms: SVD, Tikhonov and ML-EM. Right: agreement between the convolution of the reconstructed spectra with the transport matrix W and the experimental data.

Bremsstrahlung emission due to the impact of RE beam on the vessel is not included in W calculation, since it can be easily identified from sharp peaks in the measured counting rate graph and excluded from the analysis.

AN EXAMPLE OF DECONVOLUTION

AUG shot #34084 has been previously analysed using ML-EM only [5]. The same data have been analysed using the three deconvolution methods described above. The three solutions reasonably fit the experimental data, as shown in figure 2 (left picture) where the convolution

$W * F$ evaluated for the three methods is shown over S . ML-EM and Tikhonov reconstructions (figure 2 right picture) agree within statistical errors all over the whole dynamic range. Among the two, Tikhonov allows a stronger smoothing of the reconstructed distribution while keeping the residual low and so it might give better results when dealing with noisy data. On the other hand SVD roughly reproduce the same spectrum as the other two methods, but it also suffers severe artefacts in parts of the reconstruction while others are apparently reconstructed well. SVD is not constrained to be non-negative, so that a typical artefact is the negative count rate for low energies.

RECONSTRUCTION PARAMETERS

It is convenient to evaluate some parameters of the reconstructed spectrum both for data analysis and to compare reconstructions with first principle simulations. For example, the first few moments of the RE distribution are useful and the precision of their reconstruction has been studied using synthetic tests. I.e. RE spectra, generated with a known distribution (e.g. Gaussian or exponential), were convolved with the matrix W to create synthetic measured spectra, which were then deconvolved to find an estimate of the original RE spectrum. In all the tests conducted so far, the mean of the original distribution is correctly reconstructed with an error lower than 5%, while higher order moments appear to be less reliable. The cut-off

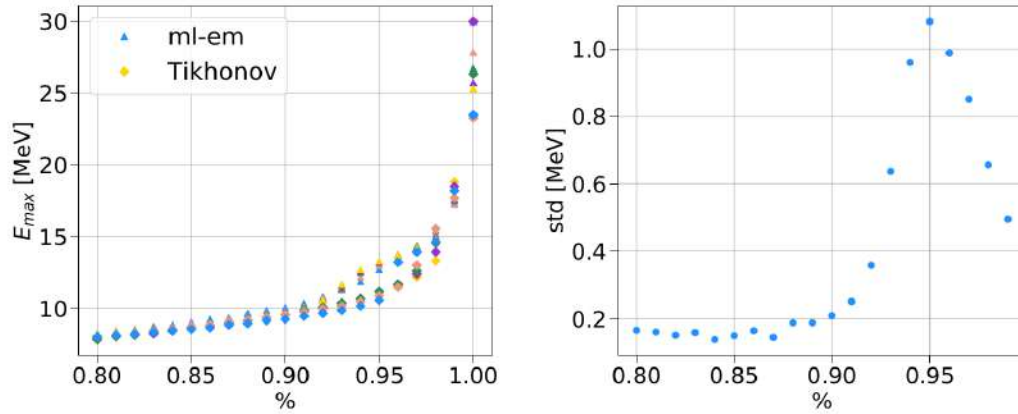


Figure 3: AUG shot #34084. Left: relations between the max RE energy (E_{max}) and the fraction of REs that have an energy less than E_{max} . Triangles and squares represent respectively ML-EM and Tikhonov reconstructions, different colors refer to different smoothing levels. Right: standard deviations of the graph on the left. energy of the spectrum is expected to be influenced by some plasma parameters (e.g. the current drop experienced during the disruption). It is evaluated as the energy at which the RE cumulative pdf is equal to X%. For AUG shot #34084 X was set to 90% (see figure 3): this value was chosen performing many reconstructions of the measured gamma-ray spectrum using different deconvolution parameters. The highest point in the cumulative pdf with low standard deviation was chosen as the ending energy and it is: $E_{0.9}=9.8$ MeV.

CONCLUSIONS

Three deconvolution methods have been implemented and tested on the reconstruction of runaway electron energy distribution using measurements of gamma ray spectra performed with a single detector. Their combined use allows the identification both of artefacts and reliable parameters of the deconvolved spectrum. W will be computed for other diagnostics, in particular the new gamma camera installed at JET [6] (figure 2), which will allow to perform 2D tomography (energy + spatial distribution) both of runaway electron and of fast ions. Reconstructed spectra will be compared with first principle simulations in order to improve the understanding of RE physics.

Acknowledgemnt


This work has been carried out within the framework of the EUROfusion Consortium and has received funding from the Euratom research and training programme 2014-2018 and 2019-2020 under grant agreement No 633053. The views and opinions expressed herein do not necessarily reflect those of the European Commission.

References

- [1] A. Dal Molin et al “Development of gamma-ray spectrometers optimized for runaway electrons bremsstrahlung emission in fusion devices”, these proceedings - [2] A.E. Shevelev et al 2013 Nucl. Fusion 53 123004 - [3] A S Jacobsen et al 2016 Plasma Phys. Control. Fusion 58 045016 - [4] M. Nocente et al 2017 Nucl. Fusion 57 076016 - [5] M. Nocente et al., Rev. Sci. Instrum. 89, 10I124 (2018) - [6] D. Rigamonti et al Rev. Sci. Instrum. 89, 10I116 (2018) - [7] Salewski et al. (2016) NF 56 106024

First spatially resolved measurements of the D-³He α -particle source with the upgraded JET gamma-ray camera

Cite as: Rev. Sci. Instrum. **92**, 053529 (2021); <https://doi.org/10.1063/5.0043776>
Submitted: 11 January 2021 . Accepted: 07 April 2021 . Published Online: 11 May 2021

 E. Panontin,  D. Rigamonti,  M. Nocente,  A. Dal Molin, A. Broslawski,  T. Craciunescu, G. Croci,  N. Cruz,  J. Figueiredo,  L. Giacomelli,  G. Gorini, M. Gosk, G. Kaveney, Ye. O. Kazakov,  V. Kiptily, S. Korolczuk, G. Marcer, A. Murari, E. Perelli Cippo,  M. Salewski, A. Urban,  I. Zychor, M. Tardocchi, and JET Contributors

COLLECTIONS

Paper published as part of the special topic on [Proceedings of the 23rd Topical Conference on High-Temperature Plasma Diagnostics](#)



View Online



Export Citation



CrossMark

ARTICLES YOU MAY BE INTERESTED IN

[Physics and applications of three-ion ICRF scenarios for fusion research](#)

Physics of Plasmas **28**, 020501 (2021); <https://doi.org/10.1063/5.0021818>

[A new tangential gamma-ray spectrometer for fast ion measurements in deuterium and deuterium-tritium plasmas of the Joint European Torus](#)

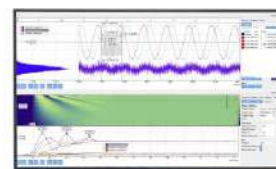
Review of Scientific Instruments **92**, 043537 (2021); <https://doi.org/10.1063/5.0043806>

[Fast-ion orbit sensitivity of neutron emission spectroscopy diagnostics](#)

Review of Scientific Instruments **92**, 043526 (2021); <https://doi.org/10.1063/5.0040696>

Challenge us.

What are your needs for periodic signal detection?



Zurich
Instruments

First spatially resolved measurements of the D-³He α -particle source with the upgraded JET gamma-ray camera

Cite as: Rev. Sci. Instrum. **92**, 053529 (2021); doi: 10.1063/5.0043776

Submitted: 11 January 2021 • Accepted: 7 April 2021 •

Published Online: 11 May 2021



E. Panontin,^{1,a)} D. Rigamonti,² M. Nocente,^{1,2} A. Dal Molin,¹ A. Broslawski,³ T. Craciunescu,⁴ G. Croci,^{1,2} N. Cruz,⁵ J. Figueiredo,^{5,6} L. Giacomelli,² G. Gorini,^{1,2} M. Gosk,³ G. Kaveney,⁷ Ye. O. Kazakov,⁸ V. Kiptily,⁷ S. Korolczuk,³ G. Marcer,¹ A. Murari,^{6,9} E. Perelli Cippo,² M. Salewski,¹⁰ A. Urban,³ I. Zychor,³ M. Tardocchi,² and JET Contributors^{b)}

AFFILIATIONS

¹Dipartimento di Fisica "G. Occhialini", Università degli Studi di Milano-Bicocca, 20126 Milano, Italy

²Istituto per la Scienza e Tecnologia dei Plasmi, Consiglio Nazionale delle Ricerche, 20126 Milano, Italy

³Narodowe Centrum Badań Jądrowych (NCBJ), 05-400 Otwock-Swierk, Poland

⁴National Institute for Laser, Plasma and Radiation Physics, 077125 Magurele-Bucharest, Romania

⁵Instituto de Plasmas e Fusão Nuclear, Instituto Superior Técnico, Universidade de Lisboa, 1049-001 Lisboa, Portugal

⁶EUROfusion Programme Management Unit, Culham Science Centre, OX14 3DB Abingdon, United Kingdom

⁷Culham Centre for Fusion Energy, OX14 3EB Culham, United Kingdom

⁸Laboratory for Plasma Physics LPP-ERM/KMS, 1000 Brussels, Belgium

⁹Consorzio RFX (CNR, ENEA, INFN, Università di Padova, Acciaierie Venete SpA), 35127 Padova, Italy

¹⁰Department of Physics, Technical University of Denmark, DK-2800 Kgs. Lyngby, Denmark

Note: This paper is published as part of the Special Topic on Proceedings of the 23rd Topical Conference on High-Temperature Plasma Diagnostics.

^{a)}Author to whom correspondence should be addressed: e.panontin@campus.unimib.it

^{b)}See the author list of E. Joffrin *et al.*, Nucl. Fusion **59**, 112021 (2019), <https://doi.org/10.1088/1741-4326/ab2276>.

ABSTRACT

The Joint European Torus (JET) gamma-ray camera has been recently upgraded with the installation of new gamma-ray detectors, based on LaBr₃(Ce) scintillation crystals, which add spectroscopic capability to the existing system allowing measurements with good energy resolution (5% at 0.622 MeV), a dynamic range from hundreds of keV up to about 30 MeV, and high counting rate capabilities of MCps. First gamma-ray measurements during the C38 campaign of the JET have been successfully carried out, in particular, in D-³He plasmas from three-ion ion cyclotron resonance heating experiments, where the detection of 16.4 MeV γ -rays from D+ ³He $\rightarrow \gamma + ^5\text{Li}$ reactions with the gamma-ray camera upgrade allowed determining the spatial profile of alpha particles born in D+ ³He fusion reactions.

Published under license by AIP Publishing. <https://doi.org/10.1063/5.0043776>

I. INTRODUCTION

The gamma-ray camera of the Joint European Torus (JET) is a system of 19 detectors that observes the plasma along 10 horizontal and 9 vertical lines of sight (LOS). It has been developed to measure the spatial profile of the gamma-ray emission from nuclear reactions induced by fast ions,^{1,2} which is of relevance in experiments that aim

at studying the physics of MeV range ions in the plasma, such as those obtained by the application of radio-frequency (RF) heating or born from fusion reactions.

In view of the upcoming JET deuterium-tritium (DT) campaign,³ the system has undergone a major upgrade,⁴⁻⁶ within the EUROfusion enhancement program by the Gamma-ray Camera Upgrade (GCU) project, to meet the demanding conditions for

measurements in plasmas at different tritium concentrations. The DT campaign will allow the study of the dynamics of fusion born alpha particles, which is also of interest for ITER;⁷ thus, the detection of the 4.44 MeV photons emitted in $\alpha(^9\text{Be}, n)^{12}\text{C}^*$ reactions under high neutron fluxes will be of crucial importance. This requires detectors with an energy resolution better than 5%@1.1 MeV, counting rate capability >500 kCps, and the capability to operate at magnetic fields of about 100 G. In the past few years, the new system, termed the Gamma Camera Upgrade (GCU), has been equipped with advanced detectors that meet the project requirements (see Ref. 4). This made it possible to use the GCU in recent JET campaigns with deuterium and hydrogen plasmas, before experiments with tritium.

In this paper, we present first results obtained with the GCU in deuterium plasmas at the JET. After a summary of the properties of the new detectors, we describe their energy calibration and the data acquisition (DAQ) system. From the pulse height spectrum measured along each channel of the GCU, we are able to identify spectral features ascribed to fast ion reactions and integrate data in the corresponding energy windows to experimentally determine the projection of the gamma-ray emission profile along the GCU lines of sight (LOS). This, combined with a tomographic inversion and information on the magnetic equilibrium, provides an image of the gamma-ray emission from fast ion reactions in the poloidal plane.^{8,9} We here present an example from recent Ion Cyclotron Resonance Heating (ICRH) experiments on the three-ion scenario,^{10–12} where RF waves are used to accelerate a deuterium beam in D–³He mixed plasmas and the GCU determines an image of the alpha particle source born from D+³He fusion reactions.

II. DATA ACQUISITION AND ENERGY CALIBRATION

The JET gamma-ray camera has been recently upgraded enabling gamma-ray measurements in both deuterium and deuterium–tritium plasmas with neutron yields up to a few 10^{17} n/s.¹³ Custom-made detectors based on LaBr₃ scintillator crystals and coupled to Silicon PhotoMultiplier (SiPM) matrices have been developed and installed in the camera:⁴ the new system exhibits an energy resolution better than 3% at 4.44 MeV and a counting rate capability in excess of 1 MCps. SiPMs are compact ($12 \times 12 \text{ mm}^2$ and 2 mm thick) and insensitive to the magnetic field. On the downside, they have a temperature-dependent gain and a non-linear response to the energy deposited in the crystal due to their finite number of pixels. A dedicated read-out board with a real time temperature feedback sensor has been installed as a gain-temperature correction

system, whereas the non-linearity has to be considered in the calibration process. The output signal of each detector is fed into a data acquisition (DAQ) system¹⁴ that can be operated in three different modes depending on the needs and the expected fluxes. The standard one, which was employed in the measurements described in Sec. IV, stores individual events/waveforms whose amplitude is higher than a preselected value. In experiments where a burst of events is expected in a very short time window of a few hundreds of ms, a continuous storing mode without data loss can be selected. The third mode, instead, takes advantage of a real-time algorithm implemented on the Field Programmable Gate Array (FPGA),¹⁵ which allows storing only the pulse height of the event and the time stamp when that occurred.

Dedicated *in situ* calibration measurements up to about 1.5 MeV are routinely performed at the JET by using the internal activity of ¹³⁸La and the standard ¹³⁷Cs, ¹³³Ba, and ²²Na radioactive sources embedded in the collimators of the cameras. More rarely, a ²⁴¹Am–Be neutron/gamma-ray source can be deployed for exploring higher energy regions up to 7.6 MeV. At these energies, the non-linear behavior of the Silicon PhotoMultiplier becomes significant and can be corrected for with a second-degree polynomial calibration (see Fig. 1). As shown in Fig. 1, the 4.44 MeV gamma-ray peak, due to the de-excitation of ¹²C* created from the ⁹Be(α, n)¹²C* reaction in ²⁴¹Am–Be source, is clearly visible in the spectrum together with its single and double escape peaks. At higher energies, the single and double escape peaks of the 7.631 MeV prompt gamma ray due to neutron capture in ⁵⁶Fe can also be observed. In the low energy region, instead, there are two prominent peaks in the spectrum, namely, the 511 keV peak and a gamma-ray peak around 844–847 keV from ²⁷Al neutron activation and/or ⁵⁵Mn activation, which are also used for calibration. Finally, the high energy end of the dynamic range can be calibrated by extrapolation of the fitted second-degree polynomial between 10 MeV and 20 MeV: such extrapolation is shown in Fig. 1 together with the 95% confidence band of the fit.

III. TOMOGRAPHIC RECONSTRUCTION

From the spectrum measured by each GCU detector, we can determine the number of events that fall in an arbitrary energy window. This is proportional to the line integrated emission in that energy band and is here termed the signal, S. As the GCU has 19 channels, S is a vector with 19 entries. When the poloidal plane is divided into 700 pixels (20 rows \times 35 columns), the relation between S and the intensity of the gamma-ray emission in the poloidal plane, F, is

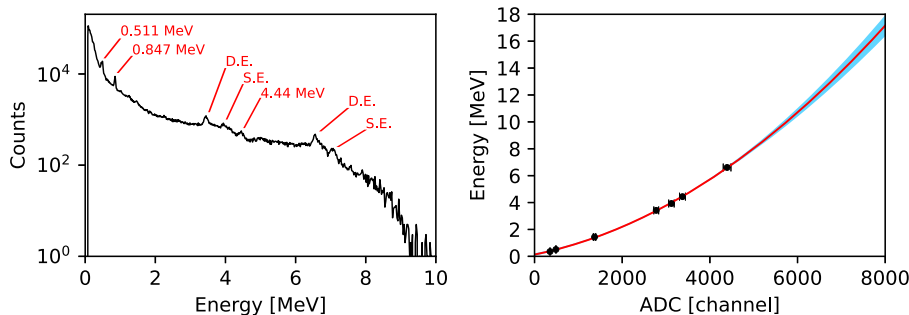


FIG. 1. (Left) Energy spectrum recorded with the GCU using an Am–Be radioactive source. S.E. and D.E. are the single and double escape peaks due to (from left to right) the 4.44 MeV peak and the prompt photons emitted at 7.63 MeV during the neutron capture on ⁵⁶Fe. (Right) Quadratic calibration curve for the detectors of the GCU as obtained from the calibration sources at the JET. The fit 95% confidence band is shown in light-blue.

$$\underline{S} = \underline{W} \cdot \underline{F},$$

where W is a 19×700 (rows \times columns) transfer matrix. Its i -th- j -th element gives the probability that a photon born within the i -th pixel in the poloidal plane is detected along the j -th channel of the GCU. One aim of the GCU is to determine F from S , which is obtained through a tomographic inversion.^{8,9}

Based on previous experience with the gamma-ray camera at the JET,^{16,17} we use the Maximum Likelihood-Expectation Maximization (ML-EM)¹⁸ method to perform the tomographic inversion. In this method, F is obtained by the iterative formula as follows:

$$F_i^{n+1} = \frac{F_i^n}{\sum_l W_{li}} \sum_j \frac{W_{ji} S_j}{\sum_k W_{jk} F_k^n}, \quad (1)$$

where the superscript n indicates the step of the iteration. As the initial step, we assume a uniform emission profile, i.e., $F_i^0 = 1$. The reconstruction is interrupted when the correlation between two subsequent iteration steps approaches unity, as in Eq. (5) of Ref. 16.

The transfer matrix W has been evaluated using an *ad hoc* script, which considers the three-dimensional geometry of the gamma-camera lines of sight (LOS). Additional information needs, however, to be considered for a satisfactory tomographic reconstruction. In our work, we follow the approach of Ref. 16. As W is sparse, due to the limited amount of lines of sight for the GCU, 17 additional, virtual LOS are generated between adjacent real LOS using sp-lines for interpolation of the measured data. Information on the magnetic equilibrium is further embedded by means of a smoothing operator. This performs a moving window average of the signal from nearby pixels that span 1/10 of each magnetic flux surface. Smoothing is applied every n_{smooth} iteration. In our reconstruction, $n_{smooth} = 1$ or 2, typically.

IV. APPLICATION AT THE JET

As an example of the capabilities of the GCU, we here present data for JET discharge no. 95689 in the time window $t = 47.5$ – 52.5 s. The discharge belongs to a series of experiments on the “three ion”

Ion Cyclotron Resonance Frequency (ICRF) scenarios,^{10–12} where radio-frequency (RF) waves are used to accelerate a beam of deuterium ions up to energies in the MeV range and in a plasma made of deuterium and ^3He , with relative concentrations of 50% and 25%, respectively. The aim of the experiments was to tailor the $\text{D}+^3\text{He}$ reaction rate by accelerating deuterium at different energies, which is in turn obtained by changes in the ratio between the neutral beam injection (NBI) and ICRH powers.¹⁰ The main reaction channel of $\text{D}+^3\text{He}$ is the production of alpha particles and protons, i.e., $\text{D}+^3\text{He} \rightarrow \alpha + p$. However, there is also a weaker ($\approx 10^5$ relative probability¹⁹) electromagnetic channel of this reaction, $\text{D}+^3\text{He} \rightarrow \gamma + ^5\text{Li}$, which leads to the generation of 16.4 MeV gamma rays and is of interest for the quantification of the fusion power from the $\text{D}+^3\text{He}$.

Figure 2 shows the gamma-ray spectrum measured by channel 1 (observing the core) and 15 (observing the periphery) of the GCU in discharge no. 95689 and in the time window $t = 47.5$ – 52.5 s on a logarithmic scale. Two spectral regions can be clearly distinguished, depending on whether $E_\gamma < 10$ MeV or $E_\gamma > 10$ MeV. The $E_\gamma < 10$ MeV region has a similar shape between the two channels and is dominated by the response function of the $\text{LaBr}_3(\text{Ce})$ scintillator to neutron background.^{20,21} In particular, the neutron induced background due to fusion born 14 MeV neutrons has been characterized in Ref. 21 and extends up to approximately 10 MeV. An experimental estimate of such a background for channels 1 and 15 is shown by the red triangles in Fig. 2.

The $E_\gamma > 10$ MeV region is significantly different between the two channels. There are almost no events for the peripheral channel 1, while there is a clear structure for channel 15 that exceeds the neutron background. From comparison with the spectrum measured by the tangential LaBr_3 spectrometers (see Ref. 22), we find that this structure is due to the 16.4 MeV gamma rays. We also note that the end point energy of the $\text{D}+^3\text{He}$ gamma-ray emission in Fig. 2 is 10% lower than expected, while the 95% confidence band of the calibration, shown in Fig. 1, accounts only for a 5% discrepancy. This suggests that the quadratic polynomial used for calibration under-corrects the non-linearity of SiPMs in this energy region.

The shape of the structure in Fig. 2 is predominantly determined by the dominant Compton interactions of 16.4 MeV gamma

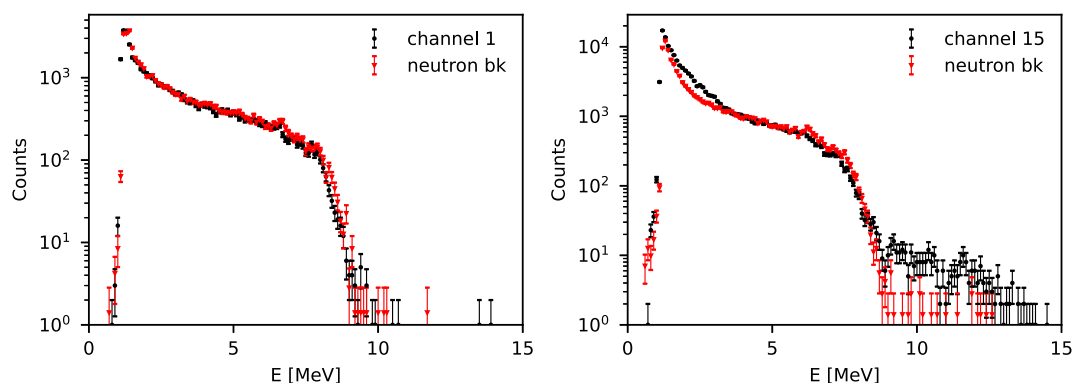


FIG. 2. Gamma-ray spectrum measured by channel 1 (left) and channel 15 (right) of the gamma-camera in the time interval $t = 47.5$ – 52.5 s of JET pulse no. 95689. For each channel, the neutron induced background is shown by red triangles.

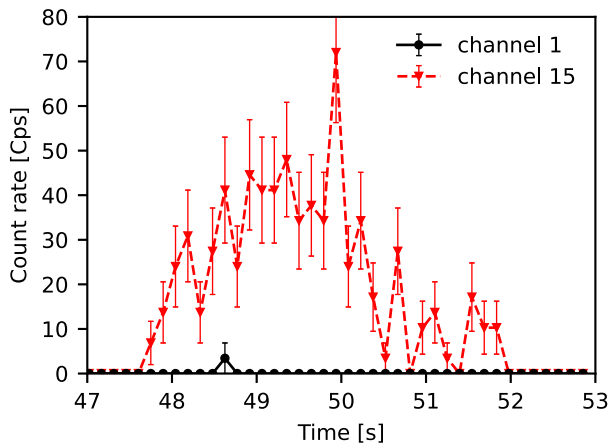


FIG. 3. Counting rate in the energy window $E_\gamma > 10$ MeV measured by channels 1 and 15 of the GCU during JET discharge no. 95689.

rays with the detector,²³ combined with the natural broadening of the emission due to the ≈ 1.5 MeV mass broadening of the unstable ${}^5\text{Li}$ nucleus.²⁴ The average counting rate in the energy band $E_\gamma > 10$ MeV is about 30 Hz for channel 15, while this is almost null for channel 1 as shown in Fig. 3.

From the energy spectrum measured at each channel of the GCU, we can integrate data in the region $E_\gamma > 10$ MeV to obtain the experimental gamma-ray profile of 16.4 MeV gamma rays from the $\text{D}+{}^3\text{He} \rightarrow \gamma+{}^5\text{Li}$ reaction¹⁹ shown in Fig. 4. After tomographic inversion of these data (see Sec. III), we finally obtain the spatial map of the 16.4 MeV gamma-ray emission, shown in Fig. 5. As 16.4 MeV gamma rays are born from the fusion reaction of D and ${}^3\text{He}$, which also leads to alpha particle production at an $\approx 10^5$ more abundant rate, the map of Fig. 5 is also an image of the alpha particle source in

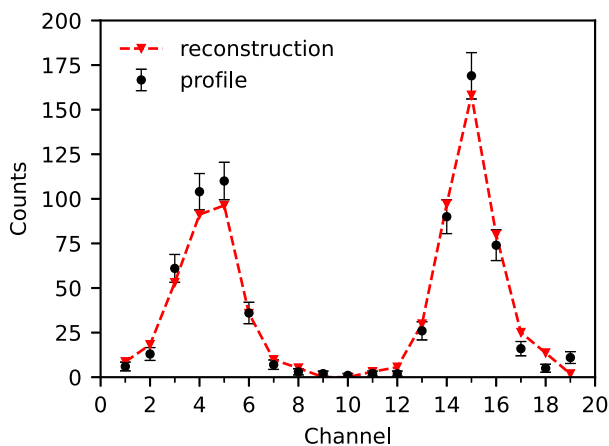


FIG. 4. Gamma-ray profile measured by the GCU for discharge no. 95689 and obtained by integrating data in the energy band $E_\gamma > 10$ MeV for each channel and in the time window $t = 47.5\text{--}51.5$ s (circular marker); reconstruction of the measured profile obtained convolving the emissivity distribution shown in Fig. 5 with the probability matrix \underline{W} (dashed line).

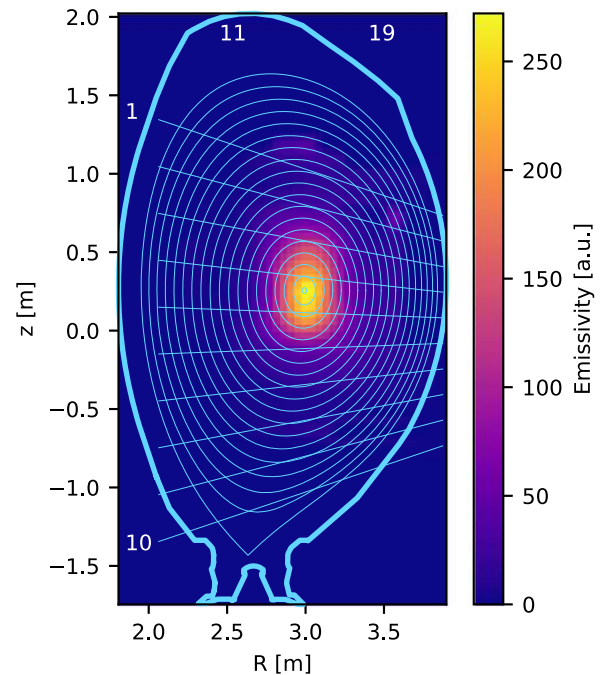


FIG. 5. Spatial profile of the $E_\gamma = 16.4$ MeV emission from the $\text{D}+{}^3\text{He} \rightarrow \gamma+{}^5\text{Li}$ reaction in the poloidal plane obtained by a tomographic inversion of the data shown in Fig. 4. GCU channel numbering is shown in white.

the experiment. We note that, as expected from theory, alpha particle production occurs in an ≈ 40 cm narrow region around the magnetic axis, which is found at $R \approx 3$ m and $z \approx 30$ cm in this discharge. This is also the volume where most of the ICRH power is absorbed by the NBI deuterons according to RF simulations.¹⁰ Finally, Fig. 4 shows good agreement between the experimental gamma-ray profile and its reconstruction, which has been obtained by multiplying the weight matrix \underline{W} with the spatial profile data of Fig. 5. The corresponding p-value of the Pearson χ^2 test is 0.55.

V. CONCLUSIONS

The gamma-ray camera upgrade (GCU) has been used in the most recent JET deuterium and hydrogen experimental campaigns. Benefiting from new gamma-ray detectors, which add spectroscopic and MHz counting rate capabilities to the previously existing system, the pulse height spectrum due to gamma-ray emission from fast ion reactions in the plasma was successfully collected for each channel of the system. An Am-Be radioactive source was used for the energy calibration and, in particular, to correct for the detector non-linearity at energies of a few MeV. The application of the system to recent ion cyclotron resonance heating experiments on the three-ion scenario in $\text{D}-{}^3\text{He}$ plasmas allowed determining an image of the alpha particle source born from $\text{D}+{}^3\text{He}$ fusion reactions in these experiments, after a tomographic inversion. The analysis of the recorded spectra shows that the extrapolation of the GCU calibration above 10 MeV underestimates the energy of the $\text{D}+{}^3\text{He} \rightarrow \gamma+{}^5\text{Li}$ 16.4 MeV peak by approximately 10%. During recent experiments, lines from ${}^3\text{He} + {}^9\text{Be}$ reactions, which extend up to about 9 MeV,

have been observed and might be used to improve the instrument calibration. However, the current calibration is robust in the energy region around 4.4 MeV, which is of interest for the study of α -particles in the upcoming DT campaign.

AUTHORS' CONTRIBUTIONS

D.R. and E.P. contributed equally to this work, and as such, they must both be considered as first authors.

ACKNOWLEDGMENTS

This work was carried out within the framework of the EURO-fusion Consortium and received funding from the Euratom research and training program 2014–2018 and 2019–2020 under Grant Agreement No. 633053. The views and opinions expressed herein do not necessarily reflect those of the European Commission.

This scientific work was also supported by the Polish Ministry of Science and Higher Education within the framework of the scientific financial resources in the years 2015–2020 allocated for the realization of the international co-financed project.

DATA AVAILABILITY

The data that support the findings of this study are available from the corresponding author upon reasonable request.

REFERENCES

- ¹M. Nocente, A. D. Molin, N. Eidielis, L. Giacomelli, G. Gorini, Y. Kazakov, E. Khilkevitch, V. Kiptily, M. Iliasova, A. Lvovskiy *et al.*, *Plasma Phys. Controlled Fusion* **62**, 014015 (2019).
- ²V. G. Kiptily, F. E. Cecil, and S. S. Medley, *Plasma Phys. Controlled Fusion* **48**, R59 (2006).
- ³E. Joffrin, S. Abduallev, M. Abhangi, P. Abreu, V. Afanasev, M. Afzal, K. Aggarwal, T. Ahlgren, L. Aho-Mantila, N. Aiba *et al.*, *Nucl. Fusion* **59**, 112021 (2019).
- ⁴D. Rigamonti, A. Broslawski, A. Fernandes, J. Figueiredo, L. Giacomelli, G. Gorini, M. Gosk, G. Kaveney, V. Kiptily, S. Korolczuk *et al.*, *Rev. Sci. Instrum.* **89**, 10I116 (2018).
- ⁵D. Rigamonti, A. Muraro, M. Nocente, V. Perseo, G. Boltruczuk, A. Fernandes, J. Figueiredo, L. Giacomelli, G. Gorini, M. Gosk *et al.*, *Rev. Sci. Instrum.* **87**, 11E717 (2016).
- ⁶M. Nocente, D. Rigamonti, V. Perseo, M. Tardocchi, G. Boltruczuk, A. Broslawski, A. Cremona, G. Croci, M. Gosk, V. Kiptily *et al.*, *Rev. Sci. Instrum.* **87**, 11E714 (2016).
- ⁷M. Salewski, M. Nocente, B. Madsen, I. Abramovic, M. Fitzgerald, G. Gorini, P. C. Hansen, W. W. Heidbrink, A. S. Jacobsen, T. Jensen *et al.*, *Nucl. Fusion* **58**, 096019 (2018).
- ⁸V. G. Kiptily, J. M. Adams, L. Bertalot, A. Murari, S. E. Sharapov, V. Yavorskij, B. Alper, R. Barnsley, P. de Vries, C. Gowers *et al.*, *Nucl. Fusion* **45**, L21 (2005).
- ⁹J. Bielecki, L. Giacomelli, V. Kiptily, M. Scholz, K. Drozdowicz, S. Conroy, T. Craciunescu, and M. Kempnaars, *Rev. Sci. Instrum.* **86**, 093505 (2015).
- ¹⁰M. Nocente, Ye. O. Kazakov, J. Garcia, V. G. Kiptily, J. Ongena, M. Dreval, M. Fitzgerald, S. E. Sharapov, Z. Stancar, H. Weisen *et al.*, *Nucl. Fusion* **60**, 124006 (2020).
- ¹¹Ye. O. Kazakov, J. Ongena, J. C. Wright, S. J. Wukitch, E. Lerche, M. J. Mantsinen, D. V. Eester, T. Craciunescu, V. G. Kiptily, Y. Lin *et al.*, *Nat. Phys.* **13**, 973–978 (2017).
- ¹²Ye. O. Kazakov, D. Van Eester, R. Dumont, and J. Ongena, *Nucl. Fusion* **55**, 032001 (2015).
- ¹³D. Rigamonti, M. Nocente, L. Giacomelli, M. Tardocchi, M. Angelone, A. Broslawski, C. Cazzaniga, J. Figueiredo, G. Gorini, V. Kiptily *et al.*, *J. Instrum.* **12**, C10007 (2017).
- ¹⁴R. C. Pereira, A. M. Fernandes, A. Neto, J. Sousa, C. A. F. Varandas, J. Cardoso, C. M. B. A. Correia, M. Tardocchi, M. Nocente, G. Gorini *et al.*, *IEEE Trans. Nucl. Sci.* **58**, 1531 (2011).
- ¹⁵A. Fernandes, R. C. Pereira, B. Santos, J. Bielecki, G. Boltruczuk, A. Broslawski, P. F. Carvalho, R. Dias, J. Figueiredo, L. Giacomelli *et al.*, *Fusion Eng. Des.* **128**, 188 (2018).
- ¹⁶T. Craciunescu, G. Bonheure, V. Kiptily, A. Murari, S. Soare, I. Tiseanu, and V. Zoita, *Nucl. Instrum. Methods Phys. Res.* **595**, 623 (2008).
- ¹⁷T. Craciunescu, G. Bonheure, V. Kiptily, A. Murari, I. Tiseanu, and V. Zoita, *Nucl. Instrum. Methods Phys. Res.* **605**, 374 (2009).
- ¹⁸L. B. Lucy, *Astro. J.* **79**, 745 (1974).
- ¹⁹F. E. Cecil *et al.*, *Phys. Rev. C* **32**, 690 (1985).
- ²⁰C. Cazzaniga, M. Nocente, M. Tardocchi, G. Croci, L. Giacomelli, M. Angelone, M. Pillon, S. Villari, A. Weller, L. Petrizzi *et al.*, *Rev. Sci. Instrum.* **84**, 123505 (2013).
- ²¹C. Cazzaniga, M. Nocente, M. Tardocchi, M. Rebai, M. Pillon, F. Camera, A. Giaz, L. Pellegrini, and G. Gorini, *Nucl. Instrum. Methods Phys. Res., Sect. A* **778**, 20 (2015).
- ²²M. Nocente, T. Craciunescu, G. Gorini, V. Kiptily, M. Tardocchi, V. Braic, M. Curuia, A. Dal Molin, J. Figueiredo, L. Giacomelli *et al.*, *Rev. Sci. Instrum.* **92**, 4 (2021), these proceedings.
- ²³M. Nocente, M. Tardocchi, R. Barnsley, L. Bertalot, B. Brichard, G. Croci, G. Brolatti, L. Di Pace, A. Fernandes, L. Giacomelli *et al.*, *Nucl. Fusion* **57**, 076016 (2017).
- ²⁴M. Nocente, J. Källne, M. Salewski, M. Tardocchi, and G. Gorini, *Nucl. Fusion* **55**, 123009 (2015).

γ -ray emission from radio frequency heating experiments with the three-ion schemes at the Joint European Torus

E. Panontin¹, D. Rigamonti², M. Nocente^{1,2}, T. Craciunescu³, N. Cruz^{4,5}, A. Dal Molin², L. Giacomelli², G. Gorini^{1,2}, M. Iliasova⁶, Ye. Kazakov⁷, E. Khilkevitch⁶, V. Kiptily⁸, E. Perelli Cippo^{1,2}, B. Santos⁴, A. Shevelev⁶, M. Tardocchi^{1,2}, I. Zychor⁹ and JET Contributors*

¹*Università degli Studi di Milano Bicocca, Milan, Italy*

²*Istituto per la Scienza e Tecnologia dei Plasmi, Milan, Italy*

³*Institute of Atomic Physics, Magurele-Bucharest, Romania*

⁴*Instituto de Plasmas e Fusão Nuclear, Universidade de Lisboa, Lisboa, Portugal*

⁵*Consorzio RFX, Padova, Italy*

⁶*Ioffe Institute, St. Petersburg, Russia*

⁷*Laboratory for Plasma Physics LPP-ERM/KMS, Brussels, Belgium*

⁸*Culham Centre for Fusion Energy, Abingdon, United Kingdom*

⁹*Narodowe Centrum Badań Jądrowych (NCBJ), Otwock-Swierk, Poland*

**See the author list of "Overview of JET results for optimising ITER operation" by J. Mailloux et al. to be published in Nuclear Fusion Special issue: Overview and Summary Papers from the 28th Fusion Energy Conference (Nice, France, 10-15 May 2021)*

INTRODUCTION

In so called ‘three-ion’ Ion Cyclotron Resonance Heating (ICRH) experiments a third, minority species is efficiently accelerated in plasmas made by two main ions. This is achieved in the vicinity of the ion-ion hybrid layer, where the wave polarization is entirely left handed [1]. At the Joint European Torus (JET) the scheme has so far been demonstrated in H-(D_{NBI})-D, H-(³He)-D and D-(D_{NBI})-³He plasmas [2], (D_{NBI}) and (³He) being the minority species.

In the latter scheme, fast deuterons injected by Neutral Beam Injection (NBI) are further accelerated by ICRH up to energies in the MeV range [3]. High D+D neutron rates (between 10¹⁵ and 10¹⁶ s⁻¹) have been achieved at moderate external heating power [4]. Reversed Shear Alfvén Eigenmodes (RSAEs) have also been systematically observed, which is indicative of a non monotonic q-profile induced by a non-inductive current driven by an intrinsic mechanism [4].

GAMMA-RAY EMISSION

JET is equipped with 4 γ -ray spectrometers, arranged on 2 vertical and 1 tangential lines-of-sight [5], and the Gamma-Camera Upgrade (GCU) [6], composed by two arrays of 10 and

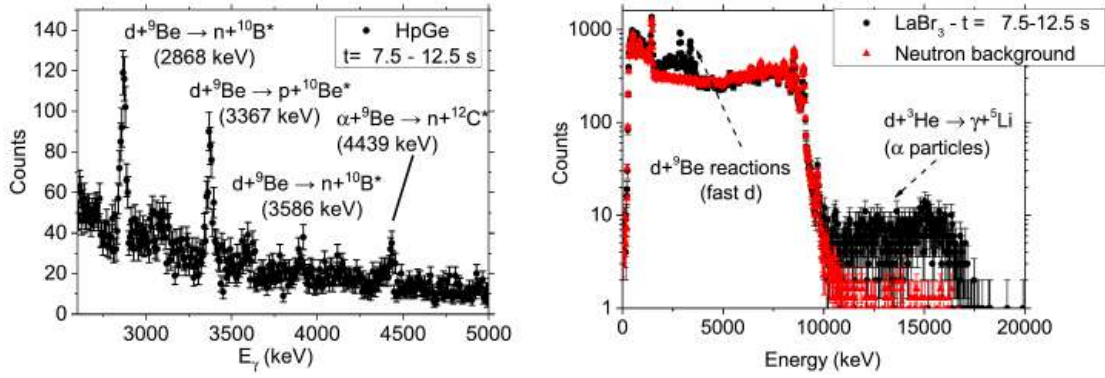


Figure 1: γ -ray spectra recorded during JET shot #95679, in time interval 7.5-12.5 s, by (left) the high-purity Germanium spectrometer (KN6G), which has a vertical line-of-sight, and (right) the new tangential LaBr₃(Ce) spectrometer (KM6T). The neutron background of KM6T (red triangles) has been calculated summing spectra recorded during the NBI only phase of all shots allocated for the D-(D_{NBI})-³He experiment.

9 lines-of-sight that observe the plasma on the poloidal plane. These diagnostics allow us to investigate the nuclear processes that take place in the plasma during a discharge (e.g. JET shot #95679).

When only NBI heating is applied, all the spectrometers measure a signal induced by fusion born neutrons (red triangles in figures 1 and 2). When also ICRH is turned on, i.e. between 7.5 and 12.5 s, γ -ray signals are detected over the neutron background. In particular the D+⁹Be emission (fig. 1) between 2 and 5 MeV confirms the acceleration of D_{NBI} up to energies in

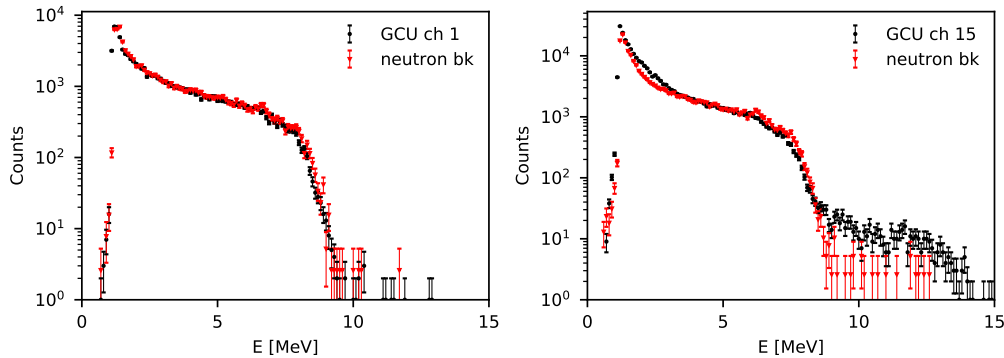


Figure 2: γ -ray spectra recorded during JET shot #95679, in time interval 7.5-12.5 s, by (left) channel 1, whose line-of-sight observes the upper part of the poloidal plane, and (right) channel 15, whose line-of-sight observes the magnetic axis vertically, of the Gamma-Camera Upgrade. See figure 3 for a sketch of the GCU lines-of-sight. The neutron-induced background for each channel (red triangles) has been calculated as in figure 1.

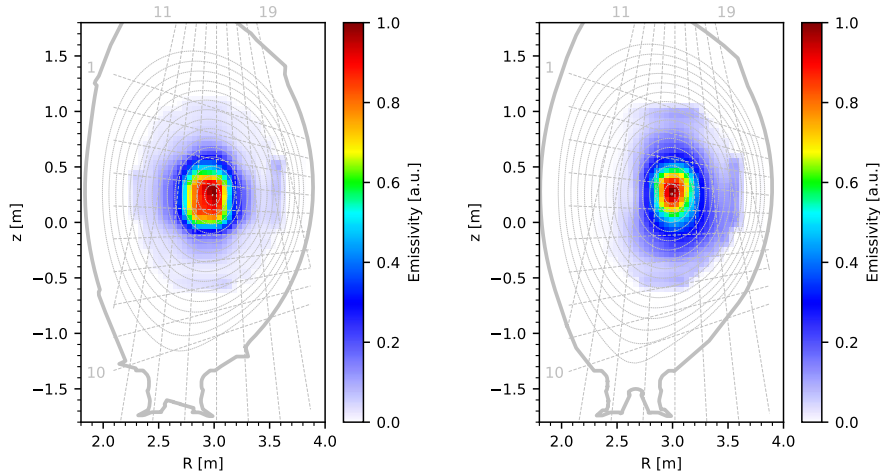


Figure 3: *Spatial profiles of the source of (right) α -particles born in $D+{}^3\text{He}$ fusion reactions (left) neutrons born in $D+D$ fusion reactions (the latter can be compared with figure 1 in [4] for a benchmark of the tomography code here presented). Both reconstructions have been performed during time interval 8.-12. s of JET shot #95679. GCU lines-of-sight and their numbering are shown in grey.*

excess of 0.5 MeV [4]. The simultaneous detection of the 16.4 MeV gamma-rays produced in a minor branch of the $D+{}^3\text{He}$ reaction [4, 6] and the 4.4 MeV gamma-rays emitted in $\alpha+{}^9\text{Be}$, proves the generation of fusion born alpha particles.

Figure 2 shows the spectra recorded by the peripheral ch 1 and the central ch 15 of the GCU. The camera was able to detect the $D+{}^3\text{He}$ 16.4 MeV gamma-rays as well, giving us spatial information about the distribution of this emission, which can be used to perform a tomographic reconstruction of the source of the α -particles born in the $D+{}^3\text{He}$ fusion reactions.

NEUTRONS AND α -PARTICLES SOURCES

Figure 3 shows the tomographic reconstruction of the neutron profile measured by the neutron-camera and the 16.4 MeV gamma-ray profile derived from the spectra shown in figure 2 [7, 8].

The two reconstructions, which were independently performed, show respectively the D-D neutron and α -particles sources, proving that the ICRF energy deposition happened in a narrow region of ≈ 20 cm around the magnetic axis, as expected.

The two plots also represent the spatial distribution of the reaction site for $D+D$ and $D+{}^3\text{He}$, which take place between a fast D and a thermal ion. We can reasonably suppose that the distribution of thermal D and ${}^3\text{He}$ are similar, thus we can check that the two tomographies are consistent with one another. In fact the two slightly differ in the region spanned by ch 6 and 14, where the experimental data were corrupted and the profile was interpolated from the closest channels.

SYNTHETIC ANALYSIS

The line shape of the emission spectrum can be modelled with GENESIS code. In figure 4 the sum of KN6G measurement of 2.87 MeV γ -rays in JET discharges #95677, #95679, #95680 and #95683 is compared with two synthetic diagnostics generated assuming the energy distribution of fast deuterons as simulated by TRANSP and two pitch-angle distribution centered at $\lambda \approx 0$ and $\lambda \approx 0.4$ [4]. It confirms that, differently from traditional ICRF scheme, the D-(D_{NBI})-³He three-ion ICRF heating scenario generates co-passing fast D ions with $\lambda \approx 0.3 - 0.5$. This particles are candidates for driving the non-inductive current that induces the non monotonic q-profile. This suggests the necessity to study in more detail the relationship between fast deuterons and the excitation of RSAEs.

CONCLUSIONS

The acceleration of D_{NBI} to energies in the MeV-range and the generation of fusion born α -particles from D+³He has been confirmed by the spectral analysis of the plasma γ -ray emission. The spatial distribution of D+³He born α -particles source has been reconstructed using the profile of the 16.4 MeV emission measured by the GCU. This distribution is in good agreement with the tomography of the neutron-camera profile. Synthetic modelling of the 2.87 MeV emission has been carried out and the results confirms the generation of co-passing deuterium ions, which are candidates to drive non-inductive current. Further studies on this topic will be conducted in the future.

References

- [1] Kazakov Ye. O. et al., Nature Physics 13 (2017) 973
- [2] Ye.O. Kazakov et al 2020 Nucl. Fusion 60 112013
- [3] M. Nocente et al., Proc. 45Th EPS Conf. On Plasma Physics, O5.103 (2018)
- [4] M. Nocente et al., Nuclear Fusion 60, 124006 (2020)
- [5] M. Nocente et al., Rev. Sci. Instrum. 92, 043537 (2021)
- [6] D. Rigamonti et al., Review of Scientific Instruments 89, 10I116 (2018)
- [7] E. Panontin et al., Review of Scientific Instruments 92, 053529 (2021)
- [8] T. Craciunescu et al. Nucl. Instrum. Methods Phys. Res 595, 623 (2008)

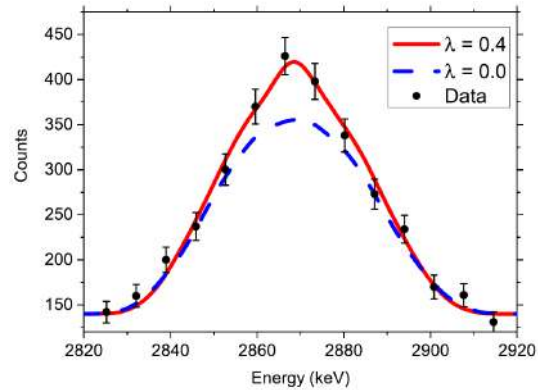


Figure 4: (black points) Sum over JET shots #95677, #95679, #95680 and #95683 of the measured emission of $E_\gamma = 2.87$ MeV peak emitted by $D+^9\text{Be}$ reactions. Line shape computed with GENESIS using deuterons energy distribution calculated with TRANSP and setting pitch-angle to $\lambda \approx 0$ (blue dashed line) and $\lambda \approx 0.4$ (red solid line).

4TH EUROPEAN CONFERENCE ON PLASMA DIAGNOSTICS (ECPD2021)
7–11 JUNE, 2021
ONLINE

Comparison of unfolding methods for the inference of runaway electron energy distribution from γ -ray spectroscopic measurements

E. Panontin,^{a,*} A. Dal Molin,^b M. Nocente,^{a,b} G. Croci,^{a,b} J. Eriksson,^c L. Giacomelli,^b G. Gorini,^{a,b} M. Iliasova,^d E. Khilkevitch,^d A. Muraro,^b D. Rigamonti,^b M. Salewski,^e J. Scionti,^b A. Shevelev,^d M. Tardocchi,^{a,b} the Eurofusion MST1 Team¹ and the ASDEX Upgrade Team²

^aDipartimento di Fisica “G. Occhialini”, Università degli Studi di Milano-Bicocca, piazza della Scienza 3, 20126 Milano, Italy

^bIstituto per la Scienza e Tecnologia dei Plasmi, Consiglio Nazionale delle Ricerche, via R. Cozzi 53, 20126 Milano, Italy

^cDepartment of Physics and Astronomy, Uppsala University, Regementsvagen 1, SE-752 37 Uppsala, Sweden

^dIoffe Institute, 26 Politekhnikeskaya, St Petersburg 194021, Russian Federation

^eDepartment of Physics, Technical University of Denmark, Fysikvej 311, DK-2800 Kgs. Lyngby, Denmark

E-mail: e.panontin@campus.unimib.it

ABSTRACT: Unfolding techniques are employed to reconstruct the 1D energy distribution of runaway electrons from Bremsstrahlung hard X-ray spectrum emitted during plasma disruptions in tokamaks. Here we compare four inversion methods: truncated singular value decomposition, which is a linear algebra technique, maximum likelihood expectation maximization, which is an iterative method, and Tikhonov regularization applied to χ^2 and Poisson statistics, which are two minimization approaches. The reconstruction fidelity and the capability of estimating cumulative statistics, such as the mean and maximum energy, have been assessed on both synthetic and experimental spectra. The effect of measurements limitations, such as the low energy cut and

*Corresponding author.

¹See author list of B. Labit et al., *Dependence on plasma shape and plasma fueling for small edge-localized mode regimes in TCX and ASDEX Upgrade*, *Nucl. Fusion* **59** (2019) 086020.

²See author list of H. Meyer et al., *Overview of physics studies on ASDEX Upgrade*, *Nucl. Fusion* **59** (2019) 112014.

few number of counts, on the final reconstruction has also been studied. We find that the iterative method performs best as it better describes the statistics of the experimental data and is more robust to noise in the recorded spectrum.

KEYWORDS: Nuclear instruments and methods for hot plasma diagnostics; Plasma diagnostics - interferometry, spectroscopy and imaging; Analysis and statistical methods; Plasma diagnostics - charged-particle spectroscopy

Contents

1	Introduction	1
2	Analysis techniques	1
3	Synthetic tests	2
4	Application to AUG data	3
5	Conclusions	5

1 Introduction

In recent years, the development of a new generation of hard-X ray (HXR) spectrometers, based on LaBr₃ inorganic scintillators with counting rates capabilities up to 1 MCps and energy resolution of $\lesssim 5\%$ @ 661 keV [1, 2], allowed to measure the Bremsstrahlung radiation emitted from the interaction between runaway electrons (REs) and background ions during plasma disruptions in tokamaks [3]. From this HXR spectrum, the 1D energy distribution of the beam can be reconstructed using suitable unfolding techniques [4, 5], unveiling precious information for the study of REs dynamics and the design of avoidance or mitigation strategies for ITER. In addition to being computationally less expensive, measured 1D energy distribution functions can challenge computations from first principles to improve our understanding of REs.

The performance of unfolding techniques strongly depends on the process under analysis, thus the comparison of different deconvolution methods on synthetic distributions can help assessing the capability and limits of the unfolding procedure. In this work we present a comparison of four unfolding techniques, which are presented in section 2 and then applied to synthetic signals (section 3) as well as to experimental data collected with the 1'' \times 1'' cylindrical LaBr₃ scintillator installed in the Bragg Bunker at ASDEX Upgrade (AUG) (section 4).

2 Analysis techniques

The HXR spectrum \underline{S} and the RE energy distribution \underline{F} follow the convolution equation: $\underline{S} = \underline{W} \cdot \underline{F}$, which is the same method as applied in energetic ion distribution functions [6]. Here the matrix \underline{W} describes the Bremsstrahlung emission probability, which was calculated using the GENESIS code [7], and the interaction of a photon with a LaBr₃ scintillator, which was simulated using the MCNP code [8]. Figure 1 shows a sketch of \underline{W} 's columns, which represent the spectra emitted by a ideally mono-energetic RE beam, and rows, which are also called weight functions [19, 20] and describe the diagnostic sensitivity to different regions in the RE energy spectrum. In this section we present four unfolding techniques, whose performances on the problem at hand will be compared in sections 3 and 4.

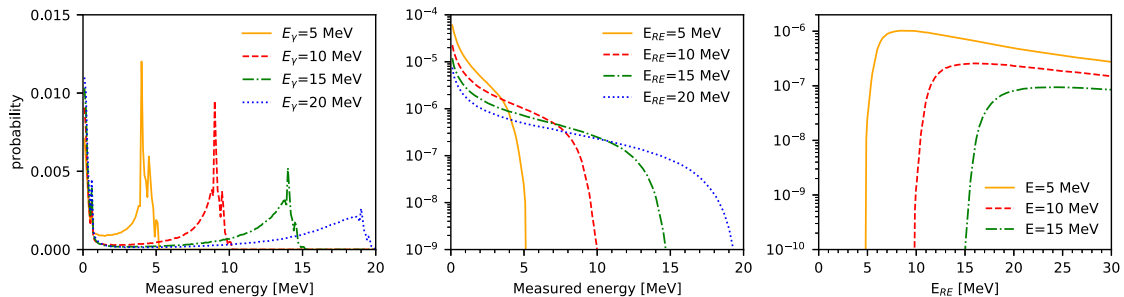


Figure 1. (Left) MCNP simulation of the DRF of the LaBr₃ scintillator installed at AUG in the Bragg Bunker. Transfer matrix $\underline{\underline{W}}$ columns (centre) and rows (right), the latter for 5, 10 and 15 MeV measured signals.

Singular Value Decomposition (SVD) [9] is a linear algebra method for the spectral decomposition of a rectangular matrix into orthogonal matrices, which in turn can be transposed to give the truncated pseudo inverse: $\underline{\underline{W}}^{-1} = \underline{\underline{V}} \cdot \underline{\underline{\Sigma}}^{-1} \cdot \underline{\underline{U}}^T$. Here $\underline{\underline{U}}$ and $\underline{\underline{V}}$ are the singular vectors matrices, while $\underline{\underline{\Sigma}}$ is the diagonal matrix containing $\underline{\underline{W}}$ singular values. In order to smooth any computational and experimental noise that might degrade the reconstruction $\underline{\underline{\Sigma}}$ is usually truncated by neglecting all singular values smaller than a custom threshold. Maximum Likelihood-Expectation Maximization (ML-EM) is an iterative algorithm commonly used in tomographic inversions [4, 10]: it makes a first guess (e.g. $F_i^0 = \sum_j \frac{W_{ji}}{\sum_i W_{ji}} S_j$) and evolves according to: $F_i^{n+1} = F_i^n \sum_j \frac{W_{ij}}{\sum_i W_{li}} \frac{S_j}{\sum_k W_{jk} F_k^n}$, n being the iteration number. Every $n_{\text{smoothing}}$ iteration the estimate is smoothed by applying a sliding window average filter to prevent the formation of artifacts. Tikhonov regularization traditionally minimizes the χ^2 statistics and a smoothing operator $\underline{\underline{L}}$ [11–16], that in the present work has been chosen of the first order (i.e. it penalizes steep gradients in the reconstruction). The solution, then, is chosen as: $\underline{\underline{F}} = \arg \min_{\underline{\underline{F}} \geq 0} \left(\|\underline{\underline{W}} \cdot \underline{\underline{F}} - \underline{\underline{S}}\|^2 + \alpha \|\underline{\underline{L}} \cdot \underline{\underline{F}}\|^2 \right)$, where the parameter $\alpha \geq 0$ determines the intensity of the smoothing. Finally, we have also tested a variation of Tikhonov regularization, where the χ^2 has been substituted by the Poisson log-likelihood calculated in ref. [17]: $\ell = \sum_i \left(\left[\underline{\underline{W}} \cdot \underline{\underline{F}} \right]_i + \beta \right) - \sum_i \left(S_i \log \left(\left[\underline{\underline{W}} \cdot \underline{\underline{F}} \right]_i + \beta \right) \right)$, which better describes our data. Here β is a small arbitrary parameter that prevents the cost function from diverging.

In all four methods the smoothing parameters have been set according to the L-curve method, as in ref. [11], while the confidence band of the reconstruction has been computed with the Monte Carlo procedure proposed in ref. [18]. Since each of the methods presented suffers from the generation of artifacts in the reconstructed distribution, cumulative statistics has been studied as well. In particular the RE mean energy and the maximum energy, calculated as the X percentile of the energy distribution, with $X = 90\%$ and 99% and 99.9% .

3 Synthetic tests

The performance of the methods explained in section 2 have been tested on four synthetic RE energy distributions (figure 2): a Gaussian ($\mu = 12$ MeV, $\sigma = 3$ MeV), an exponential ($\tau = 10$ a.u.), a Maxwellian ($\tau = 40$ a.u.) and the sum of a Maxwellian and a Gaussian ($\tau = 40$ a.u., $\mu = 12$ MeV,

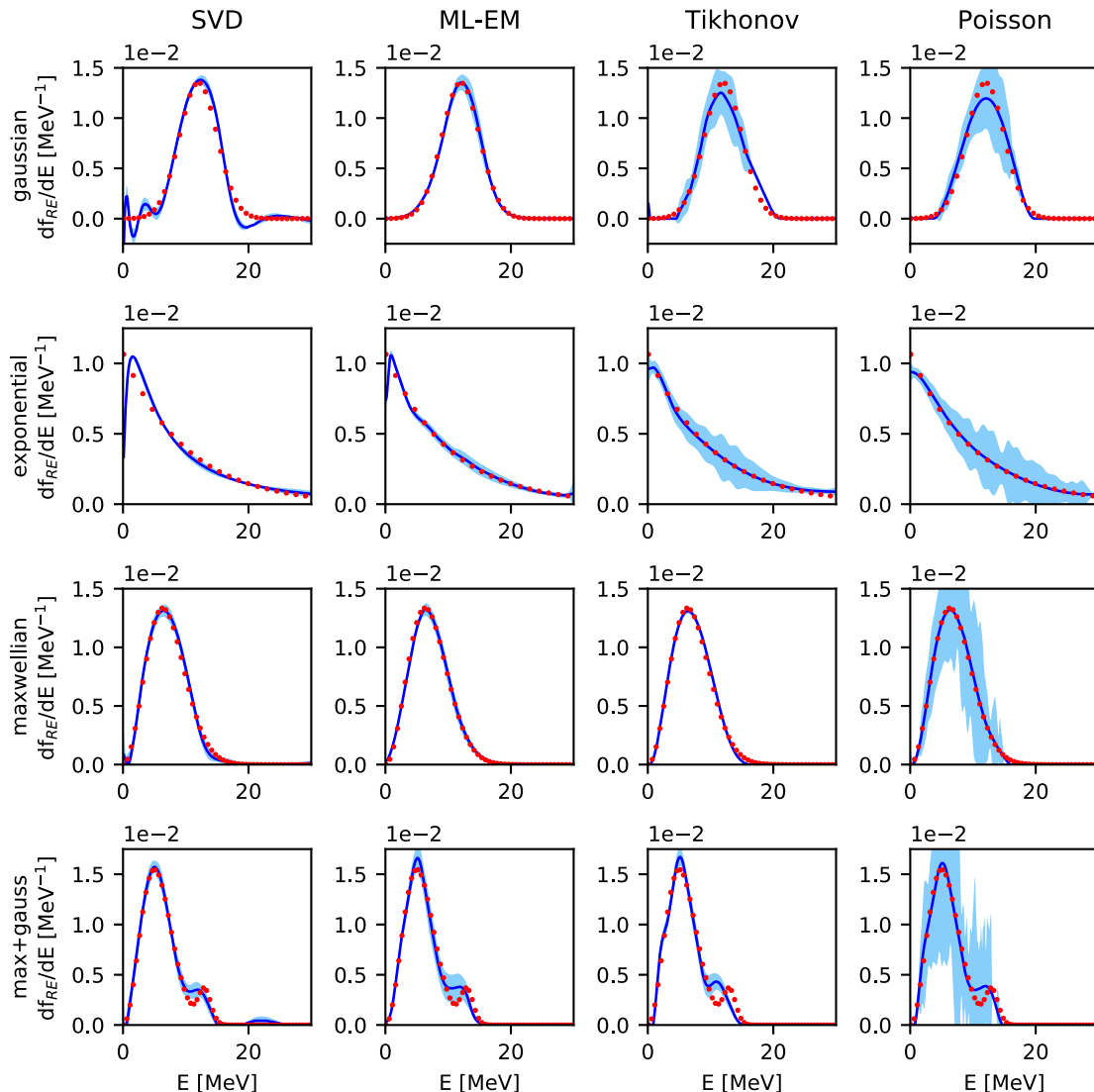


Figure 2. Reconstructions of four synthetic signals: a Gaussian, an exponential, a Maxwellian and the superposition of a Maxwellian with a Gaussian. The RE distribution used to generate the synthetic signal is reported in red dots, while its reconstruction is shown as a blue line with statistical errors shown as a light-blue band.

$\sigma = 1$ MeV). SVD shows severe artifacts in most reconstructions: negative probability functions and evident oscillations around 0 at high and low energy. The other three methods give better results, even though traditional Tikhonov regularization often underestimates the high-energy tail of the distribution. Table 1 reports the estimates of the mean energy of the RE beam ($\langle E \rangle$) and its maximum energy, as defined in section 2. The errors (σ) of the estimates have been computed using the Monte Carlo procedure of ref. [18]. The worst results are again obtained using SVD, which will not be included in the analysis of section 4. The best results are obtained using ML-EM: the estimates always differ from the true statistics less of $\approx 5\%$ and the Monte Carlo error always accounts for this difference within one σ .

Table 1. Mean energy and maximum energy (calculated as the 90, 99, 99.9 percentiles) of the synthetic distribution function shown in figure 2 reconstructed with the four methods presented in section 2. The errors are estimated using a Monte Carlo procedure on the reconstructed RE distribution.

gaussian [MeV]	SVD [MeV]	ML-EM [MeV]	Tikhonov [MeV]	Poisson [MeV]
$\langle E \rangle = 12.00$	11.80 ± 0.10	12.01 ± 0.12	12.18 ± 0.3	11.95 ± 0.4
$E^{90} = 15.76$	15.15 ± 0.10	15.8 ± 0.1	16.47 ± 0.5	15.97 ± 0.5
$E^{99} = 18.91$	16.58 ± 2	18.91 ± 1.7	19.22 ± 1.5	18.10 ± 1.3
$E^{99.9} = 21.25$	25.83 ± 0.3	21.66 ± 5	20.24 ± 1.3	19.02 ± 1.2
exponential	SVD	ML-EM	Tikhonov	Poisson
$\langle E \rangle = 8.48$	8.55 ± 0.06	8.54 ± 0.09	8.79 ± 0.19	8.53 ± 0.4
$E^{90} = 19.32$	20.03 ± 0.3	19.22 ± 0.4	20.34 ± 1.1	19.22 ± 1.6
$E^{99} = 28.27$	28.68 ± 0.5	28.47 ± 0.9	28.88 ± 1.4	28.58 ± 2
$E^{99.9} = 29.80$	29.90 ± 0.4	29.90 ± 0.5	29.90 ± 0.9	29.90 ± 1.8
maxwellian	SVD	ML-EM	Tikhonov	Poisson
$\langle E \rangle = 7.14$	7.04 ± 0.07	7.18 ± 0.06	7.05 ± 0.02	7.10 ± 0.5
$E^{90} = 11.08$	10.78 ± 0.10	11.19 ± 0.15	10.88 ± 0.1	10.98 ± 1.0
$E^{99} = 15.05$	14.13 ± 7	15.46 ± 1.1	13.63 ± 0.2	14.13 ± 2.0
$E^{99.9} = 18.00$	22.78 ± 2	19.22 ± 7	15.05 ± 1.0	15.25 ± 1.9
maxwellian+gaussian	SVD	ML-EM	Tikhonov	Poisson
$\langle E \rangle = 6.25$	6.06 ± 0.11	6.18 ± 0.12	6.11 ± 0.08	6.18 ± 0.6
$E^{90} = 10.98$	10.47 ± 0.4	10.88 ± 0.4	10.58 ± 0.2	10.88 ± 2
$E^{99} = 14.13$	13.32 ± 5	13.63 ± 4	13.32 ± 0.9	13.52 ± 1.7
$E^{99.9} = 15.35$	13.73 ± 6	14.74 ± 4	14.34 ± 0.9	14.24 ± 1.6

4 Application to AUG data

The reconstructions of AUG shot #34084 (see also ref. [3]), obtained using the unfolding methods presented in section 2, are compared in figure 3. All methods retrieve admissible solutions, which well fit the experimental data. The reconstructed RE energy distributions are in good agreement up to ≈ 10 MeV, while they differ in the high-energy tail. As already pointed out in section 3, Tikhonov regularization with χ^2 statistics is prone to underestimate such a tail.

A cut at low energy between 0.1 and 0.5 MeV is always applied to the measured spectra in order to remove the electronic noise due to the acquisition chain. To determine the effect of this loss of information on the final reconstruction, shot #34084 has been analysed after applying different energy cuts from 0.1 to 6 MeV (figure 4). Some minor artifacts appear in a region of $\approx 2 - 3$ MeV right above the cut and the peaks in the high energy part of the distribution are accentuated. However the overall spectral shape of the reconstruction is preserved, showing that the low energy cut determines mainly the reconstruction below ≈ 5 MeV, while the shape of the high-energy part of the RE energy distribution is mostly influenced by the high-energy counts in the HXR spectrum.

We are also interested in studying the minimum number of counts necessary to perform a reconstruction of the RE energy distribution. Statistically independent, uniformly drawn, random samples of the shot #34084 HXR spectrum, with 1, 5, 10 and 20 kcounts have been analysed. The reconstructions performed with Tikhonov minimization applied to the Poissonian statistics show substantial differences already when 20 kcounts draws are analysed, thus suggesting that

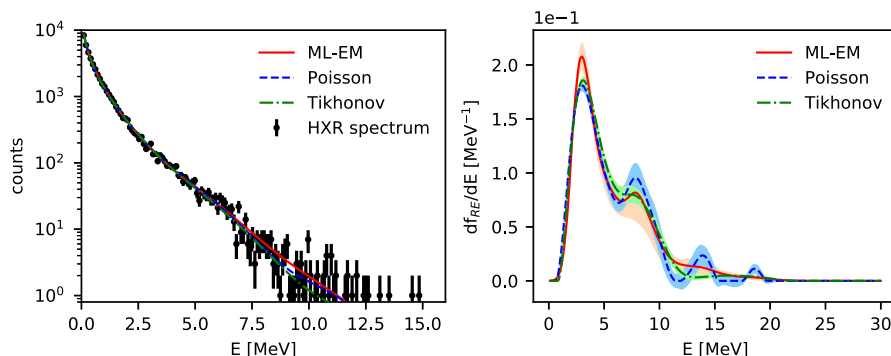


Figure 3. (Left) The experimental HXR spectrum measured during AUG shot #34084 in the time interval 1.00–1.13 s and its reconstruction obtained convolving the RE distributions (see graph on the right) with the transfer matrix W (see figure 1). (Right) REs energy distribution reconstructed from the experimental spectrum shown on the left, using ML-EM, Poisson and Tikhonov regularizations.

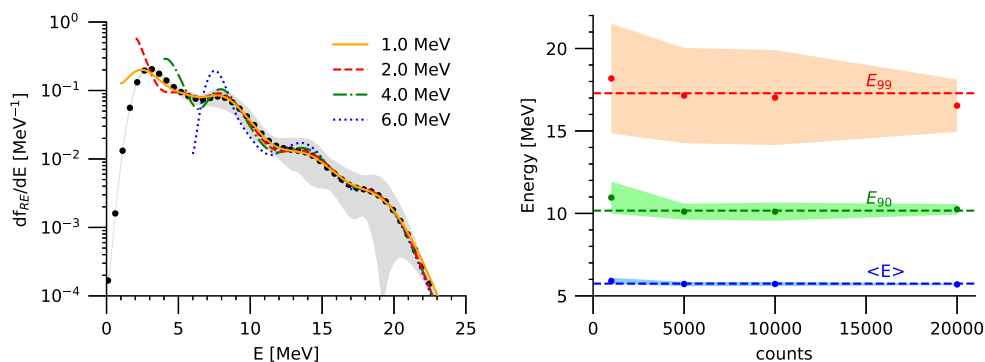


Figure 4. (Left) Multiple reconstructions of the RE energy distribution in AUG shot #34084 for different low energy cuts, performed with ML-EM. Black dots show the reconstruction of figure 3 for reference. (Right) Average and standard deviation of RE distribution statistics obtained by reconstructing random draws of the experimental data set, with variable size (1, 5, 10, 20 kcounts), using ML-EM. Dashed lines refer to the statistics of the reconstruction in figure 3.

the signal to noise ratio of the high-energy tail of the RE Bremsstrahlung emission is unfavorable for the Poissonian cost function and that the two peaks above 10 MeV in figure 3 are probably an artefacts. Better results are achieved using ML-EM and traditional Tikhonov regularization, which can retrieve the overall shape of RE energy distribution even with only 5/10 kcounts. When only global features of the RE beam are sought, the above recommendation can be relaxed: figure 4 shows the average and standard deviation of $\langle E_{RE} \rangle$, E_{RE}^{90} and E_{RE}^{99} calculated on multiple draws. The inference of the mean RE energy gives good results also on spectra with only 1 kcounts, while the estimates for the maximum energy are reliable on average up to 5 kcounts (the higher the percentile of the estimate, the more counts are needed).

5 Conclusions

Four unfolding techniques have been applied to the reconstruction of the runaway electrons energy distribution from their Bremsstrahlung HXR emission. ML-EM has produced the most reliable reconstruction of the synthetic signals. With all four methods, the mean and maximum energy of the RE beam has been estimated within 5% from the true value, proving those estimates to be robust against the presence of artifacts in the reconstruction. The tests performed on experimental data show that ML-EM and Tikhonov with χ^2 statistics give good results also when a generous low-energy cut is applied. The two methods also perform well with limited statistics, reaching a maximum time resolution of $\approx 10^{-2}$ s if the complete spectral information is required, which can be pushed to $\approx 10^{-3}$ s for the estimate of the cumulative statistics.

Acknowledgments

This work has been carried out within the framework of the EUROfusion Consortium and has received funding from the Euratom Research and Training Programme 2014–2018 and 2019–2020 under Grant Agreement No. 633053. The views and opinions expressed herein do not necessarily reflect those of the European Commission.

References

- [1] D. Rigamonti et al., *The upgraded JET gamma-ray cameras based on high resolution/high count rate compact spectrometers*, *Rev. Sci. Instrum.* **89** (2018) 10I116.
- [2] M. Nocente et al., *Gamma-ray spectroscopy at MHz counting rates with a compact LaBr₃ detector and silicon photomultipliers for fusion plasma applications*, *Rev. Sci. Instrum.* **87** (2016) 11E714.
- [3] M. Nocente et al., *High resolution gamma-ray spectrometer with MHz capabilities for runaway electron studies at ASDEX Upgrade*, *Rev. Sci. Instrum.* **89** (2018) 10I124.
- [4] A.E. Shevelev et al., *Reconstruction of distribution functions of fast ions and runaway electrons in fusion plasmas using gamma-ray spectrometry with applications to ITER*, *Nucl. Fusion* **53** (2013) 123004.
- [5] A. Dal Molin, *Reconstruction of the velocity space of runaway electrons by spectral measurements of the hard x-ray emission in tokamaks*, Ph.D. Thesis (2021), <https://boa.unimib.it/handle/10281/304289>.
- [6] M. Salewski et al., *Combination of fast-ion diagnostics in velocity-space tomographies*, *Nucl. Fusion* **53** (2013) 063019.
- [7] M. Nocente et al., *Conceptual design of the radial gamma ray spectrometers system for α particle and runaway electron measurements at ITER*, *Nucl. Fusion* **57** (2017) 076016.
- [8] T. Goorley et al., *Initial MCNP6 release overview*, *Nucl. Technol.* **180** (2012) 298.
- [9] D. Kalman, *A singularly valuable decomposition: the SVD of a matrix*, *Coll. Math.* **27** (1996) 2.
- [10] E. Panontin et al., *First spatially resolved measurements of the D-³He α -particle source with the upgraded JET gamma-ray camera*, *Rev. Sci. Instrum.* **92** (2021) 053529.
- [11] A.S. Jacobsen et al., *Inversion methods for fast-ion velocity-space tomography in fusion plasmas*, *Plasma Phys. Control. Fusion* **58** (2016) 045016.

- [12] B. Madsen et al., *Fast-ion velocity-space tomography using slowing-down regularization in EAST plasmas with co- and counter-current neutral beam injection*, *Plasma Phys. Control. Fusion* **62** (2020) 115019.
- [13] B. Madsen et al., *Tomography of the positive-pitch fast-ion velocity distribution in DIII-D plasmas with Alfvén eigenmodes and neoclassical tearing modes*, *Nucl. Fusion* **60** (2020) 066024.
- [14] M. Weiland et al., *Enhancement of the FIDA diagnostic at ASDEX Upgrade for velocity space tomography*, *Plasma Phys. Control. Fusion* **58** (2016) 025012.
- [15] M. Weiland et al., *Phase-space resolved measurement of 2nd harmonic ion cyclotron heating using FIDA tomography at the ASDEX Upgrade tokamak*, *Nucl. Fusion* **57** (2017) 116058.
- [16] M. Salewski et al., *High-definition velocity-space tomography of fast-ion dynamics*, *Nucl. Fusion* **56** (2016) 106024.
- [17] J.M. Bardsley and N. Laobeul, *Tikhonov regularized Poisson likelihood estimation: theoretical justification and a computational method*, *Inverse Probl. Sci. Eng.* **16** (2008) 199.
- [18] D.G. Shirk and N.M. Hoffman, *Monte-Carlo error analysis in x-ray spectral deconvolution*, *Rev. Sci. Instrum.* **56** (1985) 809.
- [19] M. Salewski et al., *Fast-ion energy resolution by one-step reaction gamma-ray spectrometry*, *Nucl. Fusion* **56** (2016) 046009.
- [20] M. Salewski et al., *Velocity-space observation regions of high-resolution two-step reaction gamma-ray spectroscopy*, *Nucl. Fusion* **55** (2015) 093029.

Runaway electron velocity-space observation regions of bremsstrahlung hard X-ray spectroscopy

E. Panontin,^{a,1} M. Nocente,^{a,b} A. Dal Molin,^b J. Eriksson,^c G. Gorini,^{a,b} E. Perelli Cippo,^{a,b} D. Rigamonti,^b M. Salewski,^d M. Tardocchi^b, and and JET Contributors²

^aDipartimento di Fisica "G. Occhialini", Università degli Studi di Milano-Bicocca, Milano, Italy

^bIstituto per la Scienza e Tecnologia dei Plasmi, Consiglio Nazionale delle Ricerche, Milano, Italy

^cDepartment of Physics and Astronomy, Uppsala University, Uppsala, Sweden

^dDepartment of Physics, Technical University of Denmark, Kgs. Lyngby, Denmark

¹ Electronic mail: e.panontin@campus.unimib.it

² See the author list of "Overview of JET results for optimising ITER operation" by J. Mailloux et al. to be published in Nuclear Fusion Special issue: Overview and Summary Papers from the 28th Fusion Energy Conference (Nice, France, 10-15 May 2021)

ABSTRACT

The reconstruction of the distribution function of runaway electrons (RE) in magnetically confined fusion plasmas gives insights on the runaway electron beam dynamics during plasma disruptions. In view of enabling a two-dimensional, energy-pitch reconstruction of the RE velocity space, in this work we present a calculation of the weight functions for the bremsstrahlung emission by the REs. The weight functions allow bridging the bremsstrahlung spectrum with the RE velocity space, as they tell the region of the velocity space that contributes to a particular spectral measurement. The results are applied to investigate the RE velocity-space sensitivity of the hard X-ray diagnostic installed at the Joint European Torus.

1 INTRODUCTION

The study of runaway electrons (REs) in magnetically confined fusion plasmas focus on the development of suppression or at least mitigation techniques for safeguarding the structural integrity of future large devices such as ITER [1]. The effects of such techniques on the dynamics of the RE phase-space distribution can be studied using unfolding algorithms that reconstruct the RE distribution from experimental measurements: in particular the 1D energy distribution can be retrieved from the measurements of the bremsstrahlung photons emitted in the Hard X-Ray (HXR) energy region during collisions between REs and ions in the background plasma [2, 3, 4, 5].

Such an analysis is made possible on the Joint European Torus (JET) thanks to three sets of HXR diagnostics which observe the plasma on different lines of sight (LOS). A 7.62 cm × 15.2 cm (width × depth) cylindrical LaBr₃ doped Ce spectrometer (KM6T), coupled with a traditional PMT, observes the plasma tangentially [15]. Its LOS runs on the equatorial plane and spans octants from 8 to 3, intersecting the center of the poloidal plane with an angle of about 50 deg with respect of the toroidal axis. Two spectrometers (KM6S1 and KM6S2), equipped with similar scintillators as KM6T and coupled with a traditional PMT as well, observe the plasma core vertically [17]. Finally the gamma camera

upgrade (GCU) observes a poloidal section of the torus with a set of 19 spectrometers arranged in two perpendicular arrays of 10×9 detectors [16]. Each detector is made of a $2.54 \text{ cm} \times 1.69 \text{ cm}$ $\text{LaBr}_3:\text{Ce}$ scintillator coupled to a silicon photomultiplier (SiPM) [16]. All the diagnostics here described are usually operated with a energy dynamic range of $[0, 30] \text{ MeV}$.

The 1D analysis of the energy distribution of REs can be extended to the 2D velocity-space thanks to the fact that the bremsstrahlung cross section depends on both the energy of the RE and the direction of emission [6, 7, 8], which in turn is defined by the pitch angle and the gyro-phase of the particle. This probability is also named weight function and has been widely used for the study of fast-ions [10, 9] thanks to its many fold relevance. In fact, weight functions allow to study the velocity-space sensitivity of the HXR spectrometer under consideration: in particular they show to which regions the diagnostic is most sensitive to and which ones are beyond the reach. They also give hints on the contribution of the various regions of the RE 2D velocity distribution function to the measurements and they can be used to calculate synthetic measurements from RE distributions computed from first principles simulations. Finally, these weight functions are a key piece of 2D reconstruction of RE distribution; however, due to the challenges of inverting a highly undetermined system, such reconstruction will be attempted in future works. A 3D reconstruction can also be achieved by calculating orbit-based weight functions [11, 12, 13]. In this sense, the entries of the weight functions calculated in the present work represent the expected bremsstrahlung signal emitted by an RE in a certain instant of its orbit: the sum over all the RE orbit (i.e. all energy and pitch assumed by the RE during its orbit) gives a 3D orbit-based weight function.

In the present work we will present the weight functions of the RE HXR emission, expressed as a function of energy and pitch-angle of the REs, for the HXR diagnostics installed at JET. In section 2 we introduce 2D weight functions and their computations, while in section 3 we present some examples of weight functions calculated for two Lines Of Sight (LOS) installed at JET: a tangential and a radial one.

2 WEIGHT FUNCTIONS

2D velocity-space weight functions $W(E_{measured}, E_{RE}, p_{RE})$ represent the probability that an RE having energy E_{RE} and pitch p_{RE} will emit a photon of energy E_{HXR} that will subsequently deposit an energy $E_{measured}$ in the detector. In the present work $p_{RE} = \frac{v_{RE,\parallel}}{v_{RE}}$ is defined using the same definition commonly used in fast-ions works in order to make more evident the direction of motion the the REs with respect to the magnetic field. With this definition, on JET REs mostly have negative pitch. In order to avoid confusion, it is worth underlying that in many study about REs the pitch is defined using the opposite of the RE velocity so that it can be positive.

$W(E_{measured}, E_{RE}, p_{RE})$ links the RE 2D velocity-space probability distribution function $F(E_{RE}, p_{RE})$ to the measurement of the bremsstrahlung spectrum $S(E_{measured})$ emitted by REs. In particular it defines the inverse problem:

$$S(E_m) = \int_{LOS} n_{RE}(\underline{x}) \int_0^\infty \int_{-1}^1 W(E_m, E_{RE}, p_{RE}, \underline{x}) F(E_{RE}, p_{RE}, \underline{x}) dp_{RE} dE_{RE} d\underline{x}. \quad (1)$$

Here $S(E_m)$ is the number of counts having energy in an energy bin centered in E_m and having width ΔE : $E_{measured} \in [E_m - \Delta E, E_m + \Delta E]$. $S(E_m)$ can be conveniently normalized to the time interval

over which the measurement has been performed and to the width of the energy bin ΔE , in which case its units are [counts / s / MeV]. $S(E_m)$ is the sum, performed over the detector LOS, of the signals generated by all REs having the desired energy E_{RE} and pitch p_{RE} . In each position \underline{x} inside the LOS, the number of such REs is $n_{RE}(\underline{x})F(E_{RE}, p_{RE}, \underline{x}) dp_{RE} dE_{RE} d\underline{x}$ and the signal they generated in the detector can be calculated as $W(E_m, E_{RE}, p_{RE}, \underline{x}) n_{RE}(\underline{x})F(E_{RE}, p_{RE}, \underline{x}) dp_{RE} dE_{RE} d\underline{x}$. Thus, $W(E_{measured}, E_{RE}, p_{RE}, \underline{x})$ can be seen as the spectrum generated by a mono energy and mono pitch beam, normalized to the number of REs, and its units are the same as $S(E_m)$, in this case: [counts / s / MeV].

As already pointed out $W(E_{measured}, E_{RE}, p_{RE}, \underline{x})$ can be divided in two independent processes:

$$W(E_{measured}, E_{RE}, p_{RE}, \underline{x}) = \int_0^\infty W_{DRF}(E_{measured}, E_{HXR}) \cdot W_B(E_{HXR}, E_{RE}, p_{RE}, \underline{x}) dE_{HXR} \quad (2)$$

where $W_{DRF}(E_{measured}, E_{HXR})$ is the Detector Response Function that describes the interactions between hard X-rays of energy E_{HXR} and the scintillator, and it has been calculated with the MCNP code [14]. On the other hand $W_B(E_{HXR}, E_{RE}, p_{RE}, \underline{x})$ is the emission rate of the bremsstrahlung emission and has been calculated using the GENESIS code [6], that implements the semi-empirical cross section $\frac{d\sigma}{dE_{HXR} d\Omega}(E_{HXR}, E_{RE}, \theta)$ introduced in Refs. [7, 8]:

$$W_B(E_{HXR}, E_{RE}, p_{RE}) = \frac{|v_{RE}|}{2\pi} n_i d\Omega \int_0^{2\pi} \frac{d\sigma}{dE_{HXR} d\Omega}(E_{HXR}, E_{RE}, \theta(p_{RE}, \phi, \alpha)) d\phi. \quad (3)$$

where $|v_{RE}|$ is the speed of the RE, n_i is the ion density in the background plasma, $d\Omega$ is the solid angle subtended by the detector. The double differential cross section $\frac{d\sigma}{dE_{HXR} d\Omega}$ is averaged over all possible gyro-phases ϕ of the RE orbit in \underline{x} . In particular it is a function of the angle of emission $\theta = \arccos(L\hat{O}S \cdot \hat{v}_{RE})$, which in turn can be calculated from the particle pitch, its gyro-phase and the angle α between the versor $L\hat{O}S$ defining the direction of the LOS and the magnetic field.

For the sake of simplicity, in section 3 we consider a purely toroidal and uniform magnetic field, and a point-shaped RE beam positioned at the centre of the LOS under consideration. This simple situation allows us to uncover the relationship between the direction of the LOS and the magnetic field, which is the building block necessary to interpret weight functions calculated considering the full geometry of the LOS and the experimental magnetic equilibrium.

3 APPLICATION TO JET DIAGNOSTICS

In the geometry adopted in this work (see section 2), only the toroidal magnetic field is considered, thus all radial LOS observe the magnetic field at an angle of 90 deg. Between one detector and another the main differences are the dimensions of the scintillator crystal and the distance of the spectrometer from the plasma, i.e. the solid angle observed by the LOS. As an example of the weight functions of radial LOS, in figure 1 we present the 2D weight function for 1 MeV and 10 MeV signals measured by the radial LOS of channel 5 of the JET Gamma Camera Upgrade (GCU or also KN3G) [16]. In this particular case, particles having negative and positive pitch exhibit a symmetric behaviour and the sensitivity of the diagnostics has a peak at $p = 0$. The width of this peak is inversely proportional to the energy of the particle, as in fact the more energetic the particle the more polarized the emission. The weight functions show a cutoff for $E_{RE} < E_{measured}$ as in fact the conservation of energy imposes that the energy of the emitted bremsstrahlung photon must be

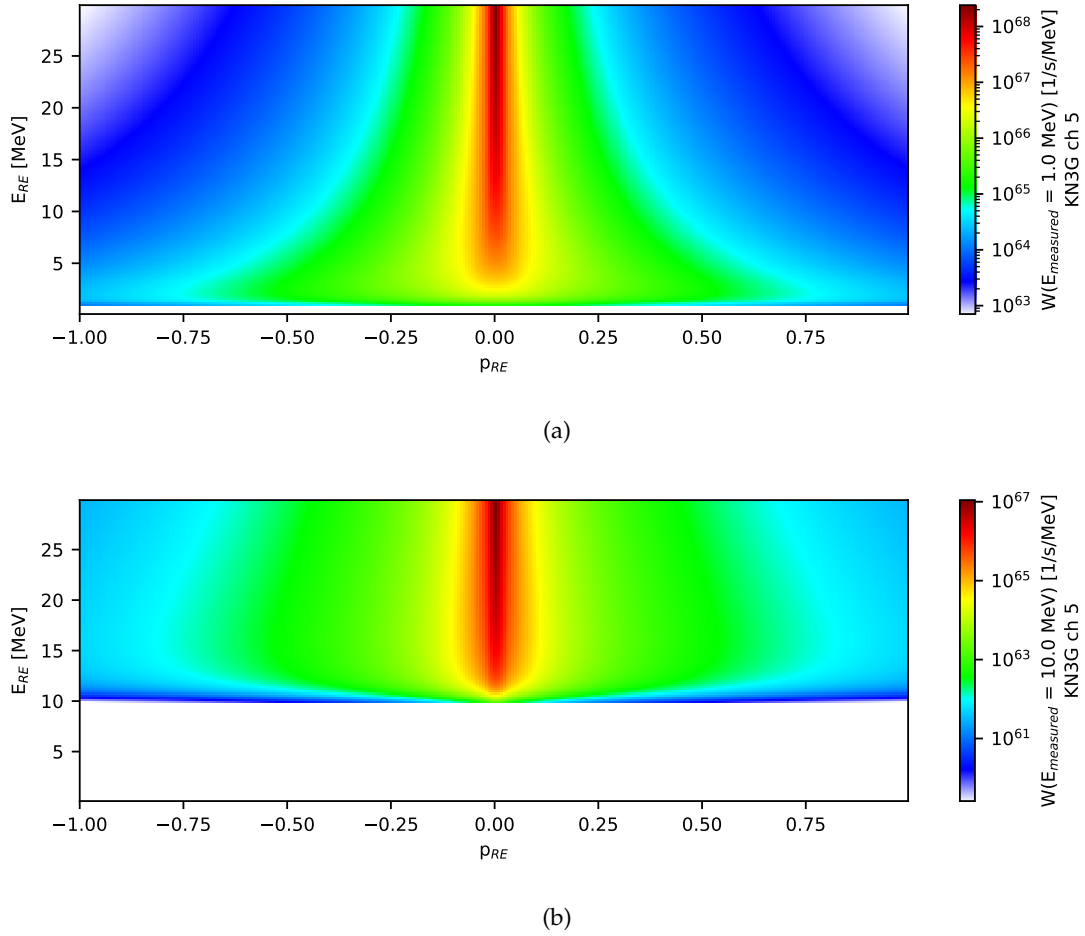


Figure 1: Weight functions of channel 5 of JET GCU, that has a radial LOS, considering an energy measured by the detector of $E_{measured} = 1$ MeV (a) and $E_{measured} = 10$ MeV (b).

lower than the energy of the emitting RE. This is clearly visible in figures 1(a) and 1(b), where the weight functions for a measured energy of 1 MeV and 10 MeV are presented and the cutoff is at energy $E_{RE} = 1$ MeV and $E_{RE} = 10$ MeV respectively. As the measured energy increases, the position of the sensitivity peak remains constant and the symmetry between negative and positive pitches is also conserved. The weight functions of the other channels of the GCU and of the two vertical spectrometers are similar to the one presented in figure 1, the only difference is in the maximum value of the weight function, which changes according to the distance of the detector from the plasma and the dimension of the crystal.

The study of the weight functions for KM6T is made more complex by the fact that the angle α between its tangential LOS and the magnetic field depends on the poloidal position of the point-shaped RE beam considered for the calculations. In figure 2, the beam is placed at the center of the poloidal plane, where the angle α is about 50 deg. Also in this case, two energies are considered: $E_{measured} = 1$ MeV and $E_{measured} = 10$ MeV. The weight functions lose the symmetry observed in figure 1 for radial LOS. In figure 2 the sensitivity peak is positioned at $p = \cos(50 \text{ deg}) = 0.64$ and the diagnostics is 3 order of magnitudes more sensitive to particles having positive pitch (i.e. moving

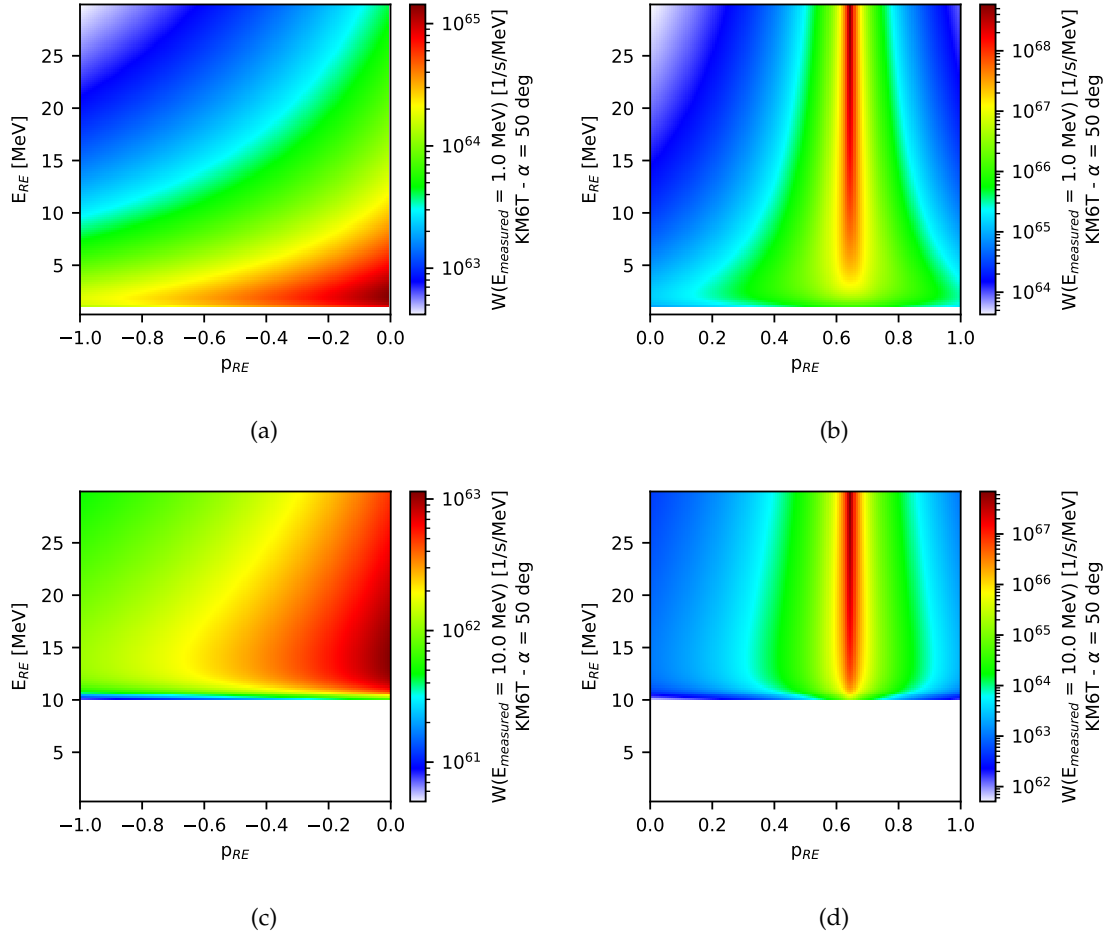


Figure 2: Weight functions of the JET tangential spectrometer (KM6T) calculated for $E_{measured} = 1$ MeV (a) (b) and $E_{measured} = 10$ MeV (c) (d). The RE beam has been placed at the center of the poloidal plane, where the LOS forms an angle $\alpha = 50$ deg with respect to the magnetic field.

clockwise) than particles having negative pitch (i.e. moving counterclockwise). As before, the width of the sensitivity peak in the pitch-axis depends of the RE energy and the weight functions show a cutoff at $E_{RE} < E_{measured}$. In figure 2, the contributions of particles having positive pitch (figures (b) and (d)) and negative pitch (figures (a) and (c)) are reported separately with different color scales in order to include as many details as possible. The detection of the backward emission from particles having negative pitch is more probable if E_{RE} is close to $E_{measured}$, this is again an effect of the anisotropy of the bremsstrahlung emission, which is more pronounced for higher E_{RE} .

In many JET disruptions, the RE beam often drifts to the high-field side and the α between KM6T LOS and the magnetic field at the position of the RE beam decreases. The minimum value admissible is $\alpha = 0$ deg, which is considered in figure 3. In this case the weight function is peaked at $p = 1$ and the width of the peak is narrower than in figures 1 and 2, regardless of the measured energy or the energy of the RE. This is due to the fact that the width of the distribution of the emission angle sampled in the gyro-phase scan is proportional to α itself and for $\alpha = 0$ deg the detector observes the photon emitted with the same θ regardless of the RE gyro-phase. Moving the position of the core

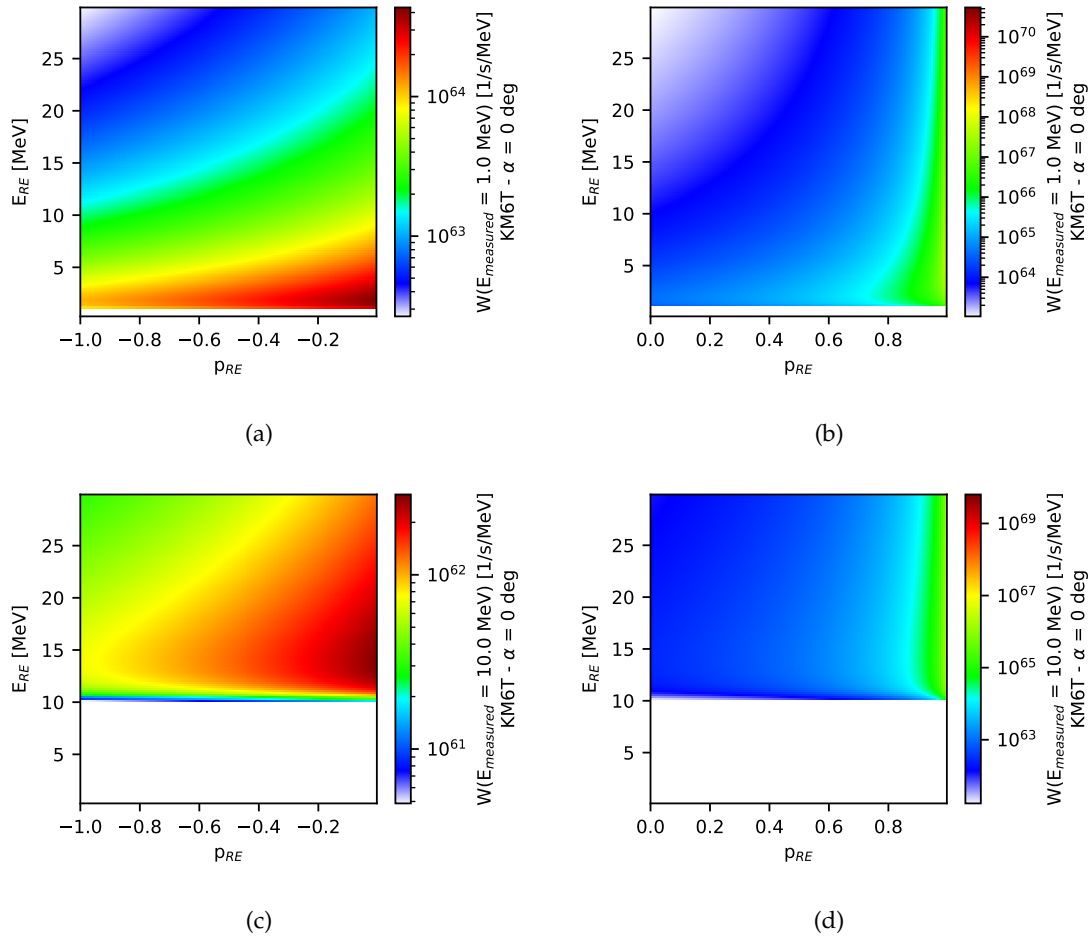


Figure 3: Weight functions of the JET tangential spectrometer (KM6T) calculated for $E_{measured} = 1$ MeV (a) (b) and $E_{measured} = 10$ MeV (c) (d). The RE beam has been placed at the high-field side, where the LOS forms an angle $\alpha = 0$ deg with respect to the magnetic field.

of the RE beam from the high-field side to the low-field side, the angle between KM6T LOS and the toroidal magnetic field can vary from $\alpha = 0$ deg to $\alpha = 60$ deg. The peak in sensitivity of the weight function for KM6T, then, moves from $p = 1$ to $p = 0.5$ depending of the position of the RE beam and the total sensitivity of the diagnostics, calculated as $\sum_{E_{measured}, E_{RE}, p_{RE}} \underline{W}$, decreases of 1 order of magnitude.

In general, the weight function of a LOS exhibits a maximum for $p = \cos(\alpha)$, in fact for such a pitch there exists a gyro-phase for which the detector observes the photons emitted frontward, i.e. at $\theta = 0$ deg. In principle one can set this peak on a desired pitch by varying the LOS inclination, thus scanning all the pitch-space. The width of this peak depends on the angle α between the LOS and the magnetic field: the peak is wider for α close to 90 deg and is narrower for α close to 0 deg or 180 deg. Finally it is worth noting that on JET the plasma current flows clockwise also during plasma disruptions and this means that REs have negative pitch. For example, in Refs. [4, 2, 3] the unfolding of the RE 1D energy distribution has been conducted supposing that all REs have $p = -1$. KM6T is not very sensitive to those particles and, in order to maximise the sensitivity of a tangential LOS to

the RE emission, it should have an orientation opposite to the one of KM6T. One such a LOS would also ease a 2D reconstruction of the velocity-space distribution of REs as its weight function would exhibit a peak for a negative pitch. The different position of the sensitivity peak observed in figures 1, 2 and 3 also suggests the possibility to use multiple LOS with different orientations to discriminate between different RE orbits and calculate orbit-based weight functions, similarly to what has been recently done for fast ions in refs. [11, 12, 13].

4 CONCLUSIONS

In the present work, the 2D velocity-space weight functions for channel 5 of the JET gamma camera upgrade and for JET tangential spectrometer KM6T have been presented as a function of the energy E_{RE} and pitch p_{RE} of the runaway electrons. In particular the weight function of the gamma camera channel is representative of all the spectrometers having radial LOS installed at JET. In the calculations presented a point-shaped runaway electron beam has been considered and the magnetic field has been set to be toroidal. The weight functions showed a peak in the diagnostics sensitivity for a pitch corresponding to the minimum angle of emission observed by the detector. It has been noted that the position and width of such a peak is determined by the angle between the LOS and the magnetic field. These matrices pave the way to a 2D reconstruction of the velocity-space distribution of runaway electrons, which will be attempted in future works.

ACKNOWLEDGEMENTS

This work has been carried out within the framework of the EUROfusion Consortium and has received funding from the Euratom research and training programme 2014-2018 and 2019-2020 under grant agreement No 633053. The views and opinions expressed herein do not necessarily reflect those of the European Commission.

REFERENCES

- [1] M. Gobbin et al, *Runaway electron mitigation by 3D fields in the ASDEX-Upgrade experiment*, *Plasma Phys. Control. Fusion* **60** (2018) 014036
- [2] A. Dal Molin *PhD thesis* (2021) <https://boa.unimib.it/handle/10281/304289>
- [3] E. Panontin et al, *Comparison of Unfolding Methods for the Inference of Runaway Electron Energy Distribution from γ -ray Spectroscopic Measurements*, *JINST* **16** (2021) C12005
- [4] M. nocente et al, *High resolution gamma-ray spectrometer with MHz capabilities for runaway electron studies at ASDEX Upgrade*, *Rev. Sci. Instrum.* **89** (2018) 10I124
- [5] A.E. Shevelev et al, *Reconstruction of distribution functions of fast ions and runaway electrons in fusion plasmas using gamma-ray spectrometry with applications to ITER*, *Nucl. Fusion* **53** (2013) 123004
- [6] M. nocente et al, *Conceptual design of the radial gamma ray spectrometers system for α particle and runaway electron measurements at ITER*, *Nucl. Fusion* **57** (2017) 076016
- [7] F. Salvat et al, *Monte Carlo simulation of bremsstrahlung emission by electrons*, *Radiat. Phys. Chem.* **75** (2006) 1201-1219

- [8] F. Salvat and J. M. Fernández-Varea *Semiempirical cross sections for the simulation of the energy loss of electrons and positrons in matter*, *Nucl. Instrum. Methods Phys. Res. B* **63** (1992) 255-269
- [9] M Salewski et al, *Fast-ion energy resolution by one-step reaction gamma-ray spectrometry*, *Nucl. Fusion* **56** (2016) 046009
- [10] M Salewski et al, *Velocity-space observation regions of high-resolution two-step reaction gamma-ray spectroscopy*, *Nucl. Fusion* **55** (2015) 093029
- [11] L. Stagner, and W. W. Heidbrink, *Action-angle formulation of generalized, orbit-based, fast-ion diagnostic weight functions*, *Phys. Plasmas* **24** (2017) 092505
- [12] H. Järleblad et al., *Fast-ion orbit sensitivity of neutron emission spectroscopy diagnostics*, *Rev. Sci. Instrum.* **92** (2021) 043526
- [13] H. Järleblad et al., *Orbit Weight Functions for Neutron Emission and One-step Reaction Gamma-ray Spectroscopy*, *17th IAEA Technical Meeting on Energetic Particles and Theory of Plasma Instabilities in Magnetic Confinement Fusion* (2021)
- [14] T. Goorley et al., *Initial MCNP6 Release Overview*, *Nuclear Technology* **180** (2012) 298-315
- [15] M. Nocente et al., *A new tangential gamma-ray spectrometer for fast ion measurements in deuterium and deuterium-tritium plasmas of the Joint European Torus*, *Rev. Sci. Instrum.* **92** (2021) 043537
- [16] D. Rigamonti et al., *The upgraded JET gamma-ray cameras based on high resolution/high count rate compact spectrometers*, *Rev. Sci. Instrum.*, **89** (2018) 10I116
- [17] M. Nocente et al., *High Resolution Gamma Ray Spectroscopy at MHz Counting Rates With LaBr₃ Scintillators for Fusion Plasma Applications*, *IEEE Transactions on Nuclear Science*, **60.2** (2013) 1408–1415